Università degli Studi di Roma Tor Vergata

Dipartimento di Ingegneria dell'Impresa "Mario Lucertini"
Ingegneria per la Progettazione e Produzione Industriale

TOR VERGATA
UNIVERSITY OF ROME

Towards Digital Twin Technologies for Ascending Aortic Aneurysm Growth Prediction and Real-Time Diagnosis

Supervisor:
Prof. **Pier Paolo Valentini**

Candidato:
Leonardo Geronzi

Co-Supervisor:
PhD **Michel Rochette**

Corso di Dottorato: 36° Ciclo
Anno Accademico 2022/2023

Contents

Preface

This PhD dissertation is submitted to the University of Rome "Tor Vergata" in fulfillment of the requirements for the degree of Doctor of Philosophy. This manuscript consists of a recapitulation of the research work carried out from September 2020 to September 2023 between Ansys France, Villeurbanne, France and the Department of Enterprise Engineering "Mario Lucertini" of the University of Rome "Tor Vergata", Rome, Italy, as part of the European research project MeDiTATe, the Medical Digital Twin for Aneurysm Prevention and Treatment. The work has been supervised by Professor Pier Paolo Valentini and PhD Michel Rochette. Professor Marco Evangelos Biancolini, as principal investigator of the MeDiTATe project, has assumed a pivotal role in providing guidance for the research endeavours within this project.

List of Abbreviations

AA abdominal aorta

AI artificial intelligence

AAA abdominal aortic aneurysm

AAr aortic arch

AsA ascending aorta

AsAA ascending aortic aneurysm

AUROC area under the receiver operating characteristic

BC boundary condition

BAV bicuspid aortic valve

BCA brachiocephalic artery

CN compactness

CT Computed Tomography

CAE Computer-Aided Engineering

CFD computational fluid-dynamics

CSM computational solid mechanics

CVS cardiovascular system

DA descending aorta

DL deep learning

DP Design Point

DT Digital Twin

DTr Decision Tree

ECG electrocardiogram

FE Finite Element

FN false negative

FP false positive

FDM Finite Difference Method

FEM Finite Element Method

FMU Functional Mock-up Unit

FOM full order model

FSI fluid-structure interaction

FVM Finit Volume Method

GE generalization

GR growth rate

GARS Genetic Aggregation Response Surface

HPC high performance computing

ICP iterative closest point

ITK Insight Toolkit

KNN K-nearest Neighbours

LD Liniar Discriminant

LM Levenberg-Marquardt

LR Logistic Regression

LHR likelihood ratio

LOO leave-one-out

LSA left subclavian artery

LCCA left common carotid artery

LVOT Left Ventricular Outflow Tract

ML machine learning

MRA Magnetic Resonance Angiography

MRI Magnetic Resonance Imaging

MSE mean square error

NB Naive Bayes

NIPALS non-linear iterative partial least squares

ODE ordinary differential equation

PCA principal component analysis

PDE partial differential equation

PLS partial least squares

POD proper orthogonal decomposition

RS Response Surface

RBF radial basis function

ROM reduced order model

RMSE root mean square error

SP Source Point

SSA statistical shape analysis

SSM statistical shape model

SVD singular value decomposition

SVM Support Vector Machine

TA thoracic aorta

TN true negative

TP true positive

TAV tricuspid aortic valve

TEE transesophageal echocardiography

TTE transthoracic echocardiography

VTK Visualization Toolkit

VENC velocity encoding

VMTK Vascular Modelling Toolkit

WSS wall shear stress

List of Figures

The captions provided below have been abbreviated for clarification purposes.

Appendix A

List of Tables

The captions provided below have been abbreviated for clarification purposes

Summary

In this thesis, some of the fundamental aspects related to the implementation of a Digital Twin of the thoracic aorta for the study of ascending aortic aneurysms have been addressed. The work is motivated by the ongoing demand for digital solutions capable of rapidly extracting biomarkers for the accurate diagnosis and prognosis of this pathology. The current guidelines for the ascending aortic aneurysm treatment recommend surgery mainly according to the maximum diameter value. This criterion has already proven to be often inefficient in identifying patients at high risk of aneurysm growth and rupture.

A fundamental requirement of a Digital Twin is its ability to follow a system over time. Moreover, a virtual model reproducing a physical system should be capable of predicting its evolution and future state. Consequently, in creating a replica of a pathological organ such as an aorta with an aneurysm, the possible evolution of the disease over the years and the subsequent growth of the vessel should be considered. However, ascending aortic aneurysm growth prediction is still challenging in clinics. In this context, the first portion of this work concerns the determination of shape features able to improve the prediction of the aneurysm growth. In this study, we included 70 patients with aneurysm, for which at least two longitudinal 3D acquisitions were available. We exploited these data to compute the growth rate and evaluate the evolution of the disease. From the first acquisition of each patient, a set of local shape features (computed directly from each aortic geometry) and a collection of global shape features (derived from the entire dataset using mathematical reduction techniques) were extracted. The correlation between local shape features and growth rate has been investigated. After, the dataset was divided into two classes according to the growth rate value: all patients with growth rate not exceeding 3 mm/year, risk threshold identified in the clinical guidelines, were part of the low-risk group. The remaining were part of the high-risk group due to rapid growth. The local shape features were first employed to assess the ascending aortic aneurysm risk of growth. To this aim, we used six different classifiers with

input data exclusively from the first exam to predict the class to which each patient belonged. A first classification was performed using only the maximum diameter and a second with all the local shape features together. The performances have been evaluated by computing accuracy, sensitivity, specificity, area under the receiver operating characteristic curve and positive (negative) likelihood ratio. Subsequently, iso-topological surface meshes were created using radial basis function mesh morphing. Statistical shape analysis was performed and global shape features were identified. At this point, all the shape features were used and compared to directly infer the aneurysm growth rate. Three different regression models were set and compared for growth rate prediction based on local and global shape features.

In predicting the risk of growth, the classifiers based on local shape features outperformed the same ones based only on the maximum diameter. Globally, the classifiers based on local shape features outperformed the corresponding classifiers based on the maximum diameter alone. Among the local shape features-based classifiers, relatively good results in terms of accuracy (90%), sensitivity (77.8%), specificity (91.8%), area under the receiver operating characteristic curve (0.83), positive (9.5) and negative (0.24) likelihood ratio were returned by support vector machine. For the direct prediction of the growth rate, the prediction root mean square error from leave-one-out cross-validation went from 0.112 mm/month for local shape features to 0.066 mm/month when using global shape features. In general, aneurysms close to the root with a large initial diameter reported faster growth. This demonstrates how automatic shape feature detection combined with risk classification criteria could be crucial in planning the follow-up for patients with ascending aortic aneurysms and might provide a crucial contribution for predicting the aneurysm growth and rupture. Moreover, this information is essential in enabling the Digital Twin to dynamically adapt its anatomical representation over time and make predictions about potential long-term clinical outcomes.

A second issue that we addressed in this research concerns the generation of a high-fidelity model that should serve as foundation of an accurate Digital Twin in reproducing the kinematics of a real aorta. It ensures that predictions closely mirror real-world physiological responses, enabling effective treatment planning and personalized simulations. In this regard, we proposed a procedure for calibrating 4 parameters governing the mechanical boundary conditions of a thoracic aorta model derived from one patient with ascending aortic aneurysm. The boundary conditions reproduced the visco-elastic structural support provided by the soft tissue and the spine and allowed for the inclusion of the heart motion effect. The thoracic

aorta was first segmented from magnetic resonance imaging (MRI) angiography and the annulus motion derived by tracking it from 2D cine-MRI. A rigid-wall fluid-dynamic simulation was performed to extract the time-varying wall pressure field. We built a Finite Element Model considering patient-specific material properties and imposing the derived pressure field and the motion at the annulus boundary. The calibration, which involved the zero-pressure state computation to include the pre-stress, was based on purely structural simulations. After obtaining the vessel boundaries by segmenting the cine-MRI sequences, an iterative procedure was performed to minimize the distance between them and the corresponding boundaries derived from the deformed structural model. A strongly-coupled fluid-structure interaction analysis through a partitioned resolution penalty-coupling method was finally performed with the tuned parameters and compared to the purely structural simulations.

The calibration with structural simulations allowed to reduce maximum and mean distances between image-derived and simulation-derived boundaries from 8.64 mm to 6.37 mm and from 2.24 mm to 1.83 mm, respectively. The maximum root mean square error between the deformed structural and fluid-structure interaction surface meshes was 0.19 mm. This procedure could prove crucial for increasing the Digital Twin fidelity in replicating the real aortic root kinematics. Moreover, enhanced accuracy in replicating the patient-specific behaviour potentially results in a derived virtual replica more accurate in evaluating stress and strain at the wall. This, in turn, increases the precision of the model when assessing the risk of rupture associated with conditions such as ascending aortic aneurysm or dissection.

An active Digital Twin, both for a physical system and a biological one, should provide real-time responses when queried. This is one of the fundamental aspects that should be considered when building an advanced Digital Twin suitable for clinical use, where available time is often extremely limited. In this thesis, we propose a method to create and validate three-dimensional surrogate models of the thoracic aorta capable of predicting almost in real-time patient-specific hemodynamics. The aortic anatomy has been automatically extracted from the systolic phase of 4D flow MRI sequences using a 3D U-net architecture. A rigid registration algorithm was used to align all the shapes of the available dataset to an initial meshed template. Radial basis function mesh morphing was performed to obtain computationally iso-topological and anatomically corresponding grids. The set of shapes obtained was then used to build a statistical shape model from which aortic atlases used to reproduce a huge cohort of virtual patients were extracted. For every virtual model, computational

fluid-dynamics simulation was performed and results in terms of wall pressure and shear stress magnitude were stored. Using non-intrusive model order reduction techniques based on proper orthogonal decomposition, surrogate 3D models were built to predict the wall pressure and shear stress results in real-time. The surrogate models were subsequently converted into Functional Mock-up Units and imported in the segmentation environment. This allowed for managing a single complete framework where a user could rapidly transition from medical images to the results of numerical simulation in order to immediately assess patient-specific hemodynamics. A validation approach conducted by excluding every time one original real patient from the creation of the statistical shape model and subsequently attempting to represent its hemodynamics using data derived from the remaining patients has been executed.

With a maximum absolute error of approximately 10 mmHg only for a few patients and since such values were exclusively attributable to a small number of nodes, considering, in addition, an average relative prediction error of 1.3%, the surrogate model related to the pressure demonstrated reasonably good capabilities in predicting this output. On the other hand, errors up to 55 Pa were detected for the wall shear stress magnitude. These were quite high, especially if observing an average relative error equal to 42%. Therefore, the surrogate model pertaining to the wall shear did not prove to be accurate enough to predict this outcome. This was because the wall shear stress at peak systole exhibited high spatial gradients on the aortic surface that the ROM was not able to replicate. This work describes a pipeline to successfully augment medical images with simulation data, but the results have demonstrated how estimating certain outputs strongly linked to local flow phenomena still pose challenges for a Digital Twin aimed at providing accurate and reliable real-time results.

Keywords: Digital Twin, Ascending Aortic Aneurysm, Risk Assessment, Growth Prediction, High-fidelity Modeling, Reduced Order Modeling, Real-time Simulation

Organization of the work

This thesis is structured as follows: Part I, comprising Chapters 1 and 2, concerns the introduction about the clinical and computational problems related to the ascending aortic aneurysm. Part II, encompassing Chapters 3, 4 and 5, showcases the development of all the methodologies for the development of shape-based growth prediction methods, for the establishment of high-fidelity reliable computational models and for predicting in real-time clinical outcomes derived from numerical simulation. Part III contains the results obtained in this work related to the methods previously mentioned and encompasses Chapters 6, 7 and 8. Lastly, Part IV includes Chapter 9, which consists of the general conclusions drawn from the entire research described here.

More in detail, the content of each chapter is organized as follows:

- In **Chapter 1**, we introduce the cardiovascular system and the clinical problem concerning the ascending aortic aneurysm, highlighting the related risk and the possible complications. We explain the use of the diameter as criterion for surgical intervention and then discuss the available therapeutic methods. We provide a brief excursus of the current diagnostic imaging techniques and conclude the chapter by discussing clinical challenges related to this pathology.

- In **Chapter 2**, we describe the use of numerical modeling tools for the analysis of the aortic aneurysm. We mainly focus on computer-aided engineering methods for anatomical analysis, as well as numerical simulation techniques for evaluating biomechanical and hemodynamic properties. We then introduce the concept of 'Digital Twin' in relation to the new techniques driven by artificial intelligence. We conclude the chapter by discussing the computational challenges related to the modeling of this particular anatomical and pathological condition.

- A primary challenge in developing a Digital Twin for an organ like the aorta lies in finding methods to track and follow the evolution of the specific anatomical

region over the months and predict potentially dangerous situations for a specific patient. In this context, in **Chapter 3**, we illustrate some methodologies for predicting the risk of rapid growth associated with patient-specific aortic anatomies and we present a shape-based approach for predicting the growth rate of the aneurysm.

- In **Chapter 4**, we delve into high-fidelity modeling, which sets the foundation for the development of accurate digital replicas of organs, including their behaviour. Specifically, we detail methods for calibrating the parameters governing the mechanical boundary conditions of a thoracic aorta model, including the patient-specific material properties, accounting for the calculation of wall pre-stress, the effect of the cardiac motion imposed at the annulus level and the interaction of the aorta with the spine and the soft tissue.

- In **Chapter 5**, we delve into another crucial aspect for the realization of a Digital Twin: the assessment of the results in real-time. To predict patient-specific hemodynamics, by combining statistical shape modeling and model order reduction techniques, we propose an approach to create and validate surrogate 3D models reproducing aortas affected by ascending aortic aneurysms. The meta-models are adaptable to a wide range of patients' anatomies obtainable by automatic segmentation procedures and can represent multiple fluid-dynamic inlet and outlet conditions depending on the desired input parameters. The deployment methods in an augmented reality environment easily navigable by the clinicians have been described.

- **Chapter 6** is the first chapter presenting the results of the work. Specifically, the findings about growth prediction methods described in Chapter 3 are presented and discussed, comparing the prediction results derived from local shape features such as diameter or the ratio of known lengths derived from the ascending aorta anatomy with those derived from global shape features represented by the shape modes extracted through principal component analysis or partial least squares.

- **Chapter 7** examines the results of calibrating the mechanical boundary conditions of the patient-specific high-fidelity aortic model discussed in Chapter 4. The results have been evaluated by comparing the displacement of the simulated model with the displacement of the real aorta derived from the images. Once the boundary condition parameters have been obtained from the calibration,

the results of a purely structural model and a fluid-structure interaction model have been compared, and the effect of cardiac motion on wall strain have been assessed.

- In **Chapter 8**, we propose and discuss the outcomes of surrogate-based modeling for real-time hemodynamics assessment proposed in Chapter 5. We describe, in particular, the validation results related to wall pressure and wall shear stress magnitude achieved through a leave-one-patient-out approach and we discuss the limitations, especially related to the computational complexity required to obtain robust and accurate reduced order models for creating valuable Digital Twins.
- Finally, **Chapter 9** consists of a comprehensive critical analysis of the complete research, emphasizing the significant achievements reached while highlighting the remaining challenges and limitations associated with creating a Digital Twin of a highly complex organ like the aorta.

Part I

Introduction

Chapter 1

The clinical problem

This introductory chapter provides an anatomical and physiological description of the cardiovascular system with a major focus on the aorta and the clinical context related to one of the most common cardiovascular diseases: the ascending aortic aneurysm. The spread of this pathology is outlined along with its underlying etiology. The complications that this disease can cause are described and the surgical interventions and treatment options available are detailed. Finally, the clinical challenges related to this condition are explored, focusing specifically on the diameter assessment to access surgery, which still remains a decision-making criterion of considerable debate.

1.1 The cardiovascular system

The cardiovascular system (CVS) is a complex structure comprising blood, vessels and the heart [1]. The blood supplies essential nutrients and oxygen to the body's tissues while concurrently facilitating the removal of waste products such as carbon dioxide [2]. This exchange occurs through a complex network of vessels interconnecting all body organs. Blood transport has the additional purposes of regulating the body temperature, transporting the cells responsible for the immune response and maintaining the fluid balance in the body.

The circulatory system (Figure 1.1) can be divided into two main parts: (1) the pulmonary circulation, which concerns the blood oxygenation through the lungs and (2) the systemic circulation, which involves the distribution of the blood to the rest of the body. The heart acts as a vital link between these two parts, pumping blood from one to the other. The whole blood circulation, discovered by Harvey in 1628, can be briefly described as follows [3]: the circulatory process starts with the reception of

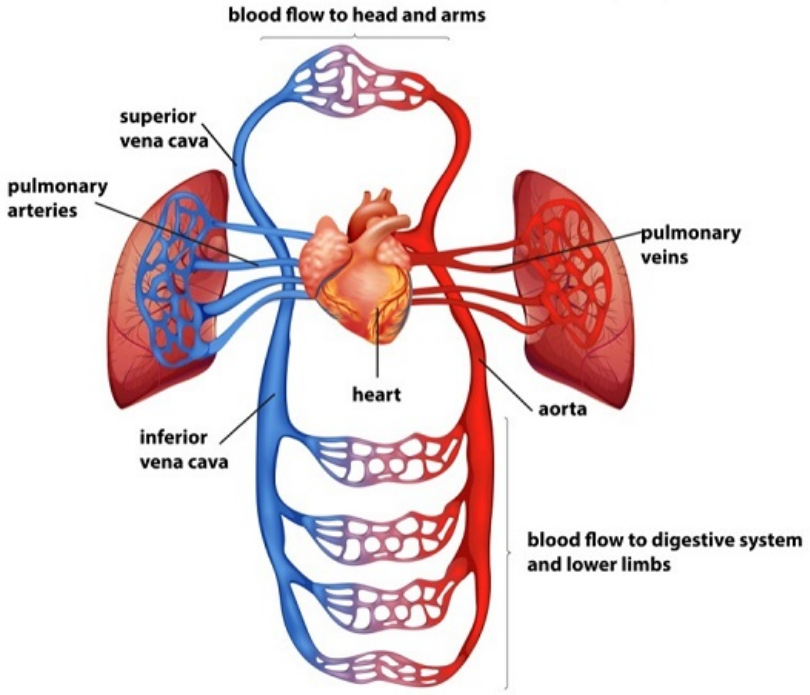

Figure 1.1: The circulatory system. From *www.stock.adobe.com*.

deoxygenated blood by the right atrium. The second step is the contraction of the atrium chamber, that allows the blood to be pushed into the right ventricle. The right ventricle, in turn, transfers the deoxygenated blood through the pulmonary valve into the pulmonary artery, allowing the transport to the lungs for oxygenation. The blood, now rich in oxygen, is then directed back to the heart through the pulmonary veins. Once filled, the left atrium undergoes contraction, pushing the blood into the left ventricle. The left ventricle executes a forceful contraction, ejecting the blood through the aortic valve into the aorta that distributes it to the rest of the body. Lastly, oxygen-poor blood returns to the heart and the process repeats in a new cycle to sustain the body's circulation [4].

The series of events constituting one complete heart contraction is called cardiac cycle. It comprises two phases: systole and diastole [5]. Regarding the ventricles, which are the heart's lower chambers, systole involves the contraction of both left and right ventricles, forcing blood into the aorta and pulmonary artery, respectively [6]. During atrial systole, which occurs earlier in the cardiac cycle, the atria (the heart's upper chambers) contract to push the remaining blood into the ventricles. During

diastole, the heart muscles relax, allowing the blood to fill the heart's chambers. Ventricular diastole involves the relaxation of the ventricles, enabling them to fill with blood coming from the atria. Similarly, during atrial diastole, the atria relax and receive blood from the veins, preparing for the next cardiac cycle.

1.2 The aorta

The aorta is the largest artery of the human body. It plays a crucial role in cardiovascular circulation, serving as the main conduit for oxygenated blood pumped from the left ventricle of the heart to the rest of the body [7]. The left ventricle is connected to the aorta through the aortic valve which guarantees unidirectional blood flow.

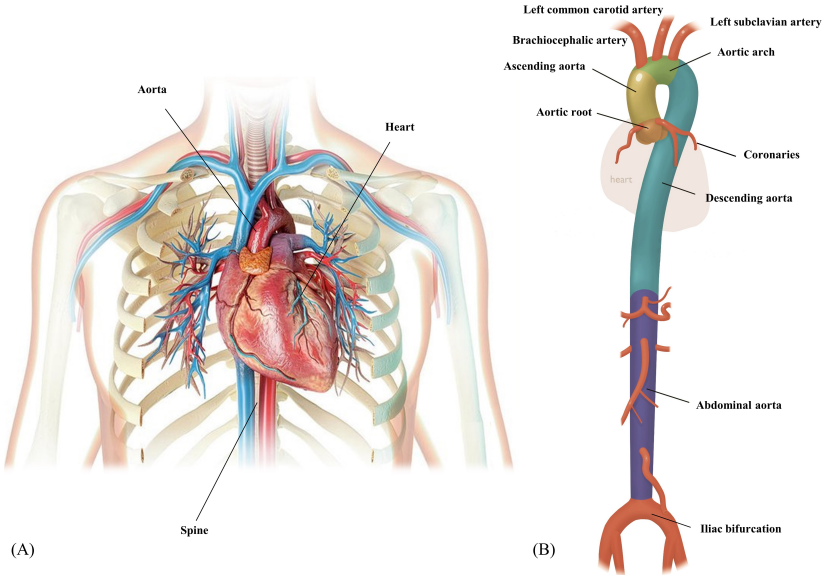

Figure 1.2: (A) Representation of the heart, aorta, rib cage and the main vessels of the cardiovascular system. (B) The aortic anatomy from the aortic root to the iliac bifurcation.

Its structure, composition, and mechanical properties are essential for preserving blood flow and ensuring efficient distribution of nutrients and oxygen [8]. The thoracic aorta (TA) arises from the left ventricle at the level of the aortic root (Figure 1.2 (A)) and propagates up to the diaphragm where the abdominal aorta (AA) starts. The aortic root consists of the Valsalva sinuses, the aortic valve leaflets, the aortic commissures and the inter-leaflets triangles [9]. The sinuses, namely the right, left, and non-coronary sinuses, are bulges in the aortic root connected to the three aortic

valve leaflets and the sino-tubular junction, named based on the coronary arteries arising from them. The thoracic aorta can be divided into three main segments: the ascending aorta (AsA), the aortic arch (AAr) and the descending aorta (DA) (Figure 1.2 (B)). From the AsA, the coronary arteries originate. They supply oxygenated blood to the myocardium. The aortic arch forms a characteristic arch-like shape and gives off several branches, including the brachiocephalic artery (BCA), the left common carotid artery (LCCA), and the left left subclavian artery (LSA) [10]. These branches supply blood to the head, neck, and upper limbs, respectively. A particular anatomical variation of the aortic arch called "bovine arch" can be detected in some individuals. It is characterized by the presence of only two major branches arising from the aortic arch due to an aberrant origin of the left common carotid artery [11]. The descending thoracic aorta runs along the posterior mediastinum parallel to the spine [12]. It is located between the lungs and gives off various branches that supply blood to the organs and tissues of the thoracic region. In healthy adults, aortic diameters do not usually exceed 40 mm and tend to gradually decrease in size downstream.

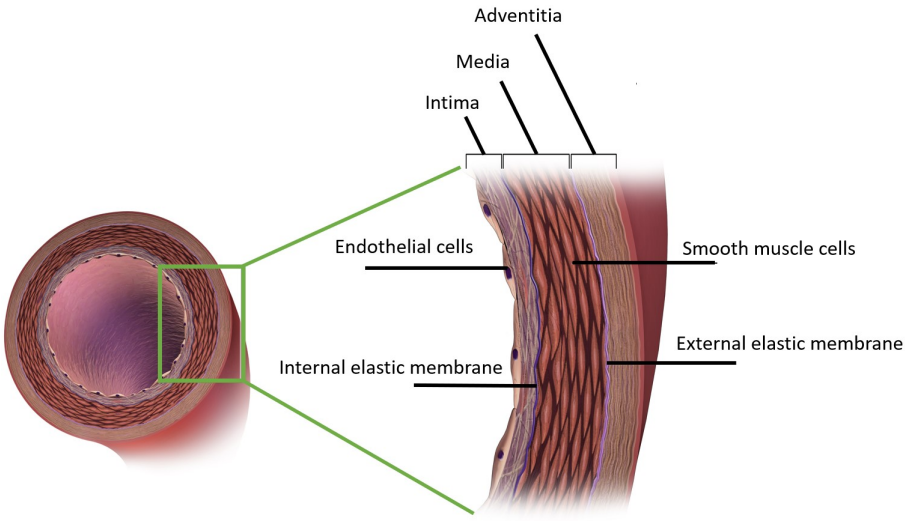

Figure 1.3: The aortic layers.

The inner hollow space or passage of the aorta or more generally of a blood vessel, where the blood flows, is called lumen. The other part consists of the wall. It is composed of three main layers: intima, media, and adventitia (Figure 1.3) [13].

- The intima is the innermost part, consisting of a single layer of endothelial cells that provides a smooth lining for blood flow.

- The media, the middle layer, is predominantly composed of smooth muscle cells embedded in an extracellular matrix rich in elastin and collagen fibers [14]. This layer provides strength and elasticity to the aorta, allowing it to expand during systole and recoil during diastole, contributing to the efficient ejection of blood from the heart.

- The adventitia, the outermost layer, provides structural support and contains nerves, blood vessels, and fibroblasts that contribute to maintaining the aortic wall [15].

Collagen and elastin are the two primary load-bearing proteins in the vessel wall, each with distinct mechanical properties that contribute to the non-linear stress-strain behaviour of the arterial wall [16]. While collagen is the most prevalent protein in humans, it imparts stiffness to blood vessels and other tissues. When collagen is unloaded, the main mechanical properties are given by elastin. During life, collagen undergoes a continuous process of synthesis and degradation, whereas elastin expression is limited to the perinatal period and is not renewed thereafter [17]. The distribution of elastin and collagen within the aorta is not uniform. In the ascending aorta, elastin predominates, but moving more distantly, the proportion of elastin decreases [18]. This is due to the specific biomechanical requirements and functional demands of each region: the ascending aorta needs to expand to accommodate the blood volume pulse and then recoil during diastole and has to dampen the pressure fluctuations, preventing sudden increases in blood pressure downstream in the arterial system [19].

1.3 The ascending aortic aneurysm

Among cardiovascular diseases, ascending aortic aneurysms (AsAAs) are characterized by localized dilation and weakening of the ascending aorta [20]. By definition, an aneurysm is a permanent enlargement of more than 50% of the standard diameter of the aortic lumen [21]. There are two primary types of ascending aortic aneurysms: fusiform and saccular (Figure 1.4) [22]. Fusiform AsAAs involve a uniform dilation of the entire circumference of the aortic wall, resulting in tubular-shaped aneurysms. This type of aneurysm typically extends along a significant length of the ascending aorta. On the other hand, saccular aneurysms exhibit a localized outpouching or sac-like bulge that protrudes from a specific area of the aortic wall. Unlike fusiform aneurysms, saccular aneurysms are characterized by a more focal and asymmetric

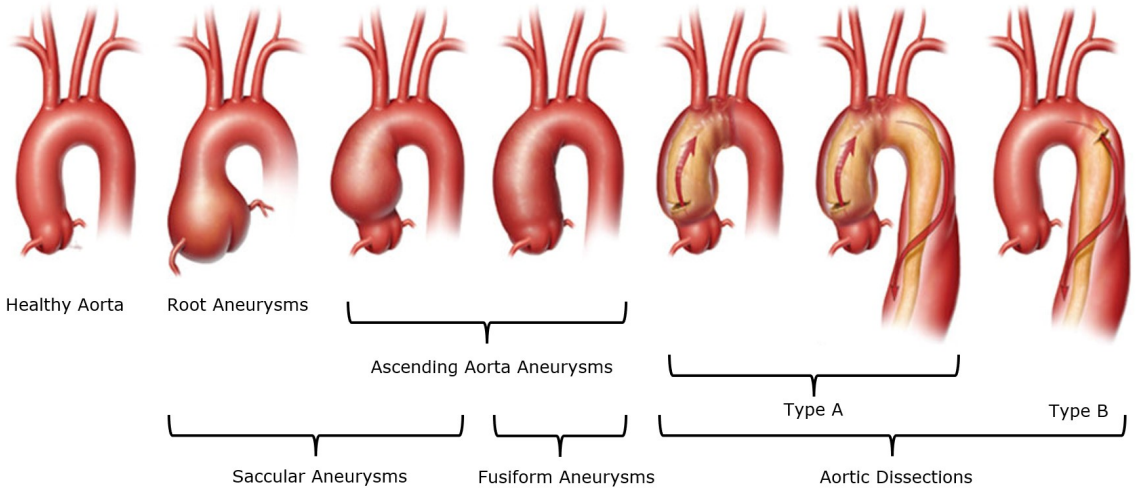

Figure 1.4: Ascending aortic aneurysms and dissections. From *www.cardiosurgeon.co.uk*.

enlargement. In the case of a tear of the inner lining of the aorta, which allows the blood to flow between the aortic layers, a more severe situation defined as aortic dissection (Figure 1.4) is involved [23]. Even more dangerous is the phenomenon of the rupture in which the blood flows directly out of the vessel. Rupture shows high morbidity and mortality if not detected and managed promptly [24].

Several pathomechanisms have been associated with AsAAs, often involving a combination of factors such as the loss of elastin and smooth muscle cells, thinning of the tunica media, and infiltration of inflammatory cells [25]. Elastin degradation is responsible for the aneurysmatic dilatation of the vessel, while experimental collagenolysis is necessary for rupture to occur [26]. Bicuspid aortic valve (BAV) is considered one of the main risk factors for developing AsAAs. It is a congenital heart valve anomaly characterized by the presence of only two cusps instead of the normal three of a tricuspid aortic valve (TAV) [27]. BAV is the most common congenital heart defect, detectable in approximately 1-2% of the population [28]. This structural abnormality can lead to altered blood flow patterns and increased mechanical stress on the ascending aorta. More details on the causes of ascending aortic aneurysms are given in the following section.

1.4 Epidemiology and etiology

The epidemiology of ascending aortic aneurysms provides valuable insights into the prevalence, incidence and demographic characteristics related to this pathology

[29]. Following the Centers for Disease Control and Prevention data, the estimated incidence of AsAA is approximately 10 cases per 100,000 person-years [30]. Although less common than abdominal aortic aneurysms, the pooled incidence of ascending aortic aneurysms is estimated to be between 3% and 5% in the general population [31]. While both women and men have similar incidences, women tend to be diagnosed in their 70s, about a decade later than men [32]. The pooled prevalence of AsAA, resulting from one of the most extensive state-of-the-art review works of 2020, was 0.16% (95% confidence interval: 0.12; 0.20) [31].

AsAA shares many common risk factors with other cardiovascular diseases. Generally speaking, aortic aneurysms have a multifactorial etiology involving a combination of genetic and acquired factors [33].

Genetic predisposition plays a significant role, with inherited disorders such as Marfan syndrome, Ehlers-Danlos syndrome, and Loeys-Dietz syndrome contributing to the aneurysm formation [34, 35, 36, 37]. These genetic disorders are characterized by mutations in genes involved in synthesising and maintaining structural proteins, such as the fibrillin-1 in Marfan syndrome. As consequence, the disruption of the structural integrity of the connective tissue occurs, leading to weakened and dysfunctional aortic walls [38]. The identification of these genetic causes not only provides insights into the etiology of ascending aortic aneurysms but also highlights the importance of genetic testing and early diagnosis for individuals at risk of developing these connective tissue disorders. Approximately 20% of individuals diagnosed with an aortic aneurysm have a familial history of aortic disease [39]. A familial predisposition should be investigated for patients who exhibit symptoms at a relatively young age.

The second aspect that plays a significant role in the development of aortic aneurysms is related to the acquired risk factors. First, hypertension contributes to the progressive weakening and dilation of the aortic wall [40]. Atherosclerosis, characterized by plaque accumulation in the arteries, compromises the structural integrity of the aortic wall, increasing the risk related to this disease [41]. Cigarette smoking, through its detrimental effects on vascular health, promotes inflammation and oxidative stress, accelerating the degenerative process [42, 43]. Advanced age is also associated with a higher prevalence of aortic aneurysms, likely due to the cumulative effects of genetic and environmental factors over time [44]. Moreover, chronic inflammation within the aortic wall, mediated by immune and inflammatory pathways, further worsens the degenerative process [45]. Abnormalities in the extracellular matrix components, such as collagen, elastin and proteoglycans or

deficiencies in vascular smooth muscle cell function and contractility or dysregulation of matrix metalloproteinases, enzymes involved in extracellular matrix remodeling, can contribute to the degradation of the wall [46, 47]. Infection-related etiologies, such as syphilis or bacterial/fungal infections, can directly damage the aortic wall or induce inflammatory responses leading to aneurysm formation [48]. Trauma or iatrogenic causes, including surgical procedures, can also lead to aortic wall injury [49]. Finally, it has been demonstrated that hormonal imbalances, such as those affecting sex hormone production or function, have been implicated in the pathogenesis of aortic aneurysms [50].

In addition to acquired and genetic factors, hemodynamic stress plays a critical role in the pathogenesis of ascending aortic aneurysms [51]. Increased wall shear stress [52] and altered blood flow patterns, particularly in the area of vessel curvature and branch ostia, contribute to endothelial dysfunction, inflammation, and oxidative stress within the aortic wall [53]. These pathological processes further weaken the structural integrity of the aorta, triggering a cascade of events that promotes aneurysm formation and progression.

The knowledge of all these aspects is essential to study and understand the activation mechanisms related to this pathology and to develop targeted preventive strategies and therapeutic interventions to mitigate the risks associated with aortic aneurysms.

1.5 Complications

The most common complications of aortic aneurysms are aortic dissections and aortic rupture. Aortic dissection, already introduced before, occurs when there is a tear in the inner lining of the aorta, allowing blood to flow between the layers of the vessel wall [54]. This can lead to the formation of a false channel (called false-lumen) within the aorta, potentially preventing the blood from flowing to vital organs. If the ascending aortic aneurysm continues to enlarge in an uncontrolled manner, it can weaken the aortic wall to the point of rupture. An aortic rupture is a catastrophic event that causes massive internal bleeding and is often fatal if not promptly treated. The first consequences of rupture can include massive hemorrhage, cardiac tamponade, and organ ischemia. While the aneurysm may be asymptomatic, the patient often experiences pain after rupture. When rupture occurs, it is fatal in a large proportion of patients prior to hospital presentation [55]. Patients who arrive at the hospital necessitate an urgent surgical intervention associated with a

mortality risk of around 20% [56].

While not reaching these catastrophic outcomes, other complications can also occur in presence of aneurysms. Large ascending aortic aneurysms can exert pressure on adjacent structures, such as the pulmonary artery, coronary arteries or the nearby heart chambers [57, 58]. This compression can impede blood flow and compromise the function of these structures, potentially leading to various cardiac complications. Additionally, the enlargement of the ascending aortic aneurysm may affect the functioning of the aortic valve, which can lead to valve regurgitation (leaking of blood backwards) or stenosis (narrowing). This can further strain the heart and, as a consequence, lead to heart failure [59].

1.6 The treatments

Treatment options for ascending aortic aneurysms can be categorized into conservative (non-surgical) and non-conservative (surgical) approaches. Asymptomatic small aneurysms are often managed with the conservative approach, involving the regular surveillance described before. For example, maintaining optimal blood pressure levels through lifestyle modifications and medications is essential to reduce stress on the weakened aortic wall and slow the disease progression [60]. Commonly used antihypertensive drugs include ACE inhibitors, beta-blockers, calcium channel blockers and angiotensin receptor blockers (ARBs) [61]. Patients are advised to make lifestyle changes to support their cardiovascular health. This includes quitting smoking, adopting a healthy diet low in sodium and saturated fats, engaging in regular physical activity and carefully managing other risk factors such as cholesterol levels and diabetes [62, 63].

Given the risk of complications associated with bigger ascending aortic aneurysms, surgical intervention is often necessary to prevent catastrophic events. The decision to proceed with prophylactic surgery depends on various factors, including the size of the aneurysm, the rate of expansion and patient-specific characteristics [29] always looking for a balance between risk of rupture and risk of intervention. Till 2022, European and American guidelines recommended surgery for patients with root or ascending aorta aneurysms (1) in presence of symptoms related to the disease, (2) if the diameter was higher than 5.5 cm or (3) if there was rapid enlargement of the wall (aneurysm growth > 3 mm/year) [64]. The threshold for surgery shifted to 5 cm in presence of bicuspid valve [65]. It was also reasonable to consider surgery already with a 5 cm threshold when the undergoing tricuspid aortic valve had to be replaced

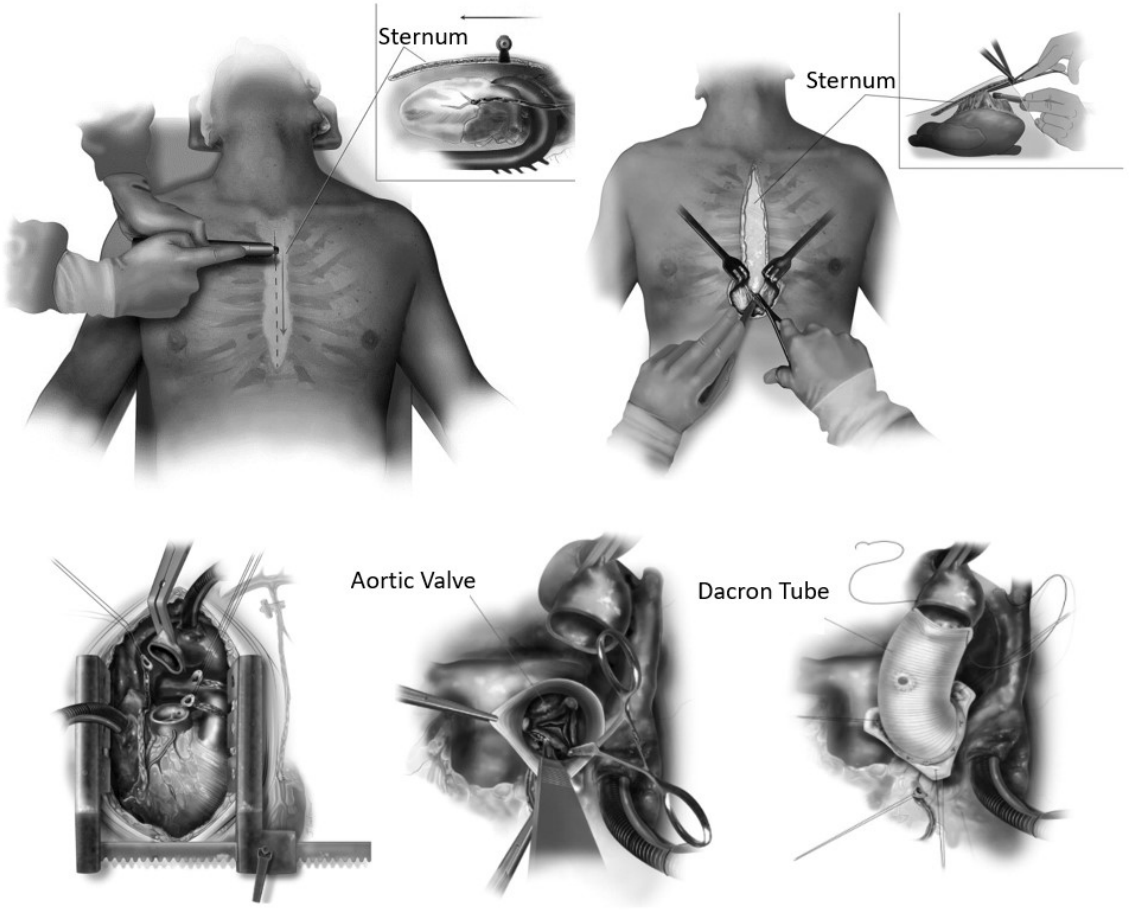

Figure 1.5: The open surgery procedure for ascending aortic aneurysm involves accessing the thoracic aorta through an incision made in the patient's chest (sternotomy). Once the aorta is exposed, the surgeon carefully cuts the aorta, removing the portion with the aneurysm and in some cases the valve, too. A synthetic graft is inserted to replace the weakened portion of the aorta. After the surgery, the patient typically spends one/two days in intensive care and usually remains in the hospital for a period from four to seven days for postoperative care and recovery.

due to pathological conditions such as stenosis, regurgitation or collapse [66]. With the new guidelines [67], given the decreasing intra and post-operative mortality [68], a skilled surgeon may consider surgery starting from 5 cm for a standard AsAA or in patients whose height is more than once the standard deviation above or below the mean, with a cross-sectional aortic area to height ratio higher than 10 cm^2/m or if a tricuspid aortic valve replacement is required even if the aortic diameter is just beyond 4.5 cm.

The size criterion can be easily understood by thinking in terms of Laplace's

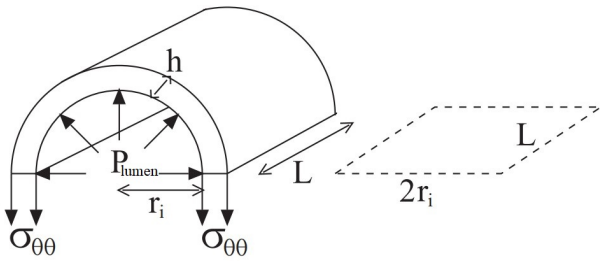

Figure 1.6: Free body diagram of a pressurized vessel with a luminal pressure (P_{lumen}), a length (L), an inner radius (r_i), and a wall thickness (h).

law, which establishes a relationship among the inner radius (r_i), luminal pressure (P_{lumen}), and tensile wall stress ($\sigma_{\theta\theta}$). It is derived from equilibrium principles, considering the simplified case of a pressurized vessel free body diagram (Figure 1.6) where the hemodynamic force due to pressure must balance the elastic force caused by the tensile stress in the vessel wall. In other words, it ensures an equilibrium between the forces acting on the vessel to maintain stability:

$$P_{lumen} 2 r_i L - 2 \sigma_{\theta\theta} h L = 0 \Leftrightarrow \sigma_{\theta\theta} = \frac{P_{lumen} r_i}{h} \tag{1.1}$$

The hemodynamic force is determined by projecting the pressure onto an imaginary plane that cuts the cylinder. The stress increase is directly proportional to the radius, meaning that as the radius grows, the stress also increases. Consequently, larger diameters pose a higher risk of rupture due to the elevated stress levels within the vessel wall [69]. However, the aneurysm rupture potential of the Laplace's law is inaccurate for two reasons [70]: first, the aortic wall is not a simple cylinder but has a complex shape with superficial alterations and both major and minor wall curvatures. Second, the wall stress assessment alone is not sufficient as it does not consider local properties and material failure [71, 72].

Surgical options include the most common open surgical repair (Figure 1.5) where a tubular graft is placed performing aortic clamping, with the distal anastomosis just below the aortic arch but also some minimally invasive endovascular approaches, such as thoracic endovascular aortic repair (TEVAR) which currently is specifically aimed at patients for which the risk of open surgery is too high [73, 74]. The artificial prosthesis, therefore, constitutes the replaced part of the aorta with aneurysm. The 30-days post-surgery mortality rate oscillates between 1.5% and 8% depending on the clinical centre, age and other well-known cardiovascular risk factors at the time of operation [75, 76]. Patients who undergo elective surgery for ascending aortic

aneurysm and survive the postoperative period not only experience long-term survival but also fully regain their life expectancy [68].

1.7 Diagnoses and monitoring

Accurate diagnosis and long-term surveillance are crucial for an effective management and prevention of life-threatening complications such as aortic rupture or dissection. Regular monitoring allows for the detection of any significant changes in aneurysm size or morphology [77]. Additionally, surveillance allows a prompt treatment of associated risk factors such as hypertension. In fact, by closely monitoring patients with ascending aortic aneurysms, healthcare providers may rapidly vary therapies and suggest lifestyle modifications to optimize clinical outcomes and reduce the risk of adverse events.

In the detection and evaluation of ascending aortic aneurysms, a crucial role is played by imaging techniques. Several imaging modalities are commonly employed and each of them brings its own strengths and limitations. Selection should be based on individual patient characteristics and specific clinical scenarios. These techniques are often complementary in returning information about the disease [78].

Ultrasounds are generally preferred for abdominal aortic aneurysms (AAAs) screening. However, in some cases, echocardiography [79], including non-invasive transthoracic echocardiography (TTE) and transesophageal echocardiography (TEE), is used for assessing the ascending aortic diameter. Unfortunately, ultrasounds present limited visualization of the entire ascending aorta for the presence of the ribcage or in cases of obese patients or with lung diseases that limit the acoustic acquisition window [80]. In case of TEE, conscious sedation is required and the superior airways must be absolutely unobstructed if issues arise with the insertion of the probe through the oral cavities. Moreover, this modality only returns a two-dimensional measurement and is strictly dependent on the position and angle of the probe, potentially leading to under or overestimation of the aortic diameter [81].

Computed Tomography (CT) and Magnetic Resonance Imaging (MRI) provide detailed three-dimensional high-contrast anatomical information, allowing for more accurate measurements of aortic dimensions and assessment of aneurysm progression over time [82]. CT scans are particularly valuable in assessing the size and morphology of the aneurysm, identifying associated complications such as dissection or intramural hematoma. This acquisition is very fast and used in both acute and non-acute circumstances. However, it requires ionizing radiation and often iodinated contrast

agents, which may pose risks, especially in patients with impaired renal function or contrast allergies. Minimizing radiation exposure and optimizing contrast media injection protocols are essential factors for the future development of this technology. CT scans can be performed in gating with the electrocardiogram (ECG) to acquire a specific phase of the cardiac cycle or in multiphase mode over several phases. The new Photon Counting technologies easily achieve temporal resolutions of 50 ms and fine spatial resolutions with voxel size equal to 0.25 x 0.25 x 0.25 mm [83, 84].

3D MRI has emerged as a valuable alternative to CT for assessing ascending aortic aneurysms. It returns excellent soft tissue contrast and allows for detailed evaluation of aortic morphology, including accurate measurement of aneurysm dimensions, flow dynamics assessment and aortic wall characterisation [85]. Generally, the spatial resolution is lower than CT (around 1 x 1 x 1 mm in voxel size). MRI does not involve ionizing radiation, making it a preferred choice for patients requiring serial imaging or those with contraindications to contrast agents. However, MRI is associated with longer acquisition times and can be challenging in patients with claustrophobia, metallic implants, or arrhythmias. Furthermore, this technique may not be available in all clinical centers. A cutting-edge non-invasive type of MRI is the time-resolved 3D phase-contrast (4D flow) that allows the in-vivo assessment of flow dynamics in both healthy individuals and patients with thoracic aortic diseases [86]. Through 4D flow MRI, 25 different cardiac phases can be easely extracted. This modality, which generally has worse spatial resolutions, can potentially enable the calculation of hemodynamic parameters like the wall shear stress (WSS) through indirect estimations. However, since it results in averaging the measured velocity field during several cardiac cycles, it negatively affects the computation of the velocity gradient at vessel edges and, therefore, the wall shear assessment [87]. Another dynamic imaging technique that captures 2D images of moving structures, such as the heart and blood vessels, is cine-MRI. It can provide valuable insights into the pulsatile behaviour of the aortic wall during the cardiac cycle and helps in assessing size, shape and the response to the pressure changes due to the blood flow [88].

1.8 The clinical challenges

Despite the advancements in imaging techniques, challenges remain in accurately detecting and characterizing ascending aortic aneurysms. Early-stage detection and growth rate prediction for determining the appropriate timing for intervention are still two of the biggest challenges in this field, as aneurysms are highly variable

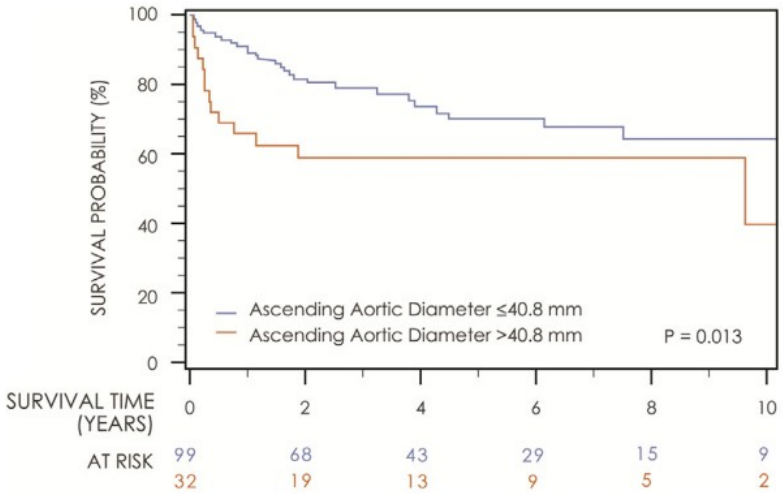

Figure 1.7: Kaplan-Meier plot related to the survival probability of 131 patients with uncomplicated acute type B aortic dissection: maximum ascending aortic diameter <40.8 mm vs >40.8 mm [89].

in their growth patterns and rates. Besides growth, assessing the risk of rupture requires considering multiple factors, including the knowledge of wall properties and several patient-specific characteristics. The diameter assessment is often with a high degree of uncertainty due to the operator, the quality of the available images and the various criteria for its determination. Another problem is the insidious 'small aorta' [90]. The formation of aortic dissections at diameters below 5 centimetres has been discussed several times in the literature [91] and can also be deduced by observing the Keplan-Meier from [89] in Figure 1.7. In general, there may be cases where small aneurysms experience rupture while huge aneurysms remain stable over time, perhaps with only pharmacological treatment [92]. A non-negligible percentage of ruptures occurs in presence of diameters below 50 mm [93]. Similarly, aneurysms with a diameter exceeding 70 mm have frequently been reported not to undergo rupture [94]. The annual risk of severe complications (dissection or rupture) for ascending aortas with diameters of 4, 5, 6, and 7 cm was estimated of 4.4%, 4.7%, 7.3%, and 12.1%, respectively [95]. On one hand, these numbers show the risk's tendency to increase with the diameter. However, on the other, the possible complications in patients with diameters well below the surgical threshold appear evident. Consequently, these findings indicate a need for reliable, robust, and precise risk assessment metrics to address the existing clinical demand. Such metrics will prove indispensable for aiding clinicians in their clinical diagnoses and decision-making

processes. Although the quality has improved over the years, medical images still do not allow detailed estimation of parameters such as wall shear stress and turbulence phenomena occurring. Managing aneurysms in older patients may require careful consideration of age-related factors and potential comorbidities. Aneurysms involving the distal ascending aorta, near the aortic arch or the aortic root, can be particularly challenging due to the anatomical complexity and superimposition of adjacent structures [96]. Finally, the patient-specific variability should be considered: each subject's response to treatment can vary significantly, requiring tailored approaches for accurate diagnosis and management.

Chapter 2

Computational modeling

As mentioned in the previous Chapter, current clinical guidelines for aortic disease diagnosis and treatment are still associated with a certain level of uncertainty. This results in an urgent need for more robust risk assessment techniques. In this Chapter, computational models and their respective applications in the diagnosis of cardiovascular pathologies are introduced. Particular focus is given to the significance of extracting vascular anatomical geometry as well as conducting structural, fluid-dynamic, and fluid-structure interaction simulations to assess clinically relevant parameters. A step forward is taken with a glimpse of the future roles that artificial intelligence could have in the diagnosis and prognosis of aortic pathologies. We introduce the concept of Digital Twins, providing an overview of the origins of virtual representations, and describe the role of human Digital Twins in healthcare. Finally, similar to the clinical aspects treated before, all computational challenges related to the numerical modeling of the aortic aneurysm are discussed. We conclude the Chapter by presenting the outline and objectives of the thesis.

2.1 The role of computational modeling

The convergence of extensive disease diagnosis information, clinical trial results and subject health characteristics have paved the way for revolutionary advancements in the medical practice during the era of big data [97]. For quite a few years, computational modeling has been established as a fundamental tool in cardiovascular medicine, offering detailed and personalized insights into the hemodynamic and biomechanic behaviours of the cardiovascular system [98]. A computational model is a mathematical representation of a real-world object, system or process, simulated to analyze and understand its behaviour [99].

Computer-Aided Engineering (CAE) refers to a set of computational techniques and simulation tools based on numerical calculation that allows researchers and clinicians to analyze complex physiological problems [100]. Through accurate simulations, CAE methods could contribute to a comprehensive understanding of the underlying mechanisms of cardiovascular diseases, thereby assisting in improved diagnostics and personalized treatment strategies. The successful application of CAE methods relies on integrating multi-modal medical data, including imaging, clinical and genetic information. These crucial steps significantly enhance the reliability of the considerations derived from the obtained results. By creating patient-specific models based on individual medical imaging data, clinicians can tailor treatments to a patient's unique anatomical and physiological characteristics. This patient-centric approach optimizes treatment outcomes and minimizes potential complications. These models are created by defining boundary conditions and numerically solving governing equations in both fluid and solid domains. The simulations allow for a detailed investigation of blood flow dynamics, vessel wall mechanics and interactions between blood and vascular structures under realistic conditions. Considering the potential influences of wall elasticity, vessel curvature, and residual stress, it is reasonable to suggest that using patient-specific biomechanical analysis of the aorta through advanced computer models can enhance the evaluation of mechanical stresses within the aortic wall beyond what is achievable with the simplified Laplace law. Relating to the aorta, the process involves generating the anatomical geometry, setting up solid and fluid models, and, if possible, coupling the solutions through fluid-structure interaction (FSI) methods. From the simulation results, fundamental biomarkers associated with the aneurysm growth could be identified and extracted [101]. Biomarkers are measurable indicators that can provide insights into the presence, progression or severity of the disease [102]. There is no consensus on the gold standard technique to model the haemodynamics and structure dynamics of the aortic wall. Several computational techniques, such as the Finite Element Method (FEM), Finit Volume Method (FVM), Finite Difference Method (FDM) and machine learning (ML) have been used covering the entire range of numerical approaches, especially computational solid mechanics (CSM), computational fluid-dynamics (CFD) and FSI [103]. These three numerical approaches are discussed in the following sections, preceded by some considerations concerning the importance of extracting the patient-specific geometry.

2.2 The computational geometry

The aortic geometry often includes irregular shapes, bulges and asymmetric expansions, making an accurate and reliable diagnosis through traditional two-dimensional (2D) images definitely tricky. In addition, this diagnosis may be subject to uncertainty due to factors such as image resolution, slice thickness, image plane selection and inter-observer variability [104]. Sometimes, valvular or aortic wall calcifications could exist and their extension is challenging to grasp by exploiting only the image dataset [105]. In this regard, patient-specific 3D aortic models can be used to create personalized representations of the individual's anatomy and biomechanics, extracting precious information including size, shape and location of the aneurysm. CT and MRI are the most common medical imaging techniques used to extract the real geometry. After collecting medical images usually in DICOM (Digital Imaging and Communications in Medicine) format, 3D patient-specific models can be reconstructed by performing segmentation [106]. Here, the aortic lumen and, in the best cases, the wall thickness are extracted separately to differentiate these zones. The 3D model obtained through segmentation may contain protrusions and tight internal corners, necessitating the use of additional geometric refinement and smoothing algorithms to prepare a suitable domain for computational analysis and effectively discretize it into finite elements [107]. From the 3D anatomical model, clinicians and researchers can visualize the complex details of the vessel or the regions close to it, such as the valve area and potential dissection lumens, providing comprehensive insights into the pathology. The extraction of accurate geometry is especially crucial for longitudinal analysis, enabling clinicians to accurately track the evolution of the aneurysm over time. Furthermore, by performing the segmentation of 2D or 3D plus time datasets, it is possible to extract the dynamic behaviour of the aorta in several cardiac phases, allowing to study the presence of possible pathological alterations during the cardiac cycle [108].

2.3 Computational solid mechanics

When studying complex phenomena, structures and systems subjected to a broad range of loading conditions, including quasi-static and dynamic loads, computational solid mechanics could be used. In the cardiovascular field, it is mainly based on FEM and requires solving partial differential equations (PDEs) [109].

The domain of interest, the aortic wall in this case, is typically first discretized (meshed) into shell or volume elements with specific material properties and then

loaded, reproducing specific physiological conditions [110]. The equilibrium equations for each element are then solved by yielding displacements, strains and stresses for the whole structure. Patient-specific models derived from medical imaging data can be tested using CSM simulations to predict stress and strain distribution within the aneurysmal wall [111]. For building a detailed structural model, aortic root motion and the pre-stress at the wall should be considered, as they definitely influence the conditions under which rupture occurs [112, 113].

By comparing computational results from aneurysms that ruptured with those that were electively repaired, researchers have discovered that aneurysm formation is associated with increased wall stress and decreased wall strength [114]. Furthermore, studies have shown that the rupture point commonly coincides with locations of peak wall stress [115]. This information could be fundamental in determining the potential risk of wall failure and guiding decisions regarding surgical intervention or conservative management and proves the potentially significant contribution of computational analysis for optimal prognosis achievements.

2.4 Computational fluid-dynamics

The influence of anatomical variations on hemodynamics should be thoroughly studied. This examination is crucial for identifying altered flow patterns and critical flow-related parameters like wall shear stress (WSS). These parameters can be associated with alterations in aortic size, as shown in [116], may provide valuable insights into aneurysm development and help assess the risk of dissection, as discussed in [117]. In this regard, computational fluid-dynamics can be used to solve the governing equations of fluid mechanics: the continuity and Navier-Stokes equations [118]. CFD simulations can be exploited to identify regions of disturbed flow, flow recirculation and areas of elevated wall shear stress, all critical factors contributing to aneurysm pathogenesis [119]. The blood flow analysis needs a tri-dimensional detailed vessel geometry and inlet and outlet boundary conditions, which often prove to be one of the most challenging parts to be accurately set. Outlet boundary conditions can be established through lumped parameter models, such as the Windkessel model [120]. It describes the behaviour of the distal arterial system in terms of a pressure-flow relationship using an electrical analogy for fluid flow. To non-invasively quantify patient-specific in vivo blood velocity profiles from which the boundary conditions for computational models can be extrapolated, imaging data, especially MRI, could be used [121]. The primary focus of numerous CFD studies exploiting MRI information

has been on flow irregularities caused by BAV, one of the most important predisposing factors for the development of AsAA [122]. Patient-specific models were employed to reveal distinct hemodynamic patterns in AsAA between patients with BAVs and those with TAV, also emphasising the importance of the opening angle of the valve on the direction and impact of the valvular jet [123].

2.5 Fluid-structure interaction analysis

Despite its valuable utility, CFD is limited to exploring disturbed hemodynamics in the fluid domain without considering the wall compliance effects and the interaction between pulsatile blood flow and the arterial wall with the volume accumulation during systole and its release in diastole that may affect the estimation of parameters such as WSS.

On the other hand, CSM allows for wall stress analysis in the deformable solid domain but does not take into account the behaviour of blood flow. The mutual effects between fluid domain and vessel wall should be considered to increase the accuracy of the results. The majority of recent computational models rely on the fluid-structure interaction approaches [124, 125], which provide a more realistic and accurate numerical description and have gained relevance in the past decade as large computing platforms have become more available and parallel computing has significantly evolved. Fluid-structure interaction analysis requires simultaneous and coupled solutions of governing fluid flow and tissue displacement equations. In this technique, fluid-dynamic forces deform the structural wall and the wall displacement affects the fluid flow behaviour. FSI simulation has been frequently used to understand the effect of wall stiffness on flow-derived parameters [126], study the rheological effects on the hemodynamics within the aneurysm sac [127] and evaluate the blood flow behaviour in proximity to dissected areas of the thoracic aorta [128].

2.6 The role of artificial intelligence

Several definitions have been given regarding the concept of artificial intelligence (AI). The definition here used is ‘a simulation system able to collect and process knowledge and information in order to take actions maximizing its chance of success’ [129]. In recent years, AI has begun to permeate and boost the field of cardiovascular medicine. The integration of AI techniques in computational modeling has the

potential to revolutionize the way cardiovascular diseases are diagnosed and treated [130]. So far, statistics has been the standard method for engineering and particularly medical research with the aim of showing the benefit of new therapies, identifying risk factors and revealing disease mechanisms. On the other hand, AI methods are not intended to estimate and explain data or information but to directly use them for making predictions of new unknown details [131].

Machine learning can be defined as a subfield of applied AI (Figure 2.1) with the capability of automatically discovering patterns of data without using explicit instructions [132]. It involves several algorithms for prediction and classification tasks that perform well especially on big data [133]. Machine learning can be divided into supervised and unsupervised learning. In supervised learning, machine learning algorithms are trained with labeled data and are adapted or fit to provide an output for a given task. These models are used to learn latent patterns within data and use the learned representations to formulate predictions through interpolation or extrapolation, particularly when a general law is discerned [134]. Most biomedical applications that rely on machine learning tend to adopt this learning approach. Once trained, supervised ML models can perform predictions rapidly and with minimal computational time. On the other side, in unsupervised learning, the inputs for the ML models are unlabelled data. This kind of learning is generally carried out for clustering or dimensionality reduction. In clustering, similar data points are grouped or clustered. In dimensionality reduction, patterns within the provided data are extracted.

Deep learning (DL) is a subset of supervised machine learning algorithms (Figure 2.1) that employ deep, multi-layered neural networks, initially inspired by the structure of the human brain [135]. Over the past years, deep learning has gained significant traction and demonstrated superior performance compared to other machine learning techniques in diverse domains, including image recognition and image segmentation of cardiovascular anatomies.

AI techniques can assist in analyzing vast amounts of medical data, including imaging scans and patient records [136]. A wide range of studies focus on developing AI-based tools that automatically estimate the diameter of the aorta from medical images, yielding results similar to those of specialists but with significant reductions in terms of time [130]. Additionally, a combination of CAE methods and AI techniques seems to be promising in suggesting the most appropriate graft sizing and personalized stent graft designs [137]. AI-driven CAE methods have the potential to streamline workflows and further enhance diagnostic accuracy. These approaches can

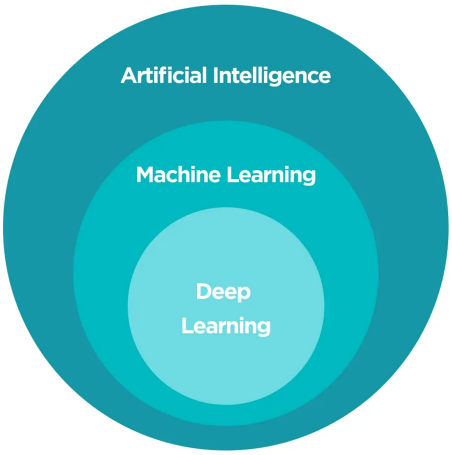

Figure 2.1: Artificial intelligence is a field of computer science that enables machine to replicate human intelligence. Machine learning is a subset of artificial intelligence that provides the machine with the ability to automatically learn. Deep learning is a subset of machine learning based on artificial neural networks to model and solve complex problems.

optimize computational processes, reducing the time required for simulations and analyses. This efficiency is particularly valuable in time-sensitive situations, such as emergency medical scenarios, where quick decisions are necessary. Clinicians could, in fact, use CAE simulations combined with AI methods to evaluate the effectiveness of particular surgical intervention compared to conservative treatments based on individual patient's characteristics [138].

2.7 The Digital Twin

In recent years, the development of technology has transformed industries by seamlessly connecting the physical and virtual realms. Initially rooted in engineering and manufacturing sectors, Digital Twins (DTs) have transcended traditional boundaries, finding applications in various fields, including healthcare. This Section explores the concept of Digital Twin with a particular focus on its potential to revolutionize healthcare through personalized diagnosis and prognosis.

Digital Twins are virtual representations of physical objects, systems or processes updated through the exchange of information between the real and virtual domains [139, 140]. The term 'Digital Twin' originated in 2010 by John Vickers in NASA's 2010 roadmap [141]. The predecessor of the Digital Twin in the medical field was known as 'Virtual Physiological Human' [142]. It refers to a computational representation of

a human used in medical research, simulations and other applications with a detailed model of human physiology, anatomy and even behaviour. It can be used to replicate several scenarios, test medical treatments, study diseases and predict physiological responses to different stimuli. These digital counterparts leverage historical data from the physical entity and combine it with the insights from AI models that have been trained on extensive general data. Through this fusion of historical and retrospective information and AI knowledge, DTs can be used to predict the future state of the studied entity. DTs enabled by AI solutions can be exploited to perform patient-oriented analysis using a continuous feed of data, thereby improving the clinical accessibility of the results [143, 144]. With the increasing availability of Big Data, Internet of Things, cloud computing and AI, it is now possible to create digital representations of human organs to execute real-time monitoring and return warnings in case of acute dangerous situations [145].

A Digital Twin can assist medical professionals in controlling the health of the aorta over time. Anomalies or changes in its behaviour could be promptly identified, potentially aiding in the early diagnosis of diseases like aneurysms or dissections. The Digital Twin, enabling a personalized approach to the treatment, can provide insights into the way the organ responds to ageing, drugs and other factors. Medical decisions can be tailored to individual needs by considering the patient-specific anatomy and physiology. The possibility to test many combinations of input parameters can ensure the capability of predicting significant outcomes [146]. This could even help the medical team understand the behaviour of the aorta following different corrective surgical treatments. Surgeons and clinicians can use a virtual replica to test various operations, such as surgical procedures, stent placements or medication strategies, before applying them to the real patient. A Digital Twin exploits both population and individual data to develop a replica which optimally supports decision making. It could help determine the suitability of a medical device or pharmaceutical treatment for a patient by simulating the device response or the effects of a dosage before a particular therapy is chosen. By generating synthetic patient data, DTs can also be valuable educational tools for medical students and professionals to understand complex anatomical and physiological scenarios. Moreover, the generation of virtual patients can facilitate the execution of in-silico clinical trials performed to replicate standard clinical trials on biological models, refine inclusion and exclusion criteria, test new drugs and reduce experiment times and costs [147].

A Digital Twin can be categorized into active, semi-active and passive [148]. An active DT continuously adapts with real-time physical data to perform system

monitoring. The parameters of the numerical representation, in this case, are updated continuously. This specific model potentially has the most disruptive applications in the diagnosis and control of cardiovascular diseases. An active Digital Twin should respect the following requirements:

- Lifecycle follow-up: a digital model replicating a pathological organ or tissue should evolve over time to reflect changes in the physical system. This requires the ability to update and modify the digital model.
- Interconnectivity: the twin should have a connection (preferably bidirectional) with the patient's anatomical model [149]. It can be part of a more extensive network of interconnected systems, especially in clinical applications. It needs to support communication with other digital systems and potentially share data and insights. In other words, there is a phenotyping of real-world data collected from the individual's environment using mobile data sensors and wearable devices. The continuous interaction with new data through ML methods could improve the prediction capabilities.
- (Quasi) real-time data integration: a connection with real-time data sources that provide information about the current state of the physical system is required. This might involve fast communication with sensors, devices, data historians and other data collection techniques.

In semi-active DTs, time-varying data are gathered, but rather than performing a continuous update, the information is analysed once the data collection is complete. On the other hand, a passive Digital Twin is created with a large amount of physical data but is used offline or not continuously updated. For example, it can be employed to understand the risk of aortic aneurysm growth or rupture under various input conditions that can be applied to the model.

A good compromise in terms of accuracy in representing the physical model should be achieved. This impacts its geometry, behaviour, interactions and properties. The level of detail required depends on the clinical application, ranging from high-level system overviews to highly detailed representations [150]. A user-friendly interface is often indispensable to interact with and visualize the DT. This can include dashboards, visualizations and control tools. Indeed, integrating the twin in a clinical user-friendly environment could enhance its capability to provide a holistic and inclusive visualization of the desired clinical outcomes.

2.8 The computational challenges

The integration of CAE methods in diagnosing and supporting clinical decisions for cardiovascular diseases, especially ascending aortic aneurysms, brings a significant advancement in modern healthcare. However, while CAE methods offer immense potential in cardiovascular medicine, they also present challenges related to data acquisition, image segmentation, computational complexity, clinical validation and translation that need to be mentioned [151]. The successful implementation of CAE methods in the diagnosis and management of ascending aortic aneurysms relies on the integration of multi-modal medical data [152]. Overcoming challenges related to data acquisition, data sharing and compatibility among different imaging modalities is vital to enhance the accuracy and reliability of CAE simulations. Implementing a comprehensive and thorough surveillance program to collect consistent data from patients with ascending aortic aneurysms is crucial for detecting and verifying the diagnostic and predictive effectiveness of the developed methods [153]. Advancements in medical imaging technologies, such as high-resolution imaging, offer promising avenues for improving the diagnosis and monitoring of ascending aortic aneurysms. Moreover, significant heterogeneity exists in the measurement of AsAA diameters due to varying measurement methods [104]. These variations pose challenges in clinical practice, where different imaging modalities and measurement methods are frequently used. Discrepancies may further increase when considering the variability introduced by the operator. In this regard, accurate and robust segmentation algorithms to capture the details of the aneurysm should be developed [154]. Another very delicate step concerns deriving the computational grid from the segmentation. Generating high-quality computational meshes is critical to ensure accurate results [155]. However, dealing with large-scale and highly deformable geometries can lead to challenging meshing requirements and potential numerical instability during simulations. Accurately representing the mechanical behaviour of the aortic wall and the aneurysm tissue properties is not straightforward. Aortic tissues exhibit nonlinear, inhomogeneous, anisotropic behaviour of the aortic wall, which necessitates advanced material models and experimental data for calibration [156]. Moreover, defining appropriate wall thickness [157] and boundary conditions that mimic the physiological environment and capture the dynamic behaviour of the heart during the cardiac cycle and the effects exerted by the surrounding tissues is crucial for reliable simulations [158]. Modeling the interaction between blood flow and deformable aortic wall is computationally demanding and requires advanced FSI simulations [159]. There are also open questions regarding modeling flow rheology and turbulence in

large arteries [160, 161]. Although blood presents non-Newtonian behaviour, more marked for lower velocity regimes, many contradictory evidences are present on this topic [162]. It should also be considered that validating computational models against experimental or clinical data is essential to ensure their reliability [163]. However, obtaining comprehensive experimental data for patient-specific cases and quantifying model uncertainties remain challenging tasks. Significant efforts have been made to enhance the accuracy of numerical models and a common approach is to employ optimization algorithms that enable the model to estimate these necessary parameters [164]. Once the model is validated, there is still a lack of understanding of which biomechanical features of diseased and healthy aortas are relevant to be modelled [165, 166]. There is then a whole part of extrapolation to a larger population with the aim of identifying the computational biomarkers and risk predictors associated with the growth and rupture of ascending aortic aneurysms [167]. The clinical translation of computational solutions for evaluating and predicting ascending aortic aneurysms represents a significant advancement in patient care [168]. Bridging the gap between research and clinical application requires developing efficient and robust computational tools that can be integrated into clinical practice, which involves overcoming technical, regulatory and practical challenges [169]. Last but not least, for the translation of CAE tools into the clinical environment, numerical simulations, particularly FSI analyses [128], involving the entire ascending aorta and cardiac cycle are computationally expensive and require significant computational resources. In typical clinical scenarios, clinicians frequently encounter time-sensitive situations, such as those with rapidly increasing mortality rates, where waiting for days or weeks for results is not a viable option [170]. In this regard, AI-assisted techniques and Digital Twins seem to report consistent time savings and reduced inter-reader variabilities among radiologists, thereby improving diagnostic follow-up accuracy [130]. However, it always remains truly challenging to choose the input and output parameters of the model in order to ensure its control in a clinical environment [146]. Regarding the aspects purely related to the Digital Twin, several computational challenges warrant thorough investigation and innovative solutions. One primary obstacle lies in the integration and interoperability of heterogeneous data sources, encompassing different patient data types, such as medical images, electronic health records and wearable sensor data. The complexity of creating an active system along with its inherent requisites is evident as well as the difficulties in finding a balance in terms of accuracy and time required for the twin creation. Moreover, ensuring that DTs remain relevant and accurate over time, considering

changes in patient conditions, effects of pharmacological therapies and updates to the model remains something very complex to verify. Additionally, a data-driven model requires a massive amount of data. On cybersecurity side, safeguarding sensitive patient data used in creating and updating Digital Twins to comply with privacy regulations and prevent unauthorized access appears to be very complex. Navigating regulatory processes to gain approval for using DTs in medical decision-making and treatment planning is only in its early stages and requires many steps of review [171]. Finally, the computational demands of real-time interaction between the physical and virtual domains of the Digital Twin present an additional barrier, necessitating high-performance computing infrastructure for building the underlying architecture.

Efforts are ongoing to address these limitations related to developing Digital Twins and improve the accuracy and reliability of CAE methods. Dealing with these computational challenges is pivotal to unlock the full potential of Digital Twins in healthcare, enabling personalized diagnostics and prognostic insights that can significantly enhance patient care.

2.9 Aim of the work

In the rapidly evolving landscape of medical science, where the interplay of clinical needs and technological advancements defines the future of patient care, this thesis aims to lay the groundwork for the construction of a Digital Twin of the aorta. The overarching aim of this work is three-fold, each oriented towards addressing specific challenges in the clinical domain of ascending aortic aneurysms.

Firstly, we aim to redefine the metrics used for predicting the risk associated with aortic aneurysm growth. Traditional methodologies, predominantly based on the maximum diameter criterion, have often led to misidentifications, potentially overlooking patients at high risk. Thus, we aim to extract more accurate growth predictors that could be included in the realisation of a Digital Twin that could estimate the patient's future conditions. By so doing, we strive to enhance the precision with which we can anticipate the evolution of the aneurysm, thereby bridging the current gap in early diagnosis and prognosis of this pathology.

Secondly, with the idea of developing particularly accurate Digital Twins in future, we recognize the importance of developing a high-fidelity model that replicates the kinematics of a real aorta. A model that mirrors physiological responses more closely not only allows for more effective treatment planning but also paves the way for personalized simulations that can cater to individual patient's aspects. Hence, we aim

to elevate the benchmark of accuracy by calibrating mechanical boundary conditions that factor in patient-specific physiological phenomena, such as the visco-elastic support provided by the surrounding soft tissue and the dynamic effects of heart motion.

Lastly, while precision remains at the forefront, it is the timeliness of intervention that often becomes the determinant for clinical success. To that end, our final aim concerns real-time responsiveness. We want to develop surrogate models at the bases of advanced Digital Twins that can provide instantaneous responses, particularly in clinical settings where time remains a scarce commodity. Through this, we envision a paradigm where clinicians can transition seamlessly from medical imaging to real-time simulation results, thereby making informed decisions promptly.

In summary, the objective of this work is not only to introduce a disruptively growing technology, but to lay the foundations and redefine the landscape of aortic aneurysm management through it.

Part II

Methodology

Chapter 3

Shape-based ascending aortic aneurysm growth prediction

This Chapter is the first to describe the methods proposed in this thesis. It is focused on studying the anatomy of the ascending aorta affected by aneurysm. As we have previously discussed, a Digital Twin should be capable of tracking the anatomical evolution of the model over time and, thus, the potential growth of the aneurysm. We present here growth prediction methods that rely exclusively on computational shape analysis combined with classification and regression techniques. Geometrical shape features related to the aneurysm computed from a cohort of patients with available longitudinal data are extracted. By exploiting the multiple available acquisitions of the dataset, they are first used to assess the risk of growth and, after, directly predict the growth rate.

This Chapter is based on the Introduction and Materials and Methods Sections of the following works:

- *"Assessment of shape-based features ability to predict the ascending aortic aneurysm growth", Geronzi et al., Frontiers in Physiology 14: 378, (2023)* [172].
- *"Computer-aided shape features extraction and regression models for predicting the ascending aortic aneurysm growth rate", Geronzi et al., Computers in Biology and Medicine, 162, 107052, (2023)* [173].

It is worth highlighting that the first paper analyzed a smaller cohort of patients compared to the one addressed in this manuscript and described below. Consequently, some of the numbers given here could potentially exhibit slight variations compared to the ones reported in the publication.

3.1 Introduction

The diameter ineffectiveness as criterion for surgery has already been discussed before. In literature, cases of aneurysms with diameters below the threshold for elective surgery which experience rupture or of aortas with huge diameters remaining stable over time in terms of size are often reported [174, 175]. This results in a strong need for novel risk evaluation strategies for the aortic aneurysm, incorporating additional clinical parameters and biomarkers [176]. The anatomy appears to hold significance in both diagnosing the condition and determining appropriate therapeutic approaches. Shape alterations frequently lead to functional impairments, which, in turn, can accentuate anatomical abnormalities. For these reasons, the first part of this work concerns a detailed morphological analysis aiming to identify those shape features that can contribute to predicting the aneurysm growth. With the 2022 surgical guidelines, the aneurysm growth rate (GR) became a determining factor for accessing elective surgery [177]. According to them, surgery should be considered for patients with aortic diameter growth progressing at a rate exceeding 3 mm/year during two consecutive acquisitions [67].

Several studies investigating the possible correspondence between aneurysm shape and growth, most of them dealing with the AAA, have been proposed [178, 179]. The diameter is the most common parameter for assessing the growth and automated extraction methods based on computational techniques like the maximally inscribed sphere method have already been proposed in literature [180]. Grobman et al. [181] emphasized the value of identifying local features in the shape of the abdominal aorta to assess the risks of aneurysm rupture and establish index thresholds for selecting patients for surgical treatment. The potential of using algorithms to identify higher-risk patients has been widely discussed [182]. Two measures related to the AAA shape, the vessel tortuosity and asymmetry, seemed to show significant relevance in predicting the aneurysm rupture [183, 184]. A solid contribution to the development of predictive methods has been provided by machine learning (ML) techniques [185, 186]. Piccinelli et al. [187] proposed a comprehensive framework for robustly characterizing vascular geometries, covering all steps from image segmentation to geometric characterization of the vascular structure. A retrospective dataset of 76 patients was used by Shum et al. to estimate geometric indices and regional variations in wall thickness and classify patients according to rupture risk criteria and decision three algorithm [188]. Lee et al. proposed a classifier based on statistical machine learning to evaluate the risk of rupture of the abdominal aorta from curvature features [189] while Rengarajan et al. assessed the risk integrating biological information

with geometric data [190]. Do et al. [191] developed a Dynamical Gaussian Process Implicit Surface approach to predict the evolution of abdominal aortic aneurysms. Kim et al. employed convolutional neural networks to predict the exponential growth of abdominal aortic aneurysms by integrating information on vessel radius, thrombus thickness and Time Averaged Wall Shear Stress (TAWSS) derived from fluid-dynamic simulations [192]. Meyrignac et al. [193] combined abdominal aortic lumen volume and parameters derived from numerical simulation such as wall shear stress with regression models in order to predict the abdominal aneurysm growth.

Concerning the thoracic aorta, assessing the length of the ascending segment has shown clinical significance for surgical decision-making [194, 195]. Kruger et al. proposed a risk score based on centerline length and maximum diameter [196]. Poullis et al. showed that higher curvatures of the ascending aorta corresponded to increased forces on the wall, explaining the potential impact on the risk of aortic dissection [197]. AsAA rupture risk has also been assessed by considering indices derived from the ratio of the patient's diameter and height or body surface area [198], suggestions after integrated into the clinical guidelines [67]. Liang et al. proposed a machine learning approach to evaluate a risk score for patients previously tested with a computational solid mechanics simulation resulting in rupture [199]. Jiang et al. [200], using longitudinal data on abdominal aortic aneurysms, Growth and Remodeling (G&R) techniques and Probabilistic Collocation Method, demonstrated that the diameter evolution over time could be better predicted using Deep Belief Network compared to classical non-linear mixed-effect models [201].

The three-dimensional information derived from the overall shape of the segmented aorta can be more effectively exploited through statistical shape analysis (SSA) [202], a mathematical technique that allows to model the shape variations of a given anatomy within a population [203].

This technique includes statistical shape modeling, a method to represent the shape probability distribution by a mean shape and modes describing the shape variations [204]. Statistical shape modeling has been widely used in literature for many medical purposes [205, 206, 207]. The unsupervised Principal component analysis (PCA) technique is commonly employed to extract linearly independent components that describe the shape variation within a population. It requires datasets containing the same number of points. Therefore, when dealing with computational domains, iso-topological meshes (i.e. having the same number of nodes and connectivity) are required. These can be achieved through mesh morphing methods such as: radial basis function (RBF) techniques, moving least squares (MLS)

strategies, thin plate splines (TPS) methods and Laplacian-based approaches [208]. A general shape-based framework to identify healthy or diseased anatomical structures was described by Durrleman et al. [209]. In [210], unsupervised hierarchical clustering was applied on a set of aortic segmentations and on the reduced PCA-derived dataset to replicate the diagnoses provided by clinical experts.

A second method alternative to PCA for performing statistical shape analysis is partial least squares (PLS) analysis. PLS is a multivariate supervised statistical method used to analyze the relationship between two sets of variables: predictors and response variables [211]. PLS has been used to assess the risk of myocardial infarction and predict cardiac remodelling [212, 213, 214]. PCA and PLS have already been used and compared in predicting the risk of aortic dissection [215], with the second returning better results in separating patients who will experience dissection and patients who will not.

In the first part of this study, we describe a method for extracting local shape features to identify patients at high risk of AsAA growth. In addition to the diameter, already proposed in the guidelines, these include the ratio between the diameter and the centerline length, the ratio between the lengths of the external and internal lines and the tortuosity of the ascending tract. Using longitudinal data from 70 patients, we segmented each image dataset to obtain patient-specific geometries. Subsequently, we investigated the correlation between each local shape feature computed from the first exam and the aneurysm growth rate calculated using the two acquisitions. Afterwards, we employed and compared six different machine learning classifiers to predict patients who will present adverse and rapid AsAA evolution and demonstrate how these new local features can complement the information currently provided by the diameter assessment. In the second part of the study, we combined regression methods with local and global shape features to directly infer the growth rate of each patient. The same local shape features previously mentioned were employed. Global shape features were specific shape modes derived from principal component analysis and partial least squares analysis. These techniques were applied to patient-specific iso-topological computational grids obtained by adapting a template to each segmentation through RBF mesh morphing.

The details of the methods used have been described in the following Section.

3.2 Materials and methods

The entire pipeline of this study is presented in Figure 3.1. The current Section is structured as follows: in Subsection 3.2.1, the dataset is presented, introducing the inclusion and exclusion criteria. Subsection 3.2.2 describes the developed semi-automatic segmentation method to extract the 3D anatomy. In Subsection 3.2.3, the geometric decomposition method executed for extracting local shape features, i.e., the metrics derived from calculating geometric quantities on each individual model, is illustrated. The computation of the growth rate is addressed in Subsection 3.2.4. An overview to illustrate the most well-known classification models is provided in Subsection 3.2.5 while the classification criteria for the risk of aneurysm growth are identified in Subsection 3.2.6. Moving on to Subsection 3.2.7, we provide an introduction of the mathematics related to RBF mesh morphing and in Subsection 3.2.8, we delve into its application to obtain iso-topological computational grids, which will subsequently be used to extract global shape features through principal component analysis and partial least squares analysis in Subsection 3.2.9. These features are defined global as they are derived from the entire population and encompass the overall shape of the ascending aorta with an aneurysm. Finally, Subsection 3.2.10 describes the regression methods we used to derive the growth rate for each patient-specific anatomy exploiting local and global shape features.

3.2.1 Dataset

We included patients with an official clinical report indicating a dilated aorta condition and two 3D acquisitions separated by at least 6 months. Images were derived from a retrospective dataset obtained from the registry systems of three medical centers: the University Hospital of Rennes (Rennes, France), the University Hospital of Dijon (Dijon, France) and the University Hospital of Toulouse (Toulouse, France). The study was conducted in accordance with ethical standards, and the data were collected from December 2006 to September 2022. The dataset was fully anonymized to ensure patients' privacy.

We used both CT and Magnetic Resonance Angiography (MRA) images, excluding any data with a resolution worse than 1 mm x 1 mm x 1 mm. Patients with both bicuspid and tricuspid valves were included.

To increase the likelihood of producing reliable and repeatable results, additional exclusion criteria were set: (1) patients younger than 25 years, (2) aneurysms related to systemic inflammatory diseases, (3) prior aortic valve surgery, (4) acute aortic

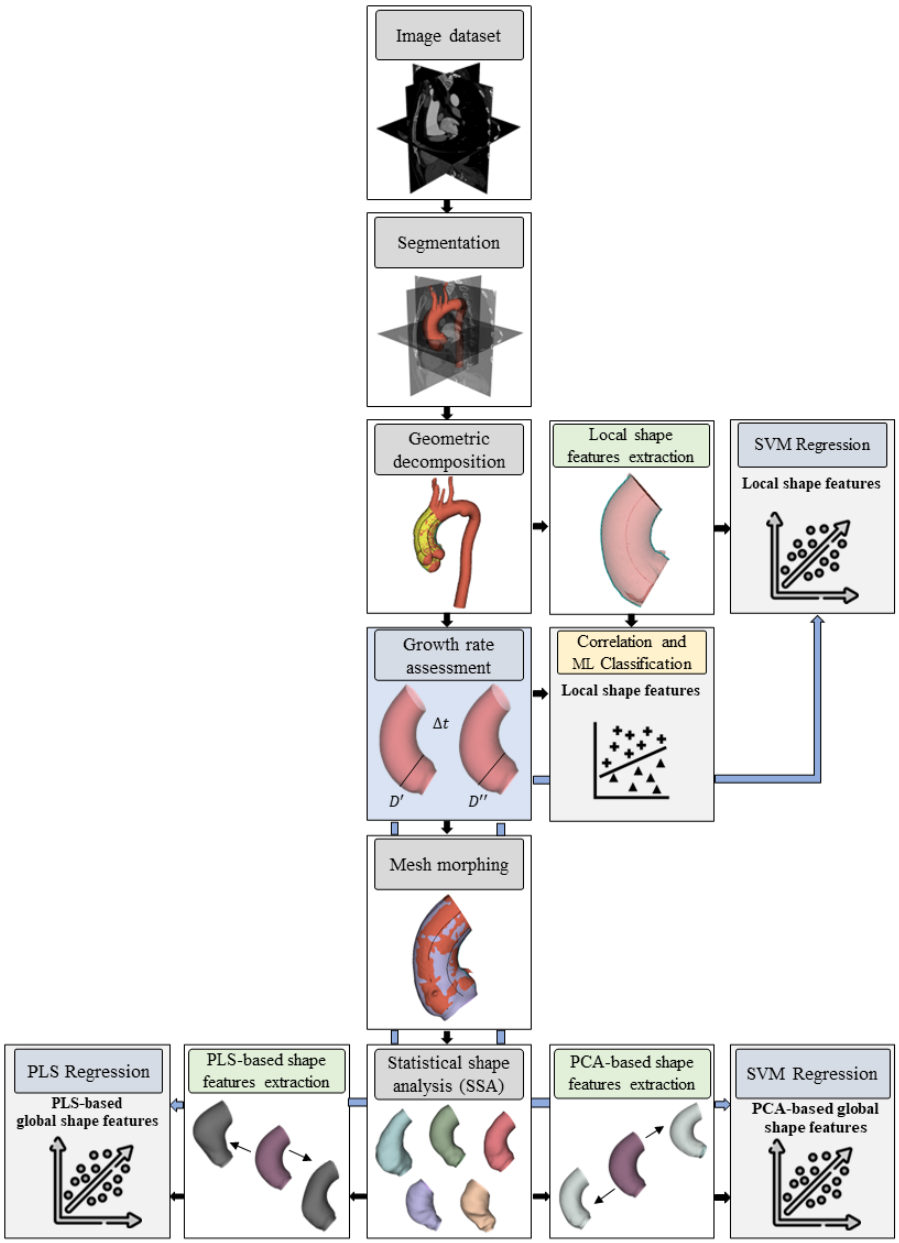

Figure 3.1: Full workflow for identifying patients at high risk of aneurysm growth through local shape features and classification methods and predicting the aneurysm growth rate by means of local and global shape features combined with regression techniques.

syndrome, (5) congenital tissue disorders such as Marfan syndrome and (6) images with artefacts. Globally, $N = 70$ patients were included. 47 (67.1%) patients had double ECG-gated acquisitions. The longitudinal dataset consisted of 120 (85.7%) CT scans and 20 (14.3%) MRA. 85 acquisitions (60.7%) were performed with contrast

agent injection and 55 (39.3%) without.

3.2.2 Segmentation

The segmentation of the whole thoracic aorta, from the aortic annulus to the descending aorta at the level of the diaphragm, was obtained using 3D Slicer [216]. 3D Slicer is a free and open-source software platform used for medical image processing and visualization. It was the software used to treat and visualize the patient's data. It provides, in fact, various tools and modules for image analysis, segmentation, registration, and three-dimensional reconstruction. We used a semi-automatic local thresholding method based on the grey-level histogram derived from analysing three sets of voxels. Each set was determined by initially identifying three points in different areas of the aorta: the ascending aorta, the aortic arch and the descending aorta. Around each point used as center, three spheres of radius 5 mm were built, as shown in Figure 3.2 (A). All the voxels distributed inside each sphere were acquired to determine the grey level interval for segmenting the aorta. After extracting the 3-dimensional surface with Flying Edges algorithm [217], a manual editing process for verifying that it corresponded to the inner lumen of the vessel and for the correction of possible improperly segmented portions was performed, especially in the case of geometries derived from MRI acquisitions. A median filter was then applied with a kernel size of 3 mm. At the end of the segmentation procedure, a patient-specific tessellated surface made up of 8000-15000 triangular elements has been obtained, as shown in Figure 3.2 (B).

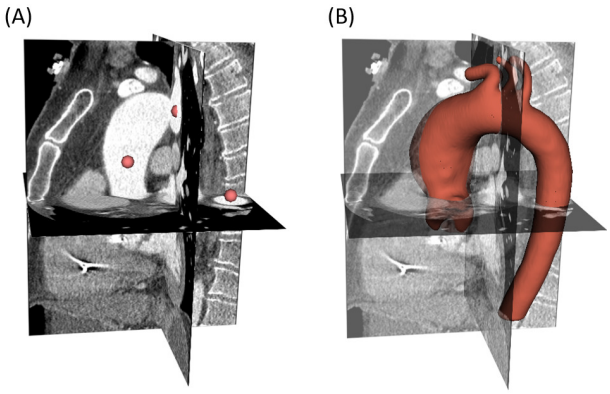

Figure 3.2: (A) Spheres built around the markers to acquire the grey levels for the thresholding method. (B) Final model derived from segmentation.

3.2.3 Local shape features extraction

The shape features extraction required a geometric decomposition of the vessel. The first step was the calculation of the centerline, as some of the metrics were directly influenced by its conformation, direction and length [218]. It was extracted using Vascular Modelling Toolkit (VMTK) through Voronoi diagrams [219] after an automatic detection of the inlet and outlets seed points [220]. The segmented domain S related to the AsA and the corresponding centerline tract C were isolated with a first cut perpendicular to C at the level of the annulus and a second one in correspondence to the ostium of the brachiocephalic trunk. The methods to derive each shape feature are detailed below.

3.2.3.1 Diameter

The AsA intra-luminal diameter was measured by extracting n=100 sections Ψ_k for k=1,...,n perpendicular to C and equally spaced along it. Figure 3.3 (A) shows one of the thoracic aorta segmentations, the isolated ascending tract and a subset of 20 sections. On each section Ψ_k, the maximum diameter D_{max_k} was obtained as the longest of the segments resulting from the intersection between Ψ_k and a rotating a plane perpendicular to Ψ_k, passing through x_{c_k} (the point of intersection between Ψ_k and C) and sweeping angles of $\alpha = 22.5°$, as shown in Figure 3.3 (B). The maximum diameter D for the entire vessel, current main criterion for elective AsA surgery, is:

$$D = \max\{D_{max_1}, ..., D_{max_n}\} \tag{3.1}$$

3.2.3.2 Diameter-centerline ratio

By using the maximum diameter D and computing the length of AsA centerline $\mathcal{L}(C)$, we defined the diameter-centerline ratio DCR:

$$DCR = \frac{D}{\mathcal{L}(C)} \tag{3.2}$$

3.2.3.3 External-internal line ratio

Given the tessellated surface S consisting of a set F of triangular faces F_i such that any point $P \in S$ lay in at least one triangle $F_i \in F$, we could identify a polygonal curve $\Gamma_j^{x_a,x_o}$ on S starting from an arbitrary point $x_a \in \Omega_{annulus}$ and reaching another arbitrary point $x_o \in \Omega_{ostium}$ where $\Omega_{annulus}$ and Ω_{ostium} were respectively

the boundaries of S at the level of the annulus and at the level of the ostium. The length $\mathcal{L}(\Gamma_j^{x_a,x_o})$ is:

$$\mathcal{L}(\Gamma_j^{x_a,x_o}) = \sum_{F_i \in F} \mathcal{L}\left(\Gamma_{j_{|F_i}}^{x_a,x_o}\right) \tag{3.3}$$

where $\mathcal{L}\left(\Gamma_{j_{|F_i}}^{x_a,x_o}\right)$ was measured according to the Euclidean distance. We defined the shortest discrete geodesic Γ_G as the shortest path:

$$\Gamma_G = \underset{x_a,x_o,j}{\operatorname{argmin}}\, \mathcal{L}(\Gamma_j^{x_a,x_o}) \tag{3.4}$$

The length $\mathcal{L}(\Gamma_G)$ resulted in being the shortest geodesic distance. We used the Dijkstra method [221] to find the set of discrete geodesic over the entire aortic domain connecting all points $x_a \in \Omega_{annulus}$ with $x_o \in \Omega_{ostium}$ and we selected the shortest of them. The resulting broken line was then smoothed to obtain the aortic internal curvature line (ICL).

After, for each section Ψ_k, defining x_{ic_k} the point of intersection between Ψ_k and ICL, the direction given by the versor $\mathbf{v_{c_k}}$ pointing towards the centre of the aorta x_{c_k} was identified:

$$\mathbf{v_{c_k}} = \frac{\overrightarrow{x_{ic_k}x_{c_k}}}{\|\overrightarrow{x_{ic_k}x_{c_k}}\|} \tag{3.5}$$

The intersection between the axis along the direction $\mathbf{v_{c_k}}$ and S defined a new point x_{ec_k}, as reported in Figure 3.3 (C). The repetition of this procedure on the n sections Ψ_k allowed the creation of the set of points controlling the spline corresponding to the external curvature line (ECL). In Figure 3.3 (D), ECL and ICL are shown. The ratio between the external and internal curvature line lengths $EILR$ was then computed:

$$EILR = \frac{\mathcal{L}(ECL)}{\mathcal{L}(ICL)} \tag{3.6}$$

3.2.3.4 Tortuosity

The last local shape feature we computed was the tortuosity T, defined as:

$$T = \frac{\mathcal{L}(C)}{\mathcal{L}(C_0)} \tag{3.7}$$

where C_0 was the straight line connecting the first and the last points of C.

Except for the manual identification of the brachio-cephalic trunk ostium, the procedure for computing the shape features was without any user interaction. The geometric decomposition methods were developed using Python, Visualization Toolkit

(VTK), Insight Toolkit (ITK) and Qt in 3D Slicer environment.

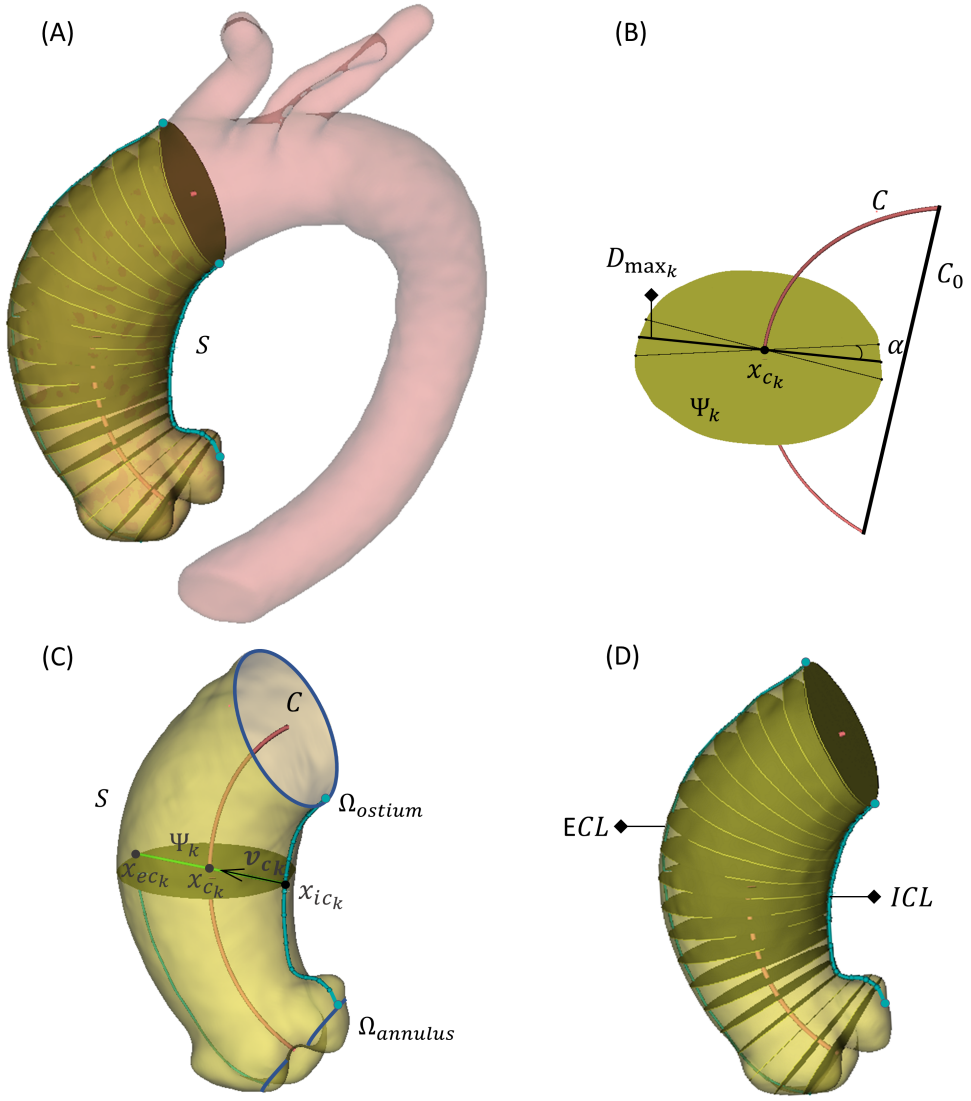

Figure 3.3: The full aorta segmentation, the discrete ascending aorta domain S and a subgroup of 20 aortic sections perpendicular to the centerline (A). A generic section Ψ_k isolated for the calculation of the related maximum diameter D_{max_k}; the centerline of the ascending section C and the segment C_0 are also shown (B). Identification of the point x_{ec_k} to compute the external curvature line (C). Isolated ascending section with the external and internal curvature line (ECL and ICL) (D).

3.2.4 Growth rate

Even if the diameter threshold for elective surgery may not have been met, patients experiencing rapid AsAA growth over time should be carefully and constantly monitored [222]. For this reason, we can deduce that the risk of aneurysm rupture is closely related to the risk of aneurysm growth [223]. Exploiting longitudinal data, the aneurysm growth rate GR_i was derived by dividing the difference in maximum diameters by the time gap $\Delta\tau_i$, measured in months, between the two acquisitions:

$$\mathrm{GR}_i = \frac{D_i'' - D_i'}{\Delta\tau_i} \tag{3.8}$$

All the growth rates were computed and stored in the vector $\mathbf{Y}$:

$$\mathbf{Y} = (\mathrm{GR}_1, \mathrm{GR}_2, \ldots, \mathrm{GR}_N) \in \mathbb{R}^N \tag{3.9}$$

The Mann-Whitney test was used to compare the GR values derived from ECG-gated data with those computed on patients for whom at least one acquisition was not gated. The relationship between the proposed local shape features and the growth rate was then evaluated using Spearman's correlation coefficients. Statistical analysis was performed using Matlab (version 9.12.0, R2022a).

3.2.5 Classification and regression models: general overview

Classification and regression are two methods that aim at predicting outcomes based on input features and labeled training data [224]. They are supervised techniques, as they require labeled data to learn the relationship between inputs and outputs. Both require a training phase and a prediction phase. The goal of classification is to assign input data points to predefined categories or classes where the output variable is categorical, and the algorithm learns from labeled data to make predictions for new unseen data. In regression, the aim is to predict a continuous numerical value rather than a discrete class label. A few more details on the ML models employed in this work are given below.

3.2.5.1 Decision Tree

Decision Tree (DTr) is a supervised machine learning algorithm used for classification and regression tasks [225]. It is a tree-like model where the data is recursively split into subsets based on the values of the input features, with the goal of making predictions or assigning labels to new data points.

The decision tree starts with a single node, known as root node, representing the entire dataset. The data are then split into subsets based on the values of a specific feature and this process continues recursively until a stopping criterion is met. The decision tree algorithm chooses the feature that best separates the data at each node based on a specific criterion (e.g., Gini impurity or entropy for classification tasks and mean squared error for regression tasks) [226]. Decision Trees can be prone to overfitting, especially when the tree is deep and not appropriately pruned. Setting maximum depth and implementing ensemble methods like Random Forest and Gradient Boosting tor pruning techniques are often valid solutions to mitigate overfitting [227].

Once the tree is built, to make a prediction for a new data point, the algorithm follows the path down the tree, evaluating the values of the features at each node and assigning the data point to the appropriate leaf node. For classification tasks, the predicted class label is determined by the majority class of the data points in the leaf node. For regression tasks, the predicted value is the average of the target values of the data points in the leaf node.

3.2.5.2 Linear Discriminant

Liniar Discriminant (LD) is a classification technique with the main objective of determining a linear combination of features that best separates two or more classes in a dataset. The linear combination is chosen to maximise the distance between the means of the classes while minimizing the variance within each class [228]. Given a dataset containing samples with their corresponding feature vectors and class labels, Linear Discriminant aims to find a lower-dimensional representation of the data that retains the most relevant discriminative information.

LD focuses primarily on projecting the features from higher dimension space to lower dimensions. The separability between classes, i.e., the distance between the mean of different classes, is computed. This is called between-class variance S_b.

$$S_b = \sum_{i=1}^{N_c} N_i \left(\bar{x}_i - \bar{x}\right)\left(\bar{x}_i - \bar{x}\right) \tag{3.10}$$

where N_c is the number of classes, N_i is the number of observation in the i-class, $\bar{x}_i$ is each mean class value, $\bar{x}$ is the overall mean. The distance between every sample

and the mean of each class is derived. It is also called within-class variance S_w.

$$S_w = \sum_{i=1}^{N_c} \sum_{j=1}^{N_i} (x_{i,j} - \bar{x}_i)(x_{i,j} - \bar{x}_i) \tag{3.11}$$

The lower-dimensional space which maximizes the between-class variance S_b and minimizes the within-class S_w variance is built. $\mathbf{P}$ is considered as the lower-dimensional space projection.

$$\mathbf{P}_{\mathrm{LD}} = \arg\max_{\mathbf{P}} \frac{\left|\mathbf{P}^T S_b \mathbf{P}\right|}{\left|\mathbf{P}^T S_w \mathbf{P}\right|} \tag{3.12}$$

Finally, the data is projected onto the selected linear discriminants to obtain the reduced-dimensional representation. This new lower-dimensional space allows for better separation between classes, making the classification easier.

3.2.5.3 Logistic Regression

Logistic Regression (LR) is a statistical method used for binary classification problems, where the goal is to predict a binary outcome based on one or more input variables (features). It is called "logistic" because it uses the logistic function (sigmoid function) to model the relationship between the input variable $\mathbf{x} \in R^n$ and the binary outcome $Y \in \{0, 1\}$ [229]. Defining a sigmoid curve $F(x)$ centered on a point u (usually 0.5) and a density function $f(x)$, the logistic formula can be written as follows:

$$\mathrm{F}(x) = P(X \leq x) = 1/(1 + \exp(-(x - u)/\gamma)) \tag{3.13}$$

The model calculates the probability of the binary outcome being true (represented as 1) given the input features and the conditional probability distribution of the binomial logistic regression model [230]:

$$\mathrm{P}(Y = 1 \mid \mathbf{x}) = \frac{\exp(\mathbf{w} \otimes \mathbf{x} + b)}{1 + \exp(\mathbf{w} \otimes \mathbf{x} + b)} \tag{3.14}$$

where $\mathbf{x} \in R^n$ is the input vector, $\mathbf{w} \in R^n$ is the weight vector, $b \in R$ is the offset, $\mathbf{w} \otimes \mathbf{x}$ is the inner product of $\mathbf{w}$ and $\mathbf{x}$. If the returned probability is higher than the sigmoid center, the model predicts the positive class (1); otherwise, it predicts the negative class (0).

3.2.5.4 Naive Bayes

Naive Bayes (NB) is a probabilistic machine learning algorithm commonly used for classification tasks based on the assumption that Bayesian principle and feature conditions are relatively independent.

The basic idea behind Naive Bayes is to calculate the probability of a particular instance belonging to a specific class, given its feature values. It assumes that the features are conditionally independent [231].

Naive Bayes operates as a conditional probability model by assigning probabilities $p\left(C_k \mid x_1, \ldots, x_n\right)$ for each of the K possible output classes C_k, given a problem instance to be classified, represented by a vector $\mathbf{x} = (x_1, \ldots, x_n)$ encoding n features (independent variables). The problem with the above formulation is that if the number of input features n is large or a feature can take on many values, then basing such a model on probability tables is infeasible. The model must be reformulated to make it more tractable. Using the Bayes theorem, the conditional probability can be decomposed as:

$$P\left(C_k \mid \mathbf{x}\right) = \frac{P\left(C_k\right) P\left(\mathbf{x} \mid C_k\right)}{P(\mathbf{x})} \tag{3.15}$$

The naive Bayes classifier incorporates this model and a decision-making rule in practical applications. A frequently used decision rule involves selecting the hypothesis that maximizes the probability of correctness to reduce the chances of misclassification. This decision criterion is known as Maximum A Posteriori (MAP) decision rule. The classifier resulting from this approach, known as a Bayes classifier, is a function responsible for assigning class labels $\hat{y} = C_k$ for some k as follows:

$$\hat{y} = \underset{k \in \{1, \ldots, K\}}{\operatorname{argmax}} P\left(C_k\right) \prod_{i=1}^{n} P\left(x_i \mid C_k\right) \tag{3.16}$$

3.2.5.5 Support Vector Machine

Support Vector Machine (SVM) is a supervised machine learning algorithm used for both classification and regression tasks [232]. It is particularly effective in scenarios with complex decision boundaries and high-dimensional feature spaces. In the context of classification, SVM aims at finding the optimal hyperplane that best separates different classes of data points [233]. The hyperplane:

$$w^T x + b = 0 \tag{3.17}$$

is the boundary for which the margin ψ, i.e., the distance between the data points of different classes, is the maximum. The data points closest to the hyperplane and determining its position are called support vectors. The main idea behind SVM is to transform the original feature space into a higher-dimensional space, allowing the effective separation of the data points of different classes by means of the hyperplane. This transformation is achieved through kernel functions, which extract the inner products between the data points in the higher-dimensional space without explicitly calculating the transformation. For a binary classification problem, the objective of SVM is to solve the following optimization problem that aims at maximizing the margin ψ while keeping all data points on the correct side of the hyperplane [234]:

$$\psi(\mathbf{w}, \mathbf{b}) = \frac{2}{\|\mathbf{w}\|} \tag{3.18}$$

where $\mathbf{w}$ is the weight of the hyperplane, $\mathbf{x}$ is the input feature vector and $\mathbf{b}$ is the bias vector. SVM can handle different kernel functions, such as linear, polynomial and sigmoid kernels.

3.2.5.6 K-nearest Neighbors

K-nearest Neighbours (KNN) is a supervised machine learning algorithm used for both classification and regression tasks [235]. It is a non-parametric and instance-based learning algorithm, meaning that it does not make any assumptions about the underlying data distribution and stores the training data points as part of its model. KNN is used to classify new data points or predict their numerical values based on their proximity to the training data.

During the training phase, KNN memorizes the entire training dataset, storing the feature vectors and their corresponding class labels in case of classification or numerical values in case of regression [236]. When making predictions for a new data point, KNN identifies the K nearest neighbours in the training dataset based on a distance metric (e.g. Hamming or Euclidean distance). The value of K is a user-defined parameter and determines how many neighbours will be considered for the prediction [237]. The choice of K is critical in KNN. A small value of K (e.g., K = 1) can lead to noisy predictions and high sensitivity to outliers. In contrast, a high value of K may cause the algorithm to lose important local patterns and result in overly smoothed predictions. The value of K is usually chosen based on cross-validation or other tuning techniques to find the optimal balance between bias and variance. For classification tasks, the predicted class for the new data point

is determined by a majority vote among the classes of the K nearest neighbours. The class that appears most frequently among the K neighbours is assigned as the predicted class. Concerning the regression, the predicted value for the new data point is calculated as the average of the target values of the K nearest neighbours.

KNN becomes computationally expensive when dealing with large datasets, especially in high-dimensional feature spaces. Additionally, it is sensitive to the scale of features, so it is common to perform feature scaling before applying the algorithm.

3.2.6 Machine learning growth risk prediction

We divided the dataset into two risk classes according to the observed growth rate. All patients with GR $\leq$ 0.25 mm/month composed the low-risk class (61 patients), while the others represented the group with rapid growth (9 patients). This threshold was chosen according to the surgery guidelines previously mentioned, where a threshold value of 3 mm/year was indicated. For every individual, we then tried to predict the belonging class by using ML classifiers based on the metrics derived from the first acquisition acting as possible predictors of growth. We initially tested the diameter D alone derived from the first exam in order to predict the GR-related risk class. Then, a second classification was conducted, selecting all the shape features together. Six different classification models [238] were used: Decision Tree, Linear Discriminant, Logistic Regression, Naive Bayes, Support Vector Machine and K-nearest Neighbours. Except for LR, the hyperparameter values were optimized minimizing the classification error. We use a leave-one-out cross-validation method to assess the predictive accuracy of the classification models. The first of the evaluated results is the accuracy, defined as:

$$\text{accuracy} = \frac{\text{TP} + \text{TN}}{\text{TP} + \text{TN} + \text{FP} + \text{FN}} \tag{3.19}$$

Sensitivity and specificity are calculated as:

$$\text{sensitivity} = \frac{\text{TP}}{\text{TP+FN}} \tag{3.20}$$

$$\text{specificity} = \frac{\text{TN}}{\text{TN+FP}} \tag{3.21}$$

where true positive (TP) is the number of fast-growing aortas correctly identified, true negative (TN) represents the number of low-risk shapes correctly identified, false negative (FN) is the number of high-risk geometries incorrectly identified as low

risk and false positive (FP) consists in the low-risk shapes incorrectly identified as high risk. We obtained these values by analyzing the confusion matrix, a 2x2 matrix where the diagonal represents the correctly classified aortas and the anti-diagonal represents misclassifications. In addition to accuracy, sensitivity and specificity, the performances were measured using the area under the receiver operating characteristic (AUROC) curve, which represents the probability that the input parameter (parameters) is (are) higher for the class with fast growth than for the one with slow growth and thus is a measure of discrimination. Finally, to describe the diagnostic value of the proposed shape features, likelihood ratios (LHRs) are used:

$$\text{LHR+} = \frac{\text{sensitivity}}{1 - \text{specificity}} \tag{3.22}$$

$$\text{LHR}- = \frac{1 - \text{sensitivity}}{\text{specificity}} \tag{3.23}$$

LHR+ (LHR-) represents the change in the odds of having a diagnosis in patients with a positive (negative) test.

3.2.7 Mesh morphing background

With the aim of obtaining a set of iso-topological grids, RBF mesh morphing can be used to adapt a reference mesh to a new patient's anatomy [239, 240]. Mesh morphing is, in fact, a technique used to modify the shape of a computational grid [241]. Among the morphing methods available in the literature, RBFs are well known for their interpolation quality [242]. Several advantages are related to the RBF mesh morphing approach: the robustness of the procedure is preserved, any kind of mesh typology is supported without the requirement to regenerate it and the process can be parallelized and integrated in any solver. On the other hand, this method is slightly slow when dealing with hundreds of millions of nodes, although this is not the case. RBFs allow to interpolate in the space a scalar function known at discrete points, called Source Points (SPs). By solving a linear system of order equal to the number of SPs employed [239], the displacement of a mesh node in the three directions in space can be described. The approach is meshless and able to manage every element type related to surface and volume meshes. The interpolation function is defined as follows:

$$s(\mathbf{x}) = \sum_{i=1}^{N} \gamma_i \varphi \left(\|\mathbf{x} - \mathbf{x}_{\mathbf{s_i}}\| \right) + h(\mathbf{x}) \tag{3.24}$$

where $\mathbf{x}$ is a generic position in space, $\mathbf{x}_{\mathbf{s_i}}$ the SP position, $s(\cdot)$ the function

which represents a transformation $\mathbb{R}^n \to \mathbb{R}$, $\varphi(\cdot)$ the radial function of order m, γ_i the weight and $h(\mathbf{x})$ a polynomial term with degree $m-1$. The unknowns of the system, namely the polynomial coefficients and the weights γ_i of the radial functions, are retrieved by imposing the passage of the function on the given values and an orthogonality condition on the polynomials. The linear problem can be also written in matrix form:

$$\begin{bmatrix} \mathbf{M} & \mathbf{P} \\ \mathbf{P}^T & \mathbf{0} \end{bmatrix} \begin{Bmatrix} \boldsymbol{\gamma} \\ \boldsymbol{\beta} \end{Bmatrix} = \begin{Bmatrix} \mathbf{g} \\ \mathbf{0} \end{Bmatrix} \tag{3.25}$$

in which $\mathbf{M}$ is the interpolation matrix containing all the distances between RBF centres $\mathbf{M}_{ij} = \varphi\left(\|\mathbf{x_i} - \mathbf{x_j}\|\right)$, $\mathbf{P}$ the matrix containing the polynomial terms that has for each row j the form $\mathbf{P}_j = [1, x_{1j}, x_{2j}, ..., x_{nj}]$ and $\mathbf{g}$ the known values at SPs. If a deformation vector field has to be fitted in 3D (space morphing), considering $h(\mathbf{x})$ as a linear polynomial made up of known $\boldsymbol{\beta}$ coefficients:

$$h(\mathbf{x}) = \boldsymbol{\beta_1} + \boldsymbol{\beta_2} x + \boldsymbol{\beta_3} y + \boldsymbol{\beta_4} z \tag{3.26}$$

Each component of the displacement prescribed at the Source Points can be interpolated as follows:

$$\begin{cases} s_x(\mathbf{x}) = \sum_{i=1}^{N} \gamma_i^x \varphi\left(\|\mathbf{x} - \mathbf{x_{s_i}}\|\right) + \beta_1^x + \beta_2^x x + \beta_3^x y + \beta_4^x z \\ s_y(\mathbf{x}) = \sum_{i=1}^{N} \gamma_i^y \varphi\left(\|\mathbf{x} - \mathbf{x_{s_i}}\|\right) + \beta_1^y + \beta_2^y x + \beta_3^y y + \beta_4^y z \\ s_z(\mathbf{x}) = \sum_{i=1}^{N} \gamma_i^z \varphi\left(\|\mathbf{x} - \mathbf{x_{s_i}}\|\right) + \beta_1^z + \beta_2^z x + \beta_3^z y + \beta_4^z z \end{cases} \tag{3.27}$$

When working with a mesh, the new nodal positions can be retrieved for each node as:

$$\boldsymbol{x_{node_{new}}} = \boldsymbol{x_{node}} + \begin{bmatrix} s_x(\boldsymbol{x_{node}}) \\ s_y(\boldsymbol{x_{node}}) \\ s_z(\boldsymbol{x_{node}}) \end{bmatrix} \tag{3.28}$$

where $\boldsymbol{x_{node_{new}}}$ and $\boldsymbol{x_{node}}$ are the vectors respectively containing the updated and original positions of the given node.

3.2.8 Mesh morphing application

The iso-topological grids required for the statistical shape analysis were built using RBF mesh morphing, whose mathematical background was previously given in Section 3.2.7. The cubic kernel $\varphi(r) = r^3$ was chosen to interpolate the displacements in 3D space [243].

The initial shape used to generate the first mesh was identified as the one reporting the median aortic diameter of our patient population, as done for the femur by Grassi et al. [244]. The baseline mesh, consisting of $E = 37400$ quadrilateral elements and $K = 37620$ nodes, was obtained using ANSA pre-processor (BETA CAE Systems, Switzerland). A preliminary step was performed to align all the segmented models to the baseline mesh through an iterative closest-point algorithm. As already done by Biancolini et al. [245], a two-step morphing procedure was applied to modify each time the reference mesh in order to exactly match the target segmentation. The first step of the morphing procedure involved approaching the target segmented surface, while the second in completely projecting the deformed surface on the target geometry to achieve a perfect fit. Controlling the mesh using morphing is particularly difficult in case of biological models with few detectable anatomical landmarks [246], as the ascending aorta. In this regard, we developed a method to extract some pseudo-landmarks from the 3D surface, avoiding the need for manual landmark placement. The SPs to drive the morphing, corresponding to the pseudo-landmarks, were automatically derived through an equally-spaced sampling of the previously derived splines from the geometric decomposition and reported in Figure 3.4. 8 splines derived from 45° angles were sampled. 10 SPs per spline were collected on the initial model for a total of 80 SPs. A displacement was imposed to the SPs of the initial model in order to match the SPs extracted from the target geometry and the mesh nodes were updated through RBF interpolation, as reported in the appendix. To ensure the overlapping of the entire wall, the modified surface nodes were projected onto the target segmentation in the second step. The direction of projection was determined by the normal of each node of the reference mesh. To reduce mesh distortion due to morphing and the influence of the model chosen as initial template, once the $N = 70$ iso-topological grids were obtained, a mean template was derived and mesh morphing was performed again on all grids starting from it. A new mean template was then generated and used for the subsequent steps.

3.2.9 Global shape features extraction

Using the collection of iso-topological grids, a data matrix $\mathbf{X}$ containing K mesh nodes was created:

$$\mathbf{X} = (\mathbf{x_1}, \mathbf{x_2}, \ldots, \mathbf{x_N}) \in \mathbb{R}^{3K \times N} \tag{3.29}$$

SSA to extract global shape features was first performed by creating a statistical

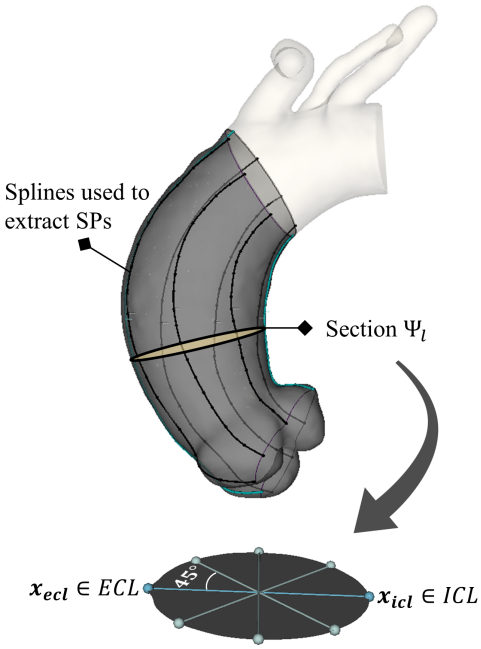

Figure 3.4: Splines used to collect the Source Points required to impose the morphing.

shape model based on the principal components and after using partial least squares analysis. All the algorithms were developed using Python.

3.2.9.1 Statistical shape model

Principal component analysis was used to extract the principal modes of variation by computing the eigenvectors of the covariance matrix $\mathbf{C}$ of the training data:

$$\mathbf{C} = \frac{1}{N-1}\mathbf{X}\mathbf{X}^T \in \mathbb{R}^{3K\times 3K} \tag{3.30}$$

The eigen-equation related to the covariance matrix is:

$$\mathbf{C}\boldsymbol{\phi_j} = \lambda_j \boldsymbol{\phi_j} \tag{3.31}$$

where $\boldsymbol{\phi_j}$ is the eigenvector corresponding to the eigenvalue λ_j and represents the directions of variation of the data. Eigenvalues and eigenvectors are ordered from high to low variance. The contribution of each shape mode to the total variance was given by its corresponding eigenvalue λ_j [247].

A factorization of the data matrix through singular value decomposition (SVD) can be performed:

$$\mathbf{X} = \mathbf{USV}^T \tag{3.32}$$

with $\mathbf{U} \in \mathbb{R}^{3Kx3K}$ and $\mathbf{V} \in \mathbb{R}^{NxN}$ unitary matrices ($\mathbf{U}^{-1} = \mathbf{U}^*$ and $\mathbf{V}^{-1} = \mathbf{V}^*$) and $\mathbf{S} \in \mathbb{R}^{3KxN}$ matrix containing the singular values s_j on the diagonal.

Thus, equation 3.30 can be written as:

$$\mathbf{C} = \frac{1}{N-1}\left(\mathbf{USV}^T\right)\left(\mathbf{USV}^T\right)^T \tag{3.33}$$

and simplifying:

$$\mathbf{C} = \frac{1}{N-1}\mathbf{US}^2\mathbf{U}^T \tag{3.34}$$

This demonstrates that the singular values of the data matrix are related to the eigenvalues of the covariance matrix:

$$\lambda_j = \frac{1}{N-1}s_j^2 \tag{3.35}$$

Once the template or mean shape $\overline{\boldsymbol{x}}$ is extracted, each patient shape $\tilde{\boldsymbol{x}}_{\boldsymbol{i}}$ belonging to the dataset can be reconstructed using the first M shape modes:

$$\tilde{\boldsymbol{x}}_{\boldsymbol{i}}(\boldsymbol{w}) = \bar{\boldsymbol{x}} + \boldsymbol{\phi w} \tag{3.36}$$

where $\boldsymbol{w}$ is the vector containing the shape feature weights for the i-patient which can be derived from:

$$\boldsymbol{w} = \boldsymbol{\phi}^T(\boldsymbol{x}_{\boldsymbol{i}} - \bar{\boldsymbol{x}}) \tag{3.37}$$

Assuming the data follows a normal distribution, each feature weight w_j is conventionally bounded within a certain range of the standard deviation:

$$-\xi_{lim}\sqrt{\lambda_j} \leq w_j \leq \xi_{lim}\sqrt{\lambda_j} \tag{3.38}$$

where ξ_{lim} is usually assumed equal to 3. In other words, w_j is a scalar value providing the geometrical influence of each shape mode on the final deformed model. Only the first M of the N eigenvectors were selected to account for a predetermined percentage of the variance and synthetically represent each aortic shape in the dataset. M can be chosen by computing the compactness (CN) and finding the number of shape modes for which the variance curve reaches 80%, 90%, 95% or 99%. CN is defined as the sum of variances normalized by the whole cumulative variance:

$$\mathrm{CN}(M) = \frac{\sum_{j=1}^{M} \lambda_j}{\sum_{j=1}^{N} \lambda_j} \tag{3.39}$$

The CN curve shows how many PCA modes are required to describe a certain amount of variation in the dataset. A second parameter to assess the quality of the statistical shape model is the generalization (GE). It is used to estimate its capability to represent unseen data and is computed as the average sum of square errors of a leave-one-out (LOO) procedure [248]. Each time, in fact, one patient is excluded and a new statistical shape model is built using the $N-1$ remaining ascending aortic shapes. The new statistical shape model is then used to reconstruct the shape of the left-out patient and the difference between the original shape and the reconstruction is quantified using the mean square error, progressively including additional modes. For this work, GE was computed using up to M shape modes:

$$\mathrm{GE}(M) = \frac{1}{N} \sum_{i=1}^{N} \left\| \mathbf{x_i} - \hat{\mathbf{x}}_\mathbf{i}\left(M\right) \right\|^2 \tag{3.40}$$

where $\mathbf{x_i}$ and $\hat{\mathbf{x}}_\mathbf{i}$ are the original and rebuilt left-out shapes, respectively.

3.2.9.2 Partial least squares analysis

PCA modes are extracted purely from the patient matrix $\mathbf{X}$ without taking into account any external information related to the examined shapes. On the other side, PLS performs a simultaneous decomposition of $\mathbf{X}$ and $\mathbf{Y}$ in order to obtain the highest correlation for the score vectors of both the input and output matrices [249]. This ensures maximal interdependencies between the shapes and the output variables, making the statistical shape decomposition application-oriented as dependent on the clinical response variables, i.e., the growth rate. Whereas PCA tries to identify hyperplanes that capture the most significant variation in the data, PLS employs a linear regression model that involves projecting the predicted and observable variables into a new space to establish the fundamental relationships between them. PCA generates a set of orthogonal components that are uncorrelated and ordered by the amount of variance. PLS, on the other hand, generates a set of latent variables that capture the maximum covariance between the $\mathbf{X}$ and $\mathbf{Y}$ matrices.

Given two standardized matrices $\mathbf{X'} = \mathbf{X}^T \in \mathbb{R}^{N \times 3K}$ and $Y \in \mathbb{R}^{N \times Z}$ where N is the number of observations (shapes), $3K$ is the number of predictor variables (point coordinates), Z is the number of predicted variables and defining the number of shape modes M, PLS returns the relations between these two matrices through score

vectors. The **X'** and **Y** matrices are decomposed as follow:

$$\begin{aligned} \mathbf{X}' &= \mathbf{T}\mathbf{P}^T + \mathbf{E} \\ \mathbf{Y} &= \mathbf{U}\mathbf{Q}^T + \mathbf{F} \end{aligned} \tag{3.41}$$

where $\mathbf{T} \in \mathbb{R}^{N \times M}$, $\mathbf{U} \in \mathbb{R}^{N \times M}$ are the matrices of the M extracted score vectors $\mathbf{t}$ and $\mathbf{u}$, $\mathbf{P} \in \mathbb{R}^{3K \times M}$ and $\mathbf{Q} \in \mathbb{R}^{Z \times M}$ represent the matrices of loadings and $\mathbf{E} \in \mathbb{R}^{N \times 3K}$ and $\mathbf{F} \in \mathbb{R}^{N \times Z}$ are the matrices of residuals. The PLS method finds weight vectors $\mathbf{b}$, $\mathbf{c}$ such that:

$$[\mathrm{cov}(\mathbf{t}, \mathbf{u})]^2 = [\mathrm{cov}(\mathbf{X}'\mathbf{b}, \mathbf{Y}\mathbf{c})]^2 = \max_{|\mathbf{r}|=|\mathbf{s}|=1} [\mathrm{cov}(\mathbf{X}\mathbf{r}, \mathbf{Y}\mathbf{s})]^2 \tag{3.42}$$

where $\mathrm{cov}(\mathbf{t}, \mathbf{u}) = \mathbf{t}^T\mathbf{u}/N$ denotes the sample covariance between the score vectors.

PLS is based on an iterative process: the non-linear iterative partial least squares (NIPALS) algorithm [250]. It starts with a random initialization of the score vector $\mathbf{u}$ and executes the following steps until convergence is reached:

- $\mathbf{b} = \mathbf{X}'^T\mathbf{u} / \left(\mathbf{u}^T\mathbf{u}\right)$
- $\|\mathbf{b}\| \to 1$
- $\mathbf{t} = \mathbf{X}'\mathbf{b}$
- $\mathbf{c} = \mathbf{Y}^T\mathbf{t} / \left(\mathbf{t}^T\mathbf{t}\right)$
- $\|\mathbf{c}\| \to 1$
- $\mathbf{u} = \mathbf{Y}\mathbf{c}$

Since in this case $Z = 1$ (we aim at predicting only the patient-specific values of the growth rate in $\mathbf{Y}$), $\mathbf{Y}$ can be denoted as $\mathbf{y}$ and $\mathbf{u} = \mathbf{y}$. Consequently, the NIPALS procedure converges in a single iteration. The weight vector $\mathbf{b}$ is equal to the first eigenvector of the following eigenvalue problem [251]:

$$\mathbf{X}'^T\mathbf{Y}\mathbf{Y}^T\mathbf{X}'\mathbf{b} = \lambda\mathbf{b} \tag{3.43}$$

After the extraction of the score vectors $\mathbf{t}$ and $\mathbf{u}$, a process of deflation of the matrices $\mathbf{X}$ and $\mathbf{Y}$ is performed by subtracting their rank-one approximations based on $\mathbf{t}$ and $\mathbf{u}$. Various deflation methods can be used, which define different versions or variants of PLS. The vectors of loadings $\mathbf{p}$ and $\mathbf{q}$ can be derived from (3.41) as coefficients of regressing $\mathbf{X}'\mathbf{c}$ on $\mathbf{t}$ and $\mathbf{Y}$ on $\mathbf{u}$, respectively:

$$\mathbf{p} = \mathbf{X}^T\mathbf{t}/\left(\mathbf{t}^T\mathbf{t}\right) \text{ and } \mathbf{q} = \mathbf{Y}^T\mathbf{u}/\left(\mathbf{u}^T\mathbf{u}\right) \tag{3.44}$$

Since $Z = 1$, the PLS1 deflection method can be used:

$$\mathbf{X} = \mathbf{X} - \mathbf{t}\mathbf{p}^T \tag{3.45}$$

It is based on the assumption that the score vectors $\mathbf{t}$ are good predictors of $\mathbf{Y}$ and that a linear inner relation between the scores vectors $\mathbf{t}$ and $\mathbf{u}$ exists, i.e:

$$\mathbf{U} = \mathbf{T}\mathbf{D} + \mathbf{H} \tag{3.46}$$

where $\mathbf{D} \in \mathbb{R}^{M\times M}$ is the diagonal matrix and $\mathbf{H}$ denotes the matrix of residuals, The deflation of $\mathbf{y}$ is technically unnecessary in PLS1.

For the PLS modes, the new patient-specific shape features score vectors $\mathbf{t}_\mathbf{i}$ were computed and used for the prediction.

3.2.10 Regression-based growth rate prediction

Once the shape features had been computed, regression models were used to directly infer the patient-specific growth rate. Our approach involved both local and global shape features. Regarding the local, given the positive and statistically significant correlation results with the growth rate reported in Chapter 6, Subsection 6.1.1, DCR, $EILR$ and T were employed together. For the global, the patient-specific weights $\mathbf{w}$ related to the PCA modes and the PLS scores $\mathbf{t}$ were used as a predictor of the growth rate. Concerning the PCA modes, we used a F-test as feature ranking algorithm to order the predictors by importance [252]. Higher scores were associated with higher-importance shape features. The null hypothesis of each F-test is that the means of the response values, which are grouped by predictor variable values, are drawn from populations with equal means. On the other side, the alternative hypothesis is that the means of the populations are not all the same. If the resulting p-value of the statistical test is small, the corresponding predictor variable has a significant impact on the response variable. We reported as output the scores of the F-test $FS = -log(p)$. Thus, a high score value indicates that the corresponding predictor is relevant. The first three ordered PCA modes were used as global shape features. Although not necessary for the PLS shape features choice, the same F-test was applied to the PLS scores to observe the differences with the scores from PCA. The regression model used for the local shape features and the PCA-based

global shape features was the SVM, which had already shown promising results in similar studies [199] and had previously demonstrated good classification capabilities, as shown in Chapter 6, Subsection 6.2.2. This machine learning model is able to describe the nonlinear relationships between shape features and aneurysm growth. A Gaussian kernel function was employed and the hyperparameters, reported in the results section, were tuned by minimizing the prediction mean square error (MSE) [253]. Regarding the PLS regression, we only considered the first three components of the PLS, as these refer to the shape features most significantly correlated with the computed growth rate. LOO cross-validation was performed to evaluate the performance of each regressor and the regression accuracy was determined through root mean square error (RMSE). R^2 values are reported for both local and global shape features to assess the regression fit quality. The marginal effect of each predictor on the response in terms of growth rate is described by reporting the partial dependence plots between the predictor variables and the predicted responses. Finally, the SVM regression surface for the representative PCA-based global shape features is provided to understand how the predicted growth rate varied as the shape changed according to the variability of the studied population.

Chapter 4

Calibration of the mechanical boundary conditions for a high-fidelity thoracic aorta model

In the previous Chapter, the importance of anatomy in the study of aortic aneurysms has been highlighted. Nevertheless, a comprehensive analysis must also be founded upon numerical simulation, particularly in developing three-dimensional numerical models to establish a reliable Digital Twin. In this Chapter, we delve into the cardiovascular patient-specific numerical simulation. Our analysis focuses on the complex interplay between the aorta and the surrounding organs, in particular soft tissue, heart and spine. We first go through the state of the art about patient-specific aortic modeling, covering the limited approaches proposed in the literature to consider the cardiac motion imposed on the annulus and the inclusion of mechanical boundary conditions accounting for the organs around the aorta. Afterwards, we present a detailed procedure to tune the parameters governing such boundary conditions in order to achieve a computational model whose kinematics closely replicate that derived from the images.

This Chapter relies on the Sections Introduction and Materials and Methods of the following publication:

- *"Calibration of the mechanical boundary conditions for a patient-specific thoracic aorta model including the heart motion effect", Geronzi et al., IEEE Transactions on Biomedical Engineering, (2023)* [254].

4.1 Introduction

Cardiovascular patient-specific simulation aims to bring a new insight into biomedical issues with the purpose of improving diagnosis, optimizing clinical treatments and predicting possible surgical outcomes [255]. Generally speaking, a patient-specific finite element model should incorporate the discretized geometry, the governing equations, the initial state information and the boundary conditions [256]. Its accuracy in reproducing the behaviour of the real vessel and potentially identifying accurate biomarkers to understand and predict the possible evolution of the aneurysm should be carefully treated [257]. To achieve a deep understanding of the phenomena concerning the evolution of AsAA, high-fidelity simulations of the human vasculature based on patient-specific geometries and precise biomechanical models appear to be essential.

Typically, the realization of these models involves integrating reconstructions from medical images with experimental data [258]. The study conducted by Beller et al. [259] demonstrated a significant improvement in accuracy when considering aortic root motion and its impact on wall stress and strain. They found that the downward displacement of the aortic root led to increased stress on the wall, potentially posing a risk for the development of aortic dissection. Wittek et al. [260] conducted a comparison of the three-dimensional time-varying wall kinematics between the ascending and abdominal aorta. They discovered that AsA experiences a complex deformation pattern characterized by alternating clockwise and counterclockwise twists. This study thereby highlighted the significant influence of heart motion in stretching the aortic root and elevating AsAA wall tension [261]. The importance of including cardiac motion in the assessment of fluid-dynamic outputs for evaluating the patient's health condition was highlighted in the study presented by Wendell et al. [262]. Weber et al. [263, 264] analysed the aortic displacement due to heartbeat in patients with chronic type B aortic dissection. Their findings revealed that the displacement was significantly higher in the ascending aorta compared to the aortic arch and descending tract. Rueckert et al. [265] proposed a technique for tracking specific sections of the ascending and descending aorta employing Spin-echo MRI. Their approach involved an energy minimization method based on a deformable model, which dynamically adapted to the aortic section over time, facilitating accurate tracking and segmentation.

On fluid-dynamics, the role of personalization is well described in [266]. To derive the patient-specific hemodynamics, personalization is typically conducted using 0D models [267]. They are used to partition the system where the fundamental variables

are presumed to be uniformly distributed and change only over time. The governing equations for these models are ordinary differential equation (ODE). 0D parameters can be exploited to represent the whole CVS physiology or any portion of it. The physiological parameters of pressure, flow and volume can be linked to voltage, current and charge in analogous electrical models [268]. The motion resulting from the heartbeat significantly influences the flow pattern within the thoracic aorta [269]. In [270], a method to model the aortic physiological distensibility response to pressure without incurring the computational cost of fluid-structure simulation was proposed. By adopting a quasi-static approach and neglecting wave propagation phenomena, the authors observed a significant underestimation of the aortic wall distensibility when the longitudinal stretch of the aorta was not considered. This finding indicated that inaccuracies induced by the heart motion were far more significant than those arising from spurious reflections on artificial boundaries.

To ensure a relevant anatomical and physiological fidelity level when analyzing wall deformation, it is crucial to incorporate patient-specific tissue material properties [271], include the pre-stress at the vessel wall [272, 273] and account for its interaction with the surrounding structures [274]. The importance of employing mechanical support at the arterial wall was shown in [275]. In [276], the effects of considering the tissues surrounding the abdominal aorta and the presence of the spine on the wall stress have been investigated by integrating information derived from ultrasound images. Gindre et al. [277] developed a model of abdominal aorta with viscoelastic external tissue support defined over the entire wall. Moireau et al. [278] and subsequently, Baumler et al. [279], without considering the presence of the valve and removing the Valsalva sinuses, introduced a boundary condition for the thoracic aorta wall consisting in a viscoelastic term representing the support provided by the surrounding tissues and organs. They opted to handle the external tissue support on the external arterial wall with Robin boundary conditions, dividing the aorta into a few large macro-areas. In [280], exploiting multi-phase CT, a first approach with a sequential method to calibrate the mechanical boundary condition for the model proposed in [278] was proposed.

In this part of the work focusing on high-fidelity modeling, we propose a method to calibrate 4 parameters governing the mechanical boundary conditions of a patient-specific thoracic aorta model, which includes the annulus motion effect. We begin describing how we introduced mechanical boundary conditions (BCs) along the artery wall consisting of visco-elastic components representing the support provided by the surrounding soft tissue and able to reproduce the interaction of the aorta with the

spine, different in each node of the computational grid. The fluid-dynamic model, built to derive the pressure field at the wall, which also involves the whole area of the Valsalva sinuses and includes the modelling of the aortic valve, is coupled with a 0D closed loop reproducing the full cardiovascular circulation. Through an iterative procedure based on purely CSM simulations, we aim at increasing the model fidelity by tuning the parameters governing the BCs with the goal of obtaining an improved correspondence between the displacement of the simulated model and that extracted from the medical images. In each simulation, the pre-stress at the wall is included by deriving the zero-pressure configuration. Afterwards, starting from this unloaded state and applying the pressure load previously derived, 4 cardiac cycles are reproduced. A strongly-coupled fluid-structure interaction analysis is finally performed with the BCs controlled by the calibrated parameters and the results are compared to the ones derived from purely structural simulation.

4.2 Materials and methods

In order to correctly include the effect of the blood flow and the deformations resulting from the flow ejection into the calibration process, we devised a decoupled fluid-structure interaction strategy. In this approach, we conducted a single CFD analysis to obtain the pressure field at the wall and then applied this load to multiple structural simulations. The accuracy of this approach was discussed for the abdominal aortic aneurysm in [281].

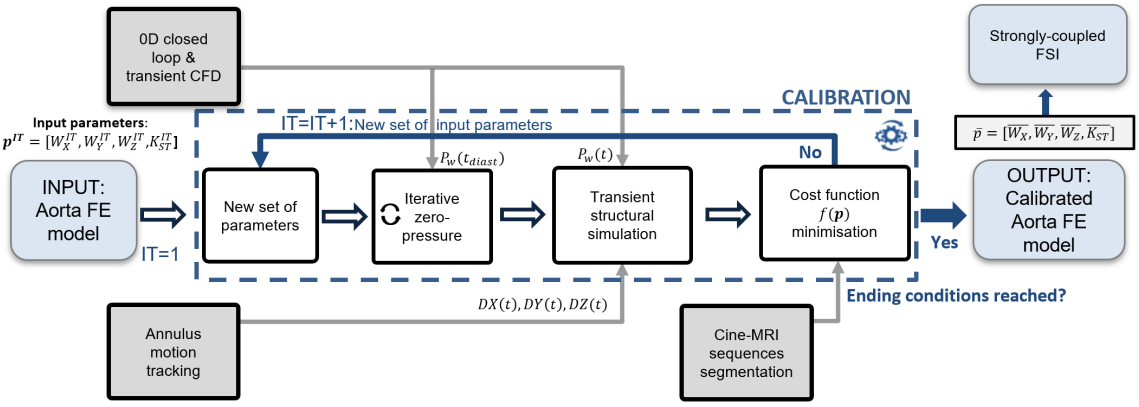

Figure 4.1: Workflow of the calibration procedure.

The general overview of the entire procedure applied to a thoracic aorta model with an aneurysm is shown in Figure 4.1. It consists of two steps: (1) a preliminary step

in which we built the thoracic aorta computational model with mechanical boundary conditions controlled by non-calibrated initial parameters taken from Gindre et al. [277]. A preliminary transient CFD simulation coupled with a 0D closed loop representing the CVS and used to impose quasi-patient-specific 0D-derived boundary conditions was performed to obtain the wall pressure field $P_w(t)$. In parallel, the motion of the annulus was tracked from cine-MRI and its global displacement in the three spatial directions ($DX(t)$, $DY(t)$ and $DZ(t)$) was derived. The splines representing the boundaries of the aorta were extracted and the alignment between them and the Finite Element (FE) model was ensured by means of the Iterative Closest Point algorithm. (2) Inside the calibration loop, first, the steady-state zero-pressure shape was derived by solving an inverse problem in which the diastolic pressure field $P_w(t_{diast})$ was applied. Then, starting from this new unloaded configuration, a structural simulation was performed reproducing 4 cardiac cycles, applying $P_w(t)$ and the displacement retrieved from the annulus motion. The intersections between the deformed FE model and the cine-MRI planes were computed and compared to the splines previously obtained from the segmentation of the 2D dataset. This iterative procedure was repeated until the convergence criteria described later in this work were reached or the number of iterations was beyond the maximum allowed. The value of the parameters at the end of the calibration was the most suitable to reproduce the aorta displacement derivable from cine-MRI data. To assess the sensitivity of the method, the calibration was conducted three additional times, each with different initial guesses. These initial guesses were carefully selected by exploring the parameter space through a Response Surface analysis [282]. Once the model was tuned, a fully-coupled fluid-structure interaction simulation was performed to verify the differences with the purely structural simulation. The different steps of the procedure are detailed in the following paragraphs.

4.2.1 Image dataset and experimental data

We used a set of retrospective and experimental data collected on a patient who underwent surgery for AsAA. The patient was part of the dataset on which the shape-based growth prediction algorithms presented in Chapter 3 were developed. He was a 67-year-old man, 184 cm tall and weighing 89 kg with a maximum ascending aorta diameter of 52 mm and a stenotic bicuspid aortic valve type 1 L-R, the most common congenital cardiac abnormality associated with ascending aortic aneurysm [283, 284]. The subject presented diastolic and systolic pressure respectively of 72 mmHg and 105 mmHg detected from non-invasive measurement at the level of the

arm during the MRI acquisition, conducted 6 days before surgery. The proposed approach relies on cine-MRI sequences to derive the aorta kinematics: this technique provides a good temporal resolution and an excellent signal-to-noise ratio [285]. MRI images were acquired using a 3 Tesla scanner equipped with a phased thoracic coil from Siemens (Siemens Healthineers, Erlangen, Germany). The acquisition was performed in apnea and the patient's heart rate during the procedure was 61 bpm. The cine-MRI sequence, consisting of 256 x 208 pixel images, was gated and returned 25 temporal frames of the cardiac cycle with a 2D spatial resolution of 1.5 mm x 1.5 mm, a slice thickness of 5 mm and a temporal resolution of 42 ms according to the patient's cardiac rhythm. In the same exam, MRA in breath-holding conditions was performed after the injection of Gadolinium contrast agent. The ECG-gated MRA images were acquired during the end-diastolic phase and their spatial resolution was 1 mm x 1 mm x 1 mm. This dataset consisted of 416 x 312 x 72 voxels.

4.2.2 Segmentation and mesh generation

9 sagittal and 2 oblique Left Ventricular Outflow Tract (LVOT) cine-MRI acquisitions from which the aorta displacement and deformation could be derived were segmented in 3D Slicer [286] by 2D region growing and subsequent manual refinement. Through each obtained mask, the boundaries corresponding to the intersection of the cine-MRI plane and the aorta were extracted by employing VTK Canny Edge Detector filters. The set of points obtained from the centroids of the pixels belonging to the aortic boundaries was used to generate some splines. These splines were subsequently relaxed using 20 iterations of Taubin Smoothing [287]. They were employed to calibrate the mechanical boundary condition parameters of the aorta as a function of the vessel kinematics. We emphasize that conventional cine-MRI is limited to capturing motion in a 2D plane. Consequently, as the vessel motion occurs in space, the aortic portion obtained at each frame corresponds to a different part of the vessel, given that its motion occurs in three-dimensional space. At each time frame, all the points generating the splines on the 11 planes resulted in a point cloud. Consequently, in each of the 25 frames, the aorta appeared slightly displaced and deformed. The initial frame of the cine-MRI sequence was identified as the end of diastole, corresponding to the cardiac phase during which the MRA was conducted. To avoid the creation of an ill-conditioned problem, the mechanical BCs were calibrated by studying the motion only in a subset of the 25 frames. In particular, assuming the point cloud derived from the first frame as initial reference, the subsequent frame with the nearest neighbour distance [288] between the related

point cloud and the reference one higher than 1.5 mm was taken as new reference and involved in the calibration. This guaranteed the inclusion of boundaries for which a displacement of at least 2 pixels occurred. In this way, only the frames numbered φ={3,5,7,9,11,13,19} were collected for the calibration procedure.

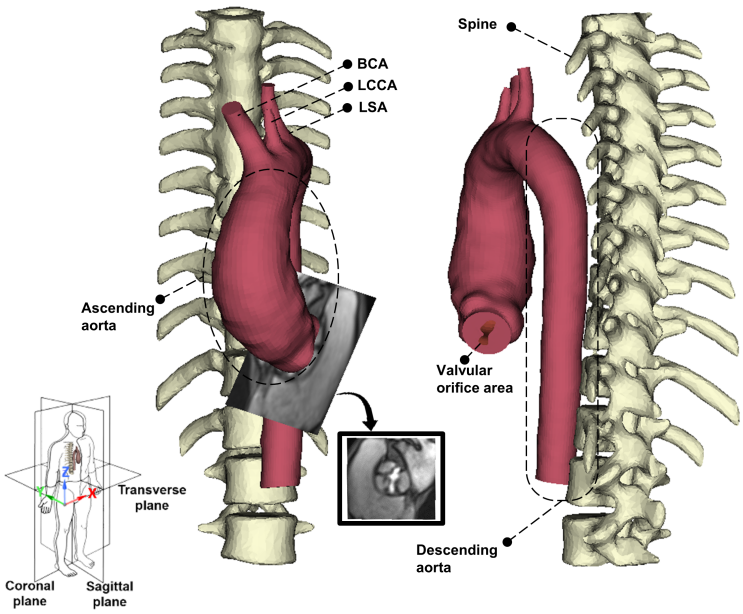

Figure 4.2: The aortic model and the spine derived from the segmentation. The cine-MRI slice from which the area corresponding to the valve jet could be detected is shown. The fluid domain inlet was created on the specific plane by segmenting the area extracted from this cine-MRI acquisition during systole.

The anatomical models shown in Figure 4.2 and representing the aorta and spine were extracted from the MRA images. The three-dimensional MRA dataset was segmented using a thresholding method. Coronary arteries were not included as they were not visible. The surface geometry was imported into ANSA pre-processor (BETA CAE Systems, Switzerland) to generate the computational grid. The structural mesh for the aortic wall Γ_W was created using 14000 fully-integrated 4-node quadrilateral shell elements. The AsA domain was identified and isolated from the rest to perform the calibration, as depicted in Figure 4.3. The CFD grid consisted of approximately 2 million structured hexahedral elements. Eight inflation layers [289] for a total thickness of 2 mm with a growth rate equal to 1.5 were generated. The inlet of the aorta was determined by segmenting a specific cine-MRI acquisition taken perpendicular to the vessel centerline and at the level of the valve leaflets. (Figure 4.2). The advantages and drawbacks of 2D valve modelling using the projection of

the orifice area have already been discussed in [290, 291, 292]. Although the images were captured in the same exam without any supposed patient movements, the diaphragm position for subsequent apnea periods may have been slightly different. To ensure accurate spatial alignment, a rigid registration process based on ten steps of the Iterative Closest Point method was employed between the 3D aortic model and the point cloud derived from the first frame of the cine-MRI sequence.

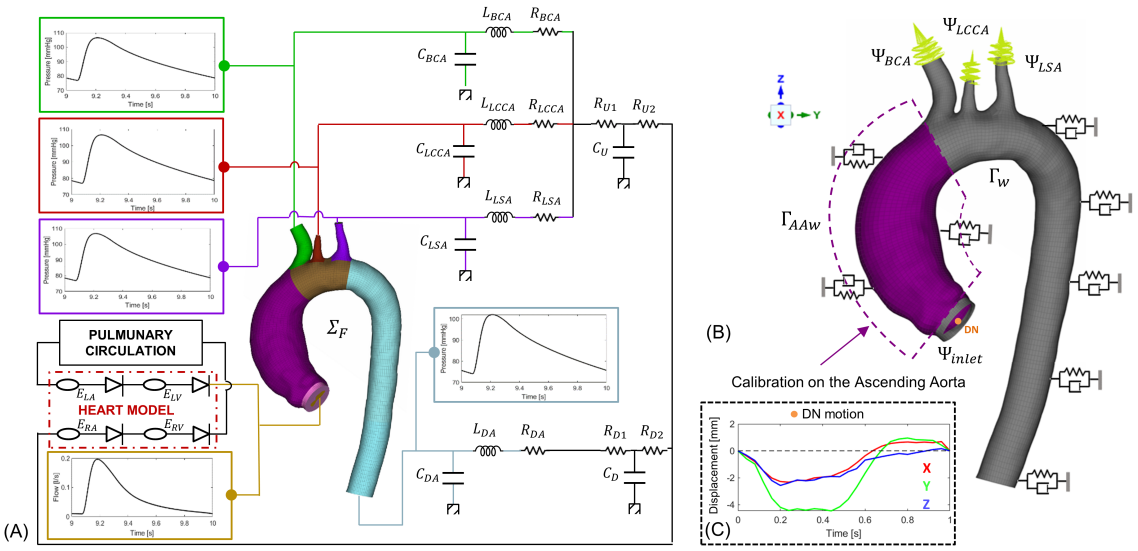

Figure 4.3: (A) The CFD model of the aorta and the lumped parameters used to generate the boundary conditions. (B) The CSM model of the aorta in which the Robin BCs, graphically represented by a parallel of a spring and damper, are used: the ascending tract on which the calibration is performed is shown in purple. (C) The dummy node displacement $dx_{DN}(t), dy_{DN}(t), dz_{DN}(t)$.

4.2.3 Annulus tracking

The aortic valve annulus was tracked with a semi-automatic algorithm relying on anatomical landmarks [293] in Blender [294]. Among the 9 sagittal slices used for the segmentation, only 5 of these encompassed the annulus and were used for the tracking. The two oblique LVOT slices were additionally employed to derive the motion in the three directions of space. For the first frame of every sequence, a landmark was placed at each annulus extremity to detect the plane on which it lay. A window pattern area of 10 x 10 pixels was automatically created around each landmark to identify the extremities of the annulus. The search area was further defined using a larger second window of 15 x 15 pixels. Starting from the first frame, in which the

initial landmarks were manually positioned, planar tracking was conducted for the subsequent frames by correlating grey levels within the new search area with the pattern area of the frame before. At each step, the reference frame was updated with the newly identified window (Figure 4.4 (A)). A successful tracking was deemed valid when the highest correlation between the grey levels of the newly positioned window pattern and its corresponding position in the previous frame was achieved. Afterwards, the 2D coordinates of the landmarks in the images were mapped back to their corresponding 3D positions using the DICOM information. To acquire the motion imposed by the cardiac muscle and minimize the effects of wall dilation due to the blood flow pressure [295], the average of all the extracted landmark displacements was obtained for each frame. In this calculation, the contribution in the x,y, and z directions of each landmark belonging to a cine-MRI plane, of which $\mathbf{n} = [n_x, n_y, n_z]$ was its normal, was respectively weighted by $w_x = 1/(1 - n_x^2)^{\frac{1}{2}}$, $w_y = 1/(1 - n_y^2)^{\frac{1}{2}}$ and $w_z = 1/(1 - n_z^2)^{\frac{1}{2}}$ to scale the value considering the orientation of the plane to which the landmark belonged. If the cine-MRI plane was perfectly perpendicular to one of the 3 main axes, the undefined weight relative to it was assumed equal to zero and the null displacement value was excluded for the average computation. A unique 3D motion ($DX(t), DY(t)$ and $DZ(t)$) shown in Figure 4.4 (B) applicable to move the inlet of the aorta was thus obtained.

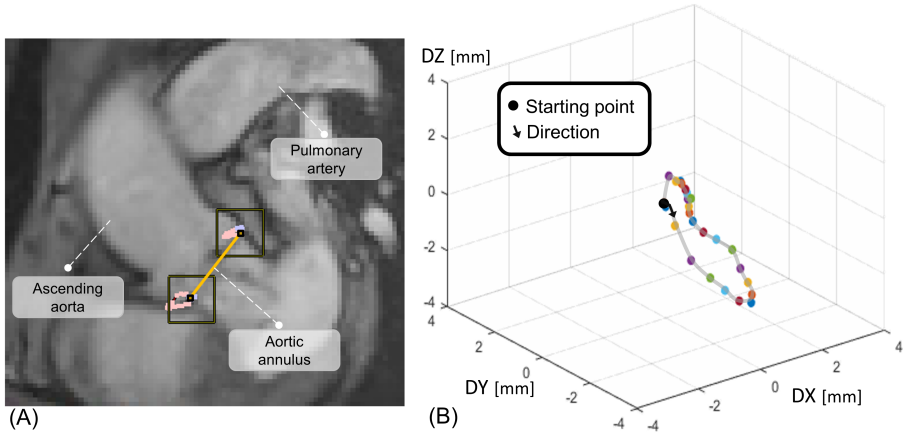

Figure 4.4: (A) The annulus plane tracked in one sagittal cine-MRI sequence. (B) The annulus motion ($DX(t), DY(t)$ and $DZ(t)$) derived from all landmark positions.

Table 4.1: 0D lumped parameters

Symbol	Name	Value
C_{BCA}	Capacitance after BCA	$1.1 \cdot 10^{-9}$ m^3/Pa
R_{BCA}	Resistance after BCA	$5.1 \cdot 10^{7}$ (Pa·s)/m^3
L_{BCA}	Inductance after BCA	$1.2 \cdot 10^{3}$ (Pa·s^2)/m^3
C_{LCCA}	Capacitance after LCCA	$1.2 \cdot 10^{-10}$m^3/Pa
R_{LCCA}	Resistance after LCCA	$2.6 \cdot 10^{7}$ (Pa·s)/m^3
L_{LCCA}	Inductance after LCCA	$1.9 \cdot 10^{7}$ (Pa·s^2)/m^3
C_{LSA}	Capacitance after LSA	$1.0 \cdot 10^{-10}$ m^3/Pa
R_{LSA}	Resistance after LSA	$1.7 \cdot 10^{7}$ (Pa·s)/m^3
L_{LSA}	Inductance after LSA	$1.0 \cdot 10^{4}$(Pa·s^2)/m^3
C_{DA}	Capacitance after DA	$9.8 \cdot 10^{-9}$m^3/Pa
R_{DA}	Resistance after DA	$1.9 \cdot 10^{7}$(Pa·s)/m^3
L_{DA}	Inductance after DA	$1.4 \cdot 10^{6}$ (Pa·s^2)/m^3
R_{D1}	Resistance 1 Downstream	$1.8 \cdot 10^{9}$ (Pa·s)/m^3
R_{D2}	Resistance 2 Downstream	$1.1 \cdot 10^{8}$ (Pa·s)/m^3
C_D	Capacitance Downstream	$3.7 \cdot 10^{-9}$ m^3/Pa
R_{U1}	Resistance 1 Upstream	$2.4 \cdot 10^{8}$ (Pa·s)/m^3
R_{U2}	Resistance 2 Upstream	$7.1 \cdot 10^{7}$ (Pa·s)/m^3
C_U	Capacitance Upstream	$1.7 \cdot 10^{-10}$ m^3/Pa

4.2.4 Fluid-dynamic model and 0D closed loop

To derive the CFD boundary conditions, a quasi-patient-specific 0D closed loop representing the entire cardiovascular system was employed [268]. The lumped parameters of the systemic circulation, shown in Figure 4.3 (A), were tuned in order to match the available cuff pressure measurement using the method proposed in [296, 297]. The obtained values are reported in Table 4.1. The time-varying elastances of the heart chambers were simulated by employing the characteristic elastances for the right and left ventricle and atrium (E_{RV}, E_{LV}, E_{RA}, E_{LA}) and the activation functions proposed in [298] and [299]. These functions were adapted by considering the peak systolic time $T_{PS} = 0.28$ s, the time of ventricular relaxation $T_{VR} = 0.45$ s and the duration of the cardiac cycle $T = 0.98$ s. The remaining parameters for the pulmonary circulation of the CVS were taken from literature [300]. The curves obtained from this loop and representing the Dirichlet boundary conditions for the fluid-dynamic simulation are displayed in Figure 4.3 (A). A no-slip boundary condition was set at the wall. For the 3D fluid-dynamic domain Σ_F, the

fluid was considered incompressible and Newtonian and the flow model selected was Viscous-Laminar. The following parameters were not directly estimated from the patient's data: the blood density $\rho = 1100$ kg/m^3 and the dynamic viscosity $\mu = 4$ cP [301]. The rigid-wall CFD simulation was performed in Ansys® Fluent v22.1 (Ansys Inc., Pittsburgh, PA, USA) solving the following Navier-Stokes equations without the effect of external forces:

$$\frac{\mathrm{D}\mathbf{u}}{\mathrm{D}t} = -\frac{1}{\rho}\nabla P + \nu\nabla^2\mathbf{u}, \text{in } \Sigma_F \tag{4.1}$$

$$\nabla \cdot \mathbf{u} = 0, \text{in } \Sigma_F \tag{4.2}$$

with $\mathbf{u}$ the velocity, P the pressure and ν the kinematic viscosity of the fluid. With a time step of 10^{-3} s, a total of 10 cardiac cycles were reproduced to achieve cycle-independent results. The time-varying wall pressure field $P_w(t)$ of the last cardiac cycle was stored.

4.2.5 Structural model

The structural model is reported in Figure 4.3 (B). The ex-vivo material properties of the patient's arterial wall were directly obtained from experimental tests conducted immediately after surgery with the techniques described by Morgant et al. and Lin et al. [302, 303]. Specifically, bi-axial tests were conducted on eight samples encompassing the lateral, medial, posterior and anterior portions of the ascending aorta. As a result, eight distinct stress-strain profiles and eight different thickness measurements were obtained. To create the FE model, the average thickness of 1.3 mm was adopted and an average stress-strain curve was computed using the collected experimental data. To replicate the global deformation behaviour of the vessel [304], we introduced a non-linear isotropic strain-energy potential W using a three-parameter hyperelastic Mooney-Rivlin model [305], expressed as a function of the first and second Cauchy invariants $\bar{I}_1$ and $\bar{I}_2$ [306].:

$$W = C_{10}\left(\bar{I}_1 - 3\right) + C_{01}\left(\bar{I}_2 - 3\right) + C_{11}\left(\bar{I}_1 - 3\right)\left(\bar{I}_2 - 3\right) \tag{4.3}$$

A least-square fitting was performed for the new averaged curve, resulting in the following parameters: C_{10} = -1.47 MPa, C_{01} = 1.62 MPa, and C_{11} = 2.31 MPa. The assessed fitting quality, including the root mean square error ($\mathrm{RMSE_{MAT}}$) and the R-square value ($\mathrm{R^2_{MAT}}$), is reported in the results.

To consider the global relationship between aorta and spine and neglecting the intra-thoracic pressure as the acquisition was performed in breath hold, as done in [277], the following equation modelling the external tissue support through Robin boundary conditions was used:

$$\boldsymbol{\sigma}_{\mathbf{ext}} = -\mathbf{K}\mathbf{x} - \boldsymbol{\eta}\dot{\mathbf{x}} \tag{4.4}$$

with $\boldsymbol{\sigma}_{\mathbf{ext}}$ the stress due to the external load, $\mathbf{K}$ and $\boldsymbol{\eta}$ the parameters that model the external tissue elastic and viscous support, $\mathbf{x}$ the displacement, $\dot{\mathbf{x}}$ the velocity. The stiffness $\mathbf{K}$ can be decomposed along the three anatomical directions: x-coronal, y-transvers, z-sagittal. On the other hand, $\boldsymbol{\eta}$ is assumed constant and set to 10^5 (Pa·s)/m for each node and direction in space, as done in [278]. More in detail, we connected each node $i \in \Gamma_W$ to three dampers and three springs, each related to the j-direction of the 3D space. The stiffness of each spring was modelled as:

$$K_{j_i} = K_{ST} + W_{d_i} W_j K_{SPINE} \tag{4.5}$$

here, K_{ST} represented the initial parameter sought to represent the stiffness of the soft tissue surrounding the aorta. We assumed that the force applied by the soft tissue was equal in all three spatial directions. W_j was the weight to be optimized for each spatial direction, while $K_{SPINE} = 10^6$ Pa/m, obtained from [277], represented the stiffness that related the aorta to the spine. W_{d_i} acted as the scaling factor taking into account the distance to the vertebrae, calculated as follows:

$$W_{d_i} = 1 - \alpha_s \frac{d_i}{d_{max}} \tag{4.6}$$

with α_s= 0.95, $\boldsymbol{d}$ the vector containing the minimum Euclidean distance of each node of the aortic wall from the spine and d_{max} the maximum distance, in this model equal to 142 mm. For BCA, LCCA and LSA, an additional set of springs (in green in Figure 4.3 (B)) was introduced to account for the upper trunk vasculature on the aortic vessel wall [307, 308]. These connected each node of the boundaries Ψ_{BCA}, Ψ_{LCCA} and Ψ_{LSA} to three new additional nodes located along their outgoing central axis at a distance of twice the mean diameter. The upstream vasculature stiffness K_{US} on each boundary was assumed to be uniform across all 2D elements and defined

by the following arithmetic mean:

$$\begin{cases} K_{US_{BCA}} = \text{mean}(\mathbf{K_{\Psi_{BCA}}}) \\ K_{US_{LCCA}} = \text{mean}(\mathbf{K_{\Psi_{LCCA}}}) \\ K_{US_{LSA}} = \text{mean}(\mathbf{K_{\Psi_{LSA}}}) \end{cases} \tag{4.7}$$

where $\mathbf{K_{\Psi_{BCA}}}$, $\mathbf{K_{\Psi_{LCCA}}}$, and $\mathbf{K_{\Psi_{LSA}}}$ represent the vectors containing the stiffnesses of the subgroup of springs belonging to Ψ_{BCA}, Ψ_{LCCA}, and Ψ_{LSA}, respectively. The time-varying pressure field $P_w(t)$ derived from the CFD was applied to the aortic wall Γ_W. Since a Dirichlet boundary condition, like the displacement from sequential images, was not concurrently compatible with the pressure load, a strategy involving a dummy node (DN) was implemented. Specifically, the motion of the inlet boundary Ψ_{inlet} was controlled using the following constraint equation:

$$\begin{cases} n_{\Psi_{inlet}} dx_{DN}(t) - \sum_1^{n_{\Psi_{inlet}}} dx_i(t) = 0 \\ n_{\Psi_{inlet}} dy_{DN}(t) - \sum_1^{n_{\Psi_{inlet}}} dy_i(t) = 0 \\ n_{\Psi_{inlet}} dz_{DN}(t) - \sum_1^{n_{\Psi_{inlet}}} dz_i(t) = 0 \end{cases} \tag{4.8}$$

where $n_{\Psi_{inlet}}$ denoted the number of nodes of Ψ_{inlet}, $dx_{DN}(t), dy_{DN}(t), dz_{DN}(t)$ the x, y and z displacements imposed to the dummy node, shown in Figure 4.3 (C) and respectively set equal to $DX(t)$, $DY(t)$ and $DZ(t)$, and $dx_i(t), dy_i(t), dz_i(t)$ the displacement of a single node of Ψ_{inlet}. This approach ensured that the inlet could deform during the cardiac cycle. It is important to point out that we neglected the effects of rotation of the aorta around the axis passing through the centre of the annulus as it was impossible to retrieve this information from the 2D images.

4.2.6 Zero-pressure computation

Typically, a segmented 3D model reconstructed from medical images corresponds to a partially deformed configuration of the vessel, resulting from an in-vivo pressure field [309]. Indeed, the geometry obtained from MRA segmentation corresponded to a loaded state at the end of the diastolic phase. In order to include the pre-stress, we computed the zero-pressure configuration [310]. To obtain it, we solved an inverse problem using the iterative method described in [311], with the updating parameter $\alpha = 1$. From the end-diastolic phase of the rigid-wall CFD simulation, the static pressure $P_w(t_{diast})$ on Γ_W was extracted and applied to the structural model. In the steady-state analysis, the aorta was only constrained by the entire set of springs, as the dampers had no effect. For the convergence criterion of the iterative algorithm,

an error on the maximum Euclidean nodal distance (threshold of 0.1 mm) between the pressurized zero-pressure model and the one derived from MRA in diastole was included and a limit of 20 iterations was established. The Ansys LS-Dyna implicit solver was used.

4.2.7 The calibration method

The calibration process was carried out exclusively on the ascending aorta wall Γ_{AAw}, which was defined from the annulus to the plane perpendicular to the centerline at the level of the BCA ostium. In this domain, the experimental tests on the aorta were indeed conducted. In each iteration of the iterative calibration procedure, we first derived a new zero-pressure model and then performed a structural analysis in which, in a time equivalent to one cardiac cycle, the unloaded aorta was forced to reach the diastolic configuration and, after that, 3 complete cardiac cycles were simulated to stabilise the results.

The update of the parameters at each iteration was carried out through a least squares optimisation using Levenberg-Marquardt (LM) method [312]. It aimed at minimizing the following loss function consisting of the L_2 norm:

$$f(\mathbf{p}) = \sqrt{\sum_{\varphi} \sum_{l=1}^{m} \sum_{k=1}^{n_l} \left| d_{l,k}^{\varphi}(\mathbf{p}) \right|^2} \tag{4.9}$$

where $m = 11$ is the number of splines derived from the segmented aortic boundaries during each selected cardiac phase, $\mathbf{p} = [W_X, W_Y, W_Z, K_{ST}]$ is the vector containing the 4 input parameters to be optimised, n_l is the number of points defining the l-spline and $d_{l,k}^{\varphi}$ is the nearest neighbour distance of each point k belonging to the spline l and all the points of the corresponding spline derived from the simulated model. In this way, for each point of the reference spline, we were searching for the nearest point in the second point cloud and computing the Euclidean distance. In other words, if $\mathbf{x}_{\mathbf{l},\mathbf{k}}^{\varphi}$ is the k-point of the l-spline and $\mathbf{x_{sim}}$ is a point of the set $\mathbf{S}_{\mathbf{l}}^{\varphi}(\mathbf{p})$ obtained from the intersection of the same planes of the cine-MRI and the 3D model, as graphically shown in Figure 4.5, the function $d_{l,k}^{\varphi}(\mathbf{p})$, used as error metric, was defined as:

$$d_{l,k}^{\varphi}(\mathbf{p}) = d(\mathbf{x}_{\mathbf{l},\mathbf{k}}^{\varphi}, \mathbf{S}_{\mathbf{l}}^{\varphi}(\mathbf{p})) = \min_{\mathbf{x_{sim}} \in \mathbf{S}_{\mathbf{l}}^{\varphi}(\mathbf{p})} \left\| \mathbf{x}_{\mathbf{l},\mathbf{k}}^{\varphi} - \mathbf{x_{sim}} \right\| \tag{4.10}$$

From now on, the superscript IT will indicate the iteration of the LM algorithm. Regarding the resolution of the optimisation, we set a maximum limit of 50 iterations and established the following termination criteria:

- parameters stability: $\max \left| h_i^{IT} / p_i^{IT} \right| < \epsilon_1$
- loss function stability: $f(\mathbf{p}^{IT}) - f(\mathbf{p}^{IT-1}) < \epsilon_2$
- gradient convergence: $\max \left| \mathbf{J}^{IT^T} \mathbf{r}^{IT} \right| < \epsilon_3$

with $\mathbf{h}^{IT}$ the vector containing the updates of the 4 parameters and $\mathbf{r}^{IT}$ the vector with the residual distances between two iterations.

The threshold parameters used were ϵ_1=10^{-3}, ϵ_2=$5{\cdot}10^{-3}$m and ϵ_3=10^{-3}. To quantify the effect of the parameters calibration and the annulus motion, we performed 3 additional simulations after the conclusion of the full procedure: the first by removing the heart motion on Ψ_{inlet} and with the non-calibrated Robin BCs; the second by considering the heart motion effect but still on the model with the non-tuned parameters; the third by removing the annulus motion but using the parameter values of the Robin BCs at the end of the calibration procedure. These simulations were compared to the complete structural simulation by reporting the differences in maximum strain at the aortic wall.

The structural simulations were performed using LS-Dyna as well. The calibration was run on a Dell Precision 7820 workstation equipped with 2 16-cores Intel® Xeon Gold 5218 and 256 Gb RAM.

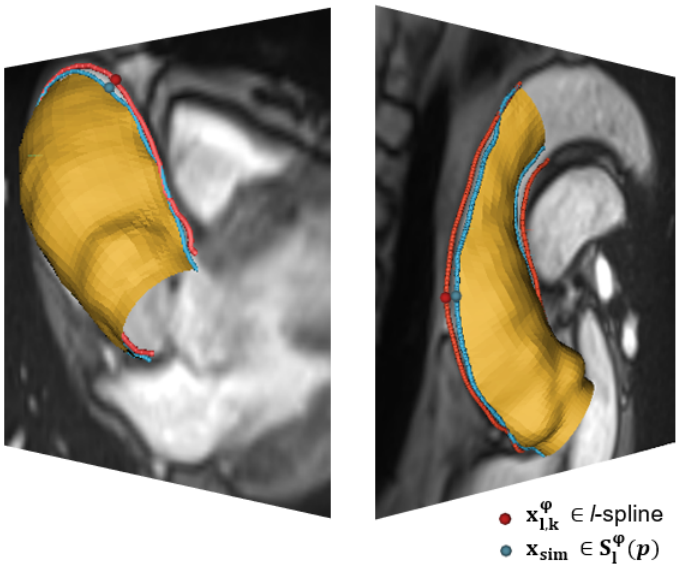

Figure 4.5: Splines represented in a specific frame for two different cine-MRI sequences used for the calibration. The wall of the computational model is shown in yellow.

4.2.8 Parameter ranges and sensitivity analysis

For the baseline FE model, we started by assuming isotropic Robin boundary conditions with values obtained from literature [277], thereby establishing an initial parameter vector $\mathbf{p^1}$=[1,1,1,10^5 Pa/m]. The minimum value of the range for the three weights W_X, W_Y, W_Z was set to 0 in case of no discernible relationship between the spine and the aorta and external support due only to the surrounding soft tissue. In this specific configuration, the minimum value for K_{ST} was also set to 10^4 Pa/m, value below which convergence could not be achieved due to the insufficiently constrained model. As the stiffness of the Robin boundary conditions increased, the model became progressively less capable of expanding during the cardiac cycle. Considering that, the procedure to obtain the maximum value of the parameters consisted in altering one parameter at a time starting from the initial guess. By assuming a change in the mean diameter of the ascending aorta between diastole and systole of at least 1 mm [313], we identified the maximum value of each range when the new parameter value resulted in diameter changes smaller than this threshold. Thus, the maximum value of the parameter ranges were 2.2, 1.3, 1.4 and $2{\cdot}10^6$ Pa/m respectively for W_X, W_Y, W_Z and K_{ST}. To find the $\boldsymbol{\varepsilon}$ vector containing the normalized updating values for constructing the Jacobian matrix $\mathbf{J}^{IT}$, we performed a sensitivity analysis by studying the convergence of the partial derivatives to preserve the linear approximation of the first-order Taylor expansion, as detailed in [314]. For each parameter of $\mathbf{p^1}$, we executed an iteration of the workflow using each time a different increment value $\in \{0.1, 0.05, 0.02, 0.01\}$. The convergence of the partial derivatives was achieved using $\boldsymbol{\varepsilon} = [0.02, 0.01, 0.01, 0.02]$.

To enhance the robustness of the method and assess the sensitivity of the output based on the choice of initial guess, the Response Surface (RS) methodology [282] was employed. A Design of Experiments consisting of 16 Design Points (DPs) (DP_1,..., DP_{16}) obtained within the parameter ranges by Latin hypercube was prepared [315]. The cost function was computed for each of the 16 Design Points. The RS was calculated using the Genetic Aggregation method [316] and cross-validated using leave-one-out, reporting the final root mean square error ($RMSE_{RS}$) and the relative maximum absolute error ($RMAE_{RS}$). The RS ability to predict the output was assessed using the coefficient of determination (R^2_{RS}). The complete calibration was then repeated using 3 of the Design Points (DP_1, DP_2 and DP_3). These three DPs were chosen because they were the ones for which the distance from the point previously chosen as initial guess in the normalized ranges, evaluated using the norm, was the highest.

4.2.9 Strongly-coupled fluid-structure interaction analysis

Once the parameters were tuned, we performed a fully-coupled fluid-structure interaction analysis to compare the differences between the deformed structural domain obtained from this simulation and the deformed aortic wall resulting from the calibration purely based on structural simulation.

The same fluid-dynamic and structural models described earlier were used, as well as the same boundary conditions. In order to start the FSI simulation with the zero-pressure state, the solid domain was deformed by RBF mesh morphing [317], technique already described in Chapter 3, Subsection 3.2.7.

As previously explained by Capellini et al. [318], mesh morphing can exploit a motion imposed on a set of surface nodes acting as Source Points in order to perform a RBF interpolation in space, which in turn modifies the positions of the volume nodes. In our case, we used all surface nodes of the original FE model derived from the segmentation in diastole as Source Points and we imposed a translation to each of them to achieve the computed zero-pressure state associated with the calibrated model. Regarding the FSI coupling details, the maximum number of sub-iterations for the resolution was set to 50.

Minimum and maximum time steps were set to 1e-5 s and 5e-5 s, respectively. A partitioned resolution approach was used. The FSI method used was the penalty-coupling algorithm available in Ansys LS-Dyna, v22.1. The fluid sub-problem and the solid sub-problem were independently solved and the FSI coupling was ensured by interface coupling conditions. To compare the FSI simulation with the structural simulation based on calibrated parameters, we analyzed the two deformed surface grids and reported the maximum error as the maximum Euclidean distance ($\mathrm{D}_{MAX_{\mathrm{FSI}}}$) between corresponding nodal positions and the maximum root mean square error ($\mathrm{RMSE}_{\mathrm{FSI}}$) throughout the entire cardiac cycle. Finally, calling $\overline{\mathbf{p}}$ the vector containing the calibrated parameters, a new cost function $f_{\mathrm{FSI}}(\overline{\mathbf{p}})$ was computed according to (4.9) but using the deformed wall of the fully-coupled FSI simulation.

Chapter 5

Real-time hemodynamics prediction through surrogate modeling

One of the main limitations of numerical simulation in enabling Digital Twins for clinical applications is the high computational cost. Surrogate modeling, also known as meta-modeling, is a technique used to create a simplified mathematical model that approximates the behaviour of a more complex and computationally expensive original system. In this context, model order reduction techniques refer to the methods aiming at reducing the computational complexity related to the high number of degrees of freedom typical of full-order models. They can be used for problems requiring real-time results or a substantial number of simulations, such as system control and optimization processes. Since a reduced-order model is a simplified approximation of a more complex and detailed original model, it is crucial to understand how well it captures the behaviour of the original system across different scenarios, especially for assessing the reliability and quality of the predictive abilities.

In this Chapter, we present the state of the art related to surrogate models built through model order reduction for cardiovascular applications. Our primary objective is to propose a pipeline to adeptly predict numerical simulation results within a short temporal window, thus facilitating their integration into a clinical environment through a possible active or semi-active Digital Twin. We propose a methodology to implement a streamlined pipeline based on model order reduction, enabling a full transition from medical images to numerical simulation results without laborious manual steps. In addition, a validation approach is described to assess the

meta-model's ability to predict the hemodynamics for new unknown anatomies.

5.1 Introduction

Numerical simulation tools allow healthcare professionals to practice, test and refine their skills in a realistic environment, enabling the visualization of the results in a safe and controlled environment [319]. Full order models (FOMs) solving the parameterized Navier-Stokes equations of blood flow dynamics, where parameters encompass geometric features, boundary conditions and physical properties, are now widely used in cardiovascular research. The translation of numerical simulation based on FOMs into clinical environments is challenging due to the long computational times and the manual work of an operator to prepare the models. The computational cost is mainly due to the requirement of solving a large-scale system of discrete PDEs. The computational power necessary to run these simulations can be expensive and can limit the number of simulations performed in a given time period. Due to the increased complexity of the models and the large datasets that need to be processed, supercomputing clusters and particular domain expertise are often required [320]. This can be particularly challenging for medical professionals who need quick decisions for patient care, especially when a large number of evaluations is required [321]. This aspect stands as one of the fundamental requisites in establishing an active or semi-active Digital Twin, particularly when prompt interaction with specialized medical personnel is required to evaluate specific conditions. Therefore, there is a strong need to develop additional algorithms and tools to reduce computational time in order to develop efficient and accurate clinical applications based on personalized solutions [322].

In recent years, the research about real-time simulation technology has become increasingly considerable, providing healthcare professionals with a more realistic, interactive experience in a simulated environment.

Different approaches have been developed and applied for order reduction of blood vessel models. As introduced in Chapter 4, a first possibility is the reduction of the 3D vessel dimension to obtain 0D, 1D or 2D models of the arteries [323]. Unfortunately, when the applications require frequent 3D model evaluations across a range of input parameters, FOMs become computationally expensive due to the substantial degrees of freedom required for an accurate flow system representation, leading to extensive computational time and memory usage. In this regard, data-driven surrogate models based on reduced order models (ROMs) could stand as valid

alternatives [324] due to their ability to efficiently capture the essential behaviour of complex systems while significantly reducing the computational cost. Model order reduction techniques are helpful in overcoming computational complexity-related problems by reducing the system degrees of freedom. They can be categorized into intrusive and non-intrusive methods [325]. Intrusive approaches modify the original governing equations by reparameterizing them or introducing additional terms [326]. They require a deep understanding of the underlying physics and equations governing the system. While intrusive methods may provide accurate results, they could be computationally expensive and require extensive and tedious modifications to the existing codes. Non-intrusive ROMs do not modify the equations and are based on existing simulations or data to approximate the final solution [327]. They are often easier to implement as they leverage existing simulations or experimental data. Usually, they are more flexible and applicable to a broader range of problems but may sacrifice some accuracy compared to intrusive methods. Thus, both intrusive and non-intrusive reduced-order models have their advantages and limitations. The choice between them depends on the specific requirements, computational resources and level of accuracy needed for the studied problem. ROM-based data-driven surrogate models seek to capture the relationship between modeling inputs (such as geometry, inlet/outlet conditions, and material properties) and computed surface (such as wall pressure and shear stress distribution) or volume (such as the flow field) outputs, using comprehensive simulation data. A purely data-driven model relies on training data to learn the mapping between input and output parameters. Consequently, it is clear that, at best, the surrogate model can reach an accuracy as good as the underlying training data. Non-intrusive reduced-order models involve projecting the complete set of governing PDEs, such as the Navier-Stokes equations in case of fluid-dynamics, onto a reduced subspace defined by a set of basis functions. One commonly used technique is the proper orthogonal decomposition (POD) [328]. Using ROMs can significantly reduce the computational cost of simulating a patient's cardiovascular system. This would allow running simulations on systems with limited resources, such as mobile devices, and obtaining results (almost) in real-time. The generation of a data-driven ROM comprises two main stages: an offline phase during which the reduced-order space is constructed based on a set of simulation results called 'snapshots' derived from different values of the physical and geometrical input parameters and an online phase that involves obtaining new unknown solutions by combining the precomputed reduced basis functions.

ROMs have become an increasingly attractive tool for obtaining real-time simula-

tions of cardiovascular systems [329]. Indeed, they have already been successfully applied to simulate a variety of cardiovascular organs and tissues. Being one of the enabling keys for personalized models, they are likely to play an increasingly important role in the future of cardiovascular medicine and Digital Twin-based technologies [330]. The importance of using reduced-order models to represent cardiac electrophysiology and hemodynamics has been discussed by Dal Santo et al. [331]. The strain on the thrombus during thrombectomy procedures was assessed through a surrogate model by Bridio et al. [332]. It was created through principal component analysis and kriging. A first approach to create a data-driven reduced-order model for blood flow simulations based on 2D geometries was proposed by Ye et al. [333]. Liang et al. performed a feasibility study on using surrogate models based on neural networks to perform real-time CFD simulation of the thoracic aorta [334]. A method to construct a ROM for deriving the flow and extracting WSS in abdominal aortic aneurysms using CFD simulations and POD, allowing comprehensive analysis of the model system across various inflow angles without repeated simulations, was presented by Chang et al. [335]. Bisighini et al. used reduced-order models to derive an approximate solution of the position of the expanded stent in an idealised cerebral aneurysm geometry [336]. A morphing approach based on non-uniform rational basis-splines (NURBS) combined with free-form deformations techniques was described by Siena et al. to create a reduced-order model of the coronaries in presence of stenosis [337]. Instead, Kardampiki et al. [338] used reduced-order models to observe the effects on fluid dynamics due to the shunt configuration chosen in modified Blalock-Taussig shunt procedures. Reduced-order models have already been employed by Biancolini et al. [240] to artificially modify the size of an ascending aortic aneurysm and evaluate changes in fluid-dynamics. A surrogate model based on deep learning was built by Du et al. to evaluate fluid-dynamics for the aortic coarctation [339].

In this work, we describe a framework to obtain real-time simulation results and augment the information derived from patient-specific medical images, one of the critical steps in enabling active or semi-active Digital Twins. We apply the procedure to predict the hemodynamics of ascending aortic aneurysms. The anatomical geometry is derived from deep learning segmentation, and rigid registration is applied to align all the shapes of the available dataset to an initial meshed template. Mesh morphing is then applied to ensure the iso-topological properties of the computational domains and respect the correspondences between the anatomical parts. The set of shapes obtained is then used to build a statistical shape model through principal component

analysis. From the derived subspace, atlases are extracted, synthesising in this way a huge cohort of patients. Computational fluid-dynamic simulations are performed for each synthetic shape, adding input parameters for the inlet (ejection velocity) and outlet (Windkessel resistance) boundary conditions. 3D surrogate models are built using model order reduction techniques. In particular, the Genetic Aggregation Response Surface method is used to reconstruct a primal output, i.e. the pressure and a derived variable, i.e. the wall shear stress. Once the reduced-order model is trained, the ability of the surrogate model to predict the simulation results is evaluated. The meta-model is then converted into a Functional Mock-up Unit and imported into the desired working environment. The complete approach presented here involves a validation process conducted by excluding one patient at a time from the creation of the meta-models and attempting to represent the left-out patient-specific hemodynamics using the latest surrogate models created.

5.2 Materials and methods

Performing hundreds of simulations to create a large training dataset is computationally prohibitive, especially when employing multiphysics models. A trade-off in terms of model fidelity has to be accepted to reduce the computational cost. In this case, since the goal is to propose an approach for hemodynamics prediction and provide a validation strategy for the prediction ability of the surrogate models, steady-state simulations are performed and a simplified CFD approach in comparison to the FSI approach discussed before is employed.

In this Section, the steps involved in creating the surrogate model for extracting the hemodynamics are detailed. The workflow of the procedure considering the validation of the predictive ability of the meta-models is summarized by Figure 5.1. The validation phase corresponds to the possible application of the meta-models created to predict the hemodynamics of a new unseen anatomy as a Digital Twin should do: in fact, an excluded new patient is processed in the online phase and the already available ROM is queried to assess its patient-specific blood flow dynamics.

A set of $n_p = 36$ medical image sequences, in this case, 4D flow MRI data, is collected. Image segmentation through automatic deep learning techniques is performed in 3D Slicer. All the models are aligned to a template mesh and mesh morphing based on automatic detection of the deformation driving Source Points is performed with the goal of creating a set of iso-topological meshes. Excluding one patient per time, a statistical shape model is created using the remaining

$n_p - 1$ models. From that, a cohort of $n_{vp} = 300$ virtual patients for computing the numerical simulation results is extracted. CFD simulation is then used to compute the hemodynamics for the 300 generated atlases. We use the results to train a ROM that is initially validated using a leave-one-out approach based on the atlases generated from the statistical shape model through the linear combination of modes derived from the PCA. A least squares fitting is executed to obtain the shape coefficients that allow to reproduce the unseen patient and the low-order solution is automatically extracted. In parallel, an automatic full-order CFD simulation is computed on the excluded patient. The results of that are used as ground truth, and full-order and reduced-order solutions are compared.

5.2.1 Dataset

A specific 4D flow MRI protocol was executed on 36 patients with ascending aortic aneurysms who had written consent. The study was registered on https://clinicaltrials.gov (clinical registration number: NCT03817008). This imaging technique also allowed to introduce into the surrogate model information about the velocity at the inlet, parameter that could be directly extracted from the sequences. This was not possible using the CT scans previously employed for the development of growth prediction methods.

The 4D flow MRI acquisitions were performed using a phased thoracic coil on a 3 Tesla Siemens scanner (Siemens Healthcare, Erlangen, Germany). Blood flow dynamics information was captured in free-breathing with ECG-gating. An echo navigator was used to account for diaphragmatic motion. The 4D flow technique combines 3D spatial encoding, three-directional velocity encoding and cine acquisition over time (3D + time) to generate a final image set consisting of one magnitude and three phase difference volumes encoded in the x, y, and z directions of space. Maxwell coefficients were corrected during reconstruction to reduce the effects of the concomitant gradient field. Additionally, non-uniform intensity and 2D distortion corrections were performed.

Each patient's 4D flow MRI sequence consisted of 25 frames of the cardiac cycle with a spatial resolution of 2 x 2 x 2 mm^3 and a temporal resolution ranging from 24 to 52 ms, depending on the patient's cardiac rhythm. The echo and repetition time were set between 2.1-2.3 ms and 38.5-40 ms, respectively, while the field of view (FOV) was 262-350 x 350. In order to prevent aliasing in 4D flow MRI, the velocity encoding (VENC) was chosen considering the value set during 2D flow MRI acquisition and adjusted as necessary. Depending on the patient, the VENC ranged

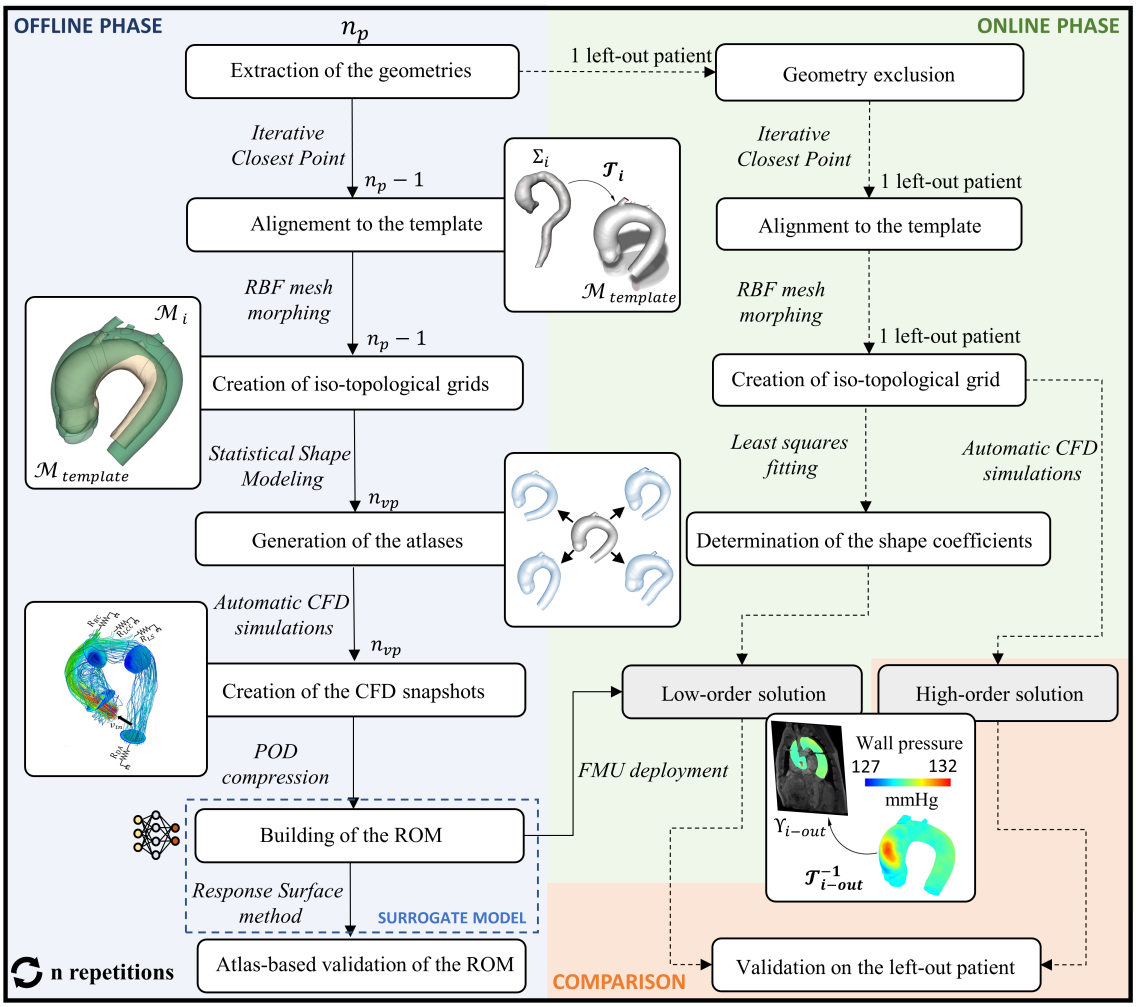

Figure 5.1: The procedure to create surrogate models and validate their predictive ability for patient-specific hemodynamics. The light blue offline part involves the construction of the meta-models through model order reduction techniques. Conversely, the green part represents the online phase, which seamlessly bridges the gap from image data to hemodynamic predictions. The orange segment is dedicated to the comparative analysis of full-order and low-order solutions, which is a pivotal component of the validation process.

from 200 to 800 cm/s. The duration of each scan was approximately 10-15 minutes. In this study, the magnitude and phase images were used without any additional post-processing after their collection. However, it is noteworthy that a very high VENC value was needed for a patient with bicuspid valve and aortic valve stenosis due to the high blood velocity involved. The cohort consisted of 26 men and 10 women with an average age of 60+/-15 years. Among this group, 18 patients had BAV and 18 reported TAV.

5.2.2 Segmentation and post-processing

This Section is briefly described since the automatic segmentation method presented here has already been discussed and applied to the same dataset by our colleagues [340]. U-Net architectures based on convolutional neural networks for 2D and 3D image segmentation are widely used [341]. The 3D U-Net proposed in [342] based on up-sampling operations was used in this work. The architecture employed 3 x 3 x 3 voxel convolution kernels and batch normalization (BN) after each layer to enhance the learning stability and performance. Following each BN process, the rectified linear unit (ReLu) activation function was used. To establish the network input, images were either cropped or padded based on the median size of the x and y axes and the maximum size of the z axis across the entire database. Consequently, the 3D U-Net input size was set to 146 x 176 x 44 voxels. The advanced methods to determine the input hyper-parameters and assess the results quality of the deep learning segmentation method have been explained by Marin et al. [340].

However, for the purpose of numerical simulation, the grid in output from the U-Net is often unsuitable for mathematical calculations. It usually contains high surface noise, holes, inlets and outlets not appropriate for the run of the simulations. In this regard, following segmentations, the surface of the aorta was smoothed to reduce any roughness while maintaining its essential geometric features. Any sharp corners detected were eliminated through ten steps of Taubin smoothing. We removed any nonphysical holes resulting from the segmentation process. The aorta was cut in the descending segment with a cutting plane perpendicular to the centerline, 5 cm before the diaphragm [343].

Again, Python algorithms were implemented in the 3D Slicer environment and the VMTK and VTK libraries were used to display the segmented geometry.

5.2.3 Template mesh generation

ANSA pre-processor (BETA CAE Systems, Switzerland) was used to generate a reference mesh for simulation that included the supra-aortic branches, which was derived from a CT-scan (OPTIMA CT660, Siemens Healthcare GmbH) of a patient involved in the study. This patient was the one who reported the ascending tract diameter corresponding to the median of the dataset. The template mesh, reported in Figure 5.2 and here named $\mathcal{M}_{template}$, consisted of three million structured hexahedral elements, with ten high-resolution inflation layers and a total thickness of 1.5 mm and a growth rate of 1.5. It represented the fluid domain Υ_F. The outlets of the

supra-aortic vessels have been extended to facilitate the proper flow development in these regions. The mesh sensitivity study has already been described in [340]. The surface mesh corresponding to the aortic wall $\mathcal{M}_{S_{template}}$ was divided into named selections to ensure local control over the model. Specifically, Γ_{AsA} contained elements belonging to the ascending part, Γ_{DA} encompassed those of the descending tract and Γ_{AAr} included the aortic arch section excluding the three supra-aortic vessels which belonged to three additional selections.

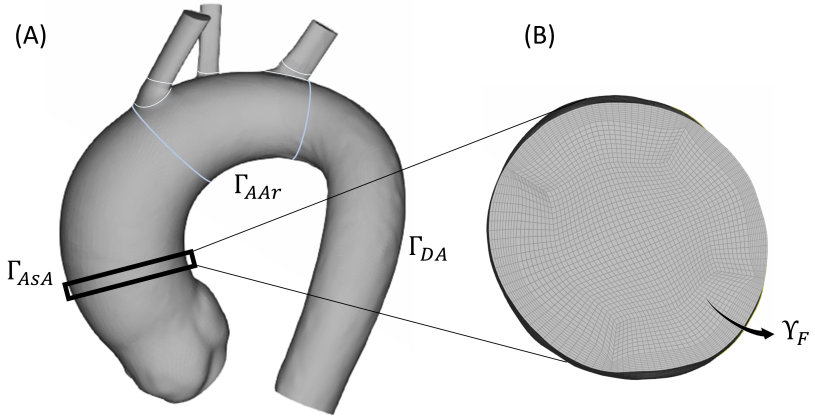

Figure 5.2: (A) The full mesh with the extruded supra-aortic vessel outlets. (B) A cross-section of the model in which the hexahedral grid and the boundary layers are visible.

5.2.4 Mesh correspondences establishment

Before building the parametrized space of shape variation, correspondences between the various anatomical models had to be ensured.

Let $\left\{\mathbf{\Lambda}^i\right\}_{i=1,\dots,n_p}$ represent the collection of original patient-specific aorta shapes, with $n_p = 36$. Each shape sample $\mathbf{\Lambda}^i$ is a tesselated surface made up of surface vertices. Our objective is to establish correspondence by deforming the surface template $\mathcal{M}_{S_{template}}$ referred as source mesh to all other aorta shapes $\left\{\mathbf{\Lambda}^i\right\}_{i=1,\dots,n_p}$ here defined as target geometries. In this case, RBF mesh morphing, whose mathematics had already been proposed in Section 3.2.8, can be used.

A rigid transformation $\mathcal{T}_i$ derived using iterative closest point (ICP) was applied to ensure consistent alignment and orientation of the anatomical samples in the 3D Cartesian coordinate system. We aligned each geometry $\left\{\mathbf{\Lambda}^i\right\}_{i=1,\dots,n_p}$ to the selected already meshed template $\mathcal{M}_{S_{template}}$ from the dataset. As in Section 3.2.7, the morphing procedure was carried out in two steps where the first step involved

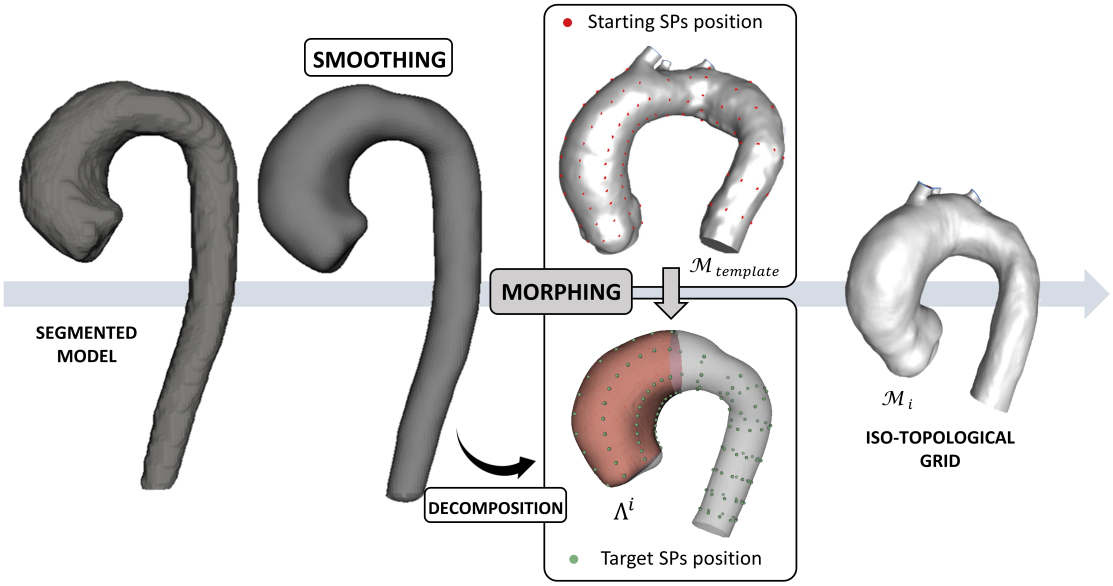

Figure 5.3: Procedure to obtain iso-topological meshes from the raw segmentations through RBF mesh morphing.

deforming the reference mesh $\mathcal{M}_{template}$ to approximate the target segmented surface while the second step involved the complete projection of the grid surface onto the segmented surface and the subsequent volumetric interpolation. In the first step, Source Points were extracted on the single surface template $\mathcal{M}_{S_{template}}$ and on every segmented aortic model. The deformation of the source template occurred by imposing the SPs calculated on it to match the SPs of the target model. They were derived exclusively on Γ_{AsA}, Γ_{AAr} and Γ_{DA}. The SPs related to the ascending tract Γ_{AsA} were obtained from a sampling of the splines derived from the same geometric decomposition proposed in Section 3.2.3. The SPs regarding the arch Γ_{AAr} and the descending aorta Γ_{DA} were derived from $n_r = 8$ artificial circular rings of $k_p = 10$ points perpendicular to the centerline of the aorta and equally spaced along it, as shown in Figure 5.3. Indeed, the first 2 rings of the aortic arch contained only 6 SPs in the lower half of the tract, thus avoiding the extraction of points belonging to the supra-aortic zone. This would have introduced inaccuracies in deforming the template model $\mathcal{M}_{S_{template}}$. Once the models were brought closer together through the first morphing action, the second step involved projecting all surface nodes onto the target segmentation to match the three controlled named selections. The supra-aortic branches, as they could not be determined from the 4D

flow magnetic resonance images, underwent a straightforward and not controlled deformation imposed by the RBFs motion field in the space. The cubic kernel $\varphi(r) = r^3$ was chosen as basis function. The commercial software RBF Morph^{TM} was used to perform the mesh morphing. Each time morphing was executed, the mesh obtained was checked in order to exclude the possibility of degenerated cells. Once the set of iso-topologic meshes was obtained, we computed a new initial template in order to replace $\mathcal{M}_{template}$. We repeated a second time the morphing operations starting from it to reduce the dependence on the initially chosen patient.

5.2.5 Statistical shape modeling

With the steps described in the previous section, from the set of aligned aortic geometries $\left\{\mathbf{\Lambda}^i\right\}_{i=1,\dots,n_p}$ we derived a set of iso-topological surface meshes $\{\mathcal{M}_S^i\}_{i=1,\dots,n_p}$. The matrix $\mathbf{M_S} \in \mathbb{R}^{3p\times n_p}$ consisted of the set of mesh nodes, with p the number of nodes on the surface. The average $\mathbf{M_{S_{mean}}}$ was extracted by calculating the average of all nodal positions. Using the anatomically and computationally corresponding surface meshes, we built a statistical shape model (SSM) framework to parameterize the complex input shape space and generate many virtual aortic atlases. This process involves two phases: (1) projecting to the latent space and (2) synthesizing virtual patients. In the first phase (1), the reference shape can be chosen as the average of the shapes that generates the atlases. Subsequently, PCA acting on $\mathbf{M_S}$ yields the eigenvectors or shape modes $\{\mathbf{W}_j\}_{j=1,\dots,n_{SM}}$ and the eigenvalues or shape coefficients $\{\lambda_j\}_{j=1,\dots,n_{SM}}$, where n_{SM} is the number of principal components employed. Each aorta shape can be decomposed as follows:

$$\tilde{\mathbf{M}_\mathbf{S}}^i \approx \mathbf{M_{S_{\text{mean}}}} + \sum_{j=1}^{n_{SM}} c_j^i \sqrt{\lambda_j}\mathbf{W}_j \tag{5.1}$$

where the coefficient vector $\mathbf{c^i}$ represents the encoded shape. Only the first n_{SM} eigenvectors were selected to account for a predetermined percentage of the variance and synthetically represent each aortic shape in the dataset. n_{SM} can be chosen by computing the compactness as described in Section 3.2.9.1, equation 3.39. Instead, generalization is evaluated through the leave-one-patient-out procedure in the form of maximum geometric deviation between the surface mesh of the excluded model and its representation resulting from the linear combination of n_{SM} modes from the statistical shape model.

Concerning the second phase (2), once the shape space has been constructed,

new unknown shapes can be generated by combining the mean shape with a set of precomputed variations, represented as deviations from the mean shape in the shape space. In other words, we generated novel synthetic aortic shapes by employing deformation vectors derived from the lower dimensional space. The generation of the atlases from the original anatomical set is performed using a tailored uniform sampling in the space of the patient-specific parameters **c**. Considering that each patient represents a point in the modal space, in the first step, the midpoint between each pair of points is extracted. This process is repeated for 5 iterations, filling the PCA-derived space with points corresponding to hypothetical virtual patients. Subsequently, in a second step, this space is sampled by selecting $n_{vp} = 300$ points (virtual patients), consisting of different values of the vector **c**, in order to maximize the intra-distances between them in the modal space of PCA. Figure 5.4 returns an example in two dimensions.

Every shape mode was associated with a deformation of the surface mesh M_S of the aorta. The points of the aortic wall were thus used as Source Points for mesh morphing, thus allowing modification of the volumetric computational grid related to the mean template M_{mean} for performing atlas-based CFD simulation.

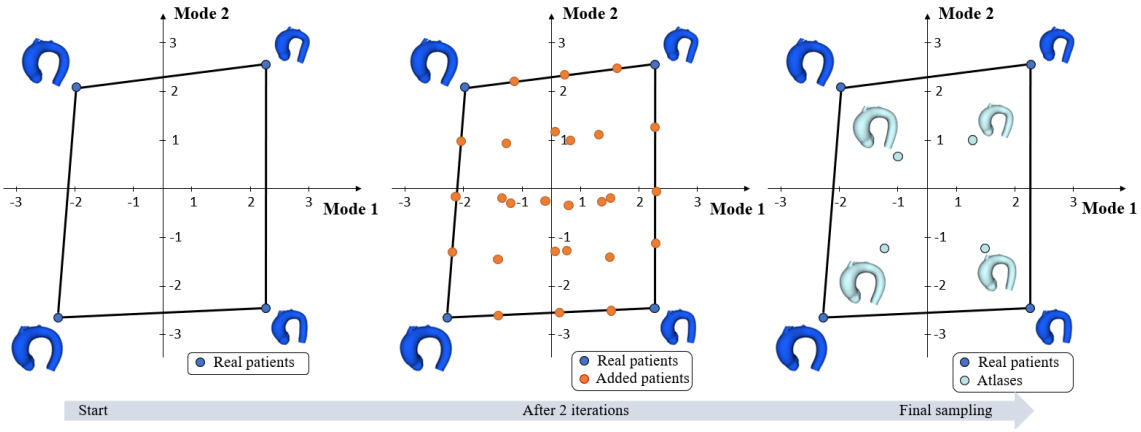

Figure 5.4: The method used to create the Design of Experiments in the simplified case of two-dimensional modal space.

5.2.6 Computational fluid-dynamics

For each virtual patient generated from the SSM, a CFD simulation was performed to compute the hemodynamics.

The blood was modeled as a Newtonian fluid with a dynamic viscosity of 0.004

$Pa \cdot s$, a density of 1033 kg/m^3 and the flow was assumed to be laminar at the systolic peak [266]. The Navier-Stokes equations govern the flow of the viscous and incompressible fluid domain Υ_F:

$$\frac{\mathrm{D}\mathbf{u}}{\mathrm{D}t} = -\frac{1}{\rho}\nabla p + \nu\nabla^2\mathbf{u} + \mathbf{g}, \text{in } \Upsilon_F \tag{5.2}$$

$$\nabla \cdot \mathbf{u} = 0, \text{in } \Upsilon_F \tag{5.3}$$

with $\mathbf{u}$ the velocity, p the pressure, ρ the density and ν the kinematic viscosity of the fluid. For this work, steady-state simulations were set up and the effect of the external body forces were not considered. The equation (5.2) thus becomes:

$$\mathbf{u} \cdot \nabla\mathbf{u} = -\frac{1}{\rho}\nabla p + \nu\nabla^2\mathbf{u}, \text{in } \Upsilon_F \tag{5.4}$$

The simulations were performed using the SIMPLE pressure-velocity coupling algorithm and second-order pressure interpolation method, setting a convergence criteria threshold equal to $1.0 \cdot 10^{-4}$.

The boundary conditions $\delta\Omega$ were:

- An inlet velocity condition controlled by a reduced-order model parameter called v_{in}. This value was derived as the maximum magnitude of the velocity vectors calculated from the grey level of the voxels intercepted by a diagonal plane perpendicular to the aortic wall at the valve level. A parabolic input velocity profile was then generated from v_{in}. It was in the range (0.7; 2) m/s.
- Four Windkessel terminal resistances at each outlet ($R_{T_{BCA}}$, $R_{T_{LCCA}}$, $R_{T_{LSA}}$, $R_{T_{DA}}$) modelled following Les et al. [344] as:

$$R_T = \frac{\overline{P}}{\overline{Q}} \tag{5.5}$$

  where R_T is a general Windkessel resistance for one of the four outlets, $\overline{P}$ is the mean pressure and $\overline{Q}$ is the mean flow rate. Given that from the available 4D flow sequences it was not possible to directly extract the velocity across the three supra-aortic vessels that could not be segmented for resolution reasons, the values of resistance for DA ($R_{T_{DA}}$), BCA ($R_{T_{BCA}}$), LCCA ($R_{T_{LCCA}}$) and LSA ($R_{T_{DLS}}$) outlets were chosen considering a flow split ratio of 70%, 20%, 5%, and 5%, respectively. The range of R_T, the second physical parameter of the ROM, required for performing the simulations, was (10^7; 10^8) (Pa $\cdot$ s)/m^3.

- A no-slip boundary condition at the rigid vessel wall.

The parameters stored as results were wall pressure and wall shear stress for every atlas of the model. The literature shows how an elevated systolic pressure exerted on the aortic wall could potentially trigger the aneurysm growth, indicating pressure as a potential risk factor [345]. As discussed in Chapter 1, also WSS plays a pivotal role in ascending aortic aneurysm expansion. Abnormal or disturbed blood flow patterns could lead to fluctuations in WSS. Consistently high values of this parameter could trigger inflammatory responses, impair endothelial function and contribute to structural changes in the vessel wall. Once the morphing atlas shape was obtained, if the model was non-consistent in terms of mesh quality (skewness over the threshold of 0.95), an automatic remeshing was performed before running the simulation and the final results in terms of wall pressure and shear were mapped onto the surface iso-topological grid. In order to automate the laborious atlas-based simulation processes [346] and automatize the setting of the boundary conditions and the saving of the results, ensuring a systematic generation of extensive CFD simulation data suitable for snapshot generation, a routine based on a journal file has been developed. The cell-centred Finite Volume Method in ANSYS Fluent - Release 2022R2 was used to solve the governing flow equations. Each time, 4 simulations were simultaneously parallelized on a Dell Precision 7820 workstation equipped with 2 16-cores Intel® Xeon Gold 5218 and 256 Gb RAM.

5.2.7 Model order reduction

The final step in creating a surrogate model and concluding the offline phase involves constructing a reduced-order model. As previously described, ROM extraction process requires that high-fidelity snapshots $\boldsymbol{\omega}^{\mathrm{FOM}}$ derived from numerical simulation are extracted.

The output snapshots $\boldsymbol{\omega}^{\mathrm{FOM}}$ from the full-order CFD simulations can be grouped in a matrix $\boldsymbol{\Omega}$, which can be factorized in the form:

$$\boldsymbol{\Omega} = \mathbf{U}\boldsymbol{\Sigma}\mathbf{V}^{\mathrm{T}} \tag{5.6}$$

where $\mathbf{U}$ and $\mathbf{V}$ are the left and right orthonormal matrices. $\boldsymbol{\Sigma}$ is the diagonal matrix containing the singular values σ_i. Through POD, a set of orthogonal bases $\boldsymbol{\Phi} = \left\{\boldsymbol{\phi}_1, \boldsymbol{\phi}_2, ..., \boldsymbol{\phi}_{N_{POD}}\right\}$ that minimizes the following Frobenius norm can be extracted:

$$\min_{\mathbf{\Phi}} \left\| \mathbf{\Omega} - \mathbf{\Phi}\mathbf{\Phi}^T\mathbf{\Omega} \right\|^2 \tag{5.7}$$

The cumulative energy $\mathcal{R}_{\text{en}}$ captured by using N_{POD} reduced bases can be evaluated:

$$\mathcal{R}_{\text{en}} = \frac{\left\| \mathbf{\Omega} - \tilde{\mathbf{\Phi}}\tilde{\mathbf{\Phi}}^T\mathbf{\Omega} \right\|^2}{\|\mathbf{\Omega}\|^2} = \frac{\sum_{i=1}^{N_{POD}} \sigma_i^2}{\sum_{i=1}^{N} \sigma_i^2} \tag{5.8}$$

where $\tilde{\mathbf{\Phi}}$ is the set of the first N_{POD} orthogonal basis.

Reduction techniques are therefore used both to extract shape parameters and derive the physical modes of fluid-dynamic outputs.

During the online phase, interpolation methods are used to predict the reduced coefficients according to new input parameters. The ROM solution of each new input configuration of parameters can be represented as a linear combination of scalar coefficients with the Genetic Aggregation Response Surface (GARS) technique [282]. It represents a direct approach that effectively addresses these issues by describing the relationship between input and output parameters [347]. The genetic aggregation technique automates the selection, configuration, and creation of the RS: it uses weighted averages of various meta-models (Full second-order Polynomial, Non-Parametric Regression, Kriging, and Moving Least Squares) to dynamically select the most suitable response surface for each output parameter [348]. Considering the dependence on $\boldsymbol{\alpha}$, shape parameters vector (the shape modes in this case), and $\boldsymbol{\beta}$, physical parameters vectors (the inlet velocity and the output resistance), reduced-order models are used to approximate the full-order field extracting the low-dimensional representation over the varying geometric and physical parameter space:

$$\boldsymbol{\omega}^{\text{FOM}}(\boldsymbol{\alpha}, \boldsymbol{\beta}) \approx \boldsymbol{\omega}^{\text{ROM}}(\boldsymbol{\alpha}, \boldsymbol{\beta}) = \sum_{i=1}^{N_{POD}} \text{w}_i \sqrt{\sigma_i(\boldsymbol{\alpha}, \boldsymbol{\beta})} \boldsymbol{\Phi}_i(\boldsymbol{\alpha}, \boldsymbol{\beta}) \tag{5.9}$$

where N_{POD} the number of modes from the POD, w_i are the weights of each reduced basis $\boldsymbol{\Phi}_i(\boldsymbol{\alpha}, \boldsymbol{\beta})$. Due to POD, the singular values of order higher than N_{POD} were not considered. Since the singular values are in decreasing order, the first modes contain more information about the approximated 3D variable than those with higher ranks.

The reduction error, i.e. the error of the POD projection, can be described as:

$$\epsilon_{\mathrm{POD}}(\boldsymbol{\alpha}, \boldsymbol{\beta}) = \frac{\left\| \boldsymbol{\omega}^{\mathrm{FOM}}(\boldsymbol{\alpha}, \boldsymbol{\beta}) - \tilde{\boldsymbol{\Phi}}\tilde{\boldsymbol{\Phi}}^{T}\boldsymbol{\omega}^{\mathrm{FOM}}(\boldsymbol{\alpha}, \boldsymbol{\beta}) \right\|}{\| \boldsymbol{\omega}^{\mathrm{FOM}}(\boldsymbol{\alpha}, \boldsymbol{\beta}) \|} \tag{5.10}$$

The building of a ROM is considered successful if it accurately predicts the target variable for input combinations not present in the training dataset. A leave-one-atlas-out procedure was performed by removing a snapshot from the dataset and verifying the ROM capability of correctly reproducing it. Both for wall pressure and shear stress, the value of N_{POD} was selected upon reaching a plateau in the curve of the reduction error $\epsilon_{\mathrm{POD}}(\boldsymbol{\alpha}, \boldsymbol{\beta})$ obtained by increasing the number of modes.

The accuracy of a ROM-based surrogate model relies on both the quantity and quality of the snapshots. The appropriateness of these snapshots enables the ROM to comprehensively capture the physical behaviour observed within the parameter space, leveraging the count of modes extracted through the POD algorithm. The construction of a ROM usually demands hours or even days, mainly due to the significant computational resources required for generating snapshots. However, once built, the ROM consumption can be performed using standalone systems in almost real-time. The validation procedure described at the end of this chapter evaluated the accuracy of each surrogate model in predicting the desired outputs for a new patient not previously considered.

5.2.8 ROM deployment and augmented reality

A crucial step for the spread of Digital Twin-based tools is the ability to make virtual replicas accessible to any user. The deployment process involved the development of a user-friendly interface, described in Appendix A that allowed users to interact with the surrogate models without requiring an in-depth understanding of the computational tools and their underlying mathematics. Such interface facilitated parameter sweeps, sensitivity analyses and "what-if" scenarios, enabling users to explore the aortic hemodynamic behaviour across various conditions. In this regard, each meta-model was exported as a Functional Mock-up Unit (FMU) component. FMUs are standard for packaging models and simulations so that they can be easily exchanged and integrated into various simulation environments and software tools [349]. They can encapsulate the full surrogate model including its equations, data and simulation behavior. For this reason, FMUs play a significant role in the context of Digital Twins due to their ability to be standardized, exchanged and integrated across different simulation environments [350]. FMUs allow the use of virtual replicas

countless times and offer the possibility of modifying and maintaining only a specific part of the Digital Twin without rebuilding it from scratch. The FMU was thus easily managed and interfaced with any C++ or Python-based application.

Two FMUs are exported for the occasion, one for every ROM-based surrogate model to derive a physical output quantity: wall pressure and shear stress. The FMUs were imported through the 3D Slicer extension for the calculation of wall pressure and wall shear stress magnitude values.

Each FMU has as input the values of the shape weights $\mathbf{c}$ to build new patients after the PCA decomposition, the resistance associated with the output pressure and the input velocity. The outputs of the FMU were instead the modal coefficients associated with each ROM. With the eigenvectors and eigenvalues obtained from the POD, pressure and wall shear stress field were thus entirely reconstructed in (almost) real-time according to equation 5.2.7.

An inverse transformation $\mathcal{T}_i^{-1}$ computed from the original ICP alignment was applied to transfer the simulation results in the original reference system derived from the segmentation of the DICOM. The DICOM transparency was controlled to allow the user to visualize the numerical simulation results overlaid on the medical images. From the MRI image data, the velocity perpendicular to the inlet plane was obtained, as shown in Figure 5.5. The maximum value was calculated and a parabolic inlet profile was applied for the simulation, with the velocity at the center of the profile corresponding to the maximum value derived from the image dataset. The FMUs of the output physical quantities allowed the user to modify the input physical parameters in order to observe what happened to the precomputed hemodynamics when the fluid-dynamic resistance at the outlet or the inlet velocity varied, ensuring the possibility of interacting with the underlying surrogate models.

5.2.9 Leave-one-patient-out validation

While Digital Twin technologies exhibit encouraging research findings within the cardiovascular domain, only a restricted portion of models have made their way into clinical application. The challenges faced encompass the requirement for heightened validation and lack of clinical interpretability [322].

In this regard, the ability of the meta-model to represent a new unseen shape and predict the related hemodynamics was assessed with a leave-one-patient-out procedure. One patient per time was removed and a new SSM with $n_p - 1$ patients was built every time. Following, a new mean template was computed by extracting the average of the $n_p - 1$ models. The shape modes were obtained again, the set of

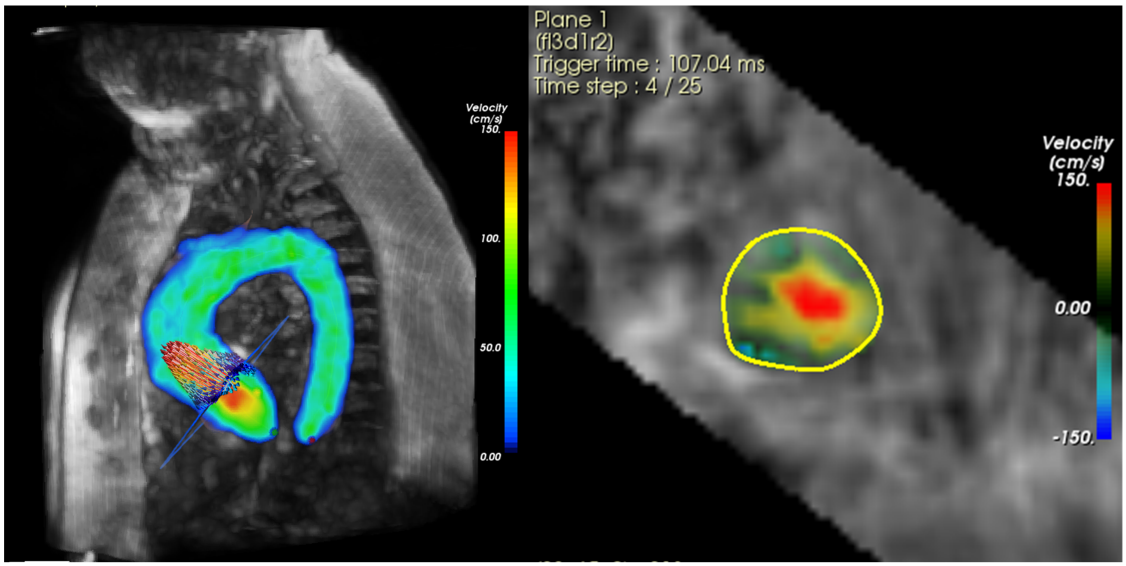

Figure 5.5: Velocity detection on an inlet plane perpendicular to the valvular jet using 4D flow MRI images. As can be seen, it is difficult to determine the supra-aortics given the resolution of the MRI images.

virtual patients extracted and the atlases results computed. New ROMs were created with the newly generated snapshots. Given that the equations that relate nodes and PCA weights are overdetermined (more equations than unknowns), a least squares fitting approach was employed to determine the shape coefficients required for the meta-model to reproduce the excluded patient's computational domain.

To this regard, the following system should be solved:

$$\mathbf{Ax} = \mathbf{B} \tag{5.11}$$

where $\mathbf{x}$ is the vector containing the patient-specific shape coefficients to be sought (the coefficient vector $\mathbf{c^{i-out}}$ of equation 5.1) multiplied by the square root of the eigenvalues, $\mathbf{A} \in \mathbb{R}^{n \times n_{SM}}$, corresponding to $\mathbf{W}$ of equation 5.1, is the matrix containing the eigenvectors from the PCA and $\mathbf{B}$ is the vector containing the node to node difference between the patient-specific mesh nodes $\mathbf{M_S}^{i-out}$ and the nodes of the average SSM template $\mathbf{M_{Smean}}$. A residual or error can be defined as:

$$\mathbf{r} = \mathbf{Ax} - \mathbf{B} \tag{5.12}$$

Since we are employing a finite number of modes, the least squares approach

approximately solves $\mathbf{Ax_{ls}} \approx \mathbf{B}$ finding $\mathbf{x} = \mathbf{x_{ls}}$ that minimizes $||\mathbf{r}||$. Assuming $\mathbf{A}$ is full rank and $(\mathbf{A^T A})$ is invertible, to find $\mathbf{x_{ls}}$ we minimize the norm of residual squared setting the $\mathbf{x}$ gradient of the squared norm equal to zero:

$$\mathbf{x_{ls}} = (\mathbf{A^T A})^{-1}\mathbf{A^T B} \tag{5.13}$$

Once the $\mathbf{x_{ls}}$ vector was obtained, it was sufficient to divide each element by the square root of the corresponding eigenvalue to obtain the modal coefficients required to represent the desired shape in the modal basis of the PCA space. The least-squares fitting was implemented directly inside 3D Slicer. Once the shape coefficients were extracted, the following input parameters related to the boundary conditions were set: an inlet velocity equivalent to the average contribution perpendicular to the inlet plane from the 4D flow MRI sequences during the systolic peak and resistances generated by a pressure equal to the systolic pressure obtained from the patient at the time of image acquisition. High-fidelity simulations were performed on each excluded patient, imposing the same boundary conditions. The error between low-order and high-order CFD solution was derived for every left-out patient.

With regards to the left-one-patient-out validation, the maximum Euclidean distance between the node positions of the excluded patient $\mathbf{M}_S^{i-out}$ and the node positions reconstructed from the surrogate models through a linear combination of modal coefficients derived from least squares fitting using the surrogate model based on the n_p - 1 aortas and n_{SM} shape modes is reported in the results section. The simulation results from the CFD on the original left-out surface mesh $\mathbf{M}_S^{i-out}$ and the ROM reconstructed fields from $\tilde{\mathbf{M}}_S^{i-out}$ were compared extracting the errors considering all nodal values and extracting violin plots. Concerning the error in predicting the fluid-dynamic results, two different types of errors were calculated: the relative ROM error $e_{\text{ROM}}^{\text{rel,i-out}}$ and the absolute ROM error $e_{\text{ROM}}^{\text{abs,i-out}}$. These errors were defined as follows:

$$e_{\text{ROM}}^{\text{rel,i-out}} = \frac{\|\boldsymbol{\omega}_{\text{i-out}}^{\text{FOM}} - \boldsymbol{\omega}_{\text{i-out}}^{\text{ROM}}\|}{\|\boldsymbol{\omega}_{\text{i-out}}^{\text{ROM}}\|} \tag{5.14}$$

$$e_{\text{ROM}}^{\text{abs,i-out}} = max(\left|\boldsymbol{\omega}_{\text{i-out}}^{\text{FOM}} - \boldsymbol{\omega}_{\text{i-out}}^{\text{FOM}}\right|) \tag{5.15}$$

where $\boldsymbol{\omega}_{\text{i-out}}^{\text{FOM}}$ indicates the high-fidelity FOM output field (i.e. the full-order solution of wall pressure or wall shear stress) and $\boldsymbol{\omega}_{\text{i-out}}^{\text{ROM}}$ stands for the ROM predicted field. Furthermore, 2 of the models with lower prediction errors and 2 with higher prediction errors were reported in the results for both wall pressure and shear stress.

The differences between the nodal values of the FOM and ROM fields were reported, showing the error contours and the corresponding Bland-Altman plots.

Part III

Results

Chapter 6

Shape-based ascending aortic aneurysm growth prediction

In this Chapter, we analyze and discuss the outcomes of Chapter 3. Specifically, we examine the correlation between local shape features and aneurysm growth rate. Subsequently, we compare the performance of the six classifiers in predicting the growth risk class of each patient belonging to the analyzed dataset. Furthermore, we assess and comment the regression model's capability to predict the growth rate of each patient.

Part of the content of this Chapter has already been published in:

- *"Assessment of shape-based features ability to predict the ascending aortic aneurysm growth", Geronzi et al., Frontiers in Physiology 14: 378, (2023)* [172].
- *"Computer-aided shape features extraction and regression models for predicting the ascending aortic aneurysm growth rate", Geronzi et al., Computers in Biology and Medicine, 162, 107052, (2023)* [173].

6.1 Results

The full dataset presented a mean follow-up of 18 ± 16 months with a range between 6 and 98 months. The population mean age at the baseline acquisition was 62.7 ± 15.5 years. 21 women (30%) and 49 men (70%) were included in the dataset. AsAA segmentations were performed for all 140 acquisitions and the shape features were extracted for the first exam of all patients. At the baseline, the maximum diameter was 49.4 ± 4.1 mm whereas at the follow-up it was 51.9 ± 4.6 mm. The full

dataset presented a median growth rate of 0.118 mm/month with an interquartile range IQR = 0.133 mm/month.

The null hypothesis of the Mann-Whitney test establishing that GRs computed from ECG-gated and non-gated acquisitions can be attributable to a distribution with equal median was accepted (p = 0.045).

The local shape features reported in terms of mean value and standard deviation were: $EILR = 2.336 \pm 0.323$, $CDR = 0.496 \pm 0.052$ and $T = 1.213 \pm 0.072$.

6.1.1 Correlation local shape features and growth rate

The relationship between local shape features and the growth rate is shown in Figure 6.1: the GR value can be inferred from the colour of each marker, ranging from light green (indicating no growth) to bright red (representing fast growth). A positive correlation is observed between GR and all four derived measurements. The following Spearman's coefficients were derived: r = 0.087 (p = 0.231) for D, r = 0.478 (p = 1.4e-5) for DCR, r = 0.411 (p = 2.0e-4) for $EILR$, r = 0.311 (p = 4.1e-3) for T. A statistically significant moderate correlation between DCR and GR, between $EILR$ and GR and between T and GR (although weaker) is thus evident while the shape features D does not reach the significance p-level.

6.1.2 Machine learning growth risk prediction

	DTr	LD	LR	NB	SVM	KNN
Accuracy (D)	**88.6%**	85.7%	85.7%	87.1%	87.1%	84.3%
Accuracy (D+DCR+$EILR$+T)	78.8%	**90%**	**90%**	88.6%	**90%**	88.6%
Sensitivity (D)	**33.3**%	0%	0%	0%	0%	22.2%
Sensitivity (D+DCR+$EILR$+T)	22.2%	44.4%	44.4%	44.4%	**77.8%**	55.6%
Specificity (D)	96.7%	98.4%	98.4%	**100%**	**100%**	93.4%
Specificity (D+DCR+$EILR$+T)	86.9%	**96.7%**	**96.7%**	95.1%	91.8%	93.4%
LHR+ (D)	**10.1**	0	0	//	//	3.36
LHR+ (D+DCR+$EILR$+T)	1.7	**13.5**	**13.5**	9.1	9.5	8.4
LHR- (D)	**0.69**	1.02	1.02	1	1	0.83
LHR- (D+DCR+$EILR$+T)	0.89	0.57	0.57	0.58	**0.24**	0.48

Table 6.1: Classification scores for the six classifiers obtained with leave-one-out cross-validation: decision tree (DTr), linear discriminant (LD), logistic regression (LR), naive bayes (NB), support vector machine (SVM) and k-nearest neighbours (KNN). The symbol // indicates undefined. Best performances are marked in bold.

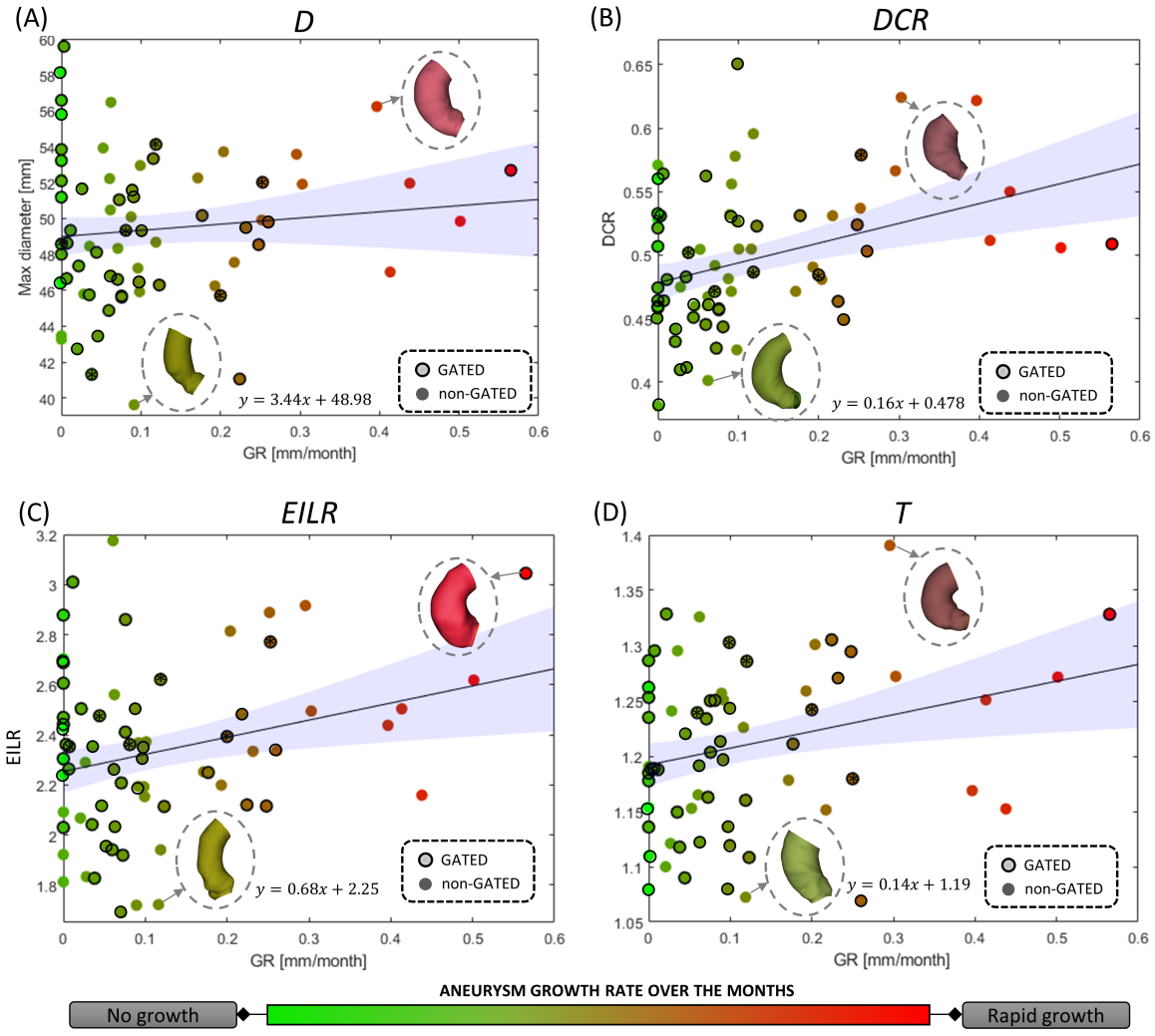

Figure 6.1: Correlation between growth rate and (A) maximum aneurysm diameter D, (B) ratio of maximum diameter and centerline length DCR, (C) ratio of external and internal curvature line length $EILR$ and (D) tortuosity T. The circles around the marker edges indicate patients with two gated acquisitions in the same phase of the cardiac cycle. The line for linear correlation with 95% fitting confidence bounds is reported, the fitting equation provided and some of the AsAA shapes shown.

Concerning the classification, 9 patients (12.9% prevalence) were identified with growth rates above the threshold of 0.25 mm/month. The confusion matrices are reported in Figure 6.2 both for the diameter alone as growth predictor and for the four shape features together. Table 6.1 reports the performance of the six classifiers in terms of accuracy, sensitivity, specificity, LHR+ and LHR-.

Using only D as risk class predictor, four of the classifiers (LD, LR, NB and

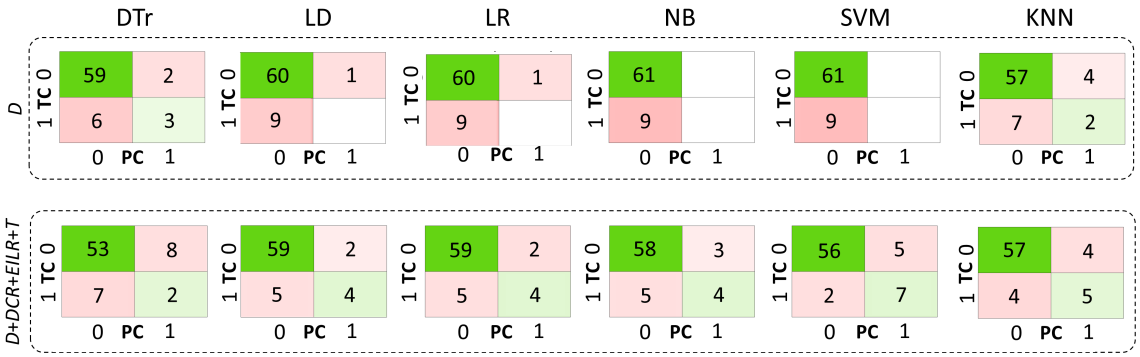

Figure 6.2: Confusion matrices related only to D on the first row and to D, DCR , $EILR$ and T on the second row for the Decision Tree (DTr), Linear Discriminant (LD), Logistic Regression (LR), Naive Bayes (NB), Support Vector Machine (SVM), K-nearest Neighbours (KNN) classifiers. TC means true class while PC means predicted class.

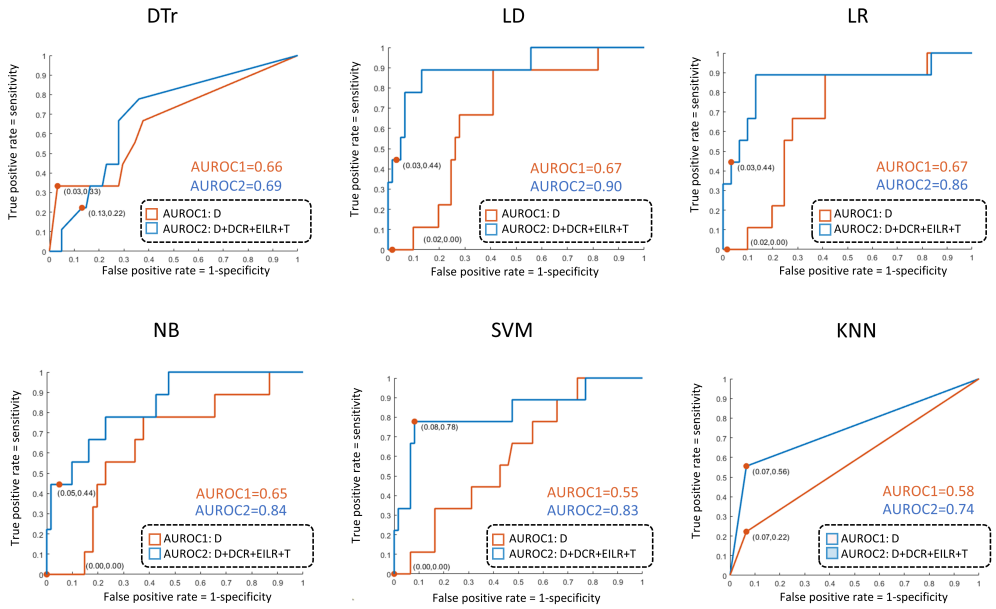

Figure 6.3: AUROC results for the Decision Tree (DTr), Linear Discriminant (LD), Logistic Regression (LR), Naive Bayes (NB), Support Vector Machine (SVM), K-nearest Neighbours (KNN) classifiers.

SVM) prove unable to identify high-risk patients (sensitivity = 0%). Among the D-based classifiers, DTr reports the highest accuracy (88.6%), sensitivity (33.3%), acLHR+ (10.1) and the lowest LHR- (0.69). Instead, the DTr specificity is 96.7%, lower than that resulting from LD (98.4%), LR (98.4%), NB (100%), SVM (100%) but higher than the values obtained through KNN (93.4%). Concerning the AUROC,

LD (0.67) and LR (0.67) perform only slightly better than DTr (0.66). On the other side, considering the four shape features together, the best performances in terms of accuracy (90%), sensitivity (77.8%), LHR- (0.24) are given from SVM. The specificity of SVM (91.8%) is lower than that of LD (96.7%), LR (96.7%), NB (95.1%) and KNN (93.4%). LHR+ of SVM is 9.5, lower than LD (13.5) and LR (13.5). Regarding AUROC, LD (0.90), LR (0.86), NB (0.84) perfom better than SVM (0.83). The AUROC for the six classifiers is shown in Figure 6.3. It is always superior for the classifiers with the four shape parameters as input compared to the equivalent diameter-only based classifiers. This is also clear by analyzing Table 6.1 where, except for DTr, most of the values related to accuracy, sensitivity, LHR+ and LHR- calculated for the classification with the four parameters outperform those of the classification with the diameter alone.

6.1.3 Regression-based growth rate prediction

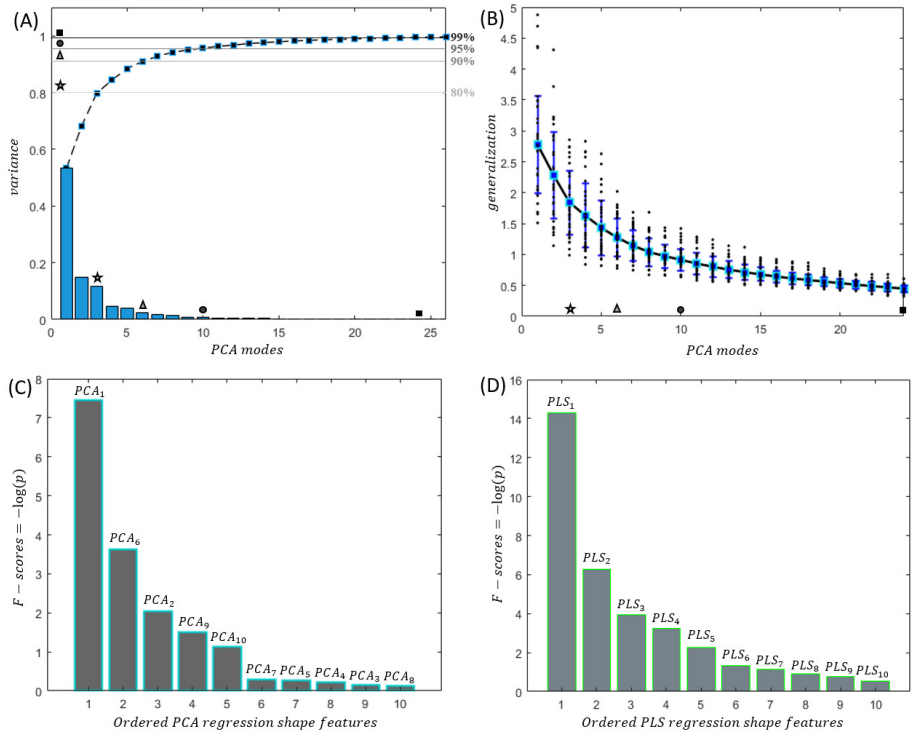

Figure 6.4: (A) SSM compactness according to the number of PCA modes used: the symbols indicate the PCA mode for which 80%, 90%, 95% and 99% of the cumulative variance is reached. (B) Generalisation curve when increasing the number of PCA modes. (C) FS for selecting the PCA modes to perform SVM regression. (D) FS for the PLS modes.

To extract global features, mesh morphing was used on all geometries. The first step of the method guaranteed a proper correspondence between the areas near the pseudo-landmarks calculated on the template model's surface and the regions in proximity to the pseudo-landmarks identified on the target anatomy. The second step based on the projection ensured a perfect match of the surfaces.

The statistical shape analysis was performed including all computational surface grids.

Concerning the SSM, the compactness curve is reported in Figure 6.4 (A). The first PCA mode alone accounted for 52.4% of the anatomical variability in the population, whereas the first 3 PCA modes together captured 80% of the overall variance. 90%, 95% and 99% of the compactness curve were achieved using 6, 10 and 24 PCA modes, respectively. The generalization ability is instead reported in Figure 6.4 (B) for the first 24 PCA modes. By including additional shape modes, its mean value, representing the mean square error between shapes reconstructed by LOO and shapes reconstructed by the SSM over the entire population, went from 2.81 mm^2 to 0.52 mm^2, where it tends to stabilise. In Figure 6.4 (C), the results of the F-test for choosing the PCA modes to be used for the regression are reported. Based on FS, the PCA modes selected as global shape features were 1, 2 and 6. Figure 6.4 (D) shows the same outputs for PLS score vectors $\mathbf{t}$. Concerning the first 10 shape modes, PLS globally reported higher FS values than PCA.

The contribution of each mode can be visualized by deforming the mean template from low ($\xi = -\xi_{lim}$) to high ($\xi = +\xi_{lim}$) standard deviation, as reported in Figure 6.5 for the three selected PCA and PLS modes.

Hyperparameters	local shape features	global shape features (PCA)
Kernel size	1.72	1.89
Box constraint	0.41	1.82
Epsilon	0.008	0.039

Table 6.2: Support Vector Machine regression hyperparameters

The first PCA mode determines the position of the aneurysm along the ascending tract. Negative weight values indicate aneurysms located closer to the root, while positive weight values are associated with aneurysms situated more towards the end of the ascending aorta. The second PCA mode primarily characterizes the curvature and tortuosity of the ascending tract. In contrast, the sixth PCA mode visually corresponds to the dimension of the aneurysm, where an increase in the weight of this mode corresponds to an increase in size of the aneurysm. On the other hand, the

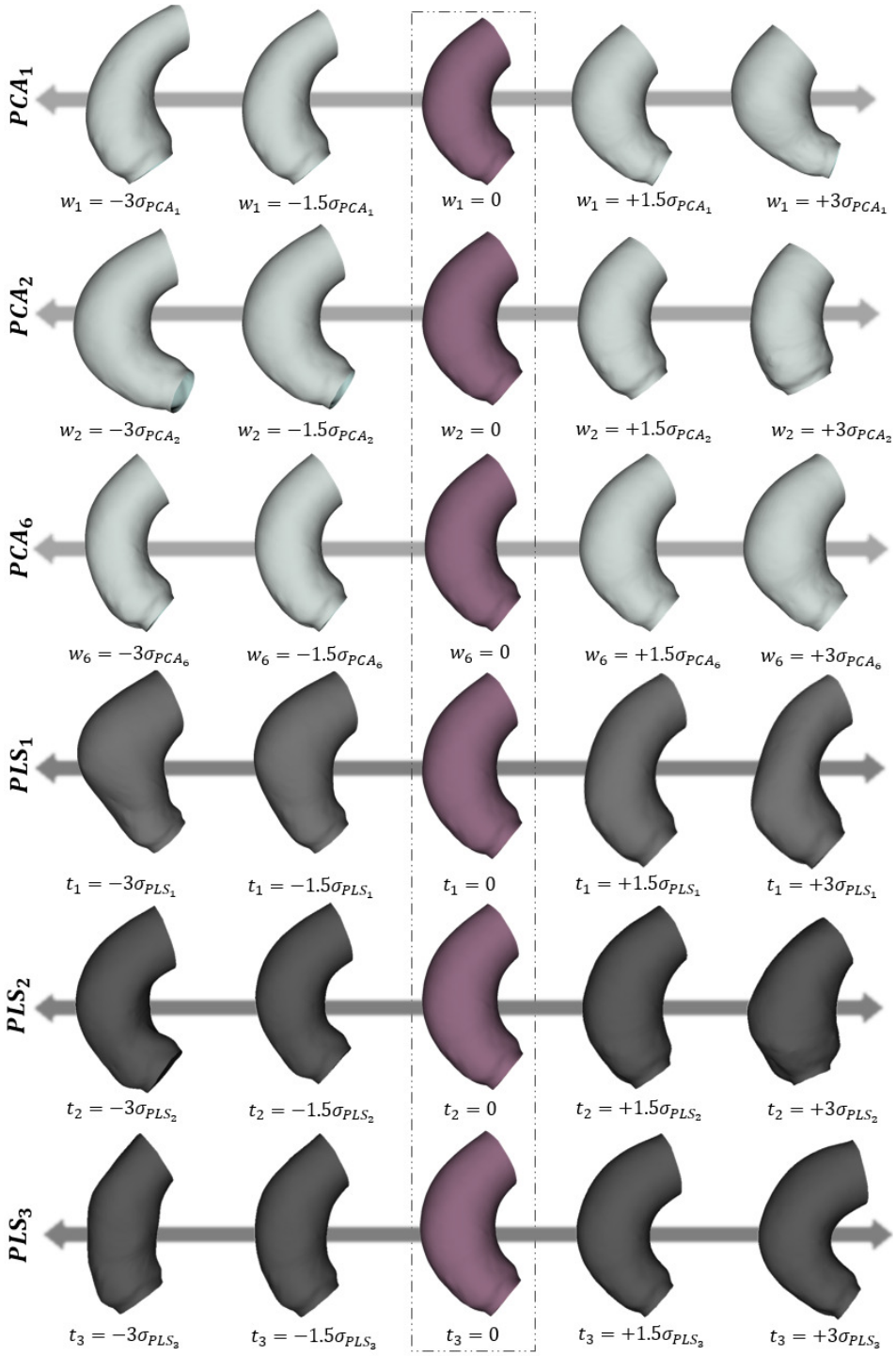

Figure 6.5: Shape modification due to PCA modes 1, 2 and 6 and PLS modes 1, 2 and 3.

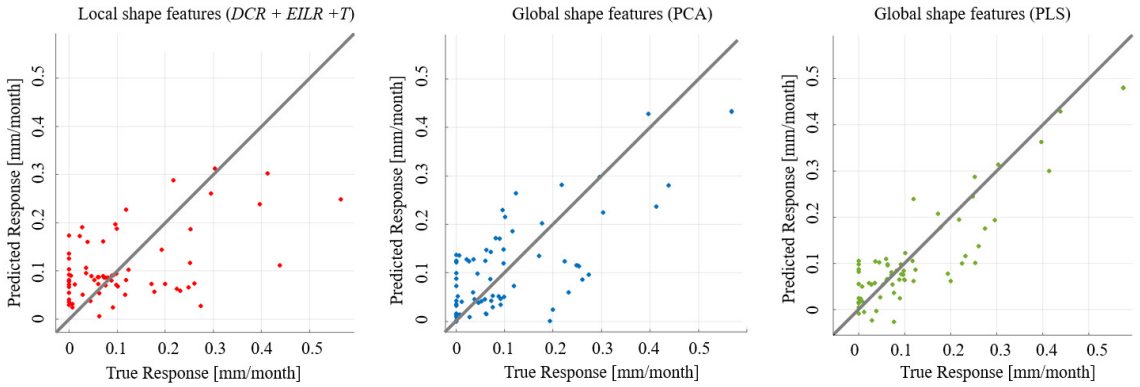

Figure 6.6: Predicted versus true response plot for the growth rate using the three local shape features (red), the global shape features extracted from PCA (blue) and the global shape features derived from PLS (green).

first PLS mode seems to represent both the location and size of the aneurysm. The second PLS mode is visually associated mainly with the diameter of the aneurysm, while the third mode is graphically linked to the tortuosity of the ascending aorta.

The hyperparameters for the Gaussian SVM regression models derived from LOO cross-validation are given in Table 6.2.

The regression performances in terms of R^2 and $RMSE_{reg}$ values are the following: $R^2_{lsf} = 0.28$ and $RMSE_{lsf} = 0.112$ mm/month, $R^2_{PCA} = 0.42$ and $RMSE_{PCA} = 0.083$ mm/month and $R^2_{PLS} = 0.63$ and $RMSE_{PLS} = 0.066$ mm/month. The comparison between real and predicted growth rate values for the three regression models is shown in Figure 6.6.

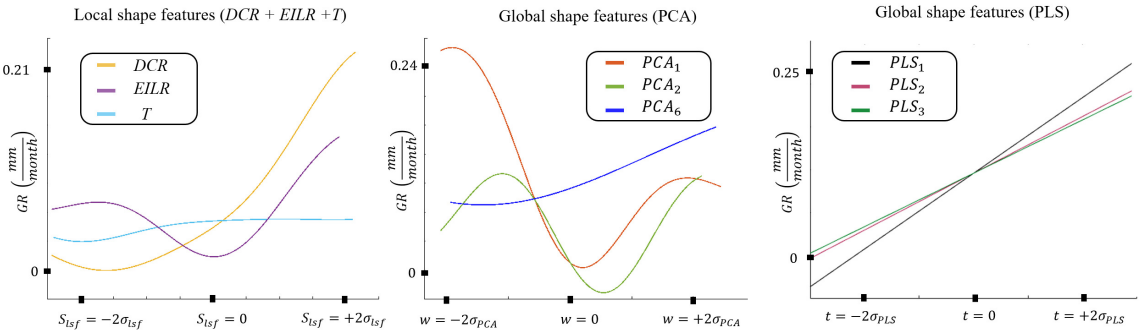

Figure 6.7: Partial dependencies plots for local and global shape features.

The partial dependencies plots for the three cases are displayed in Figure 6.7. The first plot illustrates the dependence of the Gaussian SVM regression model on

the three local shape features. The second plot shows the influence of the selected PCA modes on the SVM prediction. Meanwhile, the third plot returns the estimated linear relationship between the three selected modes and the growth rate due to PLS regression.

Moving on to Figure 6.8, the regression surface is presented, built using the modes extracted from the statistical shape model. In comparison to the typical linear regression of PLS, the data from partial dependencies plots are, in fact, more challenging to interpret in the case of Gaussian regression for PCA. Specific ascending aorta shapes are associated with portions of the surface to better understand their relationship between shape and the estimated growth rate.

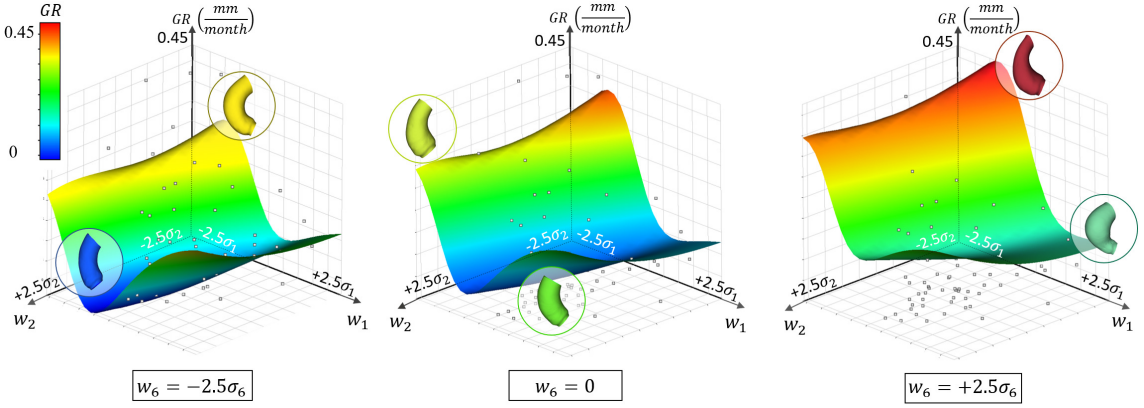

Figure 6.8: Regression surface derived from the global shape features obtained with PCA.

6.2 Discussion

In this first part of the work, we presented a method to derive and exploit local and global shape features for ascending aortic aneurysm growth risk assessment and for direct prediction of the aneurysm growth rate. We compared the ability of local shape features to identify patients at high risk of aneurysm growth through 6 classifiers based on the set of local parameters together with the same classifiers based on the maximum diameter alone. Subsequently, we employed regression models based local and global shape features to directly estimate the future aneurysm growth rate. The patients used for computing the shape metrics were selected from both gated and non-gated acquisitions. To ensure more reliable results, we imposed a temporal filtering criterion of 6 months between the first and second exams, particularly to reduce the uncertainty in the calculation of the growth rate [351, 352].

Patients with Marfan syndrome or other congenital degenerative wall diseases have been excluded. This decision was made to avoid potentially spurious factors, as these conditions could lead to rapid aneurysm growth, potentially affecting the results.

Although both CT scan and MRA were employed, the uncertainties due to the different imaging modalities were mitigated by applying well-defined exclusion criteria and ensuring that only intra-luminal regions were segmented from both imaging types. In fact, minor and non-significant differences were observed in literature when comparing diameters obtained from these two imaging techniques [353, 354].

Upon segmentation and identification of the ascending aorta, shape features were computed for the entire domain, encompassing the Valsalva sinuses. This inclusive approach also allowed the investigation of aneurysms in the root region.

The obtained growth rate results are consistent with what has been reported in literature [95, 177]. The growth rate was here derived by calculating the difference between the maximum diameters obtained from two exams and then normalizing it based on the time between the two exams (measured in months). It is worth pointing out here that this assumption of linear growth is rather simplifying, as the evolution of aneurysms is believed to follow an exponential rather than a linear pattern over time, as indicated by [355]. According to Laplace's law described in Chapter 1, Subsection 1.6, the wall tension is directly proportional to the vessel radius at a given blood pressure. Consequently, as the aorta enlarges progressively, the growth rate should tend to increase non-linearly.

Various empirical models have been proposed to account for this exponential growth behaviour, leveraging multiple time exams [180]. Understanding when aortic dilatation accelerates over time could potentially enhance prediction accuracy. However, in our study, most patients only had two acquisitions and validating exponential growth rate laws typically requires controls over at least three different time points [356]. Hence, for the sake of simplicity and feasibility, we opted for the linear model.

Furthermore, it is essential to note that D'' and D' may be located at different centerline levels. By determining the maximum diameter at a specific distance from the annulus in the first exam and evaluating the diameter from the model for the second acquisition using the same distance without searching for the maximum along the centerline again, slightly different results in terms of growth rate would be derived. These GR results would likely be lower or, at most, equal to the values we employed in our analysis.

6.2.1 Correlation local shape features and growth rate

As reflected in the data subdivision, only 9 (12.9%) patients showed a rapid evolution. The predominance of patients with slow-growing aneurysms can be attributed to the clinical practice of conducting a second 3-dimensional acquisition after some months. Clinicians make this decision based on their assessment of the patient's clinical data, assuming that the disease will not progress rapidly and the dilatation process will not be abrupt and dangerous. In the dataset, only 6 (8.6%) patients report maximum diameter over 55 mm and 4 of them show a close to zero growth rate. We suppose they did not undergo surgical treatments due to a precarious health state or because manual diameter measurements returned values close to the threshold for surgery, but still below it. Analysing the proposed local shape features, D provides non-normalized local information concerning the aortic shape. DCR offers a diameter measurement relative to a local length, which helps understand the variations between tall and robust patients and more slender individuals. $EILR$, on the other hand, returns information on the relationship between the external and the internal curvature line, to be carefully considered in the case of wall expansion toward the external direction of the aorta, as in saccular or root aneurysm [357]. Lastly, T provides essential details regarding the degree of twist and contortion present in the ascending tract, adding another dimension of understanding. Using diameter alone as a predictor of growth may not be effective as it does not account for variations in body size among individuals. Aneurysm growth could be significantly different for taller and more robust individuals compared to slender subjects, making diameter alone an inadequate predictor. The other metrics, being computed as distance or length ratios, could consider this aspect more effectively.

It is worth noting that additional parameters like volume and surface area of the ascending tract were excluded from the correlation analysis as they are considered characteristic measures of vessel size rather than shape [358].

6.2.2 Machine learning growth risk prediction

The diameter-based classifiers showed relatively low performance, suggesting again that the diameter alone, current criterion for rupture risk, fails to accurately predict the growth, at least with respect to the data we collected.

DTr and KNN are the unique classifiers able to discern at least 2 (3 in the case of DTr) of the 9 patients of the high-GR risk class. However, integrating the four features together and using the same classification models, a performance

improvement in determining true positive cases can be observed for KNN but not for DTr (Table 6.1). The diameter-based NB and SVM classifiers report 100% of specificity and LHR+ tending to $+\infty$, indicating that in case of a positive result, a patient definitely belongs to the high-risk group. However, sensitivity equal to zero combined with maximum specificity indicates that the classifier is absolutely unable to separate between the various classes.

Among the classifiers based on all metrics, good results are obtained using SVM. Although the sensitivity of SVM, i.e., the correct prediction rate for high-risk patients, never exceeds the 77.8% threshold, its accuracy, LHR+ and LHR- make it a good candidate in terms of utility [359]. LHR- = 0.24 means that a person effectively belonging to the low-risk group is about 4.2 (= 1/0.24) times more likely to have a negative test than someone whose aorta is growing faster. Since LHR+ and LHR- do not depend on the prevalence value, they are considered robust measures of the diagnostic capacity of the proposed classifiers.

As reported in [360], an excellent classification method should return a LHR+ higher than 10 and a LHR- lower than 0.1. Unfortunately, even if close to the optimal value for LHR+, SVM fails to reach the ideal threshold related to LHR-.

The presence of FNs in this type of classification is critical as it could result in patients with rapidly evolving pathology not receiving timely treatments. In this regard, it is interesting to report the geometries related to the 2 patients classified as FNs for the full set of shape features, whose complete segmentations are shown in Figure 6.9. One of them exhibits aortic coarctation (also another in the dataset which is, however, correctly identified), whereas one reports an abrupt change between aortic arch and descending aorta, characterized by a very small radius of curvature. These morphological anomalies, altering the pressure gradient, inevitably affect the fluid-dynamics of the ascending aorta [361]. This could be the reason why, although the shape features of the ascending tract are not such as to characterize the patient as being at high risk, the disease undergoes a severe and rapid evolution over time.

Overall, machine learning classification methods prove to be valid candidates in enhancing the prediction of ascending aortic aneurysm shapes prone to rapid growth [362] and facilitating more personalized control and treatment plans [363]. These methods are well-suited for integrating vast amounts of data, including patient demographics, lifestyle factors, clinical history and medical images [364]. Moreover, ML algorithms can be used to track shape modifications in time and provide dynamic predictions of aortic aneurysm growth [200], enabling timely interventions. Unfortunately, the lack of multiple 3D longitudinal data for a significant number of

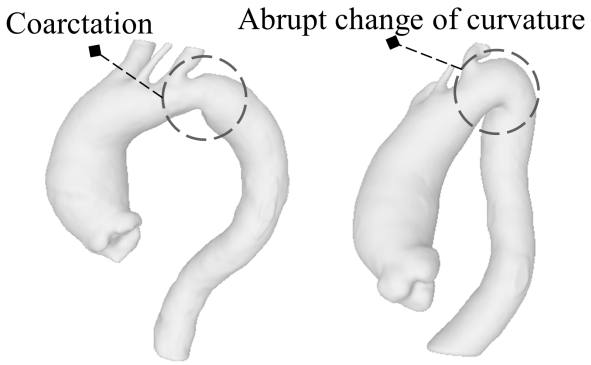

Figure 6.9: The models classified as FNs by SVM based on the four local shapes features: the first exhibits aortic coarctation while the second shows a reduced radius of curvature between arch and descending aorta.

patients poses a challenge to robustly validate the predictive ability of these models.

6.2.3 Regression-based growth rate prediction

By integrating the information derived from geometric decomposition, mesh morphing, statistical shape analysis and regression, we were able to extract global shape features potentially valuable for improving the direct prediction of the aneurysm growth rate. The results of this study show that the partial least squares regression model based on global shape features can outperform the Support Vector Machine regression models based on local shape features and global shape features derived from principal component analysis.

Concerning the initial grid, the initial patient's model reporting the median diameter was chosen to reduce the mesh degradation after mesh morphing [365]. This starting model is, in fact, a reasonable compromise to reach the aneurysms with the smallest and largest diameter in the dataset without degrading the mesh too much due to very pronounced morphing transformations. The geometric decomposition also ensured the possibility of identifying sections perpendicular to the centerline, enabling the creation of the splines. A fundamental requirement for building accurate statistical shape models is the anatomical correspondence of the domains, guaranteed from the one-to-one correspondence between the positions of the landmarks driving the morphing on each geometry of the dataset. Since it is very complex to identify landmarks for the isolated ascending tract, the proposed morphing method allows associating points of the splines resulting from the geometric decomposition of the

initial template to the same ones computed on the target aorta. This allowed better control of the grid distortion than using purely distance-based methods in which iterative energies stabilization and recursive smoothing techniques, i.e. not driven by statistical information, are usually performed [202].

The SSA was performed only on the ascending tract and not on the entire aorta because a detailed and restricted correspondence between ascending aortic aneurysm shape and growth rate was sought. This approach ensured that any spurious components related to other parts of the thoracic aorta was excluded. While in other research studies [191], PCA modes were associated with the cumulative energy of aneurysm growth over time for individual patients, in this work, the modes indicated which shape feature within the population could be related to the growth of the disease. The parametric 3D model offers the advantage of capturing complex ascending aortic morphological features and the opportunity to synthetically represent them visually and numerically using the modes. These features are difficult to be obtained using conventional morphometric measurements [366].

In constructing PCA-based statistical shape models, the high-frequency modes are typically discarded since considered mainly related to noise. However, they could be significant in explaining the pathological growth associated with the disease. Despite including shape modes up to 99% of the variability, one limitation of PCA-based growth prediction is that there could be an excluded high-frequency mode that is nevertheless strongly associated with growth. The compactness values obtained for the statistical shape model are aligned with those indicated by Casciaro et al. [367]. Their study on healthy aortas revealed that a subset of only 6 modes was sufficient to capture 84% of the variance, while a congenital aortic set required 19 modes to capture 90% of the variability. These values are quite consistent with our findings considering that we only selected the ascending part in building the SSM and the variability, in our case, is consequently lower.

Furthermore, the obtained compactness and generalization outcomes fit within the variability range reported in similar studies [210, 199]. This demonstrated the valuable SSM ability to represent a broad population. The F-test results using the PCA components give high importance to shape modes determining the aneurysm location, its size and the tortuosity of the ascending tract. This agrees with the correlation study between local shape features and growth reported in Section 6.2.1.

Only three global shape features were selected because it was the number for which the root mean square prediction error was the lowest. In fact, using a different number of shape features for the regression, RMSE_{PCA} went from 0.089 mm/month

to 0.142 mm/month and RMSE_{PLS} went from 0.066 mm/month to 0.121 mm/month.

The selection of only three global shape features for the regression was based on minimizing the derived root mean square prediction error of the LOO cross-validation. Based on this dataset, the value of R^2_{lsf} and RMSE_{lsf} and the representation of real versus predicted response values for local shape features in Figure 6.6 indicate that the SVM regression method is highly inaccurate in predicting the growth rate, especially for patients whose growth is very rapid, particularly if the prediction error is compared to the median GR of the dataset. However, results improve when using global shape features. The RMSE was, in fact, lowered using SVM with a combination of PCA-based shape features and was further reduced by approximately 56% from RMSE_{lsf} using PLS regression. Better results when using global shape features compared to local shape features were already reported by Liang et al. [199] for classifying patients whose aneurysms might burst according to numerical simulation results. In addition, it is worth observing that partial dependencies plots (Figure 6.7) for local shape features highlight a major dependence on DCR than $EILR$ and even more than T, an aspect already emerged from the results of the correlation previously studied (Section 6.1.1).

Concerning the three PCA-based global shape features, it is evident that patients with ξ values close to zero generally experience slower growth. On the other hand, the partial dependencies observed from PLS analysis indicate that aneurysms located closer to the root, with a larger initial diameter and related to ascending tracts with high tortuosity, exhibit a tendency to grow rapidly. The elevated risk associated with root aneurysms compared to mid-aortic dilatations has already been highlighted by Kalogerakos et al. [368].

In Figure 6.8, the surface resulting from the regression for the three PCA modes is reported, which can be related to the observations reported for Figure 6.7. Rapid AsAA growth seems to be related to highly negative w_1 and w_2 and positive w_6. These findings align with the conclusions of Della Corte et al. [369], who noted that a root phenotype characterized by aortic dilatation at the sinuses may indicate a more severe level of aortopathy. In contrast, slow growth occurs for aneurysms with values close to 0 for w_1 and w_2 and negative w_6, i.e. for less tortuous ascending aortas, with aneurysms located far from the root and with a smaller initial diameter, findings consistent with what discussed in previous studies [222, 370].

Obviously, additional research is essential to deeply understand the interplay between aortic shape, wall properties, haemodynamics, mechanical behaviour and aneurysm growth or rupture [371].

The integration of SSA and regression methods offers a powerful approach to model the relationship between shapes and growth rate. Accurately identifying which patients with AsAA will require surgery within a specific timeframe would significantly improve the risk-benefit analyses and aid in defining surveillance protocols [372]. This distinction becomes crucial as slow-growing AsAAs may not require frequent monitoring, while rapid-growing cases would demand close and timely observation.

6.2.4 Limitations and future works

Although this work shows that training ML classifiers based on shape features could be a promising approach for growth risk assessment and using SSA combined with regression models could help improve the growth rate prediction, some limitations need to be mentioned. The most critical concerns the small dataset of patients in this retrospective study. Classification and regression necessitate larger datasets for a robust validation of the outcomes. With regard to this, the statistical shape analysis requires a large population of representative training samples: the more comprehensive the diversity between anatomical models, the higher the number of samples required. The set of shapes that the feature space can describe is limited to the deformation modes derived from the included cohort. Therefore, there is no guarantee that a feature vector can accurately represent every new given anatomy. Concerning the risk assessment, the unequal distribution of classes could then introduce a bias towards the majority class, as classifiers usually tend to prioritize accuracy on the dominant class. Uncertainty is introduced by using both MRI images and CT-Scans and considering non-gated acquisition in the cohort. However, we tried to mitigate it by including the resolution criterion, segmenting the intra-luminal aortic region and filtering out the patients with less than six months between two acquisitions. A robust automatic segmentation method that removes manual corrections would then be required, thus avoiding any bias introduced by the operator [373]. Another significant limitation concerns the already discussed linear growth rate hypothesis. It is also interesting to consider that some patients were probably treated between one acquisition and the following with drugs such as beta-blockers that definitely affected the growth of the vessel over the months. In performing the prediction, we exclusively focused on the properties of the ascending aorta shape. We did not incorporate the patient's valve type, despite its potential influence on hemodynamics and, consequently, the aneurysm growth rate [374]. Probably, a subdivision into two different subsets according to the valvular type would improve the prediction results [284], even if Cosentino et al. showed that, especially for

the first principal modes related to PCA, there is not a significant difference in terms of AsA wall shape [375]. Various other factors could also be considered, such as aortic annulus disjunction, dislocation of the coronary ostia, or possible aortic wall thinning [376]. Furthermore, this research does not encompass the arch and descending tract, where anatomical and functional variations could also impact the growth of the ascending aortic aneurysm [377], as we noticed for coarctation. It should also be mentioned that, as this study was exclusively related to the shape, we did not consider other important features such as patient's condition (hypertension, presence of calcifications, diabetes) and material properties of the aorta wall [378] which could further improve the results in terms of accuracy.

In future work, numerical simulation should be used to extract biomechanical and hemodynamic biomarkers, complementing the information provided by the related aneurysm shape features. Parameters such as wall shear stress have, in fact, proven to be good candidates for predicting aortic wall weakening phenomena [379]. After further validations of the predictive capabilities through large-scale studies by including these multiple factors and overcoming the limitations described before, the reliability of these methods in clinical environments could be definitively established.

6.3 Findings and remarks

This work showed how to compute and exploit a set of local and global shape features helpful in classifying patients at high risk of rapid AsAA growth and to directly infer the aneurysm growth rate. The first results indicate that a set of local shape features could outperform the single diameter in predicting the risk class of each patient. Machine learning has the potential to revolutionize the management and treatment of this critical disease by efficiently processing massive datasets and handling complex relationships. Moreover, global shape features integrated with regression models could be fundamental for improving the direct ascending aortic aneurysm growth rate prediction. Specific to this work, while PCA appears to be more suitable for exploratory data analysis and dimensionality reduction, PLS seems to more accurately predict and model the relationships between the ascending aortic shape and the growth rate. Shape features alone are obviously not sufficient to predict the aneurysm growth. However, the results of this work clearly demonstrate the importance of considering the shape in studying the evolution of the pathology. Deepening this combination of non-invasive geometric quantification and statistical machine learning methods and integrating these results with those derived from the

numerical simulation could help in identifying aortic shapes potentially at risk of aneurysm growth and could undoubtedly be helpful not only for surgery planning but also for both the choice of therapy and the follow-up timing. Obviously, the new shape features proposed here should not replace the diameter but complement it to have a more detailed understanding of this complex biological problem. In order to consider and treat these shape parameters as accurate biomarkers related to the AsAA evolution, the predictive capacity needs to be further strengthened by identifying and preparing more extensive prospective studies. Further research employing 3D aneurysm anatomies and integrating predictive methods potentially employing neural network-based architectures with vascular health indicators remains essential to not only predict the potential growth rate but also estimate the possible aortic shape at known future intervals.

Chapter 7

Calibration of the mechanical boundary conditions for a high-fidelity thoracic aorta model

In this Chapter, we present and discuss the results of the calibration procedure of the mechanical boundary conditions of the aorta, taking into account the heart motion and the interaction with soft tissue and spinal column, proposed in Chapter 4. Subsequently, the differences between the structural model and the fluid-structure interaction model are analysed and the effect of the boundary conditions on strain is described. Lastly, an in-depth examination of the comprehensive limitations inherent to this study is performed. Part of the results discussed in this Chapter has been published in:

- *"Calibration of the mechanical boundary conditions for a patient-specific thoracic aorta model including the heart motion effect", Geronzi et al., IEEE Transactions on Biomedical Engineering, (2023)* [254].

7.1 Results

7.1.1 Calibration

Following a thorough development of the fluid-dynamic and structural models, the iterative calibration procedure based on Levenberg-Marquardt was completely automated, ensuring reproducibility and eliminating any potential user errors. During the final five iterations of the ICP algorithm, rigid displacements of less than 0.08 mm were observed, confirming that the FE model and the splines were accurately

aligned. We verified the fitting quality related to the 3-parameter Mooney-Rivlin model based on the derived experimental material properties. It returned RMSE_{MAT} = 1840 Pa and $\text{R}^2_{\text{MAT}} = 0.994$.

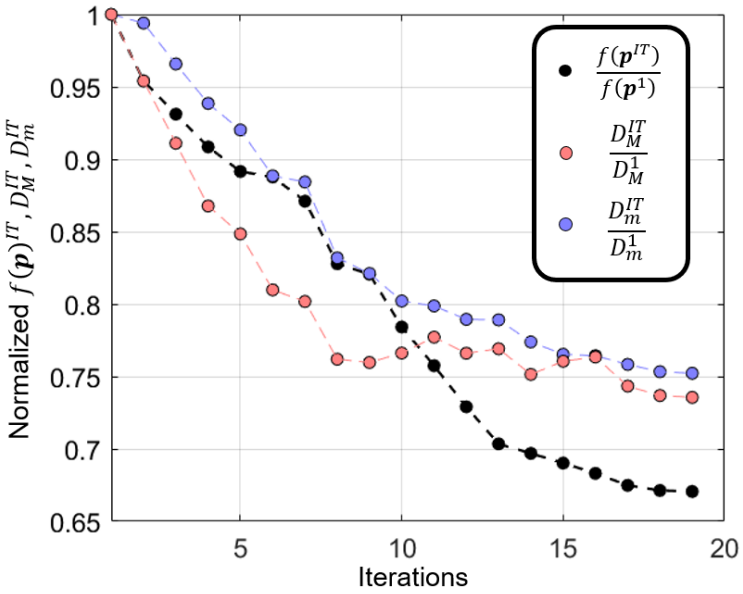

Figure 7.1: Evaluation of the normalized loss function $f(\mathbf{p}^{IT})$, maximum D_M^{IT} and mean D_m^{IT} neighbour distance for each of the iterations of the Levenberg-Marquardt optimisation.

During each iteration of the Levenberg-Marquardt optimization, a new zero-pressure state was computed using the patient-specific diastolic pressure field $P_w(t_{diast})$, which was in a range between 9330 Pa and 9730 Pa (70 mmHg and 73 mmHg) depending on the aortic region.

The calibration process was successfully performed on the analyzed patient and the loss function $f(\mathbf{p})$ was reduced by approximately 34% after 19 iterations, decreasing from 0.343 m to 0.227 m. The entire calculation required a total of 32 hours. The algorithm stopped due to the second optimization ending condition. At the end of the calibration, the value of the parameters governing the mechanical boundary conditions was $\overline{\mathbf{p}} = [0.6, 0.02, 0.04, 1.5 \cdot 10^4 \text{ Pa/m}]$. The cost function assessment during the procedure, normalised with respect to the value of the first iteration, is reported in Figure 7.1. In the same Figure, for each iteration, the maximum and mean normalized neighbour distance between the splines, denoted as D_M^{IT} and D_m^{IT}, respectively, are reported. These quantities are determined as the maximum and mean values of the vectors containing the evaluation of (4.10) on each point. The maximum distance between the points belonging to the two sets of splines decreased

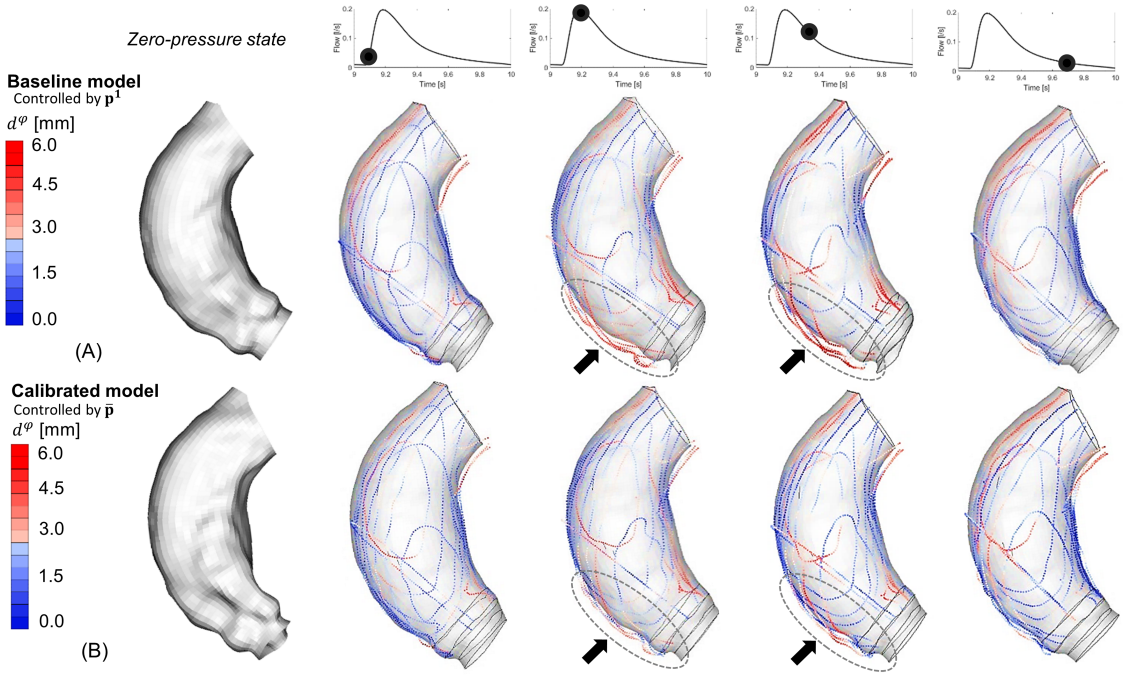

Figure 7.2: Moving to the right: ascending part after the zero-pressure calculation, deformed vascular structure and error in terms of neighbour distance on the cine-MRI-derived splines during the early systole, peak systole, late systole and early diastole for (A) the baseline model above, (B) the calibrated model below. It can be observed how the error is reduced mainly in the anterior-lateral zone of the initial ascending part during the peak and late-systolic frames.

from 8.64 mm to 6.37 mm, and the mean distance reduced from 2.24 mm to 1.83 mm. At the conclusion of the calibration, the maximum error in terms of distance between the points belonging to the two sets of splines was observed in the region of the sinotubular junction during the phase immediately following the systolic peak (Figure 7.2), when the displacement of the annulus was more pronounced.

In performing each LM iteration, the number of simulations required to obtain the zero-pressure state varied from 4 to 15, in accordance with what reported in [311]. In general, as the spring stiffness decreased, a higher deformation corresponded and consequently a higher number of iterations to reach the convergence criterion was required. In fact, the baseline model controlled by the initial guess $\mathbf{p^1}$ required an average displacement on the ascending aorta of 1.1 mm to reach the unloaded configuration, whereas the final calibrated model, whose mechanical BCs were governed by $\bar{\mathbf{p}}$, distinguished by globally lower-value parameters, presented an average displacement of 5.4 mm.

The Response Surface, computed to investigate the area surrounding the initial guess, along with the three Design Points used to confirm the calibration outcomes, is shown in Figure 7.4. Being a 4-parameter space, its three-dimensional representation is derived by holding two of these parameters constant. A high quality and prediction ability was ensured by $R^2_{RS} = 0.998$, $RMSE_{RS} = 1.8 \cdot 10^{-5}$ m and $RMAE_{RS} = 2.91\%$. DP_1 and DP_3 returned the same minimum $f(\overline{\mathbf{p}}_{DP_1}) = f(\overline{\mathbf{p}}_{DP_3}) = f(\overline{\mathbf{p}}) = 0.227$ m after 21 and 16 iterations with $\overline{\mathbf{p}}_{DP_1} = \overline{\mathbf{p}}_{DP_3} = \overline{\mathbf{p}}$ while DP_2, after 25 iterations, returned a new vector $\overline{\mathbf{p}}_{DP_2} = [0.64, 0.04, 0.04, 1.4 \cdot 10^4 \text{ Pa/m}]$ for which $f(\overline{\mathbf{p}}_{DP_2}) = 0.232$ m, 2.2% higher than the minimum previously obtained. The impact of the calibration on the aortic motion is shown in Figure 7.5: the relative displacement of the computational grid in systole compared to the configuration in late diastole is shown for the baseline model simulated with the initial guess $\mathbf{p^1}$ and for the model at the end of the calibration controlled by $\overline{\mathbf{p}}$.

7.1.2 Strain assessment and fluid-structure interaction

In Figure 7.6, the von Mises equivalent strain contours are shown to display the BCs calibration and the annulus motion effects on this outcome. The maximum strain values are instead listed in Table 7.1. Introducing the heart motion in diastole did not alter the strain contours and their respective maximum value. However, they differed depending on the calibration effects. At the systolic peak, on the other hand, the maximum strain in both the baseline case and the model with tuned parameters increased due to the application of the annulus motion.

The resolution of the fully-coupled fluid-structure interaction analysis employing the model with the Robin BCs governed by $\overline{\mathbf{p}}$ required 108 hours. The streamlines for the velocity field during six different cardiac phases derived from fluid-structure interaction analysis are reported in Figure 7.3. Comparing the displacement derived from strongly-coupled FSI and structural simulation (Figure 7.7), the maximum error between corresponding nodes $D_{MAX_{FSI}} = 0.64$ mm was identified for a node close to the annulus during the systolic peak. Precisely at this phase, the solutions of the two methods showed differences in deformation patterns near the lower part of the sinuses of Valsalva. $RMSE_{FSI}$ was equal to 0.12 mm in late diastole and 0.19 mm at the systolic peak, quantity representing the maximum during the entire cardiac cycle. The cost function evaluated on the FSI deformed wall returned $f_{FSI}(\overline{\mathbf{p}}) = 0.237$ m, value 4.4% higher than $f(\overline{\mathbf{p}})$.

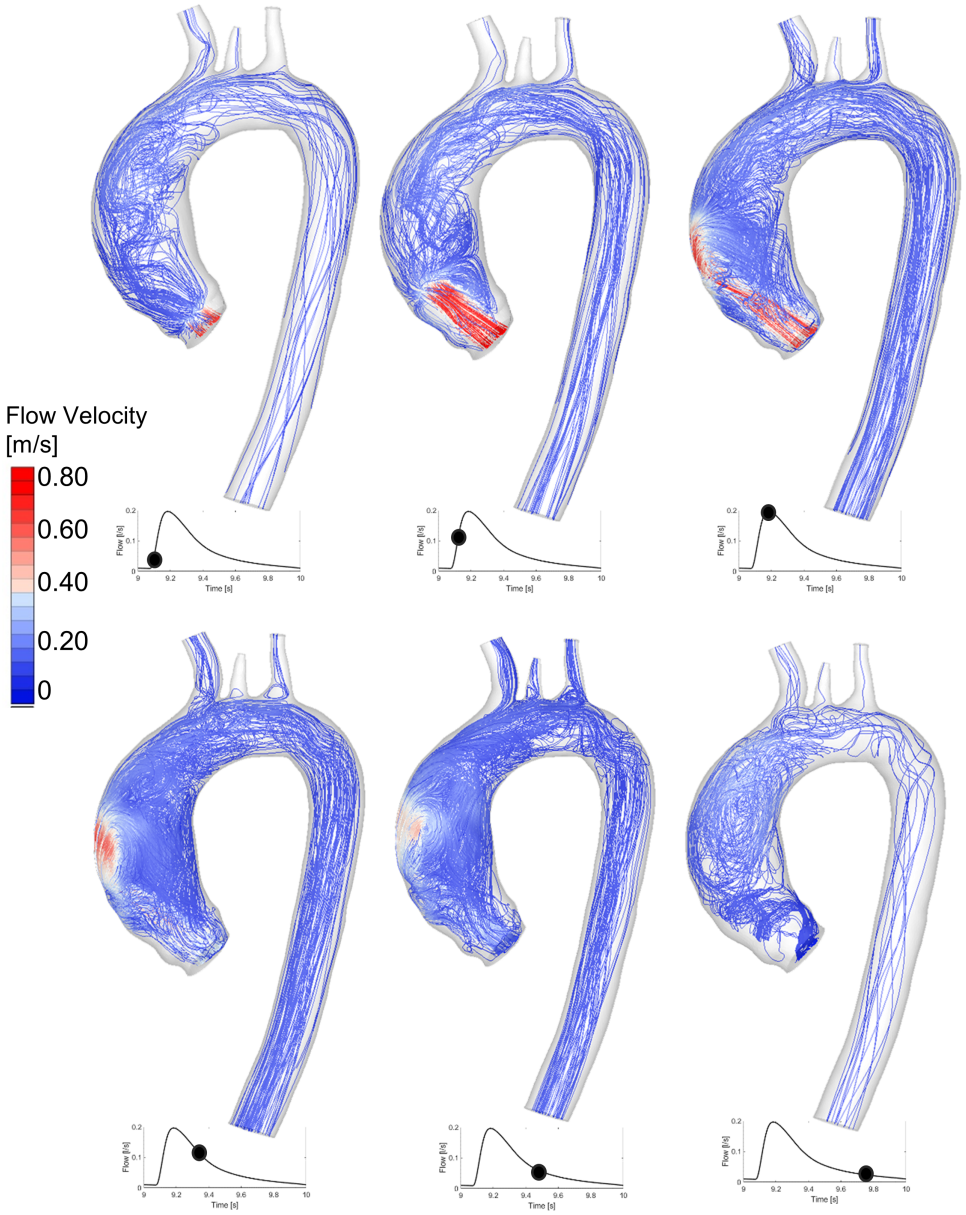

Figure 7.3: Streamlines during 6 different cardiac phases obtained from the fluid-structure interaction analysis accounting for the heart motion.

7.2 Discussion

7.2.1 Calibration, strain assessment and fluid-structure interaction

This study introduces an approach for performing a patient-specific calibration of the parameters governing the mechanical boundary conditions of a high-fidelity model

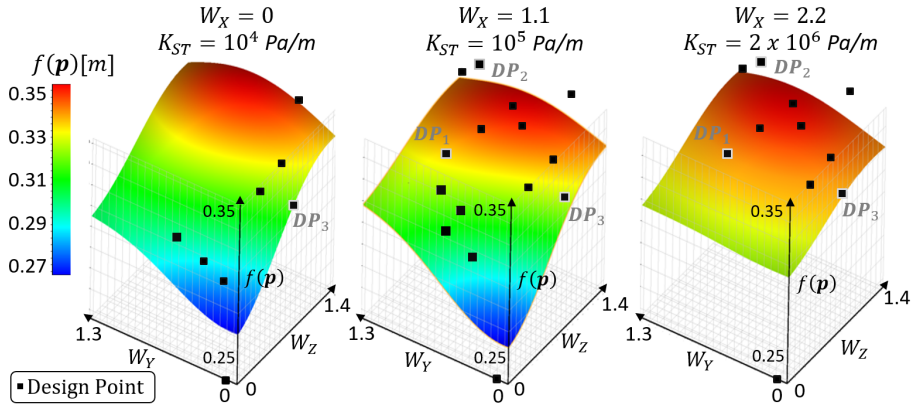

Figure 7.4: Response Surface shown by fixing 3 different values of W_X and K_{ST}. The 16 DPs are plotted and DP_1, DP_2 and DP_3 used to test the method are indicated.

Table 7.1: Maximum von Mises equivalent strain: effect of calibration (C) and heart motion (HM).

Phase	HM: no C: no	HM: yes C: no	HM: no C: yes	HM: yes C: yes
Diastole	0.051	0.051	0.119	0.119
Systole	0.131	0.294	0.251	0.262

of the thoracic aorta. The whole preparation of the workflow is time-consuming. It requires much effort as several steps, with the exception of the optimisation using Levenberg-Marquardt, are still manual: in fact, the preparation of the simulation settings, the segmentations refinements, the annulus tracking as well as constructing the FE and CFD models still require multiple user interventions.

The Robin BCs introduced in this work have two main advantages: from a clinical standpoint, they restrict the aortic movement and dilation, improving the correspondence with the motion derived from the images, whereas on computational side, they affect the movement in regions usually left unconstrained (the aortic wall) and relax sections often strongly constrained (the inlets and outlets) where the use of constraint equations for the cardiac motion allows the aorta to expand and deform under the pressure load. The decision to calibrate the whole set of BCs by exploiting only the ascending aorta domain Γ_{AAw} is due to two reasons: first, the data on the material properties were available for this region and second, the acquired cine-MRI planes do not allow for accurate identification of displacements in the arch and descending aorta due to partial volume effect or to the absence of the considered

aortic part in the sequences. Furthermore, the motion of the descending aorta is generally less pronounced, often yielding displacements of smaller magnitude than the cine-MRI resolution [380, 381].

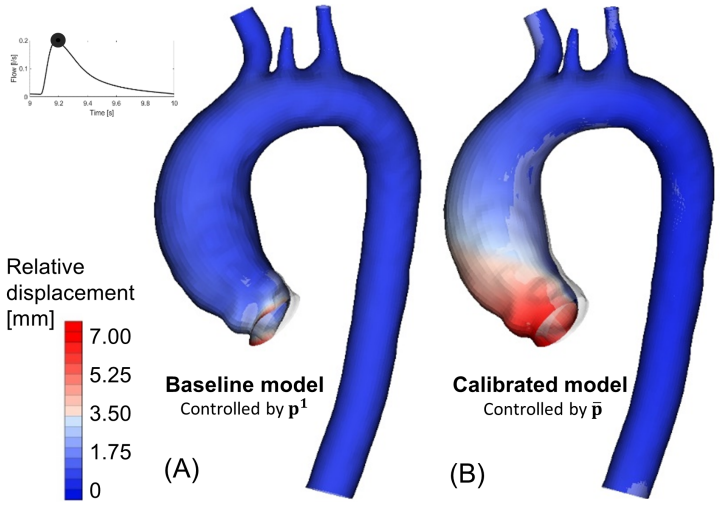

Figure 7.5: Relative systolic-diastolic displacement contours and diastolic model shown in background for (A) the case with the initial parameters guess and (B) the calibrated model.

Each iterative step of the calibration procedure required solving an inverse problem to determine the zero-pressure state. The diastolic pressure field derived from the CFD and applied in this steady-state simulation was consistent with the patient's blood pressure detected during the MRI scanning. The maximum difference between each value of the pressure field and the measured pressure was 2 mmHg, in complete agreement with the discrepancies identified by Chemla et al. [382] between aortic diastolic pressure and peripheral diastolic pressure. The achieved unloaded configuration exhibited major displacements in the ascending aorta domain primarily due to the weakest stiffness values introduced by the Robin boundary conditions and modeled in Equation (4.5). The sets of springs connected to the three upper branches representing the upstream vasculature had the additional benefit of avoiding instabilities when solving the simulation for the zero-pressure state computation. These springs further constrained the displacements in the adjacent regions, contributing to stabilising the solution of the iterative inverse problem.

The ending criteria threshold values related to the LM optimisation were intentionally not set too strictly for two main reasons: first, if lower, these would

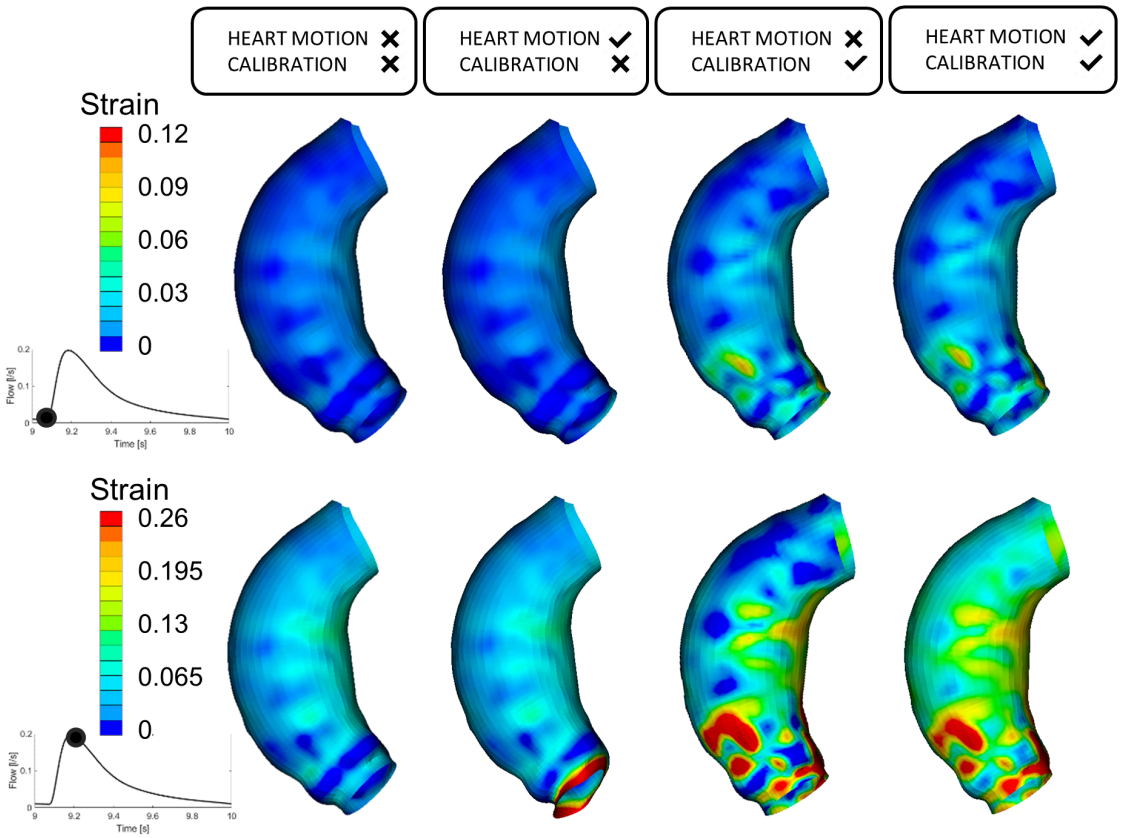

Figure 7.6: Effect of imposed annulus motion and calibration on strain contours for the ascending aorta in late diastole (top) and at the systolic peak (down).

have significantly increased the number of iterations, resulting in excessively long computation times. Second, at each evaluation of the cost function, the different residual error introduced by the inverse problem to obtain the zero-pressure state, an iterative method as well, could have been even higher than the potential enhancement determined by the new iteration of LM. This clarifies the rationale behind establishing a stringent threshold (0.1 mm) for the zero-pressure convergence: it helps to reduce the influence of the error introduced by the unloaded state computation on the final cost function assessment.

In each iteration of the workflow, the distance between the points belonging to the segmentation-derived splines and those to the simulation-derived splines, expressed by (4.10), varied across the cardiac cycle. The maximum error emerged during systole, the cardiac phase characterized by the highest dilation and displacement of the patient's vessel wall [383]. This trend is reflected by the denser frames sampling

φ in systole compared to that in diastole [384, 385]. The loss function accounted for all selected frames φ. However, the most significant impact on reducing its value following parameter adjustments was attributed to those corresponding to systole, as can be observed from Figure 7.2. Reducing the contribution of the diastolic phase effect on the error proves challenging due to segmentation bias, which introduces a residual distance between the 3D computational model and splines derived from cine-MRI. This error is mainly observed in the medial part at the end of the ascending aorta close to the pulmonary artery and in the antero-lateral zone where the vena cava comes into contact with the aorta. Such vessels close to the aorta, in fact, introduce uncertainties in the segmentation of 2D images.

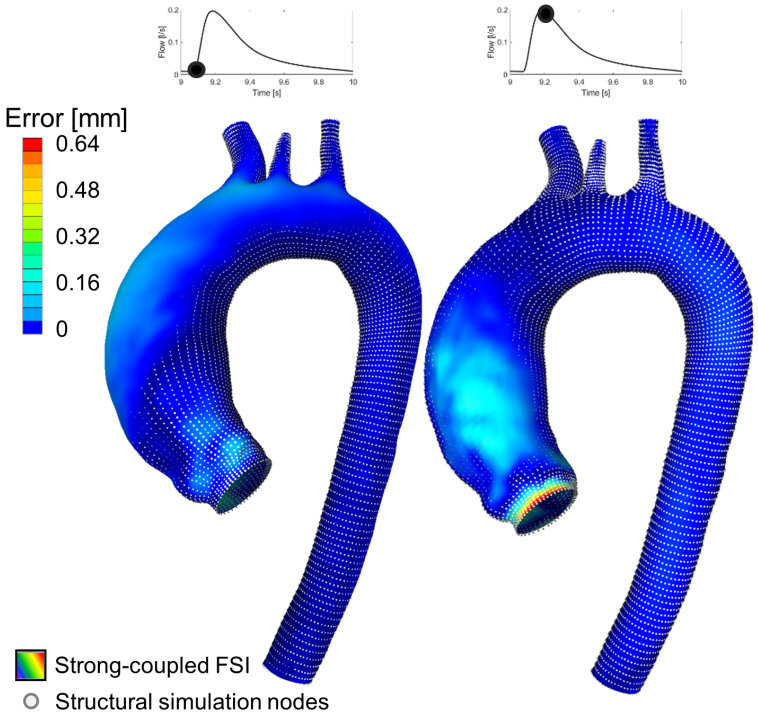

Figure 7.7: Distance between each node of the wall of the structural domain in fully-coupled FSI simulation and the corresponding node in structural simulation for the calibrated model.

At the end of this patient-specific calibration, the cost function decreased by 34% from its initial value. It is worth pointing out that this could not be reduced to 0 due to the limited control provided by only 4 variables governing the complete set of mechanical boundary conditions. To achieve better model control, additional parameters would need to be introduced. The inspection of the three Response

Surface representations (Figure 7.4) seemed to suggest a minimum for low values of W_Y and W_Z, in agreement with the minimum achieved through the LM algorithm. Moreover, the repetition of the workflow using the 3 additional Design Points as initial guesses contributed to showcasing its partial robustness in tackling this highly nonlinear problem.

Due to the choice of the initial guess, the average nodal displacement required to attain the unloaded state for the model with tuned Robin BCs exceeded that of the baseline model. This observation has already been reported by Baumler et al. [279], who noted a significant disparity in deformation necessary to achieve the zero-pressure state when considering or omitting the Robin boundary conditions in a fluid-structure interaction model of a dissected aorta. The comparison between the baseline and calibrated model in Figure 7.2 graphically shows a clear difference in terms of relative systolic-diastolic displacement after the calibration of the Robin BC values: the model generated with the initial parameter configuration was strongly constrained and the motion applied at the level of the annulus was propagated exclusively to the nearby elements up to the central part of the Valsalva sinuses. In contrast, after the calibration, the entire ascending aorta absorbed the impulse caused by the heart muscle. Additionally, it is noteworthy that the motion imposed by the dummy node resulted in a maximum relative systolic-diastolic displacement of 6.9 mm, mainly downwards at the level of the aortic root. This aligns with discussions found in the literature [386, 387].

Having made the kinematics of the vessel more consistent with the information derived from the cine-MRI sequences allows the model with the tuned BCs to reproduce the real displacement and deformation more faithfully than without calibrated parameters. This improved faithfulness in reproducing the behaviour potentially leads to a better strain assessment, bolstering the precision of the model in evaluating the rupture risk related to pathologies like ascending aortic aneurysms. Figure 7.6 illustrates the impact of the boundary conditions on the von Mises strain distribution. In diastole, no difference is observed in the strain field when applying the heart motion, contrary to the calibration as the parameters of the Robin BCs change. For this specific scenario, the strain is higher after the calibration since the zero-pressure state results more compressed. Turning to systole, when taking the baseline case without annulus movement as reference, the heart motion produces a localised increase in strain exclusively for the mesh elements belonging to the annulus. Removing the heart motion but calibrating the 4 parameters of the Robin BCs makes the strain higher due to the new zero-pressure configuration. If both

heart motion and calibration are applied, the strains become even more elevated. These observations are in accordance with the findings of Beller et al. [259].

Comparing the iso-topological surface meshes in structural and fully-coupled FSI simulation (Figure 7.7), differences are also evident in diastole. This occurs because the zero-pressure grid, whose nodal positions are the same for both the simulation approaches, was derived using the diastolic pressure field computed through rigid-wall CFD simulation and the use of deformable walls results in slight variations of the pressure load in FSI simulation modifying the final position achieved in diastole. In simpler terms, the diastolic pressure field at the wall of the FSI model differs from the field $P_w(t_{dias})$ obtained at the wall of the CFD domain, consequently introducing a bias in terms of deformation. In any case, the most significant difference between the two deformed walls occurs at the systolic peak. Although this may seem high (0.64 mm), it can be observed from Figure 7.7 that the major errors are all concentrated in the area close to the annulus. This may occur because of the control method of the annulus movement based on the constraint equations proposed in (4.8) through which we did not impose a displacement to each individual node of Ψ_{inlet} but instead controlled the overall behaviour of the entire node set with respect to the dummy node. When comparing the two simulations exclusively within the calibration domain Γ_{AAw}, thereby excluding the initial elements close to the annulus, as shown in Figure 4.3 (B), the maximum error in systole is reduced to 0.24 mm. This difference between the two methods is in agreement with what was reported in [388]. The value of the cost function $f_{\text{FSI}}(\overline{\mathbf{p}})$ demonstrates that, at least for this patient, calibrating the model using a pressure field and structural simulations yields tuned parameters that enhance fidelity even for the FSI model. Moireau et al. [280] correctly emphasized the substantial computational burden of calibration methods based on fluid-structure simulations that aimed at minimizing the discrepancy between the computational model and the image-derived information, defining it as a major drawback. Our approach stands as a viable alternative since it exploits the decoupling of the physics, providing a considerable gain in computational time. In fact, all the calibration procedure is based on structural simulations with a much lower computational cost when compared to fully-coupled FSI simulation.

Given the challenges in non-invasively estimating thoracic aorta tissue properties using current imaging methods [389], where accurate insights are typically limited to highly invasive procedures or ex-vivo techniques [390], we chose to showcase the consistency of the calibration workflow using a model derived from a patient who underwent surgical repair for aneurysm. In fact, the wealth of data collected for

this patient enabled us to extract personalized material properties data, reconstruct the 3D model, replicate the valvular inlet shape and retrieve the displacement and deformation of the vessel during the cardiac cycle. Nevertheless, the same procedure could be adapted to healthy aortas by adding new material-related parameters: in fact, this workflow can be extended to any patient if data to reconstruct the FE model and extract the vessel motion are available. The proper execution of the workflow is independent from the type of valvular inlet: a different shape would mainly influence the CFD-derived wall pressure field $P_w(t)$, particularly in the ascending aorta. It is also worth noting that the calibration methodology proposed here could be similarly applied for the abdominal aorta [391] or for other organs such as the heart [392] or the diaphragm for motion compensation in the cancer radiation therapy [393]. Finally, although cine-MRI was used to calibrate the model, this procedure could be replicated with every image set that considers dynamic acquisitions during the cardiac cycle, such as multiphase-CT or even 4D flow MRI. These techniques offer information and time-resolved data on the aortic motion, enabling the description of phenomena like aortic rotation at the annular level. Nonetheless, we consider cine-MRI data as a well-balanced compromise between spatial resolution and image quality of CT scan and good temporal accuracy of 4D flow MRI [394]. In this regard, Shidhore et al. [395] used information from 4D ultrasound images to estimate stiffness parameters for the Robin boundary conditions in a murine aorta FSI model across three macro-areas. Despite its micron-level spatial resolution, 4D ultrasound imaging is not currently part of clinical practice for analyzing ascending aortic aneurysms since the anatomical position of the ascending aorta surrounded by the thoracic cage and the interference of intra-pulmonary gas limit image acquisition [396]. However, 2D acquisitions are sometimes carried out for screening purposes. Nevertheless, they rely on user-dependent probe placement and an accurate determination of the position of the aorta, essential for effective calibration, remains challenging.

7.2.2 Limitations and future works

This work acknowledges several limitations that warrant discussion. To begin, the procedure is here applied exclusively to one patient. Extending the methodology to encompass other cases would be valuable, assessing the consistency of the derived stiffness values and exploring potential inter-patient variability. Secondly, the control of mechanical boundary conditions was achieved by employing only 4 parameters pertaining to the stiffness of the Robin boundary conditions. Further investigations are essential to understand whether introducing more parameters could enhance

model accuracy and consequently improve fidelity. We have then assumed the damping factor $\boldsymbol{\eta}$ constant and equal in the three directions of space, modelling choice whose effect should be additionally explored. Moreover, the relationship that changes the stiffness of the springs according to the distance to the spine was assumed to be linear; alternative mathematical formulations need to be tested to assess how they affect the simulation results. Another limitation concerns the simplification of the model: we did not consider the effect of the coronary arteries and the 3D valvular shape on the aorta simulation and we imposed a constant thickness and isotropic material properties for the entire vessel. It is also evident that the constitutive laws developed to model Γ_W are simplified, albeit without disrupting the procedural workflows. The model also overlooks factors like the self-balancing internal residual stress in the zero-pressure state [397] and the different types of material properties across the three layers (intima, media and adventitia) of the vessel wall [398]. Finally, it should be stressed that the robustness of this calibration method was only partially verified for the analyzed patient. When employing this method, careful selection of parameters for the Levenberg-Marquardt algorithm is necessary to ensure its applicability across multiple subjects.

The most important future extension of this study involves its application to a large dataset to effectively demonstrate the robustness of the procedure and that high-fidelity models calibrated with such methods can indeed generate reliable Digital Twins based on accurate data reproducing the real behaviour of the aorta [144, 240]. The possibility of improving the model fidelity by including various morphological and functional aspects could accelerate the comprehension of the complex biological process related to the aneurysm growth and rupture [399]. Extending this workflow to several patients, however, requires automation of specific laborious and time-consuming steps such as image segmentations and model generation. Overcoming the limitations previously described, this procedure, here presented as a proof of concept, could be used to return a patient-specific model able to provide an accurate estimation of the risk for this condition, an essential feature when aiming to create a DT with predictive abilities. Combining these boundary condition parameters with shape parameters derived from statistical shape modelling and reduced-order models could guarantee the deployment of more reliable and easy-to-use models in clinical practice [400]. In addition, the high-fidelity model proposed here could be exploited to perform numerical simulation of vascular replacement prostheses for the ascending aorta [401] but also for the analysis of thoracic endovascular procedures such as wire insertion for trans-catheter aortic valve implantation [402].

7.3 Findings and remarks

In this study, we presented a novel method for calibrating 4 parameters governing the mechanical boundary conditions of a high-fidelity thoracic aorta model, taking into account the motion imposed by the heart on the aorta at the level of the annulus. On fluid-dynamics side, the use of a closed loop circulation based on lumped parameters provided quasi-patient-specific boundary conditions. Concurrently, on the structural side, the combination of hyperelastic material properties grounded in experimental data with an iterative zero-pressure calculation allowed to more faithfully reproduce the vessel deformation behaviour in response to the blood pressure. This holds particular significance for understanding the evolution of pathologies that necessitate a deep analysis of wall dynamics, such as aneurysms and aortic dissections. Although further extensions are required, the application of the calibration procedure to a patient with an aneurysm demonstrated the possibility of enhancing the model fidelity, achieving a closer correspondence with information derived from the available image data. The procedure presented in this work has to be tested on a large dataset with the long-term goal of providing accurate and patient-specific analyses, thereby generating a wealth of information that can be integrated to create a reliable Digital Twin with faithful predictive capabilities for assessing the risk of cardiovascular diseases and delivering personalized therapeutic solutions.

Chapter 8

Real-time hemodynamics prediction based on surrogate modeling

In this Chapter, we discuss the outcomes derived from the hemodynamic prediction through surrogate modeling techniques, whose pertinent methodologies have been described in Chapter 5. Emphasis is placed on the leave-one-patient-out cross-validation conducted to achieve real-time simulation results on new unknown patients in an augmented environment easily accessible by the clinicians. Such an environment represents a pivotal component in realising active or semi-active Digital Twins within the healthcare domain. We refrain from delving into the specifics of the segmentation results, as they have been previously disseminated in collaborative works with our esteemed colleagues at the University of Burgundy and the University Hospital of Dijon, France. We mainly focus on evaluating the error of the surrogate models in reproducing new unseen patient-specific geometries and representing the wall pressure and wall shear stress magnitude field. Finally, we explore the limitations inherent the proposed approach as well as potential future developments and improvements.

8.1 Results

8.1.1 Hemodynamic prediction and validation

The performance of the U-Net in segmenting the aortas has previously been assessed by Marin et al. [340], wherein the automatically segmented anatomies were compared to the ground truth geometries achieved through meticulous manual

segmentation. In that case, the evaluative process incorporated metrics, notably the Dice coefficients and the Hausdorff distance.

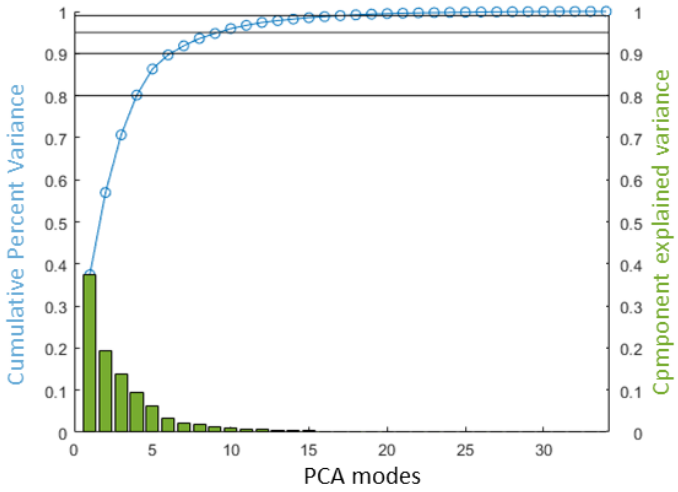

Figure 8.1: The PCA components with the explained variance. The green histogram represents the variance of each PCA shape mode. The blue curve describes the compactness, i.e., the cumulative variance.

Within our research, a comprehensive statistical shape model was established, encapsulating all $n_p = 36$ geometries derived from the dataset. The compactness properties were studied and subsequently a value of N_{POD} for determining the number of bases to use in the POD was derived. The ICP-based rigid registration was performed to subsequently derive the corresponding mapping between the reference template and the set of aortic geometries, paving the way for shape parameter extraction. Notably, during the terminal iteration of the ICP, the most pronounced rigid displacement observed was 0.26 mm. It occurred for only one model in the dataset. The others exhibited displacements in the final iteration below this value. RBF mesh morphing proved efficient in generating different atlases valid for numerical simulation. In the lower dimensional space derived from PCA applied to the 36 discretized aortic models, 80% of the total variability was reached using 4 shape modes, 90% of the variance with 7 shape modes and 95% with 10 shape modes. Remarkably, a comprehensive 99% of the total variance was captured using 19 shape modes, as depicted in Figure 8.1. The first PCA mode accounted for a significant 37% of the total variability. Subsequent modes demonstrated diminishing contributions: 20% by the second, 14% by the third, and 10% by the fourth mode. From a simple visual analysis of Figure 8.2, it is discernible that the first mode

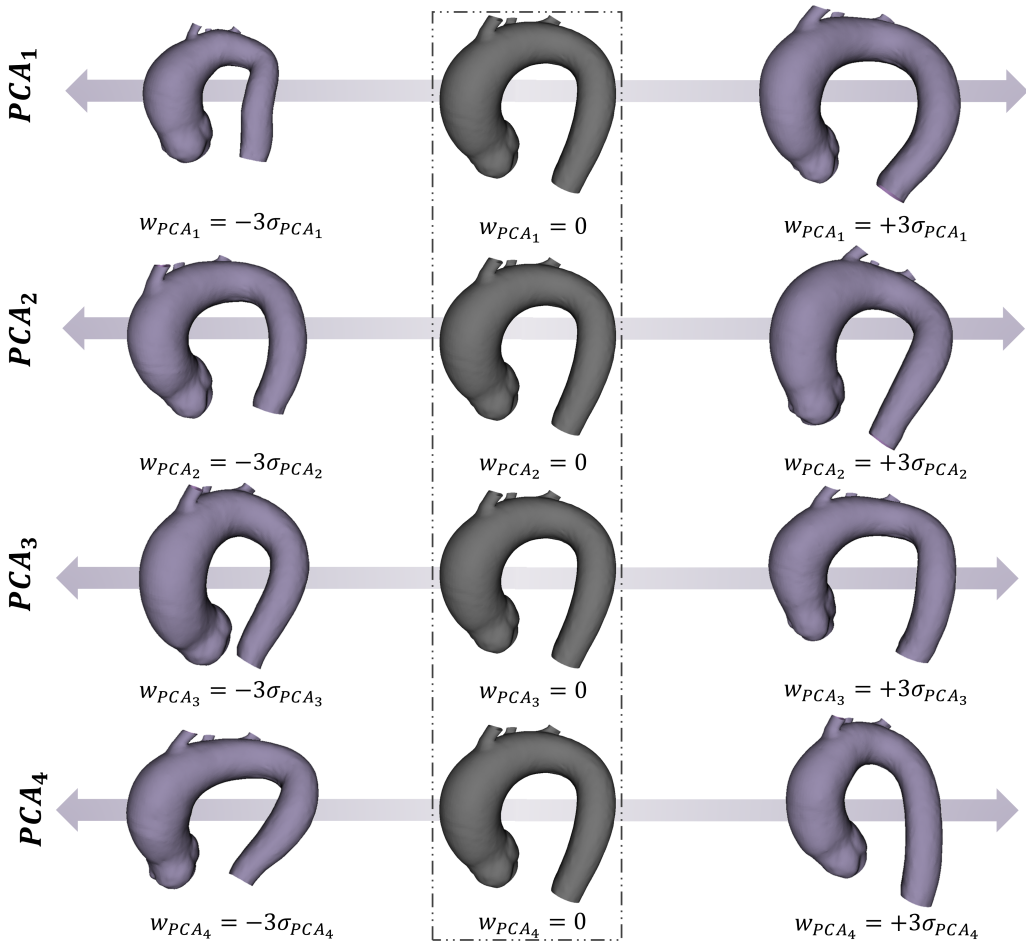

Figure 8.2: Effect of the PCA shape modes 1,2,3 and 4 on the full aorta domain.

was predominantly associated with the overall size of the aorta. The second mode portrays the length variance of the ascending and descending tracts. Mode 3 was related to the amplitude of the aortic arch, effectively modifying the distance between ascending and descending tract. The fourth mode primarily characterizes the angular divergence between the arch and the descending tract. To exploit a surrogate model that accounted for approximately 99% of the shape variability, n_{SM} was set to 19, i.e., 19 geometrical parameters corresponding to the SSM shape coefficients inside the vector $\mathbf{c}$ of eq. 5.1 were used as input for the reduced-order model. Consequently, a comprehensive set of $n_{vp} = 300$ permutations, spanning 19 varied shape modes, were employed to structure the Design of Experiments. This was pivotal in deriving the essential snapshots to construct the ROM.

The generalization ability was directly assessed during the leave-one-patient-

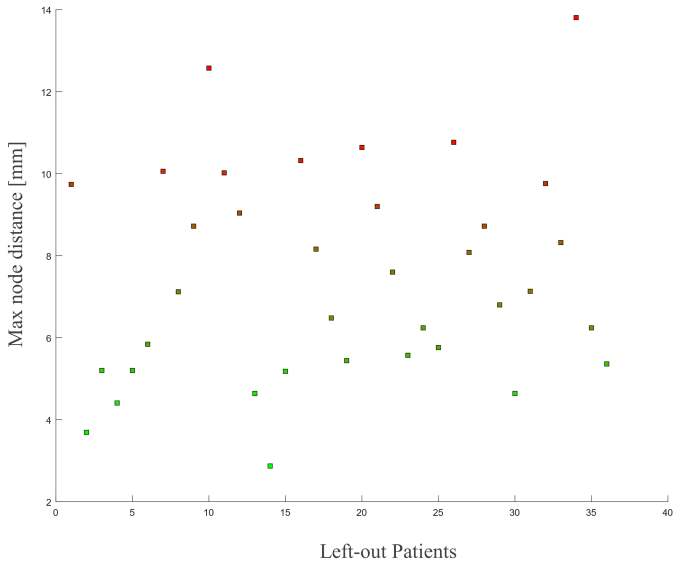

Figure 8.3: Mesh reconstruction error evaluated in terms of maximum Euclidean distance between the nodes of the mesh reconstructed from the PCA sub-space and the corresponding nodes of the original left-out mesh.

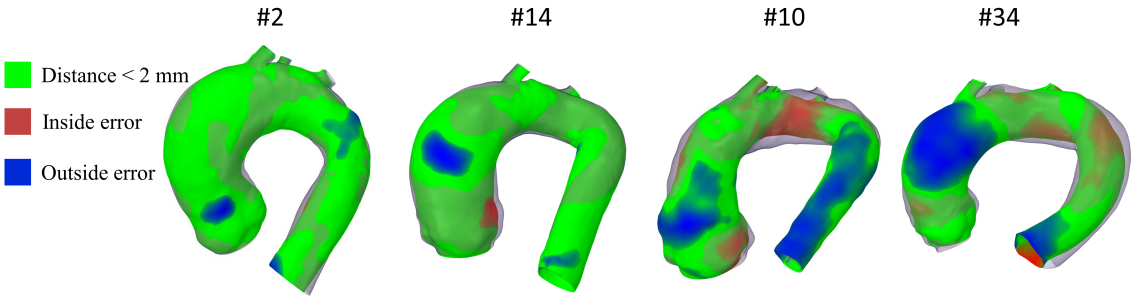

Figure 8.4: Spatial distribution of the error evaluated as distance between corresponding nodes between predicted and original computational meshes for two of the best-predicted cases and two of the worst.

out validation procedure. In this regard, the maximum error in reconstructing each left-out patient through the combination of PCA shape modes was evaluated. We computed the maximum Euclidean distance between corresponding nodes of the original mesh and the reconstructed grid, reported in Figure 8.3. Here, every square denotes a patient, and the colour of each square is related to the inaccuracy. Discrepancies observed spanned from 3 mm to 13.6 mm. For illustrative purposes, two optimally-reconstructed patients (#2 and #14) alongside two patients that posed

challenges for accurate representation by the SSM (#10 and #34) during validation are showcased in Figure 8.4.

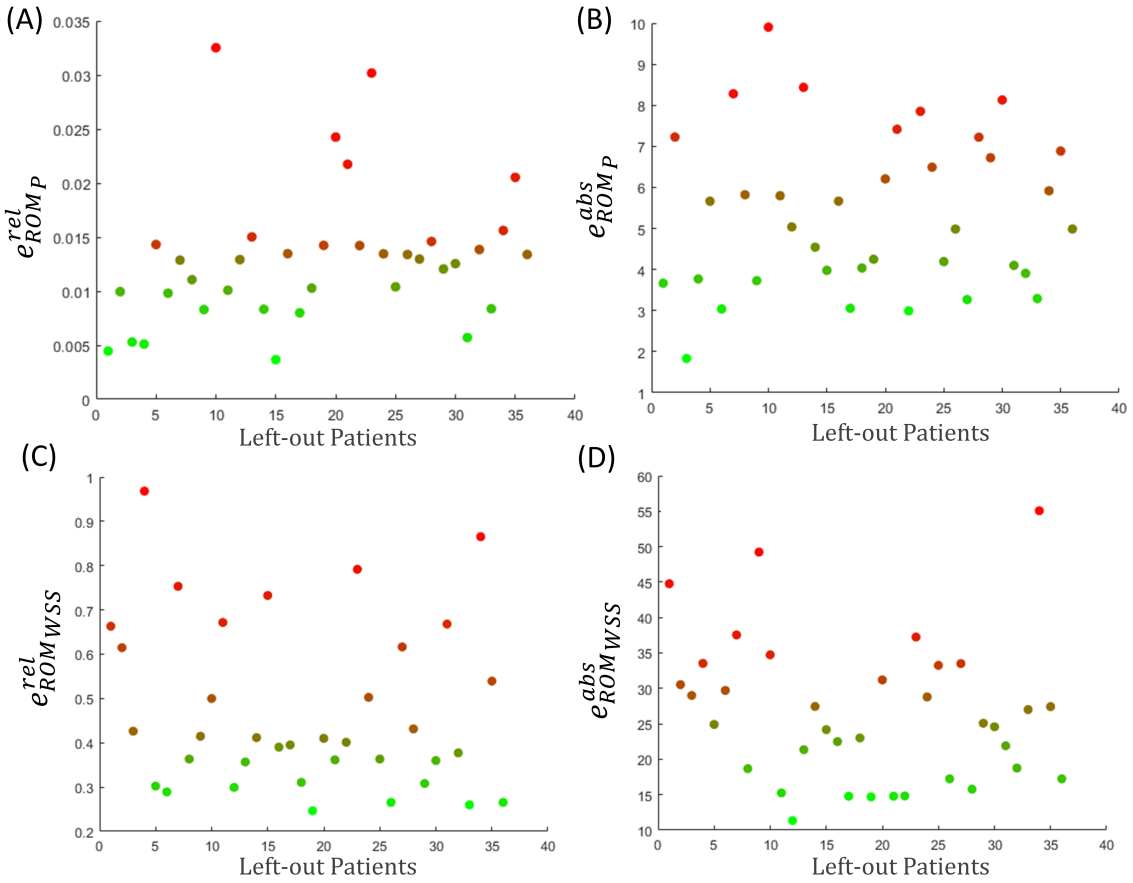

Figure 8.5: (A)-(B) Relative and absolute ROM error related to wall pressure and (C)-(D) wall shear stress for each left-out patient.

All the CFD simulations performed on the atlases were successfully executed until convergence. For cases exhibiting Skewness exceeding 0.95, remeshing was applied and the derived results were mapped onto the aortic wall. As for the shape modes, the assumption on how many physical modes to use in reconstructing the output fields was performed exclusively on the reduced-order model encompassing all $n_p = 36$ patients. $n_{POD_P} = 14$ physical modes were chosen to describe the pressure at the wall. This choice was informed by the observed plateau, approaching an error of approximately 1% in $\epsilon_{POD_P}(\alpha, \beta)$ throughout the leave-one-atlas-out validation process that utilized n_{vp}-1 snapshots. On the other side, during the same validation procedure, the error trajectory $\epsilon_{POD_{WSS}}(\alpha, \beta)$ stabilized at 20% when

employing 21 physical modes. Despite increasing the number of adopted physical modes, no substantial improvements were observed in reproducing the wall shear stress magnitude field.

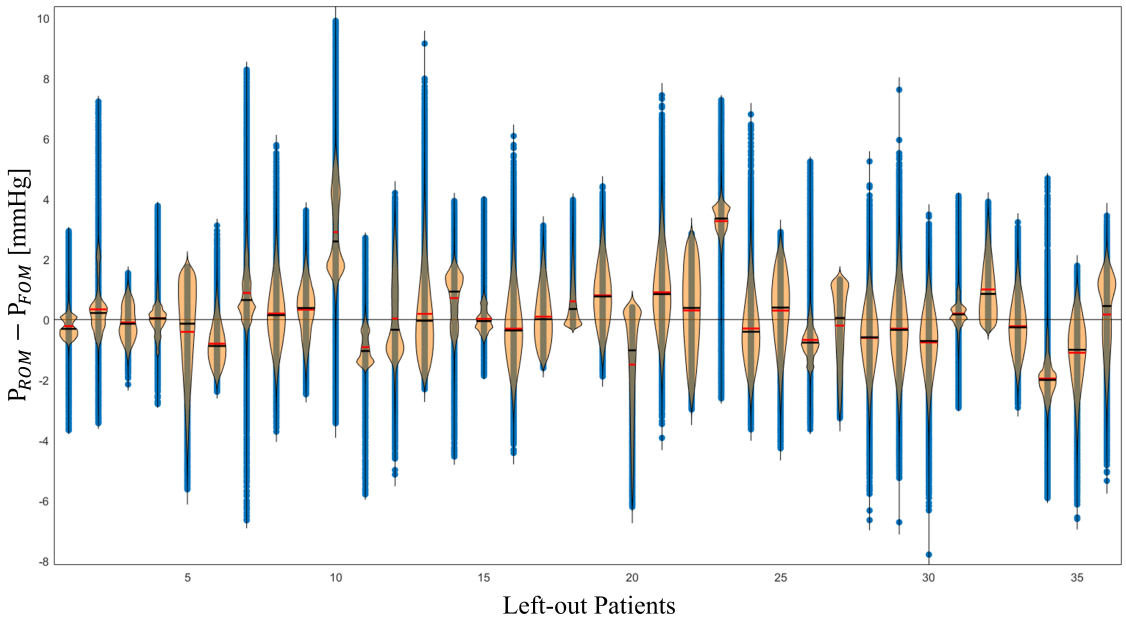

Figure 8.6: Violin plots displaying the wall pressure field reconstruction error during the leave-one-patient-out validation procedure.

The relative ROM error $e^{\text{rel}}_{\text{ROM}}$ and the absolute ROM error $e^{\text{abs}}_{\text{ROM}}$ for both the pressure and the wall shear are reported in Figure 8.5. The normalization based on the FOM field for the relative error $\epsilon_{FOM}(\alpha, \beta)$ allows identifying specific patients where the surrogate model encounters the major difficulties in correctly representing the desired outputs. An average relative ROM error of 1.3% was observed for the pressure, while it reached 42% for the wall shear stress.

In the process of evaluating wall pressure during the validation phase, discrepancies in the representation returned by the surrogate model are illustrated for all omitted patients using violin plots, as seen in Figure 8.6. The results show that the wall pressure prediction of the surrogate model is quite consistent with the high-fidelity FOM simulation results. Notably, the same figure highlights a peak deviation of approximately 10 mmHg. This was detected at a few nodes exclusively for one patient (#10), who concurrently manifested considerable errors in geometric reconstruction. As already performed for the geometrical prediction, two models with low errors (#15 and #31) and two models with high errors (#11 and #23) have been selected

for reporting the contours of the pressure in Figure 8.7. The absolute value of the node-to-node difference in terms of pressure between FOM and ROM is also computed and Bland-Altman plots are reported.

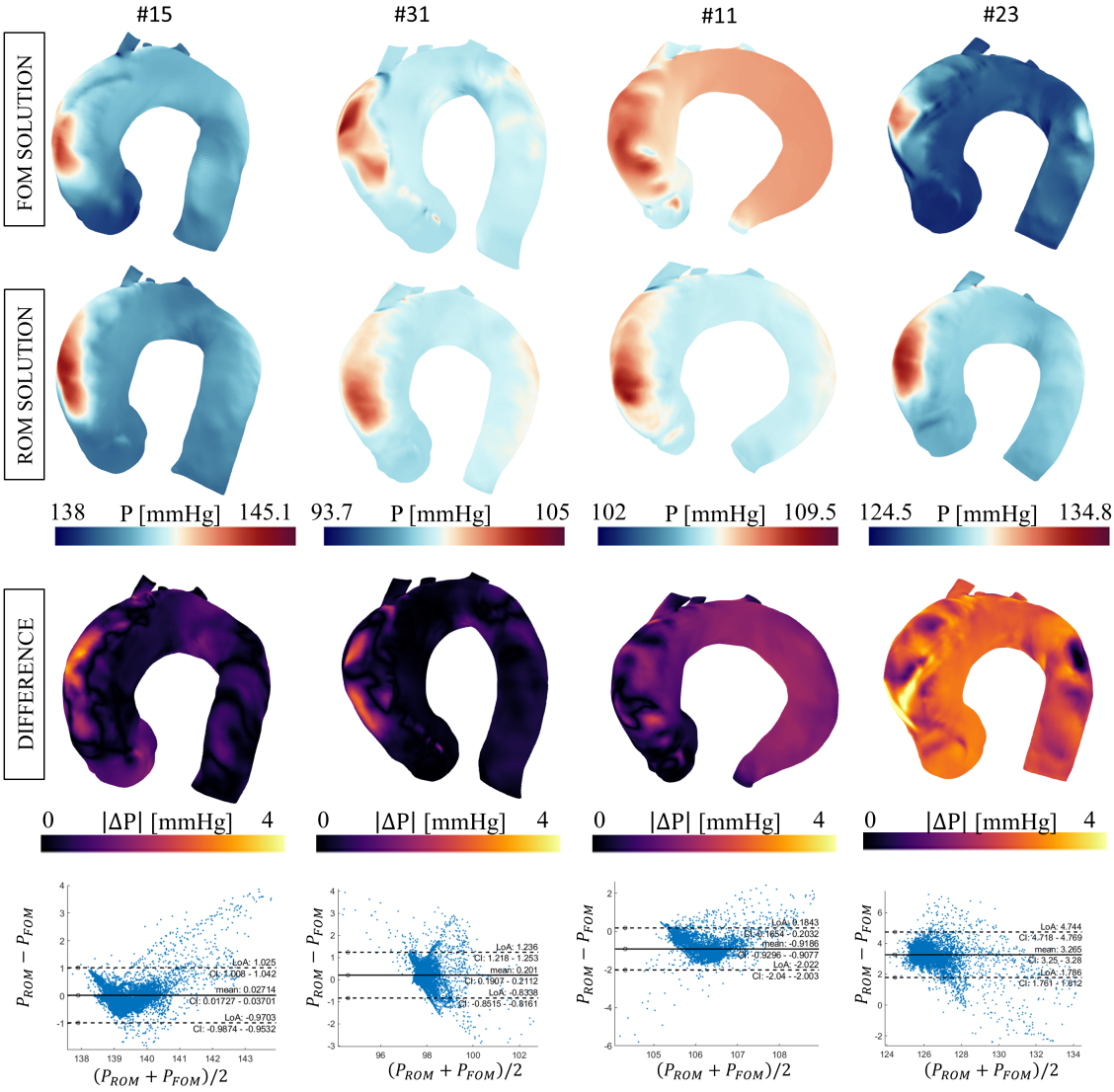

Figure 8.7: Pressure field contours from the FOM simulation (first row), the ROM simulation (second row), absolute value of the difference between FOM and ROM field (third row) and Bland-Altman plots (fourth row) for 4 different patients belonging to the dataset.

The same has been done for the wall shear stress magnitude, as shown in Figure 8.5 (C) and (D). This output parameter exhibited considerably more consistent relative ROM errors when estimating the left-out patient's WSS if compared to pressure output. Figure 8.5 (D) and Figure 8.8, reveal that these discrepancies

reached peak values of approximately 55 Pa. For clarity, two quite good predictions (#19, #26) and two significantly inaccurate reconstructions (#10, #34) are presented in Figure 8.9, inclusive of the absolute differences and the accompanying Bland-Altman plots. Overall, these findings underline the imperative to refine the wall shear stress predictions within the surrogate model, especially if future integration into a real-time responsive Digital Twin framework is envisaged.

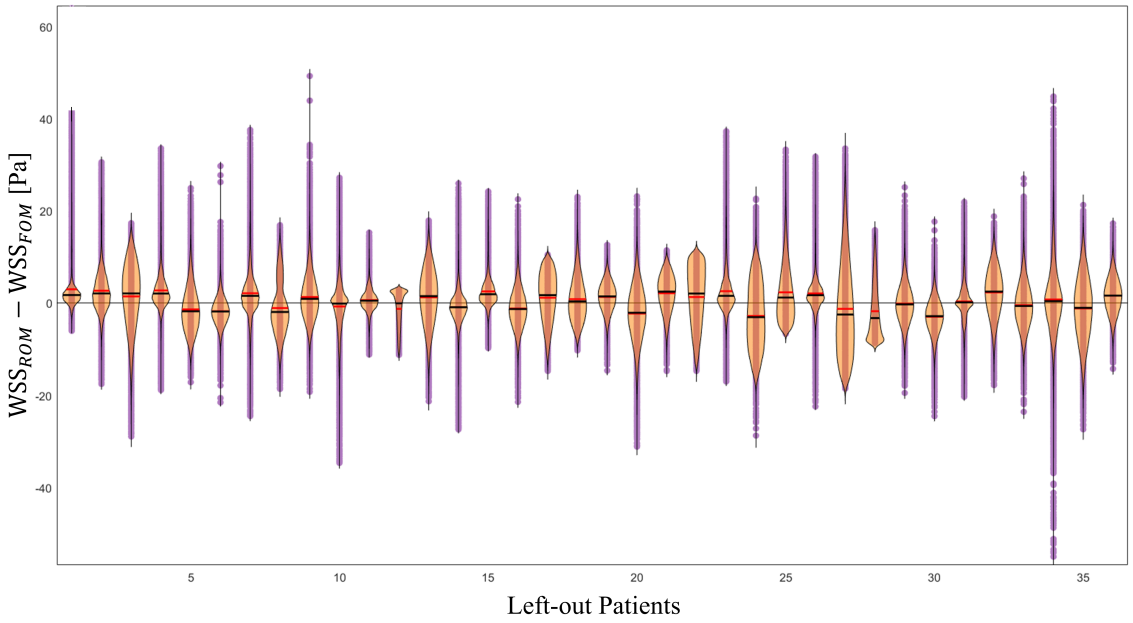

Figure 8.8: Violin plots displaying the wall shear stress magnitude field reconstruction error during the leave-one-patient-out validation procedure.

The computational time required to extract the fluid-dynamic results using the surrogate models based on the non-intrusive ROMs was on the timescale of milliseconds, much less than the approximately 5 minutes demanded to compute the FOM steady-state solution. When navigating the comprehensive process, from the initial medical images to the integration of a 3D model showcasing the desired fields within an augmented reality environment, the alignment phase utilizing the ICP methodology emerged as the most time-intensive part, lasting, in fact, several seconds.

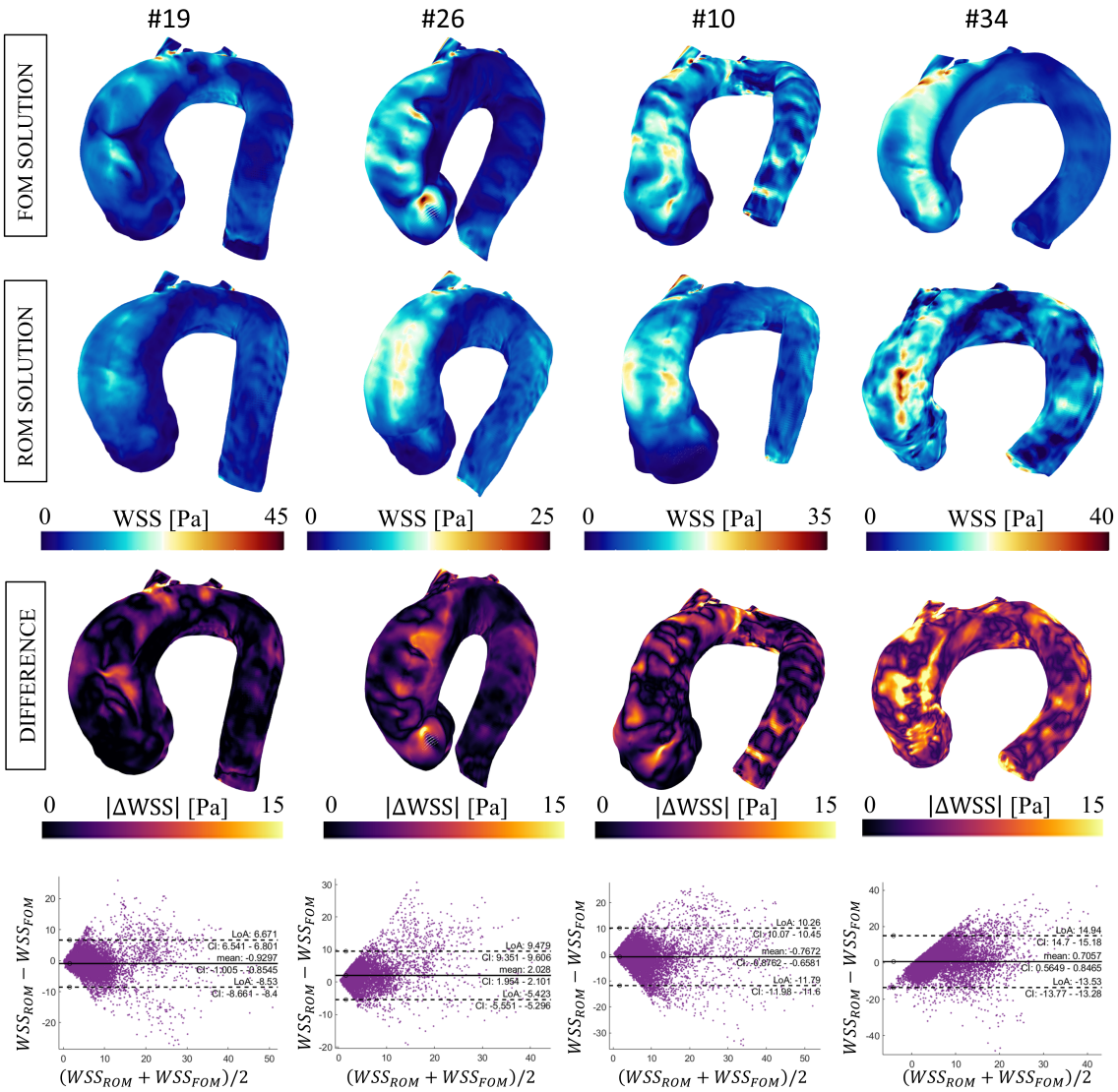

Figure 8.9: wall shear stress magnitude contours from the FOM simulation (first row), the ROM simulation (second row), absolute value of the difference between FOM and ROM field (third row) and Bland-Altman plots (fourth row) for 4 different patients belonging to the dataset.

8.2 Discussion

8.2.1 Hemodynamic prediction and validation

Several studies have investigated the fundamental contribution that CFD could provide to evaluating the thoracic aorta hemodynamics [403]. However,the adoption of this technique in clinical practice remains limited, predominantly owing to the

prohibitive computational expenses previously detailed. The research presented herein delineates a methodology for rapidly deriving hemodynamic insights from two surrogate thoracic aorta models. This was accomplished by an innovative fusion of deep-learning segmentations, mesh morphing techniques, statistical shape modelling, computational fluid-dynamics and model order reduction. We successfully proposed a combination of methods that streamline and expedite the process of transitioning from clinical images to patient-specific hemodynamic assessments. The meta-models based on non-intrusive reduced-order models allow for a quick prediction of the numerical simulation results, enabling one of the fundamental prerequisite for creating active or semi-active Digital Twins. Surrogate modeling can contribute to studying the dynamics of the aneurysm growth and, if properly validated, making predictions to support decision-making in a clinical environment. Compared to the work proposed in literature [334, 339], we built a comprehensive pipeline to augment medical image information in a single environment and proposed a cross-validation method based on patient exclusion.

The displacement returned from the last iteration of the ICP indicated the achievement of a good alignment of the anatomical models $\left\{\mathbf{\Lambda}^i\right\}_{i=1,...,n_p}$ with the computed template. To train the underlying reduced-order model with CFD-derived results, we constructed an exhaustive dataset by prompting the statistical shape model to synthesize novel virtual patients, rooted in authentic patient-specific geometries. When compared to optimal space-filling approaches, the proposed method for extracting samples from the PCA space allowed generating atlases with modal coefficients resided within the confines determined by the n_{SM}-dimensional polyhedron identified by the minimum and maximum component of the vector $\mathbf{c}_j$ with $j = 1, ..., n_{SM}$, thus reducing the presence of limit configurations with particularly complex and likely unrealistic anatomies. Nonetheless, this approach had a drawback; it restricted the capacity of the model to faithfully recreate exceptionally atypical shapes situated beyond the modal space identified by the available shape coefficients. It is worth noting how the SSM constructed here for the entire thoracic aorta requires fewer modes to capture 99% of the represented variability. This contrasts with the SSM described in Chapter 6, Section 6.1.3, exclusive for the ascending aorta part. The rationale for this disparity stemmed from the more pronounced smoothing implemented in conjunction with 4D flow-derived segmentations. Consequently, the surface anomalies prevalent in the aortic walls, identified by the upper-frequency modes within the PCA spectrum, were here attenuated.

During the leave-one-patient-out validation, the previously created SSM is queried

to represent the grid of the omitted patient. Once the shape coefficients are obtained through least squares fitting, the mean template is tailored to align to the new input anatomy, and the error quantified by the node-to-node distance is returned. Typically, patients with more complex geometric reconstructions resulting in higher errors correspond to more peculiar and non-standard anatomical features. A decision boundary, defined by a specific distance value, could be identified for systematic error evaluation. If the resultant distance remains below this demarcation, the solution derived from the ROM is accepted. Conversely, if this criterion is not met, an alert prompts the recommendation of computing a new FOM simulation through high performance computing (HPC) strategies. The unknown iso-topological model in input obtained through morphing could then be included in the calculation of a new enriched SSM. Subsequent recalculations would then necessitate the extraction of updated PCA and POD components. Any following simulations would thus benefit from the incorporation of information harvested from this newly integrated model within the dataset.

Meta-modeling techniques proved quite robust in reproducing the pressure field, while higher errors were reported for the WSS magnitude, as highlighted in Figure 8.5 (C) and (D). The surrogate models exhibit reduced precision when addressing flow characteristics possessing high spatial gradients, such as the wall shear stress, compared to output parameters that are more uniformly smoothed across the domain, like pressure. Probably, outcomes like the time-averaged wall shear stress derived from transient simulations, being averaged over all cardiac phases and therefore yielding reduced spatial heterogeneity [404], would have resulted in lower errors compared to the individual peak systolic wall shear stress. On wall pressure side, the maximum prediction discrepancies occurred for patients for which the shape reconstruction error was high or with a particularly curved shape or constricted areas culminating in pronounced pressure gradient zones that the ROM was unable to accurately represent, as shown in Figure 8.7 for patient #11 and #23. In particular, patient #11 exhibits a narrowing at the end of the descending aortic segment, while patient #23 reveals it within the Valsalva sinuses area. In case of good agreement between predicted and real hemodynamics, the Bland-Altman plot should return a mean error around zero. Conversely, for the aforementioned cases, the zero deviation value either is close to or even outside the envelope defined by 1.96 times the standard error deviation. Turning our attention to wall shear stress, from Figure 8.9, we can observe how the surrogate model tends to smooth out the WSS fluctuations compared with the FOM ground truth. It seems that high-frequency components of the output are partially

trimmed off when interpolating through the relations learned by the Response Surface method, as discussed by Du et al. [339]. Patients #10 and #34 are two examples of models with high wall shear stress prediction errors. Specifically, patient #10 exhibited a higher deviation due to the geometric reconstruction, stemming from a particularly complex shape of the ascending section. Patient #34, on the other hand, had a localized surface reconstruction that highly differed from the excluded original model. These localized characteristics led to significant variations in wall shear stress. Thus, future endeavours focused on increasing the precision should place particular attention on the wall shear stress prediction.

In our analysis, the principal sources of discrepancy in the surrogate model are likely rooted in registration, shape and output field decomposition (POD) and interpolation. The registration error can be assumed relatively low if considering the convergence of the ICP. The techniques in reconstructing correspondences amongst anatomical models are also considered to be robust, primarily due to our employment of mesh morphing algorithms grounded in the employment of pseudo-landmarks. This ensures a consistent anatomical alignment between disparate geometries. The second contribution to the error originates from the reduction in the number of shape parameters from the SSM and the POD for calculating the pressure and shear stress fields. In any case, we selected 19 shape mode bases as it provided a cumulative shape variability of 99% across all n_p cases in the full ROM. 14 and 21 bases were instead used for the results. We chose 300 snapshots for creating the ROM because this was the number needed to reach a plateau in terms of error. However, uncertainty is introduced due to the choice of modes based on the 36 patients. A more accurate selection for each surrogate model created with 35 patients during the validation should be carried out because a different number of shape modes might be needed to capture 99% of shape variability and a different number of physical modes may be required in reaching a stable reduction error plateau when constructing the ROM for pressure and wall shear stress. In [405], 35 shape modes were required to approximate 99% of the variance of the SSM. However, they considered the variability introduced by including patient-specific superior branches that were not visible using 4D flow MRI in our work. Finally, the ROM interpolation based on the Response Surface brings the last contribution to the error. Indeed, extracting the results from the ROM reconstruction far from the points used to build the Response Surface introduces discrepancies due to interpolation. We used a Response Surface technique to re-create the wall pressure and shear stress magnitude fields. It could be replaced by other interpolation methods such as RBF or neural network interpolations [406]. A deeper

exploration into these interpolation inaccuracies, juxtaposing the aforementioned techniques, is crucial before committing to a particular interpolator for clinical deployment.

Through our established workflow, we have pioneered a pathway to achieve real-time simulation outcomes within clinical contexts, predominantly leveraging the online phase of the ROM consumption. Notably, the bulk of computational intensiveness is anchored in the preceding offline phase dedicated to surrogate model formulation and generation.

We deliberately abstained from a clinical validation using patient-specific hemodynamic data, conscious of the strong assumptions embedded within our work, necessitating further data for a rigorous model producing accurate clinical results. For instance, we included the superior branches with an artificial trick since they were not visible from the dataset employed. An authentic representation of their shape and associated blood flow remains imperative for emulating patient-specific hemodynamic conditions. Of course, it is pertinent to highlight that the rigid-wall assumption we did tends to overestimate wall pressure and WSS, as discussed in [128, 407]. Nevertheless, the outcomes of the current study should remain unaffected by this factor, as our primary objective here was to assess the variability of the output parameters across full-order and reduced-order techniques.

Further investigations remain imperative to elucidate the intricate interplay between aortic anatomy, wall properties, hemodynamic patterns and phenomena like aneurysm expansion or rupture. A holistic prognostic framework, potentially encompassing shape parameters, medical imaging insights, and simulation-derived physical outputs, could significantly elevate our predictive ability concerning the progression of the pathology.

Accurately identifying which patients with AsAA will require surgery within a specific timeframe would refine the risk-benefit analyses and the definition of surveillance protocols. A slow-growing ascending aortic aneurysm, in fact, might not necessitate the rigorous oversight essential for more aggressively expanding counterparts.

The methodology delineated herein, primarily focused on predicting the ascending aortic aneurysm hemodynamics, boasts of adaptability across multiple biological structures or organs, assuming that surface registration between varied domain forms is feasible and pertinent statistical shape models are procurable. In particular, we firmly believe that the proposed approach can be applied to several vascular structures derived from medical images, such as the abdominal aorta, the carotid

artery or the pulmonary artery.

8.2.2 Limitations and future works

Several assumptions were made and limited the accuracy of the proposed models. The presented pipeline is only applied for deriving steady-state fluid-dynamic outputs. On image segmentation side, as discussed in [340], the deep learning method needs to be refined for the other cardiac phases for which the information contained in the images is more difficult to extrapolate. In fact, during the systolic peak phase, the 4D flow presents an optimal signal-to-noise ratio, thereby enhancing the efficacy of the U-net algorithm. Moving to a transient regime, time-varying simulations have the advantage of providing more valuable information, potentially even time-averaged data across the cardiac cycle, such as time-averaged wall shear stress. For scenarios encompassing transient flows, a recurrent neural network (RNN) could be implemented to create a surrogate model able to perform the prediction of several time steps spanning the full cardiac cycle [408]. RNNs are a class of neural networks specifically designed to manage sequential data such as time series. In this regard, additional variables should be included for the lumped fluid dynamic outlet parameters, thereby going beyond the reliance only on the currently employed resistance in computing the set of steady-state results. Nonetheless, incorporating parameters as outputs in the Windkessel model augments the parameter domain, inevitably requiring more simulations in the Design of Experiments. In this work, we modeled then the Windkessel behaviour by considering only a partition of the flow based on its percentage distribution while calibrating the resistances in alignment with these specific percentages. Incorporating additional parameters could provide the flexibility to more extensively modify the ROM results once the patient-specific geometry was obtained based on various simulated fluid-dynamic conditions. Such adaptability is paramount in the development of Digital Twins designed to swiftly adapt to nuanced changes in the foundational physical model. In upcoming simulations of the blood flow in the ascending domain, especially those of a transient nature, the introduction of turbulence models is imperative [409]. Different patient-specific Reynolds numbers will lead to completely dissimilar behaviours of the blood flow. When the Reynolds number reaches approximately 2000, the smooth flow experiences a transition from laminar to turbulent, and this turbulence becomes fully established in the aorta. To further refine the representation, it is essential to incorporate additional parameters that cater to the spectrum of flow conditions observed within our study cohort, ranging from highly laminar to distinctly turbulent

flow states. This is particularly relevant for hypothetical scenarios wherein the presence of aortic stenosis accentuates the turbulent behavior of the flow [410]. In constructing the statistical shape model, it would also be necessary to consider additional geometric variabilities, mainly related to the aortic valve, as well as the presence of alterations in the supra-aortic vessels, such as the bovine arch. Shape modes derived from the valve could be integrated as supplementary input parameters for the surrogate models [400], offering accurate control over the valve type and condition. However, in our current analysis, the incorporation of the valve was infeasible given that the 4D flow MRI resolution that did not provide discernible valve shapes across individual patients.

Lastly, given that 4D flow MRI offers insights spanning the entire cardiac cycle, we believe that there exists a potential to establish and fine-tune fluid-structure interaction models to delve deeper into the biomechanical attributes of the vessel wall. Beyond this, the scope extends to the integration of input parameters into advanced surrogate models that encapsulate properties like wall rigidity and thickness. A Digital Twin capable of predicting the vessel rupture requires, in fact, knowledge of patient-specific material properties, which in living systems typically evolve over time and can be estimated by analyzing the deformation of the wall captured from the images.

8.3 Findings and remarks

In this research, we introduce advanced meta-modeling strategies aimed at predicting hemodynamics within the aortic vessel lumen. The surrogate model is constructed based on geometry-informed snapshots and non-intrusive reduced-order modelling. Using surface registration methods combined with geometric decomposition and mesh morphing techniques establishes a correspondence between the reference template and target model to be simulated, offering a way to parameterize the shape.

Following this, a surrogate model based on non-intrusive model order reduction techniques is developed through proper orthogonal decomposition applied to the geometry-informed physical snapshots. The Response Surface method is applied to interpolate and predict the reduced physical coefficients to reconstruct specific hemodynamic outcomes from the reduced-order model based on the geometric parameters corresponding to shape coefficients and the physical parameters related to the inlet velocity and output flow resistance.

A validation procedure concerning the wall pressure and wall shear stress magni-

tude predictions at the systolic peak has been described. The findings demonstrate the surrogate model's ability to reproduce the wall pressure. However, they also shed light on inherent complexities and challenges when attempting to emulate more complex fields, such as wall shear stress.

Part IV

Conclusions

Chapter 9

Conclusions

Future precision medicine is likely to be built upon the concept of Digital Twin, which involves the dynamic integration and augmentation of patient data through a combination of computational and statistical models. The potential transformation of cardiovascular healthcare through the incorporation of Digital Twins represents both an ambitious goal and an emerging reality. The research for the development of a Digital Twin is progressing rapidly, but the various fragmented aspects for the construction of a virtual replica of organs like the aorta still require further in-depth analysis. This thesis has delved deep into the challenges of realizing this vision, with specific attention to the thoracic aorta and the associated risks of ascending aortic aneurysms.

In this work, all difficulties of correctly predicting the evolution of the disease and the consequences of the treatment approaches have been highlighted. Digital Twins should ideally be able to incorporate sparse longitudinal clinical data to update their structure and remain predictive during a consistent time interval of the patient's life. These features (real-time results assessment and new data integration) are core attributes that distinguish Digital Twins from conventional patient-specific models. Thus, one of the most important aspects in creating a Digital Twin of a human organ as the aorta is to enable the virtual replica to accurately represent the patient-specific anatomy during the months of follow-up. To address this, we have introduced a set of methods for estimating the growth risk and the patient-specific growth rate, enabling physicians to predict the potential progression of the condition over the months and estimate the associated risk. By relying on statistical shape modeling techniques and consistently incorporating data for parameter refinement and correction, it would be feasible to have a computational model capable of tracking a patient over multiple months. This would ensure the ongoing extraction of shape

parameters essential for assessing the risk of potentially severe associated events. However, growth prediction methods were developed only for the ascending portion of the aorta, disregarding the significance of encompassing the complete anatomy of the considered patient. Integrating artificial intelligence and machine learning techniques could also be explored to continuously refine and optimize the Digital Twin's predictive capabilities. These models could aid physicians in assessing the risk of aneurysm growth and rupture more accurately than traditional methods based only on the diameter measurements. However, it is essential to note that this work has presented an approach for predicting growth rate values rather than extracting a complete computational model of an aneurysm at known temporal distances. Taking this further step and integrating the Digital Twin into clinical practice, healthcare providers could stratify patients based on their individualized risk profiles, enabling more personalized treatment strategies. Furthermore, the deployment of a twin that is compliant with regulations should require addressing uncertainties. Uncertainty quantification techniques about the possible evolution of the pathology should be integrated to account for variations in input parameters, ensuring that the twin predictions encompass a realistic range of outcomes, for example, of possible shape deformations during the possible future evolution.

The core of an excellent and well-constructed Digital Twin based on data-driven reduced-order models will lie in the accuracy of the underlying data. Numerical simulation approaches were investigated to assess the biomechanical and hemodynamic behaviours of the thoracic aorta. We focused on computational solid mechanics and fluid-structure interaction analysis that require a calibration of the structural boundary conditions at the wall to correctly represent the kinematics of the vessel. The fundamental new contribution from this thesis lies in introducing a workflow to increase the model fidelity in representing the aortic kinematics by incorporating annulus motion effects, aortic interaction with soft tissue and the spine and introducing wall pre-stress calculation through an inverse analysis to obtain the zero-pressure geometry. The calibration procedure is performed by optimizing the parameters managing the Robin boundary conditions using the Levenberg-Marquardt algorithm, trying to maximize the correspondence between the splines derived from 2D cine-MRI sequences of the aorta throughout the cardiac cycle and the same splines obtained from the dynamic computational model. High-fidelity fluid-structure interaction analysis was implemented only for a single patient due to its computational complexity. It is evident that this method should be extended to a cohort for creating a Digital Twin. However, the practicality of implementing high-fidelity simulations for

larger patient cohorts calls for robust computational infrastructures. However, it is clear that the Digital Twin's ability to provide accurate information about potential rupture will depend on the accuracy of the underlying biomechanical models.

In developing clinical applications, the interaction between the clinicians and the Digital Twin would be facilitated by the rapid assessment of the desired clinical outcomes. A first constraint in integrating computational fluid-dynamics into the clinical practice concerns the excessive laboriousness and level of technical expertise required to prepare and run the model and the related significant computational time needed. Limited research has focused on reduced-order models derived from 3D aortic simulations and only a few studies have employed non-intrusive model order reduction techniques to yield hemodynamic parameters. When testing and validating a surrogate model in predicting hemodynamic variables in almost real-time, a trade-off between complexity and accuracy should be established. For these reasons, in our work, we moved from time-variant fluid-structure interaction analysis to steady-state computational fluid-dynamics simulation at the peak systolic phase based on the rigid wall assumption. In literature, a huge variability in CFD modeling of large arteries is discussed. A strategy involving the use of reduced-order models in an augmented environment has been suggested as an alternative to complex 3D simulations. They were derived from 3D clinical outcomes using an initial cohort of 36 patients. The proposed surrogate model was created through in-vivo data, proving that these methods in future could be applied in clinical environments after improvements and additional validations based on larger and more accurate dataset. In fact, the current poor reliability of the blood flow simulation outcomes depends on the simplified modeling assumptions made and further validations of numerical results with clinical data are still needed. Using the surrogate model, simulation results could be assessed in a few seconds for a specific combination of the input shape modes and for desired fluid-dynamic boundary conditions. Thus, the surrogate model enables the evaluation of the impact of different clinical situations, such as a change in the input cardiac jet velocity or a variation in the output flow resistances. A good correspondence between the wall pressure results of the surrogate model and the full-order simulations was achieved at the systolic phase. The results were not as good in terms of wall shear stress due to the high spatial variability of this output. As technology evolves, refining this balance between accuracy and speed will be instrumental. An in-depth exploration could be undertaken to evaluate the impact of wall motion by incorporating an accurate material model that considers different material-related parameters as input of the surrogate model, in conjunction

with the proposed fluid model. However, basing such validation on fluid-structure transient models would involve a high usage of computational resources for which supercomputers should be strictly required.

The integration of the Digital Twin into the healthcare system could lead to a paradigm shift in how cardiovascular diseases are managed. Digital Twins can trigger the transition from a reactive approach, where interventions are primarily determined by size thresholds and measured parameters, to a proactive approach based on accurate outcome predictions driven by data-rich insights. These methodological challenges posed and still represent a significant obstacle in employing AI for inductive reasoning. For instance, ensuring the applicability of findings required external validation using new patient groups, cohorts from various centres or geographical areas and multiple assessments of the robustness of the models. Ethical considerations, data privacy management and effective communication between technical experts and clinicians become critical aspects of this type of integration. In fact, besides the technical challenges, additional practical challenges, like privacy, legal ramifications, accountability and data-sharing protocols should be considered. To date, ethical, technical and financial constraints still limit the huge data acquisition needed to assist clinical decision-making [411]. The European General Data Protection Regulation (GDPR) has introduced new legal obligations, including the right to revoke consent and the right to have confidential information erased. This has sparked debates concerning the potential expenses and practicability of enforcement. Any Digital Twin solution containing sufficient data for patient identification must diligently adhere to these regulations, which also apply to historical retrospective data [412]. The complexity inherent in aggregating, refining and expanding databases to support the implementation of an interactive DTs for routine clinical decision-making can influence the preference for submitting regulatory applications focused on less complex, passive models grounded in twinning principles. Despite variations in the objectives, costs, timelines and perceived rigor associated with regulatory approval processes across different countries or regions, it is noteworthy that products employing personalized computational models for the purpose of procedure planning are currently accessible in the market. In addition, information systems and electronic health records are highly fragmented, heterogeneous and difficult to interoperate. Clinical information is stored in unstructured formats and its extraction needs either manual work or further research efforts of automation [143].

One of the hurdles in the adoption process involves enhancing the clarity regarding the evidence underpinning the creation and validation of a Digital Twin solution

used to assist in treatment decisions or prognostic assessments. To tackle these challenges, a close collaboration between clinical, scientific, industrial and regulatory departments is needed.

Building upon the achievements of this work, further research could delve into enhancing the precision and predictive capabilities of the Digital Twin model for ascending aortic aneurysms.

9.1 Future directions

The first potential area of exploration is the refinement and expansion of the predictive models. The current study showcases the efficacy of shape features in predicting aneurysm growth risk. We are currently working to incorporate a wider range of patient-specific data, including genetic markers and hemodynamic parameters, to create more comprehensive and accurate predictive models.

Future research could extend the model fidelity by incorporating even finer details, such as accurate patient-specific blood flow dynamics and variations in vessel wall properties and perform predictive studies not only of growth but also of rupture. These advancements could provide a more realistic representation of the complex interactions between fluid and structure. Another significant emphasis lies in directing research towards developing user-friendly and intuitive methods for non-technical end-users to engage with Digital Twin-based systems within their respective domains [413]. New visualization techniques through which individuals without expertise can interact with AI-generated information about the physical twin within a mirrored, networked system, should be explored. Advanced augmented reality, multidimensional holographic projections and 3D avatars are available methods to reach this goal [414]. Furthermore, the challenge of real-time simulation accuracy presents innovative research opportunities. Investigating alternative model reduction techniques and exploring the integration of real-time medical imaging data could potentially bridge the gap between simulation time and accuracy, enabling real-time monitoring and prediction. Finally, considering the evolving landscape of healthcare technology, there is scope for structuring the extension created in 3D Slicer and developing user-friendly interfaces that translate the sophisticated model outputs into clinical information for the medical experts.

Overall, we tackled several of the challenges in realizing Digital Twins for clinical applications, prioritizing follow-up capabilities, accuracy and real-time interaction. Unfortunately, the majority of the data needed are usually unavailable due to the

difficulty of making in-vivo flow measurements or because some data can only be assessed through invasive procedures. Several research perspectives can be foreseen following the present work outcomes. Firstly, it is evident that it is necessary to consider not only physiological but also anatomical aspects when assessing the risk of progression of conditions such as aortic aneurysms. Furthermore, it has been demonstrated that parameter tuning is feasible to ensure that the vessel reproduces the real behavior derived from the images at the best. Lastly, a validation procedure highlighted the strengths and weaknesses of a surrogate model based on reduced-order models for real-time assessment of relevant fluid dynamic outputs.

By integrating information derived from wearable devices as well, future research will aim to merge all the aspects studied separately in this work into the development of a full-fledged Digital Twin for the patient's follow-up, capable of extracting real-time anatomical, hemodynamic and biomechanical biomarkers predictive of aortic aneurysm growth and, ideally, rupture. The potential lies not just in diagnosing and understanding diseases but in forecasting patient-specific responses and charting optimal therapeutic pathways. This shift from descriptive to predictive healthcare is monumental and will undoubtedly reshape clinical strategies.

Appendix A

Appendix A

A.1 The 3D Slicer Extension

Applications based on medical images involve complex software systems that require a shared foundation of core functionalities coupled with the capability to be tailored to particular clinical uses. In a research environment, there is frequently a need to use prototypes that facilitate the exploration and enhancement of novel algorithms or concepts within the framework of a fully operational end-user application.

In this regard, several methods described in this manuscript were developed in 3D Slicer. 3D Slicer is an open-source software available across multiple platforms, including Linux, Windows, and MacOSX (http://www.slicer.org). The wide range of capabilities, extensibility, cross-platform compatibility, and open software license are key attributes that set 3D Slicer apart from both commercial tools. Developed over the course of two decades with the support of the National Institutes of Health and contributions from numerous institutes worldwide, this software is designed to display and manipulate imaging data of various types such as MRI CT scans. It is specifically tailored for medical image analysis and visualization, encompassing features like registration, interactive segmentation tools and volume rendering.

3D Slicer is both contributive and extensible, offering a robust plugin capability for adding new applications. It provides easy access to libraries like ITK and VTK (http://www.vtk.org) and allows for the development of fully interactive custom interfaces in either C++ or Python.

For the purpose of this work, a comprehensive extension was developed in 3D Slicer. Its development was carried out following the clinicians' requests from the university hospitals of Rennes and Dijon, France. This extension has been tested on 3D Slicer versions 4.13, 5.1 and 5.3 for both Windows and macOS. It consisted of three

modules. The first focused on model segmentation and local shape feature extraction. The second dealt with the statistical shape models, allowing the computation of the global shape features, while the third exploited the surrogate modeling techniques to augment medical images with results derived from numerical simulation. Through this extension, the user could easily upload the DICOM images of the patient and extract additional outcomes to perform analysis and prediction through a few steps and in a reduced time.

The semi-automatic segmentation method introduced in Sections 3.2.2 was implemented within the 3D Slicer environment (Figure A.1). In this regard, a specific extension was created to extract from both CT-scan and MRI angiographies the anatomical model of the aorta. The automatic method partially discussed in Section 5.2.2 was later introduced in 3D Slicer, thus allowing the possibility of also deriving the geometry of the aorta from 4D flow MRI. From these segmentations, some manual post-processing steps could be required. In this regard, the option to manually modify portions of the aortic geometry or trim unwanted parts of the aorta was incorporated, integrating functions already implemented by other modules within 3D Slicer. Of course, the option to save the realized segmentations and load them later without starting from scratch had been implemented.

Figure A.1: Segmented model using the tailor-made 3D Slicer extension.

The centerline computation and the geometric decomposition described in Section 3.2.3 were performed using the first module of the 3D Slicer extension. This allowed

the user to visualize a report table containing the local shape features values and other distinctive information related to the patient's ascending aorta, as shown in Figure A.2. The ability to generate an Excel file was established, which included the trend of mean and maximum diameter along the centerline and all data from geometric decomposition; this also included storing specific screenshots of the anatomical model. The analysis of each aortic model thus became simple and rapid, and even the medical staff was able to extract information with very few interactions by means of the dedicated user interface.

Figure A.2: Execution of shape analysis and automatic extraction of local shape features using the 3D Slicer extension.

The second module of the extension, on the other hand, was related to the rigid registration of models and shape analysis based on statistical shape modeling. The iterative closest point algorithm was configured to align new segmentations performed or imported with known templates (Figure A.3). Within the same module, mesh morphing libraries were also integrated to adapt the statistical shape model template of the ascending aorta or, in general, of the thoracic aorta to the aligned segmented models using the Source Points sampled from the created splines. When importing the statistical shape model, the deformations defined by the modal components derived from the principal component analysis were loaded into the extension, thus ensuring the ability to observe the effect of modes on the aortic template, as displayed in Figure A.4. The same module allowed to perform the least square fitting of the

statistical shape model for reproducing the computational mesh using the PCA bases, as described in Section 5.2.9.

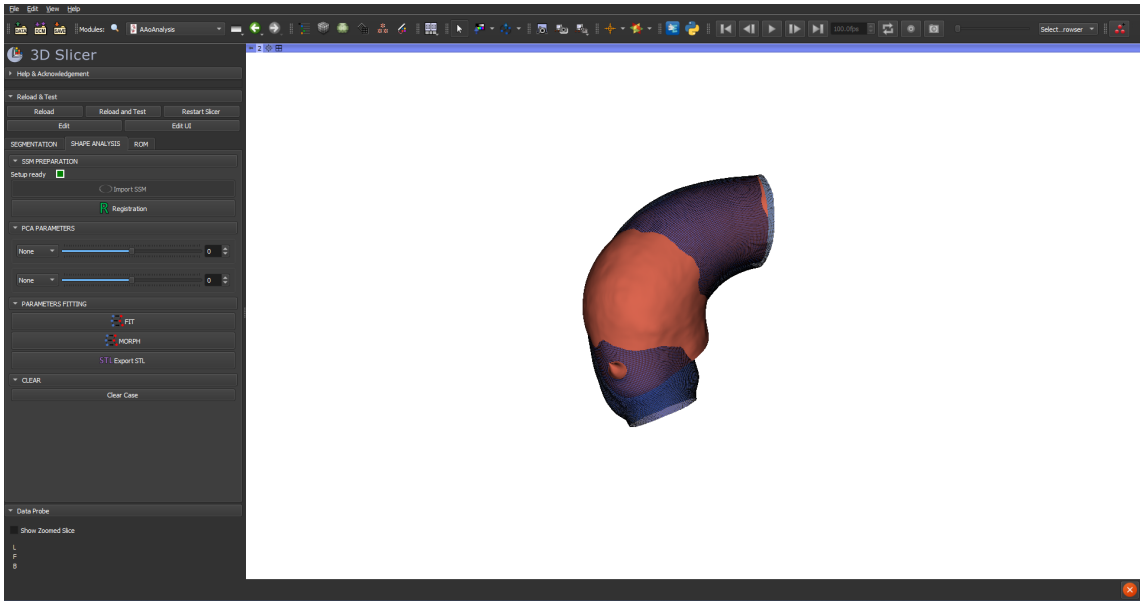

Figure A.3: Ascending aortic aneurysm shape aligned to the statistical shape model template through iterative closest point.

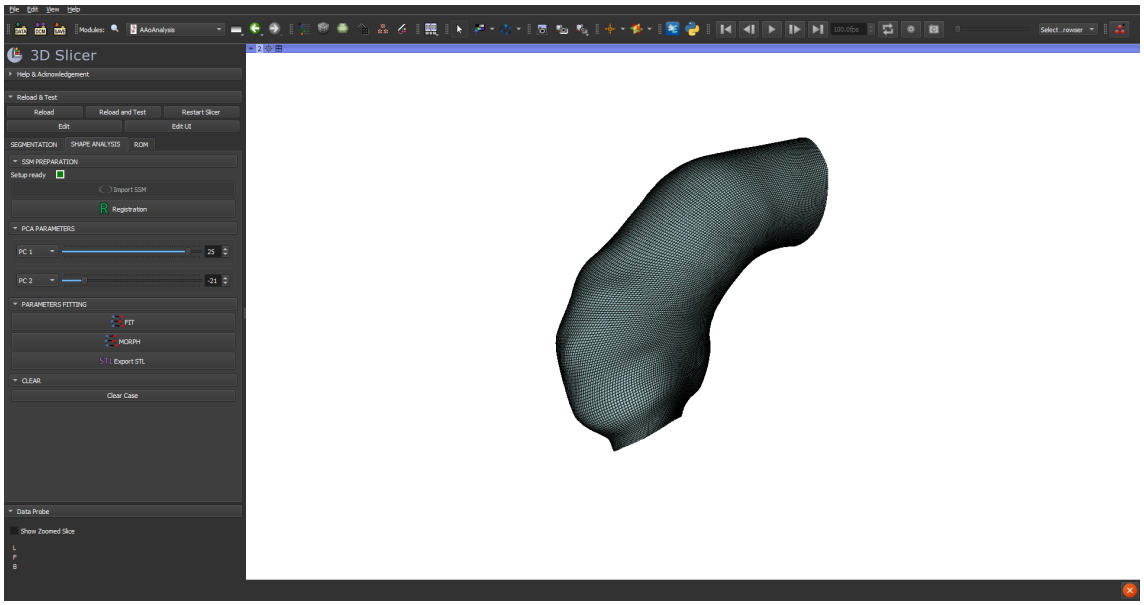

Figure A.4: Template of the statistical shape model deformed by a linear combination of shape modes.

Finally, the third module developed in this extension enabled the augmented reality environment where the simulation results derived from the surrogate models could be observed overlaid onto the patient's medical images, whose transparency could be directly controlled by the operator (Figure A.5). The surrogate models, previously created through model order reduction, as described in Section 5.2.7, were loaded and controlled as Functional Mock-up Units (see Section 5.2.8). They allowed the display of contours of outcomes of interest on specific surfaces. The inputs for each surrogate model consisted of the modal weight coefficients from the previously conducted fitting and the two physical parameters controlling the inlet velocity profile and the outlet resistances. The outputs, on the other hand, included the modal coefficients of the physical ROMs (w_i of equation 5.2.7) which, together with the already known eigenvectors, allowed for the reconstruction of the numerical solution results in just a few milliseconds during the online phase. After importing the surrogate models into the module, the user could interact with them using specific sliders to observe the effect of input parameter variations on the selected output hemodynamic parameters. Among the first future developments, there will be the possibility of computing vectors and streamlines to reproduce the blood flow in the lumen domain.

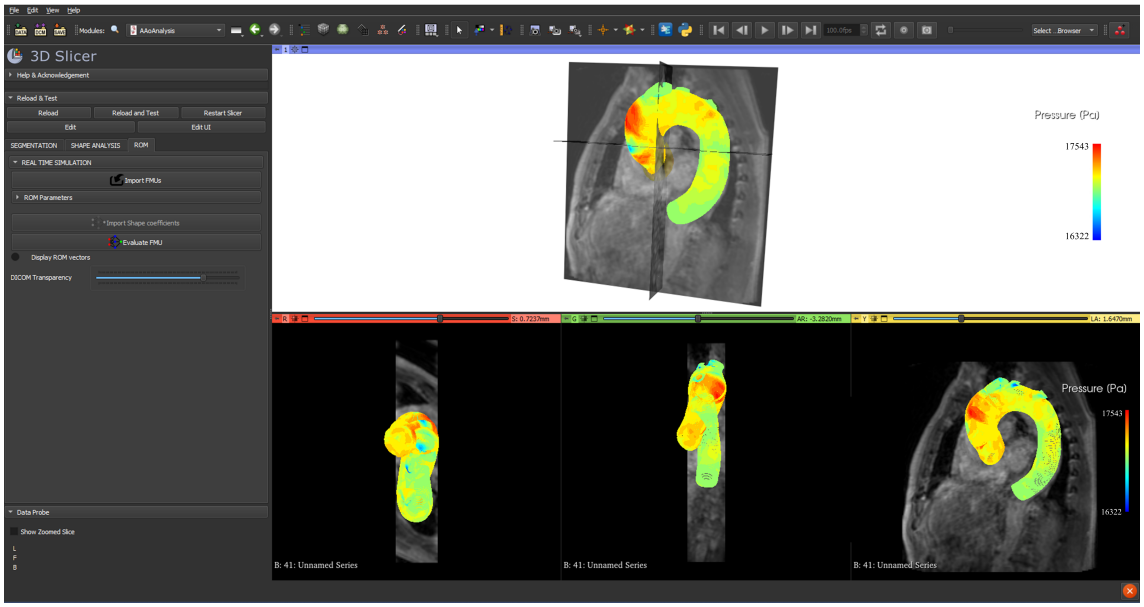

Figure A.5: Computation of hemodynamics in (almost) real-time by exploiting the surrogate model obtained by means of model order reduction: pressure at the wall superimposed on the DICOM of the 4D flow MRI.

Bibliography

[1] P. I. Aaronson, J. P. Ward, e M. J. Connolly, *The cardiovascular system at a glance*. John Wiley & Sons, 2020.

[2] D. Randall, "4 the circulatory system," in *Fish physiology*. Elsevier, 1970, volume 4, pagine 133–172.

[3] R. Bolli, "William harvey and the discovery of the circulation of the blood: Part ii," *Circulation research*, volume 124, numero 9, pagine 1300–1302, 2019.

[4] E. J. Topol e R. M. Califf, *Textbook of cardiovascular medicine*. Lippincott Williams & Wilkins, 2007.

[5] W. Grossman, "Evaluation of systolic and diastolic function of the myocardium," in *Cardiac catheterization and angiography. Third edition*, 1986.

[6] G. I. Cohen, J. F. Pietrolungo, J. D. Thomas, e A. L. Klein, "A practical guide to assessment of ventricular diastolic function using doppler echocardiography," *Journal of the American College of Cardiology*, volume 27, numero 7, pagine 1753–1760, 1996.

[7] W. D. Tucker, Y. Arora, e K. Mahajan, *Anatomy, blood vessels*. StatPearls Publishing, 2017.

[8] Q. Zhang, B. Gao, e Y. Chang, "The numerical study on the effects of cardiac function on the aortic oxygen distribution," *Medical & biological engineering & computing*, volume 56, pagine 1305–1313, 2018.

[9] R. De Paulis e A. Salica, "Surgical anatomy of the aortic valve and root implications for valve repair," *Annals of cardiothoracic surgery*, volume 8, numero 3, pagina 313, 2019.

[10] M. Rahman e A. B. Siddik, "Anatomy, arterioles," in *StatPearls [Internet]*. StatPearls Publishing, 2021.

[11] P. A. Moorehead, A. H. Kim, C. P. Miller, T. V. Kashyap, D. E. Kendrick, e V. S. Kashyap, "Prevalence of bovine aortic arch configuration in adult patients with and without thoracic aortic pathology," *Annals of Vascular Surgery*, volume 30, pagine 132–137, 2016.

[12] I. Rehman, C. C. Kerndt, e A. Rehman, "Anatomy, thorax, heart left anterior descending (lad) artery," in *StatPearls [Internet]*. StatPearls Publishing, 2022.

[13] D. P. Sokolis, E. P. Kritharis, e D. C. Iliopoulos, "Effect of layer heterogeneity on the biomechanical properties of ascending thoracic aortic aneurysms," *Medical & biological engineering & computing*, volume 50, numero 12, pagine 1227–1237, 2012.

[14] H. Weisbecker, C. Viertler, D. M. Pierce, e G. A. Holzapfel, "The role of elastin and collagen in the softening behavior of the human thoracic aortic media," *Journal of biomechanics*, volume 46, numero 11, pagine 1859–1865, 2013.

[15] K. Maiellaro e W. R. Taylor, "The role of the adventitia in vascular inflammation," *Cardiovascular research*, volume 75, numero 4, pagine 640–648, 2007.

[16] M. A. Cattell, J. C. Anderson, e P. S. Hasleton, "Age-related changes in amounts and concentrations of collagen and elastin in normotensive human thoracic aorta," *Clinica chimica acta*, volume 245, numero 1, pagine 73–84, 1996.

[17] G. Martufi e T. C. Gasser, "Turnover of fibrillar collagen in soft biological tissue with application to the expansion of abdominal aortic aneurysms," *Journal of the Royal Society Interface*, volume 9, numero 77, pagine 3366–3377, 2012.

[18] L. Liyanage, L. Musto, C. Budgeon, G. Rutty, M. Biggs, A. Saratzis, D. A. Vorp, V. Vavourakis, M. Bown, e A. Tsamis, "Multimodal structural analysis of the human aorta: from valve to bifurcation," *European Journal of Vascular and Endovascular Surgery*, volume 63, numero 5, pagine 721–730, 2022.

[19] N. Shahmansouri, M. Alreshidan, A. Emmott, K. Lachapelle, R. Cartier, R. L. Leask, e R. Mongrain, "Evaluating ascending aortic aneurysm tissue toughness: dependence on collagen and elastin contents," *Journal of the mechanical behavior of biomedical materials*, volume 64, pagine 262–271, 2016.

[20] Z. Faiza e T. Sharman, "Thoracic aorta aneurysm," in *StatPearls [Internet]*. StatPearls Publishing, 2022.

[21] K. W. Johnston, R. B. Rutherford, M. D. Tilson, D. M. Shah, L. Hollier, J. C. Stanley, *et al.*, "Suggested standards for reporting on arterial aneurysms," *Journal of vascular surgery*, volume 13, numero 3, pagine 452–458, 1991.

[22] T. Klima, H. J. Spjut, A. Coelho, A. G. Gray, D. C. Wukasch, G. J. Reul Jr, e D. A. Cooley, "The morphology of ascending aortic aneurysms," *Human pathology*, volume 14, numero 9, pagine 810–817, 1983.

[23] C. A. Nienaber, R. E. Clough, N. Sakalihasan, T. Suzuki, R. Gibbs, F. Mussa, M. P. Jenkins, M. M. Thompson, A. Evangelista, J. S. Yeh, *et al.*, "Aortic dissection," *Nature reviews Disease primers*, volume 2, numero 1, pagine 1–18, 2016.

[24] G. Thiene, C. Basso, e M. Della Barbera, "Pathology of the aorta and aorta as homograft," *Journal of Cardiovascular Development and Disease*, volume 8, numero 7, pagina 76, 2021.

[25] G. Ailawadi, C. W. Moehle, H. Pei, S. P. Walton, Z. Yang, I. L. Kron, C. L. Lau, e G. K. Owens, "Smooth muscle phenotypic modulation is an early event in aortic aneurysms," *The Journal of thoracic and cardiovascular surgery*, volume 138, numero 6, pagine 1392–1399, 2009.

[26] E. S. Di Martino, A. Bohra, J. P. V. Geest, N. Gupta, M. S. Makaroun, e D. A. Vorp, "Biomechanical properties of ruptured versus electively repaired abdominal aortic aneurysm wall tissue," *Journal of vascular surgery*, volume 43, numero 3, pagine 570–576, 2006.

[27] M. Thubrikar, *The aortic valve*. Routledge, 2018.

[28] P. W. Fedak, S. Verma, T. E. David, R. L. Leask, R. D. Weisel, e J. Butany, "Clinical and pathophysiological implications of a bicuspid aortic valve," *Circulation*, volume 106, numero 8, pagine 900–904, 2002.

[29] A. Mathur, V. Mohan, D. Ameta, B. Gaurav, e P. Haranahalli, "Aortic aneurysm," *Journal of translational internal medicine*, volume 4, numero 1, pagine 35–41, 2016.

[30] G. A. Kuzmik, A. X. Sang, e J. A. Elefteriades, "Natural history of thoracic aortic aneurysms," *Journal of vascular surgery*, volume 56, numero 2, pagine 565–571, 2012.

[31] R. G. e Melo, G. S. Duarte, A. Lopes, M. Alves, D. Caldeira, R. F. e Fernandes, e L. M. Pedro, "Incidence and prevalence of thoracic aortic aneurysms: a systematic review and meta-analysis of population-based studies," in *Seminars in thoracic and cardiovascular surgery*, volume 34, numero 1. Elsevier, 2022, pagine 1–16.

[32] E. Saliba, Y. Sia, A. Dore, e I. El Hamamsy, "The ascending aortic aneurysm: When to intervene?" *IJC Heart & Vasculature*, volume 6, pagine 91–100, 2015.

[33] E. Choke, G. Cockerill, W. Wilson, S. Sayed, J. Dawson, I. Loftus, e M. Thompson, "A review of biological factors implicated in abdominal aortic aneurysm rupture," *European Journal of Vascular and Endovascular Surgery*, volume 30, numero 3, pagine 227–244, 2005.

[34] E. L. Chou e M. E. Lindsay, "The genetics of aortopathies: Hereditary thoracic aortic aneurysms and dissections," *American Journal of Medical Genetics Part C: Seminars in Medical Genetics*, volume 184, numero 1, pagine 136–148, 2020.

[35] M. Cury, F. Zeidan, A. C. Lobato, *et al.*, "Aortic disease in the young: genetic aneurysm syndromes, connective tissue disorders, and familial aortic aneurysms and dissections," *International journal of vascular medicine*, volume 2013, 2013.

[36] C. R. Brown, R. K. Greenberg, S. Wong, M. Eagleton, T. Mastracci, A. V. Hernandez, C. M. Rigelsky, e R. Moran, "Family history of aortic disease predicts disease patterns and progression and is a significant influence on management strategies for patients and their relatives," *Journal of Vascular Surgery*, volume 58, numero 3, pagine 573–581, 2013.

[37] A. Akai, Y. Watanabe, K. Hoshina, Y. Obitsu, J. Deguchi, O. Sato, K. Shigematsu, e T. Miyata, "Family history of aortic aneurysm is an independent risk factor for more rapid growth of small abdominal aortic aneurysms in japan," *Journal of vascular surgery*, volume 61, numero 2, pagine 287–290, 2015.

[38] D. M. Milewicz, K. Michael, N. Fisher, J. S. Coselli, T. Markello, e A. Biddinger, "Fibrillin-1 (fbn1) mutations in patients with thoracic aortic aneurysms," *Circulation*, volume 94, numero 11, pagine 2708–2711, 1996.

[39] A. Biddinger, M. Rocklin, J. Coselli, D. M. Milewicz, *et al.*, "Familial thoracic aortic dilatations and dissections: a case control study," *Journal of vascular surgery*, volume 25, numero 3, pagine 506–511, 1997.

[40] E. Kobeissi, M. Hibino, H. Pan, e D. Aune, "Blood pressure, hypertension and the risk of abdominal aortic aneurysms: a systematic review and meta-analysis of cohort studies," *European journal of epidemiology*, volume 34, pagine 547–555, 2019.

[41] D. Reed, C. Reed, G. Stemmermann, e T. Hayashi, "Are aortic aneurysms caused by atherosclerosis?" *Circulation*, volume 85, numero 1, pagine 205–211, 1992.

[42] O. Leone, A. Corsini, D. Pacini, B. Corti, M. Lorenzini, V. Laus, A. Foà, M. L. B. Reggiani, L. Di Marco, e C. Rapezzi, "The complex interplay among atherosclerosis, inflammation, and degeneration in ascending thoracic aortic aneurysms," *The Journal of Thoracic and Cardiovascular Surgery*, volume 160, numero 6, pagine 1434–1443, 2020.

[43] B. F. Sode, B. G. Nordestgaard, M. Grønbæk, e M. Dahl, "Tobacco smoking and aortic aneurysm: two population-based studies," *International journal of cardiology*, volume 167, numero 5, pagine 2271–2277, 2013.

[44] T. J. Schlatmann e A. E. Becker, "Histologic changes in the normal aging aorta: implications for dissecting aortic aneurysm," *The American journal of cardiology*, volume 39, numero 1, pagine 13–20, 1977.

[45] H. Kaneko, T. Anzai, M. Morisawa, T. Kohno, T. Nagai, A. Anzai, T. Takahashi, M. Shimoda, A. Sasaki, Y. Maekawa, *et al.*, "Resveratrol prevents the development of abdominal aortic aneurysm through attenuation of inflammation, oxidative stress, and neovascularization," *Atherosclerosis*, volume 217, numero 2, pagine 350–357, 2011.

[46] K. Sobolewski, M. Wolańska, E. Bańkowski, M. Gacko, e S. Głowiński, "Collagen, elastin and glycosaminoglycans in aortic aneurysms." *Acta Biochimica Polonica*, volume 42, numero 3, pagine 301–307, 1995.

[47] S. W. Rabkin, "The role matrix metalloproteinases in the production of aortic aneurysm," *Progress in molecular biology and translational science*, volume 147, pagine 239–265, 2017.

[48] S. L. Brown, R. W. Busuttil, J. D. Baker, H. I. Machleder, W. S. Moore, e W. F. Barker, "Bacteriologic and surgical determinants of survival in patients with mycotic aneurysms," *Journal of Vascular Surgery*, volume 1, numero 4, pagine 541–547, 1984.

[49] H. Alkadhi, S. Wildermuth, L. Desbiolles, T. Schertler, D. Crook, B. Marincek, e T. Boehm, "Vascular emergencies of the thorax after blunt and iatrogenic trauma: multi–detector row ct and three-dimensional imaging," *Radiographics*, volume 24, numero 5, pagine 1239–1255, 2004.

[50] G. Makrygiannis, A. Courtois, P. Drion, J.-O. Defraigne, H. Kuivaniemi, e N. Sakalihasan, "Sex differences in abdominal aortic aneurysm: the role of sex hormones," *Annals of vascular surgery*, volume 28, numero 8, pagine 1946–1958, 2014.

[51] E. Cecchi, C. Giglioli, S. Valente, C. Lazzeri, G. F. Gensini, R. Abbate, e L. Mannini, "Role of hemodynamic shear stress in cardiovascular disease," *Atherosclerosis*, volume 214, numero 2, pagine 249–256, 2011.

[52] K. Hoshina, E. Sho, M. Sho, T. K. Nakahashi, e R. L. Dalman, "Wall shear stress and strain modulate experimental aneurysm cellularity," *Journal of vascular surgery*, volume 37, numero 5, pagina 1067, 2003.

[53] S. S. Portelli, B. D. Hambly, R. W. Jeremy, e E. N. Robertson, "Oxidative stress in genetically triggered thoracic aortic aneurysm: role in pathogenesis and therapeutic opportunities," *Redox Report*, volume 26, numero 1, pagine 45–52, 2021.

[54] R. Erbel e H. Eggebrecht, "Aortic dimensions and the risk of dissection," *Heart*, volume 92, numero 1, pagine 137–142, 2006.

[55] T. Fukui, "Management of acute aortic dissection and thoracic aortic rupture," *Journal of Intensive Care*, volume 6, pagine 1–8, 2018.

[56] M. H. Guo, J. J. Appoo, R. Saczkowski, H. N. Smith, M. Ouzounian, A. J. Gregory, E. J. Herget, e M. Boodhwani, "Association of mortality and acute aortic events with ascending aortic aneurysm: a systematic review and meta-analysis," *JAMA network open*, volume 1, numero 4, pagine e181 281–e181 281, 2018.

[57] A. Nasrallah, Y. Goussous, G. El-Said, E. Garcia, e R. J. Hall, "Pulmonary artery compression due to acute dissecting aortic aneurysm: clinical and angiographic diagnosis," *Chest*, volume 67, numero 2, pagine 228–230, 1975.

[58] A. Değirmencioğlu, E. Baysal, G. Karakus, e A. Buturak, "Severe pulmonary hypertension secondary to giant chronic dissecting aortic aneurysm presenting

as chronic right heart failure," *Journal of Cardiology Cases*, volume 7, numero 2, pagine e57–e59, 2013.

[59] D. A. Ott, "Aneurysm of the sinus of valsalva," in *Seminars in Thoracic and Cardiovascular Surgery: Pediatric Cardiac Surgery Annual*, volume 9, numero 1. Elsevier, 2006, pagine 165–176.

[60] J. Rooprai, M. Boodhwani, L. Beauchesne, K.-L. Chan, C. Dennie, G. A. Wells, e T. Coutinho, "Central hypertension in patients with thoracic aortic aneurysms: prevalence and association with aneurysm size and growth," *American Journal of Hypertension*, volume 35, numero 1, pagine 79–86, 2022.

[61] A. C. Braverman, "Medical management of thoracic aortic aneurysm disease," pagine S2–S6, 2013.

[62] E. Mehrabi Nasab e S. S. Athari, "The prevalence of thoracic aorta aneurysm as an important cardiovascular disease in the general population," *Journal of Cardiothoracic Surgery*, volume 17, numero 1, pagina 51, 2022.

[63] M. W. Li, M. O. R. Mian, T. Barhoumi, A. Rehman, K. Mann, P. Paradis, e E. L. Schiffrin, "Endothelin-1 overexpression exacerbates atherosclerosis and induces aortic aneurysms in apolipoprotein e knockout mice," *Arteriosclerosis, thrombosis, and vascular biology*, volume 33, numero 10, pagine 2306–2315, 2013.

[64] R. Erbel, V. Aboyans, C. Boileau, E. Bossone, R. Bartolomeo, H. Eggebrecht, A. Evangelista, V. Falk, H. Frank, O. Gaemperli, *et al.*, "Esc committee for practice guidelines. 2014 esc guidelines on the diagnosis and treatment of aortic diseases: Document covering acute and chronic aortic diseases of the thoracic and abdominal aorta of the adult. the task force for the diagnosis and treatment of aortic diseases of the european society of cardiology (esc)," *Eur Heart J*, volume 35, numero 41, pagine 2873–2926, 2014.

[65] L. Adamo e A. C. Braverman, "Surgical threshold for bicuspid aortic valve aneurysm: a case for individual decision-making," *Heart*, volume 101, numero 17, pagine 1361–1367, 2015.

[66] G. C. Morris, W. S. Henly, e M. E. DeBakey, "Correction of acute dissecting aneurysm of aorta with valvular insufficiency," *Jama*, volume 184, numero 1, pagine 63–64, 1963.

[67] W. C. Members, E. M. Isselbacher, O. Preventza, J. Hamilton Black III, J. G. Augoustides, A. W. Beck, M. A. Bolen, A. C. Braverman, B. E. Bray, M. M. Brown-Zimmerman, *et al.*, "2022 acc/aha guideline for the diagnosis and management of aortic disease: a report of the american heart association/american college of cardiology joint committee on clinical practice guidelines," *Journal of the American College of Cardiology*, volume 80, numero 24, pagine e223–e393, 2022.

[68] D. Hernandez-Vaquero, J. Silva, A. Escalera, R. Álvarez-Cabo, C. Morales, R. Díaz, P. Avanzas, C. Moris, e I. Pascual, "Life expectancy after surgery for ascending aortic aneurysm," *Journal of Clinical Medicine*, volume 9, numero 3, pagina 615, 2020.

[69] F. A. Lederle, G. R. Johnson, S. E. Wilson, D. J. Ballard, W. D. Jordan Jr, J. Blebea, F. N. Littooy, J. A. Freischlag, D. Bandyk, J. H. Rapp, *et al.*, "Rupture rate of large abdominal aortic aneurysms in patients refusing or unfit for elective repair," *Jama*, volume 287, numero 22, pagine 2968–2972, 2002.

[70] T. C. Gasser, "Biomechanical rupture risk assessment," *Aorta*, volume 4, numero 02, pagine 42–60, 2016.

[71] M. F. Fillinger, S. P. Marra, M. L. Raghavan, e F. E. Kennedy, "Prediction of rupture risk in abdominal aortic aneurysm during observation: wall stress versus diameter," *Journal of vascular surgery*, volume 37, numero 4, pagine 724–732, 2003.

[72] E. K. Shang, D. P. Nathan, S. R. Sprinkle, S. C. Vigmostad, R. M. Fairman, J. E. Bavaria, R. C. Gorman, J. H. Gorman III, K. B. Chandran, e B. M. Jackson, "Peak wall stress predicts expansion rate in descending thoracic aortic aneurysms," *The Annals of thoracic surgery*, volume 95, numero 2, pagine 593–598, 2013.

[73] R. P. Plichta e G. C. Hughes, "Thoracic endovascular aortic repair for the ascending aorta: experience and pitfalls," *Journal of Visualized Surgery*, volume 4, 2018.

[74] C. E. Muetterties, R. Menon, e G. H. Wheatley III, "A systematic review of primary endovascular repair of the ascending aorta," *Journal of Vascular Surgery*, volume 67, numero 1, pagine 332–342, 2018.

[75] K. Kallenbach, D. Kojic, M. Oezsoez, T. Bruckner, S. Sandrio, R. Arif, C. J. Beller, A. Weymann, e M. Karck, "Treatment of ascending aortic aneurysms using different surgical techniques: a single-centre experience with 548 patients," pagine 337–345, 2013.

[76] C. J. Beller, M. Farag, S. Wannaku, P. Seppelt, R. Arif, A. Ruhparwar, M. Karck, A. Weymann, e K. Kallenbach, "Gender-specific differences in outcome of ascending aortic aneurysm surgery," *PLoS One*, volume 10, numero 4, pagina e0124461, 2015.

[77] M. A. Coady, J. A. Rizzo, G. L. Hammond, G. S. Kopf, e J. A. Elefteriades, "Surgical intervention criteria for thoracic aortic aneurysms: a study of growth rates and complications," *The Annals of thoracic surgery*, volume 67, numero 6, pagine 1922–1926, 1999.

[78] A. P. Goldman, M. N. Kotler, M. H. Scanlon, B. Ostrum, R. Parameswaran, e W. R. Parry, "The complementary role of magnetic resonance imaging, doppler echocardiography, and computed tomography in the diagnosis of dissecting thoracic aneurysms," *American Heart Journal*, volume 111, numero 5, pagine 970–981, 1986.

[79] A. N. DeMaria, W. Bommer, A. Neumann, L. Weinert, H. Bogren, e D. T. Mason, "Identification and localization of aneurysms of the ascending aorta by cross-sectional echocardiography." *Circulation*, volume 59, numero 4, pagine 755–761, 1979.

[80] E. J. Gussenhoven, M. A. Taams, J. R. Roelandt, K. M. Ligtvoet, J. McGhie, L. A. van Herwerden, e M. K. Cahalan, "Transesophageal two-dimensional echocardiography: its role in solving clinical problems," *Journal of the American College of Cardiology*, volume 8, numero 4, pagine 975–979, 1986.

[81] L. C. Jansen, H.-M. Schwab, F. N. van de Vosse, M. R. van Sambeek, e R. G. Lopata, "Local and global distensibility assessment of abdominal aortic aneurysms in vivo from probe tracked 2d ultrasound images," *Frontiers in Medical Technology*, volume 4, pagina 1052213, 2023.

[82] G. G. Hartnell, "Imaging of aortic aneurysms and dissection: Ct and mri," *Journal of thoracic imaging*, volume 16, numero 1, pagine 35–46, 2001.

[83] M. Soschynski, F. Hagen, S. Baumann, M. T. Hagar, J. Weiss, T. Krauss, C. L. Schlett, C. von zur MÃ¼hlen, F. Bamberg, K. Nikolaou, S. Greulich, M. F.

Froelich, P. Riffel, D. Overhoff, T. Papavassiliu, S. O. Schoenberg, S. Faby, S. Ulzheimer, I. Ayx, e P. Krumm, "High temporal resolution dual-source photon-counting ct for coronary artery disease: Initial multicenter clinical experience," *Journal of Clinical Medicine*, volume 11, numero 20, 2022.

[84] A. Meloni, F. Frijia, D. Panetta, G. Degiorgi, C. De Gori, E. Maffei, A. Clemente, V. Positano, e F. Cademartiri, "Photon-counting computed tomography (pcct): Technical background and cardio-vascular applications," *Diagnostics*, volume 13, numero 4, 2023.

[85] R. V. Buijs, T. P. Willems, R. A. Tio, H. H. Boersma, I. F. Tielliu, R. H. Slart, e C. J. Zeebregts, "Current state of experimental imaging modalities for risk assessment of abdominal aortic aneurysm," *Journal of Vascular Surgery*, volume 57, numero 3, pagine 851–859, 2013.

[86] K. Takahashi, T. Sekine, T. Ando, Y. Ishii, e S. Kumita, "Utility of 4d flow mri in thoracic aortic diseases: A literature review of clinical applications and current evidence," *Magnetic Resonance in Medical Sciences*, volume 21, numero 2, pagine 327–339, 2022.

[87] P. van Ooij, A. L. Powell, W. V. Potters, J. C. Carr, M. Markl, e Barker, and Alex J. , "Reproducibility and interobserver variability of systolic blood flow velocity and 3d wall shear stress derived from 4d flow mri in the healthy aorta," *Journal of Magnetic Resonance Imaging*, volume 43, numero 1, pagine 236–248, 2016.

[88] J.-L. Rose, A. Lalande, O. Bouchot, E.-B. Bourennane, P. M. Walker, P. Ugolini, C. Revol-Muller, R. Cartier, e F. Brunotte, "Influence of age and sex on aortic distensibility assessed by mri in healthy subjects," *Magnetic resonance imaging*, volume 28, numero 2, pagine 255–263, 2010.

[89] H. M. Ray, J. M. Besho, J. Au, K. M. Charlton-Ouw, A. L. Estrera, C. C. Miller III, H. J. Safi, e A. Azizzadeh, "The role of ascending aortic size in outcomes of patients with uncomplicated acute type b aortic dissection," *Journal of Vascular Surgery*, volume 69, numero 4, pagine 1011–1020, 2019.

[90] N. A. Papakonstantinou e F.-P. Rorris, "Elective replacement of the ascending aorta: is the 5.5-cm threshold appropriate? the insidious, small aorta," *European Journal of Cardio-Thoracic Surgery*, volume 59, numero 3, pagine 554–561, 2021.

[91] A. M. Mansour, S. Peterss, M. A. Zafar, J. A. Rizzo, H. Fang, P. Charilaou, B. A. Ziganshin, U. M. Darr, e J. A. Elefteriades, "Prevention of aortic dissection suggests a diameter shift to a lower aortic size threshold for intervention," *Cardiology*, volume 139, numero 3, pagine 139–146, 2018.

[92] R. Darling, C. Messina, D. Brewster, e L. Ottinger, "Autopsy study of unoperated abdominal aortic aneurysms. the case for early resection." *Circulation*, volume 56, numero 3 Suppl, pagine II161–4, 1977.

[93] M. de Lucio, M. F. García, J. D. García, L. E. R. Rodríguez, e F. Á. Marcos, "On the importance of tunica intima in the aging aorta: a three-layered in silico model for computing wall stresses in abdominal aortic aneurysms," *Computer Methods in Biomechanics and Biomedical Engineering*, volume 24, numero 5, pagine 467–484, 2021.

[94] K. Kalisz e P. Rajiah, "Radiological features of uncommon aneurysms of the cardiovascular system," *World Journal of Radiology*, volume 8, numero 5, pagina 434, 2016.

[95] J. A. Elefteriades, B. A. Ziganshin, J. A. Rizzo, H. Fang, M. Tranquilli, V. Paruchuri, G. Kuzmik, G. Gubernikoff, J. Dumfarth, P. Charilaou, *et al.*, "Indications and imaging for aortic surgery: size and other matters," *The Journal of thoracic and cardiovascular surgery*, volume 149, numero 2, pagine S10–S13, 2015.

[96] L. A. Freeman, P. M. Young, T. A. Foley, E. E. Williamson, C. J. Bruce, K. L. Greason, *et al.*, "Ct and mri assessment of the aortic root and ascending aorta," *AJR Am J Roentgenol*, volume 200, numero 6, pagine W581–W592, 2013.

[97] J. S. Rumsfeld, K. E. Joynt, e T. M. Maddox, "Big data analytics to improve cardiovascular care: promise and challenges," *Nature Reviews Cardiology*, volume 13, numero 6, pagine 350–359, 2016.

[98] J. R. Leach, M. R. Mofrad, e D. Saloner, "Computational models of vascular mechanics," *Computational modeling in biomechanics*, pagine 99–170, 2010.

[99] M. Calder, C. Craig, D. Culley, R. De Cani, C. A. Donnelly, R. Douglas, B. Edmonds, J. Gascoigne, N. Gilbert, C. Hargrove, *et al.*, "Computational modelling for decision-making: where, why, what, who and how," *Royal Society open science*, volume 5, numero 6, pagina 172096, 2018.

[100] B. Raphael e I. F. Smith, *Fundamentals of computer-aided engineering*. John wiley & sons, 2003.

[101] H. Kuivaniemi, E. J. Ryer, J. R. Elmore, e G. Tromp, "Understanding the pathogenesis of abdominal aortic aneurysms," *Expert review of cardiovascular therapy*, volume 13, numero 9, pagine 975–987, 2015.

[102] K. Strimbu e J. A. Tavel, "What are biomarkers?" *Current Opinion in HIV and AIDS*, volume 5, numero 6, pagina 463, 2010.

[103] A. Mourato, R. Valente, J. Xavier, M. Brito, S. Avril, J. C. de Sa, A. Tomas, e J. Fragata, "Computational modelling and simulation of fluid structure interaction in aortic aneurysms: A systematic review and discussion of the clinical potential," *Applied Sciences*, volume 12, numero 16, pagina 8049, 2022.

[104] J. A. Elefteriades e E. A. Farkas, "Thoracic aortic aneurysm: clinically pertinent controversies and uncertainties," *Journal of the American College of Cardiology*, volume 55, numero 9, pagine 841–857, 2010.

[105] E. Ladich, K. Yahagi, M. E. Romero, e R. Virmani, "Vascular diseases: aortitis, aortic aneurysms, and vascular calcification," *Cardiovascular Pathology*, volume 25, numero 5, pagine 432–441, 2016.

[106] C. Kauffmann, A. Tang, E. Therasse, M.-F. Giroux, S. Elkouri, P. Melanson, B. Melanson, V. L. Oliva, e G. Soulez, "Measurements and detection of abdominal aortic aneurysm growth: accuracy and reproducibility of a segmentation software," *European journal of radiology*, volume 81, numero 8, pagine 1688–1694, 2012.

[107] A. Frydrychowicz, A. F. Stalder, M. F. Russe, J. Bock, S. Bauer, A. Harloff, A. Berger, M. Langer, J. Hennig, e M. Markl, "Three-dimensional analysis of segmental wall shear stress in the aorta by flow-sensitive four-dimensional-mri," *Journal of Magnetic Resonance Imaging: An Official Journal of the International Society for Magnetic Resonance in Medicine*, volume 30, numero 1, pagine 77–84, 2009.

[108] B. E. Muhs, K. Vincken, J. Van Prehn, M. Stone, L. Bartels, M. Prokop, F. Moll, e H. Verhagen, "Dynamic cine-ct angiography for the evaluation of the thoracic aorta; insight in dynamic changes with implications for thoracic endograft treatment," *European journal of vascular and endovascular surgery*, volume 32, numero 5, pagine 532–536, 2006.

[109] R. Courant, "Variational methods for the solution of problems of equilibrium and vibrations," *Bulletin of the American Mathematical Society*, volume 49, numero 1, pagine 1–23, 1943.

[110] M. R. Labrosse, C. J. Beller, T. Mesana, e J. P. Veinot, "Mechanical behavior of human aortas: Experiments, material constants and 3-d finite element modeling including residual stress," *Journal of biomechanics*, volume 42, numero 8, pagine 996–1004, 2009.

[111] M. M. Stringfellow, P. F. Lawrence, e R. G. Stringfellow, "The influence of aorta-aneurysm geometry upon stress in the aneurysm wall," *Journal of surgical research*, volume 42, numero 4, pagine 425–433, 1987.

[112] C. M. García-Herrera e D. J. Celentano, "Modelling and numerical simulation of the human aortic arch under in vivo conditions," *Biomechanics and modeling in mechanobiology*, volume 12, pagine 1143–1154, 2013.

[113] B. J. Doyle, A. J. Cloonan, M. T. Walsh, D. A. Vorp, e T. M. McGloughlin, "Identification of rupture locations in patient-specific abdominal aortic aneurysms using experimental and computational techniques," *Journal of biomechanics*, volume 43, numero 7, pagine 1408–1416, 2010.

[114] C. Martin, W. Sun, T. Pham, e J. Elefteriades, "Predictive biomechanical analysis of ascending aortic aneurysm rupture potential," *Acta biomaterialia*, volume 9, numero 12, pagine 9392–9400, 2013.

[115] M. F. Fillinger, M. L. Raghavan, S. P. Marra, J. L. Cronenwett, e F. E. Kennedy, "In vivo analysis of mechanical wall stress and abdominal aortic aneurysm rupture risk," *Journal of vascular surgery*, volume 36, numero 3, pagine 589–597, 2002.

[116] J. M. Dolan, J. Kolega, e H. Meng, "High wall shear stress and spatial gradients in vascular pathology: a review," *Annals of biomedical engineering*, volume 41, pagine 1411–1427, 2013.

[117] L. Boussel, V. Rayz, C. McCulloch, A. Martin, G. Acevedo-Bolton, M. Lawton, R. Higashida, W. S. Smith, W. L. Young, e D. Saloner, "Aneurysm growth occurs at region of low wall shear stress: patient-specific correlation of hemodynamics and growth in a longitudinal study," *Stroke*, volume 39, numero 11, pagine 2997–3002, 2008.

[118] P. Constantin e C. Foias, *Navier-stokes equations*. University of Chicago Press, 2020.

[119] F. Callaghan, J. Karkouri, K. Broadhouse, M. Evin, D. Fletcher, S. Grieve, *et al.*, "Thoracic aortic aneurysm: 4d flow mri and computational fluid dynamics model," *Comput Methods Biomech Biomed Eng*, volume 18, numero sup1, pagine 1894–1895, 2015.

[120] N. Westerhof, J.-W. Lankhaar, e B. E. Westerhof, "The arterial windkessel," *Medical & biological engineering & computing*, volume 47, numero 2, pagine 131–141, 2009.

[121] U. Morbiducci, R. Ponzini, D. Gallo, C. Bignardi, e G. Rizzo, "Inflow boundary conditions for image-based computational hemodynamics: impact of idealized versus measured velocity profiles in the human aorta," *Journal of biomechanics*, volume 46, numero 1, pagine 102–109, 2013.

[122] A. Della Corte, C. Bancone, C. A. Conti, E. Votta, A. Redaelli, L. Del Viscovo, e M. Cotrufo, "Restricted cusp motion in right-left type of bicuspid aortic valves: a new risk marker for aortopathy," *The Journal of thoracic and cardiovascular surgery*, volume 144, numero 2, pagine 360–369, 2012.

[123] S. Pasta, A. Rinaudo, A. Luca, M. Pilato, C. Scardulla, T. G. Gleason, e D. A. Vorp, "Difference in hemodynamic and wall stress of ascending thoracic aortic aneurysms with bicuspid and tricuspid aortic valve," *Journal of biomechanics*, volume 46, numero 10, pagine 1729–1738, 2013.

[124] F. Tan, R. Torii, A. Borghi, R. Mohiaddin, N. Wood, e X. Xu, "Fluid-structure interaction analysis of wall stress and flow patterns in a thoracic aortic aneurysm," *International journal of applied mechanics*, volume 1, numero 01, pagine 179–199, 2009.

[125] E. Vignali, E. Gasparotti, S. Celi, e S. Avril, "Fully-coupled fsi computational analyses in the ascending thoracic aorta using patient-specific conditions and anisotropic material properties," *Frontiers in Physiology*, volume 12, pagina 732561, 2021.

[126] R. Campobasso, F. Condemi, M. Viallon, P. Croisille, S. Campisi, e S. Avril, "Evaluation of peak wall stress in an ascending thoracic aortic aneurysm using fsi simulations: effects of aortic stiffness and peripheral resistance," *Cardiovascular engineering and technology*, volume 9, pagine 707–722, 2018.

[127] X. Wang e X. Li, "Computational simulation of aortic aneurysm using fsi method: influence of blood viscosity on aneurismal dynamic behaviors," *Computers in biology and medicine*, volume 41, numero 9, pagine 812–821, 2011.

[128] M. Alimohammadi, J. M. Sherwood, M. Karimpour, O. Agu, S. Balabani, e V. Díaz-Zuccarini, "Aortic dissection simulation models for clinical support: fluid-structure interaction vs. rigid wall models," *Biomedical engineering online*, volume 14, pagine 1–16, 2015.

[129] P. Hamet e J. Tremblay, "Artificial intelligence in medicine," *Metabolism*, volume 69, pagine S36–S40, 2017.

[130] J. Rueckel, P. Reidler, N. Fink, J. Sperl, T. Geyer, M. Fabritius, J. Ricke, M. Ingrisch, e B. Sabel, "Artificial intelligence assistance improves reporting efficiency of thoracic aortic aneurysm ct follow-up," *European Journal of Radiology*, volume 134, pagina 109424, 2021.

[131] N. Kagiyama, S. Shrestha, P. D. Farjo, e P. P. Sengupta, "Artificial intelligence: practical primer for clinical research in cardiovascular disease," *Journal of the American Heart Association*, volume 8, numero 17, pagina e012788, 2019.

[132] A. Rajkomar, J. Dean, e I. Kohane, "Machine learning in medicine," *New England Journal of Medicine*, volume 380, numero 14, pagine 1347–1358, 2019.

[133] J. Alzubi, A. Nayyar, e A. Kumar, "Machine learning from theory to algorithms: an overview," in *Journal of physics: conference series*, volume 1142. IOP Publishing, 2018, pagina 012012.

[134] A. Arzani, J.-X. Wang, M. S. Sacks, e S. C. Shadden, "Machine learning for cardiovascular biomechanics modeling: challenges and beyond," *Annals of Biomedical Engineering*, volume 50, numero 6, pagine 615–627, 2022.

[135] Y. LeCun, Y. Bengio, e G. Hinton, "Deep learning," *nature*, volume 521, numero 7553, pagine 436–444, 2015.

[136] M. Sermesant, H. Delingette, H. Cochet, P. Jais, e N. Ayache, "Applications of artificial intelligence in cardiovascular imaging," *Nature Reviews Cardiology*, volume 18, numero 8, pagine 600–609, 2021.

[137] J. Raffort, C. Adam, M. Carrier, A. Ballaith, R. Coscas, E. Jean-Baptiste, R. Hassen-Khodja, N. Chakfé, e F. Lareyre, "Artificial intelligence in abdominal

aortic aneurysm," *Journal of vascular surgery*, volume 72, numero 1, pagine 321–333, 2020.

[138] K. A. Williams, A. R. Podgorsak, M. M. S. Bhurwani, R. A. Rava, K. N. Sommer, e C. N. Ionita, "The aneurysm occlusion assistant, an ai platform for real time surgical guidance of intracranial aneurysms," in *Medical Imaging 2021: Imaging Informatics for Healthcare, Research, and Applications*, volume 11601. SPIE, 2021, pagine 153–160.

[139] S. A. Niederer, M. S. Sacks, M. Girolami, e K. Willcox, "Scaling digital twins from the artisanal to the industrial," *Nature Computational Science*, volume 1, numero 5, pagine 313–320, 2021.

[140] E. VanDerHorn e S. Mahadevan, "Digital twin: Generalization, characterization and implementation," *Decision support systems*, volume 145, pagina 113524, 2021.

[141] R. Piascik, J. Vickers, D. Lowry, S. Scotti, J. Stewart, e A. Calomino, "Technology area 12: Materials, structures, mechanical systems, and manufacturing road map," *NASA Office of Chief Technologist*, pagine 15–88, 2010.

[142] N. Ayache, J.-P. Boissel, S. Brunak, G. Clapworthy, G. Lonsdale, J. Fingberg, A. Frangi, G. Deco, P. Hunter, P. Nielsen, *et al.*, "Towards virtual physiological human: Multilevel modelling and simulation of the human anatomy and physiology," *Virtual Physiological Human: White paper, EC-DG INFSO and DG JRC*, volume 156, pagine 213–220, 2006.

[143] J. Corral-Acero, F. Margara, M. Marciniak, C. Rodero, F. Loncaric, Y. Feng, A. Gilbert, J. F. Fernandes, H. A. Bukhari, A. Wajdan, *et al.*, "The 'digital twin' to enable the vision of precision cardiology," *European heart journal*, volume 41, numero 48, pagine 4556–4564, 2020.

[144] G. Coorey, G. A. Figtree, D. F. Fletcher, e J. Redfern, "The health digital twin: advancing precision cardiovascular medicine," *Nature Reviews Cardiology*, volume 18, numero 12, pagine 803–804, 2021.

[145] T. Sun, X. He, X. Song, L. Shu, e Z. Li, "The digital twin in medicine: a key to the future of healthcare?" *Frontiers in Medicine*, volume 9, pagina 907066, 2022.

[146] D. R. Hose, P. V. Lawford, W. Huberts, L. R. Hellevik, S. W. Omholt, e F. N. van de Vosse, "Cardiovascular models for personalised medicine: Where now and where next?" *Medical engineering & physics*, volume 72, pagine 38–48, 2019.

[147] S. Niederer, Y. Aboelkassem, C. Cantwell, C. Corrado, S. Coveney, E. Cherry, T. Delhaas, F. Fenton, A. Panfilov, P. Pathmanathan, *et al.*, "Creation and application of virtual patient cohorts of heart models," *Philosophical Transactions of the Royal Society A*, volume 378, numero 2173, pagina 20190558, 2020.

[148] N. K. Chakshu, I. Sazonov, e P. Nithiarasu, "Towards enabling a cardiovascular digital twin for human systemic circulation using inverse analysis," *Biomechanics and modeling in mechanobiology*, volume 20, numero 2, pagine 449–465, 2021.

[149] A. G. de Lepper, C. M. Buck, M. van't Veer, W. Huberts, F. N. van de Vosse, e L. R. Dekker, "From evidence-based medicine to digital twin technology for predicting ventricular tachycardia in ischaemic cardiomyopathy," *Journal of the Royal Society Interface*, volume 19, numero 194, pagina 20220317, 2022.

[150] W. Huberts, S. G. Heinen, N. Zonnebeld, D. A. van den Heuvel, J.-P. P. de Vries, J. H. Tordoir, D. R. Hose, T. Delhaas, e F. N. van de Vosse, "What is needed to make cardiovascular models suitable for clinical decision support? a viewpoint paper," *Journal of computational science*, volume 24, pagine 68–84, 2018.

[151] J. J. Lee, G. D'Ancona, A. Amaducci, F. Follis, M. Pilato, e S. Pasta, "Role of computational modeling in thoracic aortic pathology: a review," *Journal of Cardiac Surgery: Including Mechanical and Biological Support for the Heart and Lungs*, volume 29, numero 5, pagine 653–662, 2014.

[152] W. Jin, X. Li, e G. Hamarneh, "Evaluating explainable ai on a multi-modal medical imaging task: Can existing algorithms fulfill clinical requirements?" in *Proceedings of the AAAI Conference on Artificial Intelligence*, volume 36, numero 11, 2022, pagine 11 945–11 953.

[153] G. F. Woodworth, C. J. Baird, G. Garces-Ambrossi, J. Tonascia, e R. J. Tamargo, "Inaccuracy of the administrative database: comparative analysis

of two databases for the diagnosis and treatment of intracranial aneurysms," *Neurosurgery*, volume 65, numero 2, pagine 251–257, 2009.

[154] N. A. Seada, S. Hamad, e M. G. Mostafa, "Model-based automatic segmentation of ascending aorta from multimodality medical data," *International Journal of Electrical and Computer Engineering (IJECE)*, volume 6, numero 6, pagine 3161–3173, 2016.

[155] M. Auer e T. C. Gasser, "Reconstruction and finite element mesh generation of abdominal aortic aneurysms from computerized tomography angiography data with minimal user interactions," *IEEE transactions on medical imaging*, volume 29, numero 4, pagine 1022–1028, 2010.

[156] K. R. Rajagopal e K. Rajagopal, "Modeling of the aorta: complexities and inadequacies," *Aorta*, volume 8, numero 04, pagine 091–097, 2020.

[157] E. K. Shang, E. Lai, A. M. Pouch, R. Hinmon, R. C. Gorman, J. H. Gorman III, C. M. Sehgal, G. Ferrari, J. E. Bavaria, e B. M. Jackson, "Validation of semiautomated and locally resolved aortic wall thickness measurements from computed tomography," *Journal of vascular surgery*, volume 61, numero 4, pagine 1034–1040, 2015.

[158] V. Mendez, M. Di Giuseppe, e S. Pasta, "Comparison of hemodynamic and structural indices of ascending thoracic aortic aneurysm as predicted by 2-way fsi, cfd rigid wall simulation and patient-specific displacement-based fea," *Computers in biology and medicine*, volume 100, pagine 221–229, 2018.

[159] R. Pons, A. Guala, J. F. Rodríguez-Palomares, J. Cajas, L. Dux-Santoy, G. Teixidó-Tura, J. J. Molins, M. Vázquez, A. Evangelista, e J. Martorell, "Fluid–structure interaction simulations outperform computational fluid dynamics in the description of thoracic aorta haemodynamics and in the differentiation of progressive dilation in marfan syndrome patients," *Royal Society open science*, volume 7, numero 2, pagina 191752, 2020.

[160] S. Karimi, M. Dabagh, P. Vasava, M. Dadvar, B. Dabir, e P. Jalali, "Effect of rheological models on the hemodynamics within human aorta: Cfd study on ct image-based geometry," *Journal of Non-Newtonian Fluid Mechanics*, volume 207, pagine 42–52, 2014.

[161] S. Katz, A. Caiazzo, B. Moreau, U. Wilbrandt, J. Brüning, L. Goubergrits, e V. John, "Impact of turbulence modeling on the simulation of blood flow in

aortic coarctation," *International Journal for Numerical Methods in Biomedical Engineering*, volume 39, numero 5, pagina e3695, 2023.

[162] G. Carty, S. Chatpun, e D. M. Espino, "Modeling blood flow through intracranial aneurysms: A comparison of newtonian and non-newtonian viscosity," *Journal of Medical and Biological Engineering*, volume 36, pagine 396–409, 2016.

[163] D. A. Steinman e F. Migliavacca, "special issue on verification, validation, and uncertainty quantification of cardiovascular models: towards effective vvuq for translating cardiovascular modelling to clinical utility," *Cardiovascular engineering and technology*, volume 9, pagine 539–543, 2018.

[164] S. Zeinali-Davarani, L. G. Raguin, D. A. Vorp, e S. Baek, "Identification of in vivo material and geometric parameters of a human aorta: toward patient-specific modeling of abdominal aortic aneurysm," *Biomechanics and modeling in mechanobiology*, volume 10, pagine 689–699, 2011.

[165] S. Pasta, V. Agnese, A. Gallo, F. Cosentino, M. Di Giuseppe, G. Gentile, G. M. Raffa, J. F. Maalouf, H. I. Michelena, D. Bellavia, *et al.*, "Shear stress and aortic strain associations with biomarkers of ascending thoracic aortic aneurysm," *The Annals of thoracic surgery*, volume 110, numero 5, pagine 1595–1604, 2020.

[166] T. Watanabe, H. Isoda, Y. Takehara, M. Terada, T. Naito, T. Kosugi, Y. Onishi, C. Tanoi, e T. Izumi, "Hemodynamic vascular biomarkers for initiation of paraclinoid internal carotid artery aneurysms using patient-specific computational fluid dynamic simulation based on magnetic resonance imaging," *Neuroradiology*, volume 60, pagine 545–555, 2018.

[167] E. Altobelli, L. Rapacchietta, V. F. Profeta, e R. Fagnano, "Risk factors for abdominal aortic aneurysm in population-based studies: a systematic review and meta-analysis," *International journal of environmental research and public health*, volume 15, numero 12, pagina 2805, 2018.

[168] A. G. Brown, Y. Shi, A. Marzo, C. Staicu, I. Valverde, P. Beerbaum, P. V. Lawford, e D. R. Hose, "Accuracy vs. computational time: translating aortic simulations to the clinic," *Journal of biomechanics*, volume 45, numero 3, pagine 516–523, 2012.

[169] M. Bonfanti, S. Balabani, J. P. Greenwood, S. Puppala, S. Homer-Vanniasinkam, e V. Díaz-Zuccarini, "Computational tools for clinical support: a multi-scale compliant model for haemodynamic simulations in an aortic dissection based on multi-modal imaging data," *Journal of The Royal Society Interface*, volume 14, numero 136, pagina 20170632, 2017.

[170] B. A. Ziganshin e J. A. Elefteriades, "Treatment of thoracic aortic aneurysm: role of earlier intervention," in *Seminars in thoracic and cardiovascular surgery*, volume 27, numero 2. Elsevier, 2015, pagine 135–143.

[171] A. Lal, J. Dang, C. Nabzdyk, O. Gajic, e V. Herasevich, "Regulatory oversight and ethical concerns surrounding software as medical device (samd) and digital twin technology in healthcare," *Annals of Translational Medicine*, volume 10, numero 18, 2022.

[172] L. Geronzi, P. Haigron, A. Martinez, K. Yan, M. Rochette, A. Bel-Brunon, J. Porterie, S. Lin, D. M. Marin-Castrillon, A. Lalande, *et al.*, "Assessment of shape-based features ability to predict the ascending aortic aneurysm growth," *Frontiers in Physiology*, volume 14, pagina 378, 2023.

[173] L. Geronzi, A. Martinez, M. Rochette, K. Yan, A. Bel-Brunon, P. Haigron, P. Escrig, J. Tomasi, M. Daniel, A. Lalande, *et al.*, "Computer-aided shape features extraction and regression models for predicting the ascending aortic aneurysm growth rate," *Computers in Biology and Medicine*, volume 162, pagina 107052, 2023.

[174] B. Adriaans, M. Ramaekers, S. Heuts, H. Crijns, S. Bekkers, J. Westenberg, H. Lamb, J. Wildberger, e S. Schalla, "Determining the optimal interval for imaging surveillance of ascending aortic aneurysms," *Netherlands Heart Journal*, volume 29, numero 12, pagine 623–631, 2021.

[175] M. Smoljkić, H. Fehervary, P. Van den Bergh, A. Jorge-Peñas, L. Kluyskens, S. Dymarkowski, P. Verbrugghe, B. Meuris, J. Vander Sloten, e N. Famaey, "Biomechanical characterization of ascending aortic aneurysms," *Biomechanics and modeling in mechanobiology*, volume 16, numero 2, pagine 705–720, 2017.

[176] M. E. Groeneveld, J. P. Meekel, S. M. Rubinstein, L. R. Merkestein, G. J. Tangelder, W. Wisselink, M. Truijers, e K. K. Yeung, "Systematic review of circulating, biomechanical, and genetic markers for the prediction of abdom-

inal aortic aneurysm growth and rupture," *Journal of the American Heart Association*, volume 7, numero 13, pagina e007791, 2018.

[177] D. Oladokun, B. Patterson, J. Sobocinski, A. Karthikesalingam, I. Loftus, M. Thompson, e P. Holt, "Systematic review of the growth rates and influencing factors in thoracic aortic aneurysms," *European Journal of Vascular and Endovascular Surgery*, volume 51, numero 5, pagine 674–681, 2016.

[178] M. Lindquist Liljeqvist, M. Bogdanovic, A. Siika, T. C. Gasser, R. Hultgren, e J. Roy, "Geometric and biomechanical modeling aided by machine learning improves the prediction of growth and rupture of small abdominal aortic aneurysms," *Scientific reports*, volume 11, numero 1, pagine 1–10, 2021.

[179] E. Akkoyun, S. T. Kwon, A. C. Acar, W. Lee, e S. Baek, "Predicting abdominal aortic aneurysm growth using patient-oriented growth models with two-step bayesian inference," *Computers in biology and medicine*, volume 117, pagina 103620, 2020.

[180] H. Gharahi, B. Zambrano, C. Lim, J. Choi, W. Lee, e S. Baek, "On growth measurements of abdominal aortic aneurysms using maximally inscribed spheres," *Medical engineering & physics*, volume 37, numero 7, pagine 683–691, 2015.

[181] W. A. Grobman e D. M. Stamilio, "Methods of clinical prediction," *American journal of obstetrics and gynecology*, volume 194, numero 3, pagine 888–894, 2006.

[182] A. Saeyeldin, M. A. Zafar, Y. Li, M. Tanweer, M. Abdelbaky, A. Gryaznov, A. J. Brownstein, C. A. Velasquez, J. Buntin, K. Thombre, *et al.*, "Decision-making algorithm for ascending aortic aneurysm: effectiveness in clinical application?" *The Journal of Thoracic and Cardiovascular Surgery*, volume 157, numero 5, pagine 1733–1745, 2019.

[183] S. Pappu, A. Dardik, H. Tagare, e R. J. Gusberg, "Beyond fusiform and saccular: a novel quantitative tortuosity index may help classify aneurysm shape and predict aneurysm rupture potential," *Annals of vascular surgery*, volume 22, numero 1, pagine 88–97, 2008.

[184] B. J. Doyle, A. Callanan, P. E. Burke, P. A. Grace, M. T. Walsh, D. A. Vorp, e T. M. McGloughlin, "Vessel asymmetry as an additional diagnostic tool in the assessment of abdominal aortic aneurysms," *Journal of vascular surgery*, volume 49, numero 2, pagine 443–454, 2009.

[185] T. Canchi, S. D. Kumar, E. Y. K. Ng, e S. Narayanan, "A review of computational methods to predict the risk of rupture of abdominal aortic aneurysms," *BioMed research international*, volume 2015, 2015.

[186] N. P. Ostberg, M. A. Zafar, S. K. Mukherjee, B. A. Ziganshin, e J. A. Elefteriades, "A machine learning approach for predicting complications in descending and thoracoabdominal aortic aneurysms," *The Journal of Thoracic and Cardiovascular Surgery*, 2022.

[187] M. Piccinelli, A. Veneziani, D. A. Steinman, A. Remuzzi, e L. Antiga, "A framework for geometric analysis of vascular structures: application to cerebral aneurysms," *IEEE transactions on medical imaging*, volume 28, numero 8, pagine 1141–1155, 2009.

[188] J. Shum, G. Martufi, E. Di Martino, C. B. Washington, J. Grisafi, S. C. Muluk, e E. A. Finol, "Quantitative assessment of abdominal aortic aneurysm geometry," *Annals of biomedical engineering*, volume 39, numero 1, pagine 277–286, 2011.

[189] K. Lee, J. Zhu, J. Shum, Y. Zhang, S. C. Muluk, A. Chandra, M. K. Eskandari, e E. A. Finol, "Surface curvature as a classifier of abdominal aortic aneurysms: a comparative analysis," *Annals of biomedical engineering*, volume 41, numero 3, pagine 562–576, 2013.

[190] B. Rengarajan, W. Wu, C. Wiedner, D. Ko, S. C. Muluk, M. K. Eskandari, P. G. Menon, e E. A. Finol, "A comparative classification analysis of abdominal aortic aneurysms by machine learning algorithms," *Annals of biomedical engineering*, volume 48, numero 4, pagine 1419–1429, 2020.

[191] H. N. Do, A. Ijaz, H. Gharahi, B. Zambrano, J. Choi, W. Lee, e S. Baek, "Prediction of abdominal aortic aneurysm growth using dynamical gaussian process implicit surface," *IEEE Transactions on Biomedical Engineering*, volume 66, numero 3, pagine 609–622, 2018.

[192] S. Kim, Z. Jiang, B. A. Zambrano, Y. Jang, S. Baek, S. K. Yoo, e H.-J. Chang, "Deep learning on multiphysical features and hemodynamic modeling for abdominal aortic aneurysm growth prediction," *IEEE Transactions on Medical Imaging*, 2022.

[193] O. Meyrignac, L. Bal, C. Zadro, A. Vavasseur, A. Sewonu, M. Gaudry, B. Saint-Lebes, M. De Masi, P. Revel-Mouroz, A. Sommet, *et al.*, "Combining volumetric

and wall shear stress analysis from ct to assess risk of abdominal aortic aneurysm progression," *Radiology*, volume 295, numero 3, pagine 722–729, 2020.

[194] T. Krüger, O. Forkavets, K. Veseli, H. Lausberg, L. Vöhringer, W. Schneider, F. Bamberg, e C. Schlensak, "Ascending aortic elongation and the risk of dissection," *European Journal of Cardio-Thoracic Surgery*, volume 50, numero 2, pagine 241–247, 2016.

[195] J. Wu, M. A. Zafar, Y. Li, A. Saeyeldin, Y. Huang, R. Zhao, J. Qiu, M. Tanweer, M. Abdelbaky, A. Gryaznov, *et al.*, "Ascending aortic length and risk of aortic adverse events: the neglected dimension," *Journal of the American College of Cardiology*, volume 74, numero 15, pagine 1883–1894, 2019.

[196] T. Krüger, R. Sandoval Boburg, M. Lescan, A. Oikonomou, W. Schneider, L. Vöhringer, H. Lausberg, F. Bamberg, G. Blumenstock, e C. Schlensak, "Aortic elongation in aortic aneurysm and dissection: the tübingen aortic pathoanatomy (taipan) project," *European Journal of Cardio-Thoracic Surgery*, volume 54, numero 1, pagine 26–33, 2018.

[197] M. P. Poullis, R. Warwick, A. Oo, e R. J. Poole, "Ascending aortic curvature as an independent risk factor for type a dissection, and ascending aortic aneurysm formation: a mathematical model," *European journal of cardio-thoracic surgery*, volume 33, numero 6, pagine 995–1001, 2008.

[198] M. A. Zafar, Y. Li, J. A. Rizzo, P. Charilaou, A. Saeyeldin, C. A. Velasquez, A. M. Mansour, S. U. B. Mahmood, W.-G. Ma, A. J. Brownstein, *et al.*, "Height alone, rather than body surface area, suffices for risk estimation in ascending aortic aneurysm," *The Journal of thoracic and cardiovascular surgery*, volume 155, numero 5, pagine 1938–1950, 2018.

[199] L. Liang, M. Liu, C. Martin, J. A. Elefteriades, e W. Sun, "A machine learning approach to investigate the relationship between shape features and numerically predicted risk of ascending aortic aneurysm," *Biomechanics and modeling in mechanobiology*, volume 16, numero 5, pagine 1519–1533, 2017.

[200] Z. Jiang, H. N. Do, J. Choi, W. Lee, e S. Baek, "A deep learning approach to predict abdominal aortic aneurysm expansion using longitudinal data," *Frontiers in Physics*, volume 7, pagina 235, 2020.

[201] M. Sweeting e S. Thompson, "Making predictions from complex longitudinal data, with application to planning monitoring intervals in a national screening

programme," *Journal of the Royal Statistical Society: Series A (Statistics in Society)*, volume 175, numero 2, pagine 569–586, 2012.

[202] T. Heimann e H.-P. Meinzer, "Statistical shape models for 3d medical image segmentation: a review," *Medical image analysis*, volume 13, numero 4, pagine 543–563, 2009.

[203] C. Rodero, M. Strocchi, M. Marciniak, S. Longobardi, J. Whitaker, M. D. O'Neill, K. Gillette, C. Augustin, G. Plank, E. J. Vigmond, *et al.*, "Linking statistical shape models and simulated function in the healthy adult human heart," *PLoS computational biology*, volume 17, numero 4, pagina e1008851, 2021.

[204] G. Biglino, C. Capelli, J. Bruse, G. M. Bosi, A. M. Taylor, e S. Schievano, "Computational modelling for congenital heart disease: how far are we from clinical translation?" *Heart*, volume 103, numero 2, pagine 98–103, 2017.

[205] E. Taghizadeh, A. Terrier, F. Becce, A. Farron, e P. Büchler, "Automated ct bone segmentation using statistical shape modelling and local template matching," *Computer methods in biomechanics and biomedical engineering*, volume 22, numero 16, pagine 1303–1310, 2019.

[206] J. Lötjönen, K. Antila, E. Lamminmäki, J. Koikkalainen, M. Lilja, e T. Cootes, "Artificial enlargement of a training set for statistical shape models: Application to cardiac images," in *Functional Imaging and Modeling of the Heart: Third International Workshop, FIMH 2005, Barcelona, Spain, June 2-4, 2005. Proceedings 3*. Springer, 2005, pagine 92–101.

[207] F. Ambellan, H. Lamecker, C. von Tycowicz, e S. Zachow, *Statistical shape models: understanding and mastering variation in anatomy*. Springer, 2019.

[208] E. Jolivet, Y. Lafon, P. Petit, e P. Beillas, "Comparison of kriging and moving least square methods to change the geometry of human body models," SAE Technical Paper, Report Tecnico, 2015.

[209] S. Durrleman, M. Prastawa, N. Charon, J. R. Korenberg, S. Joshi, G. Gerig, e A. Trouvé, "Morphometry of anatomical shape complexes with dense deformations and sparse parameters," *NeuroImage*, volume 101, pagine 35–49, 2014.

[210] J. L. Bruse, M. A. Zuluaga, A. Khushnood, K. McLeod, H. N. Ntsinjana, T.-Y. Hsia, M. Sermesant, X. Pennec, A. M. Taylor, e S. Schievano, "Detecting clinically meaningful shape clusters in medical image data: metrics analysis for hierarchical clustering applied to healthy and pathological aortic arches," *IEEE Transactions on Biomedical Engineering*, volume 64, numero 10, pagine 2373–2383, 2017.

[211] R. G. Brereton e G. R. Lloyd, "Partial least squares discriminant analysis: taking the magic away," *Journal of Chemometrics*, volume 28, numero 4, pagine 213–225, 2014.

[212] A. Suinesiaputra, P. Ablin, X. Alba, M. Alessandrini, J. Allen, W. Bai, S. Cimen, P. Claes, B. R. Cowan, J. D'hooge, *et al.*, "Statistical shape modeling of the left ventricle: myocardial infarct classification challenge," *IEEE journal of biomedical and health informatics*, volume 22, numero 2, pagine 503–515, 2017.

[213] K. Lekadir, X. Albà, M. Pereañez, e A. F. Frangi, "Statistical shape modeling using partial least squares: application to the assessment of myocardial infarction," in *Statistical Atlases and Computational Models of the Heart. Imaging and Modelling Challenges: 6th International Workshop, STACOM 2015, Held in Conjunction with MICCAI 2015, Munich, Germany, October 9, 2015, Revised Selected Papers 6*. Springer, 2016, pagine 130–139.

[214] T. Mansi, I. Voigt, B. Leonardi, X. Pennec, S. Durrleman, M. Sermesant, H. Delingette, A. M. Taylor, Y. Boudjemline, G. Pongiglione, *et al.*, "A statistical model for quantification and prediction of cardiac remodelling: Application to tetralogy of fallot," *IEEE transactions on medical imaging*, volume 30, numero 9, pagine 1605–1616, 2011.

[215] J. G. Williams, D. Marlevi, J. L. Bruse, F. R. Nezami, H. Moradi, R. N. Fortunato, S. Maiti, M. Billaud, E. R. Edelman, e T. G. Gleason, "Aortic dissection is determined by specific shape and hemodynamic interactions," *Annals of Biomedical Engineering*, pagine 1–16, 2022.

[216] A. Fedorov, R. Beichel, J. Kalpathy-Cramer, J. Finet, J.-C. Fillion-Robin, S. Pujol, C. Bauer, D. Jennings, F. Fennessy, M. Sonka, *et al.*, "3d slicer as an image computing platform for the quantitative imaging network," *Magnetic resonance imaging*, volume 30, numero 9, pagine 1323–1341, 2012.

[217] W. Schroeder, R. Maynard, e B. Geveci, "Flying edges: A high-performance scalable isocontouring algorithm," in *2015 IEEE 5th Symposium on Large Data Analysis and Visualization (LDAV)*. IEEE, 2015, pagine 33–40.

[218] T. K. Dey e W. Zhao, "Approximate medial axis as a voronoi subcomplex," in *Proceedings of the seventh ACM symposium on Solid modeling and applications*, 2002, pagine 356–366.

[219] L. Antiga, B. Ene-Iordache, e A. Remuzzi, "Centerline computation and geometric analysis of branching tubular surfaces with application to blood vessel modeling," *Annals of vascular surgery*, 2003.

[220] S. Saitta, F. Sturla, A. Caimi, A. Riva, M. C. Palumbo, G. Nano, E. Votta, A. D. Corte, M. Glauber, D. Chiappino, *et al.*, "A deep learning-based and fully automated pipeline for thoracic aorta geometric analysis and planning for endovascular repair from computed tomography," *Journal of Digital Imaging*, volume 35, numero 2, pagine 226–239, 2022.

[221] E. W. Dijkstra, "A note on two problems in connexion with graphs," in *Edsger Wybe Dijkstra: His Life, Work, and Legacy*. Association for Computing Machinery, 2022, pagine 287–290.

[222] S. Geisbüsch, A. Stefanovic, D. Schray, I. Oyfe, H.-M. Lin, G. Di Luozzo, e R. B. Griepp, "A prospective study of growth and rupture risk of small-to-moderate size ascending aortic aneurysms," *The Journal of thoracic and cardiovascular surgery*, volume 147, numero 1, pagine 68–74, 2014.

[223] R. R. Davies, L. J. Goldstein, M. A. Coady, S. L. Tittle, J. A. Rizzo, G. S. Kopf, e J. A. Elefteriades, "Yearly rupture or dissection rates for thoracic aortic aneurysms: simple prediction based on size," *The Annals of thoracic surgery*, volume 73, numero 1, pagine 17–28, 2002.

[224] F. Hoffmann, T. Bertram, R. Mikut, M. Reischl, e O. Nelles, "Benchmarking in classification and regression," *Wiley Interdisciplinary Reviews: Data Mining and Knowledge Discovery*, volume 9, numero 5, pagina e1318, 2019.

[225] O. T. Yildiz e E. Alpaydin, "Linear discriminant trees," *International Journal of Pattern Recognition and Artificial Intelligence*, volume 19, numero 03, pagine 323–353, 2005.

[226] S. Ali e K. A. Smith, "On learning algorithm selection for classification," *Applied Soft Computing*, volume 6, numero 2, pagine 119–138, 2006.

[227] J. Mingers, "An empirical comparison of pruning methods for decision tree induction," *Machine learning*, volume 4, pagine 227–243, 1989.

[228] P. E. Hart, D. G. Stork, e R. O. Duda, *Pattern classification*. Wiley Hoboken, 2000.

[229] S. Dreiseitl e L. Ohno-Machado, "Logistic regression and artificial neural network classification models: a methodology review," *Journal of biomedical informatics*, volume 35, numero 5-6, pagine 352–359, 2002.

[230] B. Li, S. Ding, G. Song, J. Li, e Q. Zhang, "Computer-aided diagnosis and clinical trials of cardiovascular diseases based on artificial intelligence technologies for risk-early warning model," *Journal of medical systems*, volume 43, pagine 1–10, 2019.

[231] J. Ren, S. D. Lee, X. Chen, B. Kao, R. Cheng, e D. Cheung, "Naive bayes classification of uncertain data," in *2009 Ninth IEEE international conference on data mining*. IEEE, 2009, pagine 944–949.

[232] Z.-x. Xu, J. Xu, J.-j. Yan, Y.-q. Wang, R. Guo, G.-p. Liu, H.-x. Yan, P. Qian, e Y.-j. Hong, "Analysis of the diagnostic consistency of chinese medicine specialists in cardiovascular disease cases and syndrome identification based on the relevant feature for each label learning method," *Chinese Journal of Integrative Medicine*, volume 21, pagine 217–222, 2015.

[233] C. Cortes e V. Vapnik, "Support-vector networks," *Machine learning*, volume 20, numero 3, pagine 273–297, 1995.

[234] M. Premalatha, C. V. Lakshmi, e W. Eu, "Svm trade-off between maximize the margin and minimize the variables used for regression," *International Journal of Pure and Applied Mathematics*, volume 87, numero 6, pagine 741–750, 2013.

[235] G. Guo, H. Wang, D. Bell, Y. Bi, e K. Greer, "Knn model-based approach in classification," in *On The Move to Meaningful Internet Systems 2003: CoopIS, DOA, and ODBASE: OTM Confederated International Conferences, CoopIS, DOA, and ODBASE 2003, Catania, Sicily, Italy, November 3-7, 2003. Proceedings*. Springer, 2003, pagine 986–996.

[236] N. S. Altman, "An introduction to kernel and nearest-neighbor nonparametric regression," *The American Statistician*, volume 46, numero 3, pagine 175–185, 1992.

[237] S. Zhang, X. Li, M. Zong, X. Zhu, e D. Cheng, "Learning k for knn classification," *ACM Transactions on Intelligent Systems and Technology (TIST)*, volume 8, numero 3, pagine 1–19, 2017.

[238] M. A. Silva, J. Patel, V. Kavouridis, T. Gallerani, A. Beers, K. Chang, K. V. Hoebel, J. Brown, A. P. See, W. B. Gormley, *et al.*, "Machine learning models can detect aneurysm rupture and identify clinical features associated with rupture," *World Neurosurgery*, volume 131, pagine e46–e51, 2019.

[239] M. E. Biancolini *et al.*, *Fast radial basis functions for engineering applications*. Springer, 2017.

[240] M. E. Biancolini, K. Capellini, E. Costa, C. Groth, e S. Celi, "Fast interactive cfd evaluation of hemodynamics assisted by rbf mesh morphing and reduced order models: The case of ataa modelling," *International Journal on Interactive Design and Manufacturing (IJIDeM)*, volume 14, pagine 1227–1238, 2020.

[241] M. Alexa, "Recent advances in mesh morphing," in *Computer graphics forum*, volume 21:2. Wiley Online Library, 2002, pagine 173–198.

[242] H. Yu, T. Xie, S. Paszczyñski, e B. M. Wilamowski, "Advantages of radial basis function networks for dynamic system design," *IEEE Transactions on Industrial Electronics*, volume 58, numero 12, pagine 5438–5450, 2011.

[243] U. Cella, C. Groth, e M. E. Biancolini, "Geometric parameterization strategies for shape optimization using rbf mesh morphing," in *Advances on Mechanics, Design Engineering and Manufacturing: Proceedings of the International Joint Conference on Mechanics, Design Engineering & Advanced Manufacturing (JCM 2016), 14-16 September, 2016, Catania, Italy.* Springer, 2017, pagine 537–545.

[244] L. Grassi, N. Hraiech, E. Schileo, M. Ansaloni, M. Rochette, e M. Viceconti, "Evaluation of the generality and accuracy of a new mesh morphing procedure for the human femur," *Medical engineering & physics*, volume 33, numero 1, pagine 112–120, 2011.

[245] M. E. Biancolini e P. P. Valentini, "Virtual human bone modelling by interactive sculpting, mesh morphing and force-feedback," *International Journal on Interactive Design and Manufacturing (IJIDeM)*, volume 12, pagine 1223–1234, 2018.

[246] F. Vos, P. W. de Bruin, J. Aubel, G. J. Streekstra, M. Maas, L. J. van Vliet, e A. M. Vossepoel, "A statistical shape model without using landmarks," in *Proceedings of the 17th International Conference on Pattern Recognition, 2004. ICPR 2004.*, volume 3. IEEE, 2004, pagine 714–717.

[247] R. H. Davies, C. J. Twining, T. F. Cootes, J. C. Waterton, e C. J. Taylor, "A minimum description length approach to statistical shape modeling," *IEEE transactions on medical imaging*, volume 21, numero 5, pagine 525–537, 2002.

[248] T.-T. Wong, "Performance evaluation of classification algorithms by k-fold and leave-one-out cross validation," *Pattern Recognition*, volume 48, numero 9, pagine 2839–2846, 2015.

[249] I. S. Helland, "On the structure of partial least squares regression," *Communications in statistics-Simulation and Computation*, volume 17, numero 2, pagine 581–607, 1988.

[250] H. Wold, "Path models with latent variables: The nipals approach," in *Quantitative sociology*. Elsevier, 1975, pagine 307–357.

[251] A. Höskuldsson, "Pls regression methods," *Journal of chemometrics*, volume 2, numero 3, pagine 211–228, 1988.

[252] M. Mahfouz, A. Badawi, B. Merkl, E. E. A. Fatah, E. Pritchard, K. Kesler, M. Moore, R. Jantz, e L. Jantz, "Patella sex determination by 3d statistical shape models and nonlinear classifiers," *Forensic science international*, volume 173, numero 2-3, pagine 161–170, 2007.

[253] J.-T. Jeng, "Hybrid approach of selecting hyperparameters of support vector machine for regression," *IEEE Transactions on Systems, Man, and Cybernetics, Part B (Cybernetics)*, volume 36, numero 3, pagine 699–709, 2006.

[254] L. Geronzi, A. Bel-Brunon, A. Martinez, M. Rochette, M. Sensale, O. Bouchot, A. Lalande, S. Lin, P. P. Valentini, e M. E. Biancolini, "Calibration of the mechanical boundary conditions for a patient-specific thoracic aorta

model including the heart motion effect," *IEEE Transactions on Biomedical Engineering*, 2023.

[255] M. L. Neal e R. Kerckhoffs, "Current progress in patient-specific modeling," *Brief. Bioinform.*, volume 11, numero 1, pagine 111–126, 2010.

[256] F. P. Vidal, P.-F. Villard, e E. Lutton, "Tuning of patient-specific deformable models using an adaptive evolutionary optimization strategy," *IEEE Trans. Biomed. Eng.*, volume 59, numero 10, pagine 2942–2949, 2012.

[257] C. Martin, W. Sun, e J. Elefteriades, "Patient-specific finite element analysis of ascending aorta aneurysms," *Am. J. Physiol. Heart Circ. Physiol.*, volume 308, numero 10, pagine H1306–H1316, 2015.

[258] A. Redaelli e E. Votta, "Cardiovascular patient-specific modeling: Where are we now and what does the future look like?" *APL Bioeng.*, volume 4, numero 4, pagina 040401, 2020.

[259] C. J. Beller, M. R. Labrosse, M. J. Thubrikar, e F. Robicsek, "Role of aortic root motion in the pathogenesis of aortic dissection," *Circulation*, volume 109, numero 6, pagine 763–769, 2004.

[260] A. Wittek, K. Karatolios, C.-P. Fritzen, J. Bereiter-Hahn, B. Schieffer, R. Moosdorf, S. Vogt, e C. Blase, "Cyclic three-dimensional wall motion of the human ascending and abdominal aorta characterized by time-resolved three-dimensional ultrasound speckle tracking," *Biomech. Model. Mechanobiol.*, volume 15, numero 5, pagine 1375–1388, 2016.

[261] S. Cutugno, V. Agnese, G. Gentile, G. M. Raffa, A. D. Wisneski, J. M. Guccione, M. Pilato, e S. Pasta, "Patient-specific analysis of ascending thoracic aortic aneurysm with the living heart human model," *Bioengineering*, volume 8, numero 11, pagina 175, 2021.

[262] D. C. Wendell, M. M. Samyn, J. R. Cava, M. M. Krolikowski, e J. F. LaDisa, "The impact of cardiac motion on aortic valve flow used in computational simulations of the thoracic aorta," *J. Biomech. Eng.*, volume 138, numero 9, 2016.

[263] T. F. Weber, M.-K. Ganten, D. Böckler, P. Geisbüsch, H.-U. Kauczor, e H. von Tengg-Kobligk, "Heartbeat-related displacement of the thoracic aorta

in patients with chronic aortic dissection type b: quantification by dynamic cta," *Eur. J. Radiol.*, volume 72, numero 3, pagine 483–488, 2009.

[264] T. F. Weber, T. Müller, A. Biesdorf, S. Wörz, F. Rengier, T. Heye, T. Holland-Letz, K. Rohr, H.-U. Kauczor, e H. von Tengg-Kobligk, "True four-dimensional analysis of thoracic aortic displacement and distension using model-based segmentation of computed tomography angiography," *Int. J. Card. Imaging*, volume 30, numero 1, pagine 185–194, 2014.

[265] D. Rueckert, P. Burger, S. Forbat, R. Mohiaddin, e G.-Z. Yang, "Automatic tracking of the aorta in cardiovascular mr images using deformable models," *IEEE Trans. Med. Imaging*, volume 16, numero 5, pagine 581–590, 1997.

[266] A. D. Caballero e S. Laín, "A review on computational fluid dynamics modelling in human thoracic aorta," *Cardiovasc. Eng. Technol.*, volume 4, numero 2, pagine 103–130, 2013.

[267] L. Garber, S. Khodaei, e Z. Keshavarz-Motamed, "The critical role of lumped parameter models in patient-specific cardiovascular simulations," *Arch. Comput. Methods Eng.*, pagine 1–24, 2021.

[268] Y. Shi, P. Lawford, e R. Hose, "Review of zero-d and 1-d models of blood flow in the cardiovascular system," *Biomed. Eng. Online*, volume 10, numero 1, pagine 1–38, 2011.

[269] S. Jin, J. Oshinski, e D. P. Giddens, "Effects of wall motion and compliance on flow patterns in the ascending aorta," *J. Biomech. Eng.*, volume 125, numero 3, pagine 347–354, 2003.

[270] S. Z. Pagoulatou, M. Ferraro, B. Trachet, V. Bikia, G. Rovas, L. A. Crowe, J.-P. Vallée, D. Adamopoulos, e N. Stergiopulos, "The effect of the elongation of the proximal aorta on the estimation of the aortic wall distensibility," *Biomech. Model. Mechanobiol.*, volume 20, numero 1, pagine 107–119, 2021.

[271] F. Silver, D. Christiansen, e C. Buntin, "Mechanical properties of the aorta: a review." *Crit. Rev. Biomed. Eng.*, volume 17, numero 4, pagine 323–358, 1989.

[272] S. Liu e Y. Fung, "Zero-stress states of arteries," *J. Biomech. Eng.*, volume 110, numero 1, pagine 82–84, 1988.

[273] S. De Putter, B. Wolters, M. Rutten, M. Breeuwer, F. Gerritsen, e F. Van de Vosse, "Patient-specific initial wall stress in abdominal aortic aneurysms with

a backward incremental method," *J. Biomech.*, volume 40, numero 5, pagine 1081–1090, 2007.

[274] C. A. Taylor e C. Figueroa, "Patient-specific modeling of cardiovascular mechanics," *Annu. Rev. Biomed. Eng.*, volume 11, pagine 109–134, 2009.

[275] P. Reymond, P. Crosetto, S. Deparis, A. Quarteroni, e N. Stergiopulos, "Physiological simulation of blood flow in the aorta: comparison of hemodynamic indices as predicted by 3-d fsi, 3-d rigid wall and 1-d models," *Med. Eng. Phys.*, volume 35, numero 6, pagine 784–791, 2013.

[276] N. J. Petterson, E. M. van Disseldorp, M. R. van Sambeek, F. N. van de Vosse, e R. G. Lopata, "Including surrounding tissue improves ultrasound-based 3d mechanical characterization of abdominal aortic aneurysms," *J. Biomech.*, volume 85, pagine 126–133, 2019.

[277] J. Gindre, A. Bel-Brunon, M. Rochette, A. Lucas, A. Kaladji, P. Haigron, e A. Combescure, "Patient-specific finite-element simulation of the insertion of guidewire during an evar procedure: guidewire position prediction validation on 28 cases," *IEEE Trans. Biomed. Eng.*, volume 64, numero 5, pagine 1057–1066, 2016.

[278] P. Moireau, N. Xiao, M. Astorino, C. A. Figueroa, D. Chapelle, C. Taylor, e J.-F. Gerbeau, "External tissue support and fluid–structure simulation in blood flows," *Biomech. Model. Mechanobiol.*, volume 11, numero 1, pagine 1–18, 2012.

[279] K. Bäumler, V. Vedula, A. M. Sailer, J. Seo, P. Chiu, G. Mistelbauer, F. P. Chan, M. P. Fischbein, A. L. Marsden, e D. Fleischmann, "Fluid–structure interaction simulations of patient-specific aortic dissection," *Biomech. Model. Mechanobiol.*, volume 19, numero 5, pagine 1607–1628, 2020.

[280] P. Moireau, C. Bertoglio, N. Xiao, C. A. Figueroa, C. Taylor, D. Chapelle, e J.-F. Gerbeau, "Sequential identification of boundary support parameters in a fluid-structure vascular model using patient image data," *Biomech. Model. Mechanobiol.*, volume 12, numero 3, pagine 475–496, 2013.

[281] S. Chandra, S. S. Raut, A. Jana, R. W. Biederman, M. Doyle, S. C. Muluk, e E. A. Finol, "Fluid-structure interaction modeling of abdominal aortic aneurysms: the impact of patient-specific inflow conditions and fluid/solid coupling," *J. Biomech. Eng.*, volume 135, numero 8, 2013.

[282] A. I. Khuri e S. Mukhopadhyay, "Response surface methodology," *Wiley Interdisciplinary Reviews: Computational Statistics*, volume 2, numero 2, pagine 128–149, 2010.

[283] K. L. Losenno, R. L. Goodman, e M. W. Chu, "Bicuspid aortic valve disease and ascending aortic aneurysms: gaps in knowledge," *Cardiol. Res. Pract.*, volume 2012, 2012.

[284] J. Rooprai, M. Boodhwani, L. Beauchesne, K.-L. Chan, C. Dennie, S. Nagpal, D. Messika-Zeitoun, e T. Coutinho, "Thoracic aortic aneurysm growth in bicuspid aortic valve patients: role of aortic stiffness and pulsatile hemodynamics," *Journal of the American Heart Association*, volume 8, numero 8, pagina e010885, 2019.

[285] K. M. Link, S. P. Loehr, D. M. Baker, e N. M. Lesko, "Magnetic resonance imaging of the thoracic aorta," in *Semin. Ultrasound CT MR*, volume 14, numero 2. Elsevier, 1993, pagine 91–105.

[286] R. Kikinis, S. D. Pieper, e K. G. Vosburgh, "3d slicer: a platform for subject-specific image analysis, visualization, and clinical support," in *Intraoperative imaging and image-guided therapy*. Springer, 2014, pagine 277–289.

[287] G. Taubin, T. Zhang, e G. Golub, "Optimal surface smoothing as filter design," in *Comput. Vis. ECCV*. Springer, 1996, pagine 283–292.

[288] P. J. Clark e F. C. Evans, "Distance to nearest neighbor as a measure of spatial relationships in populations," *Ecology*, volume 35, numero 4, pagine 445–453, 1954.

[289] S. Gross-Hardt, F. Boehning, U. Steinseifer, T. Schmitz-Rode, e T. A. Kaufmann, "Mesh sensitivity analysis for quantitative shear stress assessment in blood pumps using computational fluid dynamics," *J. Biomech. Eng.*, volume 141, numero 2, 2019.

[290] D. Oliveira, S. A. Rosa, J. Tiago, R. C. Ferreira, A. F. Agapito, e A. Sequeira, "Bicuspid aortic valve aortopathies: An hemodynamics characterization in dilated aortas," *Comput. Methods Biomech. Biomed. Eng.*, volume 22, numero 8, pagine 815–826, 2019.

[291] E. Faggiano, L. Antiga, G. Puppini, A. Quarteroni, G. B. Luciani, e C. Vergara, "Helical flows and asymmetry of blood jet in dilated ascending aorta with

normally functioning bicuspid valve," *Biomech. Model. Mechanobiol.*, volume 12, numero 4, pagine 801–813, 2013.

[292] D. Bonomi, C. Vergara, E. Faggiano, M. Stevanella, C. Conti, A. Redaelli, G. Puppini, G. Faggian, L. Formaggia, e G. B. Luciani, "Influence of the aortic valve leaflets on the fluid-dynamics in aorta in presence of a normally functioning bicuspid valve," *Biomech. Model. Mechanobiol.*, volume 14, numero 6, pagine 1349–1361, 2015.

[293] P. Thavendiranathan, C. Guetter, J. S. da Silveira, X. Lu, D. Scandling, H. Xue, M.-P. Jolly, S. V. Raman, e O. P. Simonetti, "Mitral annular velocity measurement with cardiac magnetic resonance imaging using a novel annular tracking algorithm: Validation against echocardiography," *Magn. Reson. Imaging*, volume 55, pagine 72–80, 2019.

[294] J. M. Blain, *The complete guide to Blender graphics: computer modeling & animation*. AK Peters/CRC Press, 2019.

[295] D. Sucha, V. Tuncay, N. H. Prakken, T. Leiner, P. M. van Ooijen, M. Oudkerk, e R. P. Budde, "Does the aortic annulus undergo conformational change throughout the cardiac cycle? a systematic review," *Eur. Heart J. Cardiovasc. Imaging*, volume 16, numero 12, pagine 1307–1317, 2015.

[296] J. Tomasi, F. Le Bars, C. Shao, A. Lucas, M. Lederlin, P. Haigron, e J. Verhoye, "Patient-specific and real-time model of numerical simulation of the hemodynamics of type b aortic dissections," *Med. Hypotheses*, volume 135, pagina 109477, 2020.

[297] R. M. Romarowski, A. Lefieux, S. Morganti, A. Veneziani, e F. Auricchio, "Patient-specific cfd modelling in the thoracic aorta with pc-mri–based boundary conditions: A least-square three-element windkessel approach," *Int. J. Numer. Methods Biomed. Eng.*, volume 34, numero 11, pagina e3134, 2018.

[298] P. J. Blanco e R. A. Feijóo, "A 3d-1d-0d computational model for the entire cardiovascular system," *Mec. comput.*, volume 29, numero 59, pagine 5887–5911, 2010.

[299] S. Bozkurt, "Mathematical modeling of cardiac function to evaluate clinical cases in adults and children," *PloS one*, volume 14, numero 10, pagina e0224663, 2019.

[300] T. Korakianitis e Y. Shi, "A concentrated parameter model for the human cardiovascular system including heart valve dynamics and atrioventricular interaction," *Med. Eng. Phys.*, volume 28, numero 7, pagine 613–628, 2006.

[301] G. R. Cokelet e H. J. Meiselman, "Macro-and micro-rheological properties of blood," *Biomedical and Health Research-Commission of the European Communities Then IOS Press*, volume 69, pagina 45, 2007.

[302] M.-C. Morgant, S. Lin, D. Marin-Castrillon, C. Bernard, A. Laubriet, A. Cochet, A. Lalande, e O. Bouchot, "Comparison of two techniques (in vivo and ex-vivo) for evaluating the elastic properties of the ascending aorta: Prospective cohort study," *PloS one*, volume 16, numero 9, pagina e0256278, 2021.

[303] S. Lin, M.-C. Morgan, A. Lalande, A. Cochet, e O. Bouchot, "Local ex-vivo evaluation of the biomechanical properties of the ascending aortic aneurysms," *Comput. Methods Biomech. Biomed. Eng.*, volume 22, numero sup1, pagine S413–S414, 2019.

[304] Z. Li, T. Luo, S. Wang, H. Jia, Q. Gong, X. Liu, M. P. Sutcliffe, H. Zhu, Q. Liu, D. Chen, *et al.*, "Mechanical and histological characteristics of aortic dissection tissues," *Acta Biomater.*, 2022.

[305] C. Wex, S. Arndt, A. Stoll, C. Bruns, e Y. Kupriyanova, "Isotropic incompressible hyperelastic models for modelling the mechanical behaviour of biological tissues: a review," *Biomed. Eng./Biomed. Tech.*, volume 60, numero 6, pagine 577–592, 2015.

[306] B. Kim, S. B. Lee, J. Lee, S. Cho, H. Park, S. Yeom, e S. H. Park, "A comparison among neo-hookean model, mooney-rivlin model, and ogden model for chloroprene rubber," *Int. J. Precis. Eng. Manuf.*, volume 13, numero 5, pagine 759–764, 2012.

[307] Y. Liu, C. Dang, M. Garcia, H. Gregersen, e G. S. Kassab, "Surrounding tissues affect the passive mechanics of the vessel wall: theory and experiment," *Am. J. Physiol. Heart Circ. Physiol.*, volume 293, numero 6, pagine H3290–H3300, 2007.

[308] A. Milan, F. Tosello, D. Naso, E. Avenatti, D. Leone, C. Magnino, e F. Veglio, "Ascending aortic dilatation, arterial stiffness and cardiac organ damage in essential hypertension," *J. Hypertens.*, volume 31, numero 1, pagine 109–116, 2013.

[309] R. N. Vaishnav e J. Vossoughi, "Estimation of residual strains in aortic segments," in *Biomedical engineering II*. Elsevier, 1983, pagine 330–333.

[310] J. Bols, J. Degroote, B. Trachet, B. Verhegghe, P. Segers, e J. Vierendeels, "A computational method to assess the in vivo stresses and unloaded configuration of patient-specific blood vessels," *J. Comput. Appl. Math.*, volume 246, pagine 10–17, 2013.

[311] M. K. Rausch, M. Genet, e J. D. Humphrey, "An augmented iterative method for identifying a stress-free reference configuration in image-based biomechanical modeling," *J. Biomech.*, volume 58, pagine 227–231, 2017.

[312] J. J. More, "The levenberg-marquardt algorithm: implementation and theory," in *Numer. Anal.* Springer, 1978, pagine 105–116.

[313] C. Stefanadis, C. Stratos, H. Boudoulas, C. Kourouklis, e P. Toutouzas, "Distensibility of the ascending aorta: comparison of invasive and non-invasive techniques in healthy men and in men with coronary artery disease," *Eur. Heart J.*, volume 11, numero 11, pagine 990–996, 1990.

[314] K. Levenberg, "A method for the solution of certain non-linear problems in least squares," *Q. Appl. Math.*, volume 2, numero 2, pagine 164–168, 1944.

[315] F. A. Viana, G. Venter, e V. Balabanov, "An algorithm for fast optimal latin hypercube design of experiments," *International journal for numerical methods in engineering*, volume 82, numero 2, pagine 135–156, 2010.

[316] V. Fiala, P. Dvořák, e R. Pechánek, "Practical approach to multi-objective optimization in ansys softwares," in *2022 20th International Conference on Mechatronics-Mechatronika (ME)*. IEEE, 2022, pagine 1–6.

[317] M. E. Biancolini, "Mesh morphing and smoothing by means of radial basis functions (rbf): a practical example using fluent and rbf morph," in *Handbook of research on computational science and engineering: theory and practice*. IGI Global, 2012, pagine 347–380.

[318] K. Capellini, E. Vignali, E. Costa, E. Gasparotti, M. E. Biancolini, L. Landini, V. Positano, e S. Celi, "Computational fluid dynamic study for ataa hemodynamics: an integrated image-based and radial basis functions mesh morphing approach," *Journal of biomechanical engineering*, volume 140, numero 11, 2018.

[319] T. Collins, L. Bergenholm, T. Abdulla, J. Yates, N. Evans, M. Chappell, e J. Mettetal, "Modeling and simulation approaches for cardiovascular function and their role in safety assessment," *CPT: pharmacometrics & systems pharmacology*, volume 4, numero 3, pagine 175–188, 2015.

[320] S. Bastrakov, I. Meyerov, V. Gergel, A. Gonoskov, A. Gorshkov, E. Efimenko, M. Ivanchenko, M. Kirillin, A. Malova, G. Osipov, *et al.*, "High performance computing in biomedical applications," *Procedia Computer Science*, volume 18, pagine 10–19, 2013.

[321] M. Ferretti e L. Santangelo, "Cloud vs on-premise hpc: a model for comprehensive cost assessment," *Parallel Computing: Technology Trends*, volume 36, numero 2020, pagina 69, 2020.

[322] R. L. Winslow, N. Trayanova, D. Geman, e M. I. Miller, "Computational medicine: translating models to clinical care," *Science translational medicine*, volume 4, numero 158, pagine 158rv11–158rv11, 2012.

[323] A. R. Ghigo, J.-M. Fullana, e P.-Y. Lagrée, "A 2d nonlinear multiring model for blood flow in large elastic arteries," *Journal of Computational Physics*, volume 350, pagine 136–165, 2017.

[324] F. Ballarin, A. Manzoni, A. Quarteroni, e G. Rozza, "Supremizer stabilization of pod–galerkin approximation of parametrized steady incompressible navier–stokes equations," *International Journal for Numerical Methods in Engineering*, volume 102, numero 5, pagine 1136–1161, 2015.

[325] M. Girfoglio, L. Scandurra, F. Ballarin, G. Infantino, F. Nicolo, A. Montalto, G. Rozza, R. Scrofani, M. Comisso, e F. Musumeci, "Non-intrusive data-driven rom framework for hemodynamics problems," *Acta mechanica sinica*, volume 37, pagine 1183–1191, 2021.

[326] C. W. Rowley, T. Colonius, e R. M. Murray, "Model reduction for compressible flows using pod and galerkin projection," *Physica D: Nonlinear Phenomena*, volume 189, numero 1-2, pagine 115–129, 2004.

[327] J. S. Hesthaven e S. Ubbiali, "Non-intrusive reduced order modeling of nonlinear problems using neural networks," *Journal of Computational Physics*, volume 363, pagine 55–78, 2018.

[328] A. Chatterjee, "An introduction to the proper orthogonal decomposition," *Current science*, pagine 808–817, 2000.

[329] S. Niroomandi, I. Alfaro, E. Cueto, e F. Chinesta, "Real-time deformable models of non-linear tissues by model reduction techniques," *Computer methods and programs in biomedicine*, volume 91, numero 3, pagine 223–231, 2008.

[330] A. Arzani e S. T. Dawson, "Data-driven cardiovascular flow modelling: examples and opportunities," *Journal of the Royal Society Interface*, volume 18, numero 175, pagina 20200802, 2021.

[331] N. Dal Santo, A. Manzoni, S. Pagani, A. Quarteroni, *et al.*, "Reduced-order modeling for applications to the cardiovascular system," *Applications; De Gruyter: Berlin, Germany*, pagine 251–278, 2020.

[332] S. Bridio, G. Luraghi, F. Migliavacca, S. Pant, A. García-González, e J. F. R. Matas, "A low dimensional surrogate model for a fast estimation of strain in the thrombus during a thrombectomy procedure," *Journal of the Mechanical Behavior of Biomedical Materials*, volume 137, pagina 105577, 2023.

[333] D. Ye, V. Krzhizhanovskaya, e A. G. Hoekstra, "Data-driven reduced-order modelling for blood flow simulations with geometry-informed snapshots," *arXiv preprint arXiv:2302.11006*, 2023.

[334] L. Liang, W. Mao, e W. Sun, "A feasibility study of deep learning for predicting hemodynamics of human thoracic aorta," *Journal of biomechanics*, volume 99, pagina 109544, 2020.

[335] G. H. Chang, C. M. Schirmer, e Y. Modarres-Sadeghi, "A reduced-order model for wall shear stress in abdominal aortic aneurysms by proper orthogonal decomposition," *Journal of biomechanics*, volume 54, pagine 33–43, 2017.

[336] B. Bisighini, M. Aguirre, M. E. Biancolini, F. Trovalusci, D. Perrin, S. Avril, e B. Pierrat, "Machine learning and reduced order modelling for the simulation of braided stent deployment," *Frontiers in Physiology*, volume 14, pagina 508, 2023.

[337] P. Siena, M. Girfoglio, F. Ballarin, e G. Rozza, "Data-driven reduced order modelling for patient-specific hemodynamics of coronary artery bypass grafts with physical and geometrical parameters," *Journal of Scientific Computing*, volume 94, numero 2, pagina 38, 2023.

[338] E. Kardampiki, E. Vignali, D. Haxhiademi, D. Federici, E. Ferrante, S. Porziani, A. Chiappa, C. Groth, M. Cioffi, M. E. Biancolini, *et al.*, "The hemodynamic effect of modified blalock–taussig shunt morphologies: A computational analysis based on reduced order modeling," *Electronics*, volume 11, numero 13, pagina 1930, 2022.

[339] P. Du, X. Zhu, e J.-X. Wang, "Deep learning-based surrogate model for three-dimensional patient-specific computational fluid dynamics," *Physics of Fluids*, volume 34, numero 8, 2022.

[340] D. M. Marin-Castrillon, L. Geronzi, A. Boucher, S. Lin, M.-C. Morgant, A. Cochet, M. Rochette, S. Leclerc, K. Ambarki, N. Jin, *et al.*, "Segmentation of the aorta in systolic phase from 4d flow mri: multi-atlas vs. deep learning," *Magnetic Resonance Materials in Physics, Biology and Medicine*, pagine 1–14, 2023.

[341] O. Ronneberger, P. Fischer, e T. Brox, "U-net: Convolutional networks for biomedical image segmentation," in *Medical Image Computing and Computer-Assisted Intervention–MICCAI 2015: 18th International Conference, Munich, Germany, October 5-9, 2015, Proceedings, Part III 18*. Springer, 2015, pagine 234–241.

[342] R. Janssens, G. Zeng, e G. Zheng, "Fully automatic segmentation of lumbar vertebrae from ct images using cascaded 3d fully convolutional networks," in *2018 IEEE 15th international symposium on biomedical imaging (ISBI 2018)*. IEEE, 2018, pagine 893–897.

[343] J. A. Collins, J.-V. Munoz, T. R. Patel, M. Loukas, e R. S. Tubbs, "The anatomy of the aging aorta," *Clinical anatomy*, volume 27, numero 3, pagine 463–466, 2014.

[344] A. S. Les, S. C. Shadden, C. A. Figueroa, J. M. Park, M. M. Tedesco, R. J. Herfkens, R. L. Dalman, e C. A. Taylor, "Quantification of hemodynamics in abdominal aortic aneurysms during rest and exercise using magnetic resonance imaging and computational fluid dynamics," *Annals of biomedical engineering*, volume 38, pagine 1288–1313, 2010.

[345] T. Hassan, M. Ezura, E. V. Timofeev, T. Tominaga, T. Saito, A. Takahashi, K. Takayama, e T. Yoshimoto, "Computational simulation of therapeutic

parent artery occlusion to treat giant vertebrobasilar aneurysm," *American journal of neuroradiology*, volume 25, numero 1, pagine 63–68, 2004.

[346] C. Catalano, V. Agnese, G. Gentile, G. M. Raffa, M. Pilato, e S. Pasta, "Atlas-based evaluation of hemodynamic in ascending thoracic aortic aneurysms," *Applied Sciences*, volume 12, numero 1, pagina 394, 2022.

[347] Q. Guo e L. Zhang, "Finite element model updating based on response surface methodology," in *Proceedings of the 22nd IMAC*. Dearborn, USA, 2004, pagine 306–309.

[348] S. Wang, G. Jian, J. Xiao, J. Wen, e Z. Zhang, "Optimization investigation on configuration parameters of spiral-wound heat exchanger using genetic aggregation response surface and multi-objective genetic algorithm," *Applied Thermal Engineering*, volume 119, pagine 603–609, 2017.

[349] L. I. Hatledal, A. Styve, G. Hovland, e H. Zhang, "A language and platform independent co-simulation framework based on the functional mock-up interface," *IEEE Access*, volume 7, pagine 109 328–109 339, 2019.

[350] D. Hauf, S. Süß, A. Strahilov, e J. Franke, "Multifunctional use of functional mock-up units for application in production engineering," in *2017 IEEE 15th International Conference on Industrial Informatics (INDIN)*. IEEE, 2017, pagine 1090–1095.

[351] L. M. De Heer, R. P. Budde, W. P. T. M. Mali, A. M. de Vos, L. A. van Herwerden, e J. Kluin, "Aortic root dimension changes during systole and diastole: evaluation with ecg-gated multidetector row computed tomography," *The international journal of cardiovascular imaging*, volume 27, numero 8, pagine 1195–1204, 2011.

[352] M. M. Zubair, H. W. de Beaufort, V. M. Belvroy, A. Schwein, A. Irshad, A. Mohamed, L. F. Gomez, P. Chinnadurai, F. Nabi, E. Y. Yang, *et al.*, "Impact of cardiac cycle on thoracic aortic geometry morphometric analysis of ecg gated computed tomography," *Annals of Vascular Surgery*, volume 65, pagine 174–182, 2020.

[353] L. R. Bons, A. L. Duijnhouwer, S. Boccalini, A. T. van den Hoven, M. J. van der Vlugt, R. G. Chelu, J. S. McGhie, I. Kardys, A. E. Van Den Bosch, H.-M. J. Siebelink, *et al.*, "Intermodality variation of aortic dimensions: How,

where and when to measure the ascending aorta," *International journal of cardiology*, volume 276, pagine 230–235, 2019.

[354] C. Frazao, A. Tavoosi, B. J. Wintersperger, E. T. Nguyen, R. M. Wald, M. Ouzounian, e K. Hanneman, "Multimodality assessment of thoracic aortic dimensions: comparison of computed tomography angiography, magnetic resonance imaging, and echocardiography measurements," *Journal of Thoracic Imaging*, volume 35, numero 6, pagine 399–406, 2020.

[355] Y. Hirose, S. Hamada, e M. Takamiya, "Predicting the growth of aortic aneurysms: a comparison of linear vs exponential models," *Angiology*, volume 46, numero 5, pagine 413–419, 1995.

[356] G. Martufi, M. Auer, J. Roy, J. Swedenborg, N. Sakalihasan, G. Panuccio, e T. C. Gasser, "Multidimensional growth measurements of abdominal aortic aneurysms," *Journal of vascular surgery*, volume 58, numero 3, pagine 748–755, 2013.

[357] T. E. David, "Surgical treatment of ascending aorta and aortic root aneurysms," *Progress in cardiovascular diseases*, volume 52, numero 5, pagine 438–444, 2010.

[358] S. Heuts, B. P. Adriaans, B. Rylski, C. Mihl, S. C. Bekkers, J. R. Olsthoorn, E. Natour, H. Bouman, M. Berezowski, K. Kosiorowska, *et al.*, "Evaluating the diagnostic accuracy of maximal aortic diameter, length and volume for prediction of aortic dissection," *Heart*, volume 106, numero 12, pagine 892–897, 2020.

[359] P. Ranganathan e R. Aggarwal, "Understanding the properties of diagnostic tests–part 2: Likelihood ratios," *Perspectives in Clinical Research*, volume 9, numero 2, pagina 99, 2018.

[360] P. Ray, Y. L. Manach, B. Riou, T. T. Houle, e D. S. Warner, "Statistical evaluation of a biomarker," *The Journal of the American Society of Anesthesiologists*, volume 112, numero 4, pagine 1023–1040, 2010.

[361] J. M. Oliver, R. Alonso-Gonzalez, A. E. Gonzalez, P. Gallego, A. Sanchez-Recalde, E. Cuesta, A. Aroca, e J. L. Lopez-Sendon, "Risk of aortic root or ascending aorta complications in patients with bicuspid aortic valve with and without coarctation of the aorta," *The American journal of cardiology*, volume 104, numero 7, pagine 1001–1006, 2009.

[362] L. D. Hahn, K. Baeumler, e A. Hsiao, "Artificial intelligence and machine learning in aortic disease," *Current Opinion in Cardiology*, volume 36, numero 6, pagine 695–703, 2021.

[363] A. Monsalve-Torra, D. Ruiz-Fernandez, O. Marin-Alonso, A. Soriano-Payá, J. Camacho-Mackenzie, e M. Carreño-Jaimes, "Using machine learning methods for predicting inhospital mortality in patients undergoing open repair of abdominal aortic aneurysm," *Journal of biomedical informatics*, volume 62, pagine 195–201, 2016.

[364] S. S. Ashkezari, F. Mut, M. Slawski, C. Jimenez, A. Robertson, e J. Cebral, "Identification of small, regularly shaped cerebral aneurysms prone to rupture," *American Journal of Neuroradiology*, volume 43, numero 4, pagine 547–553, 2022.

[365] L. Geronzi, E. Gasparotti, K. Capellini, U. Cella, C. Groth, S. Porziani, A. Chiappa, S. Celi, e M. E. Biancolini, "High fidelity fluid-structure interaction by radial basis functions mesh adaption of moving walls: a workflow applied to an aortic valve," *Journal of Computational Science*, volume 51, pagina 101327, 2021.

[366] B. Reutersberg, B. Haller, J. Mariss, H.-H. Eckstein, e S. Ockert, "Measurements after image post-processing are more precise in the morphometric assessment of thoracic aortic aneurysms: an intermodal and intra-observer evaluation," *European Journal of Vascular and Endovascular Surgery*, volume 52, numero 4, pagine 509–517, 2016.

[367] M. E. Casciaro, D. Craiem, G. Chironi, S. Graf, L. Macron, E. Mousseaux, A. Simon, e R. L. Armentano, "Identifying the principal modes of variation in human thoracic aorta morphology," *Journal of Thoracic Imaging*, volume 29, numero 4, pagine 224–232, 2014.

[368] P. D. Kalogerakos, M. A. Zafar, Y. Li, S. K. Mukherjee, B. A. Ziganshin, J. A. Rizzo, e J. A. Elefteriades, "Root dilatation is more malignant than ascending aortic dilation," *Journal of the American Heart Association*, volume 10, numero 14, pagina e020645, 2021.

[369] A. Della Corte, C. Bancone, M. Buonocore, G. Dialetto, F. E. Covino, S. Manduca, G. Scognamiglio, V. D'Oria, e M. De Feo, "Pattern of ascending aortic dimensions predicts the growth rate of the aorta in patients with bicuspid

aortic valve," *JACC: Cardiovascular Imaging*, volume 6, numero 12, pagine 1301–1310, 2013.

[370] M. van Hout, J. Juffermans, H. Lamb, E. Kröner, P. van den Boogaard, M. Schalij, I. Dekkers, A. Scholte, e J. Westenberg, "Ascending aorta curvature and flow displacement are associated with accelerated aortic growth at long-term follow-up: A mri study in marfan and thoracic aortic aneurysm patients," *IJC Heart & Vasculature*, volume 38, pagina 100926, 2022.

[371] C. M. García-Herrera, J. M. Atienza, F. Rojo, E. Claes, G. Guinea, D. J. Celentano, C. García-Montero, e R. L. Burgos, "Mechanical behaviour and rupture of normal and pathological human ascending aortic wall," *Medical & biological engineering & computing*, volume 50, pagine 559–566, 2012.

[372] A. J. McLarty, M. Bishawi, S. B. Yelika, A. L. Shroyer, e J. Romeiser, "Surveillance of moderate-size aneurysms of the thoracic aorta," *Journal of cardiothoracic surgery*, volume 10, numero 1, pagine 1–7, 2015.

[373] M. Ashok e A. Gupta, "A systematic review of the techniques for the automatic segmentation of organs-at-risk in thoracic computed tomography images," *Archives of Computational Methods in Engineering*, volume 28, pagine 3245–3267, 2021.

[374] E. Girdauskas, M. Rouman, K. Disha, B. Fey, G. Dubslaff, B. Theis, I. Petersen, M. Gutberlet, M. A. Borger, e T. Kuntze, "Functional aortic root parameters and expression of aortopathy in bicuspid versus tricuspid aortic valve stenosis," *Journal of the American College of Cardiology*, volume 67, numero 15, pagine 1786–1796, 2016.

[375] F. Cosentino, G. M. Raffa, G. Gentile, V. Agnese, D. Bellavia, M. Pilato, e S. Pasta, "Statistical shape analysis of ascending thoracic aortic aneurysm: correlation between shape and biomechanical descriptors," *Journal of Personalized Medicine*, volume 10, numero 2, pagina 28, 2020.

[376] C. Pisano, C. R. Balistreri, P. Nardi, C. Altieri, F. Bertoldo, D. Buioni, M. S. Ferrante, L. Asta, D. Trombetti, e G. Ruvolo, "Risk of aortic dissection in patients with ascending aorta aneurysm: A new biological, morphological, and biomechanical network behind the aortic diameter," *Vessel Plus*, volume 4, pagina 33, 2020.

[377] G.-Y. Suh, R. E. Beygui, D. Fleischmann, e C. P. Cheng, "Aortic arch vessel geometries and deformations in patients with thoracic aortic aneurysms and dissections," *Journal of Vascular and Interventional Radiology*, volume 25, numero 12, pagine 1903–1911, 2014.

[378] S. Lin, M. C. Morgant, D. M. Marín-Castrillón, P. M. Walker, L. S. A. Glélé, A. Boucher, B. Presles, O. Bouchot, e A. Lalande, "Aortic local biomechanical properties in ascending aortic aneurysms," *Acta Biomaterialia*, volume 149, pagine 40–50, 2022.

[379] M. Y. Salmasi, S. Pirola, S. Sasidharan, S. M. Fisichella, A. Redaelli, O. A. Jarral, D. P. O'Regan, A. Y. Oo, J. E. Moore Jr, X. Y. Xu, *et al.*, "High wall shear stress can predict wall degradation in ascending aortic aneurysms: an integrated biomechanics study," *Frontiers in Bioengineering and Biotechnology*, pagina 935, 2021.

[380] J. E. Roos, J. K. Willmann, D. Weishaupt, M. Lachat, B. Marincek, e P. R. Hilfiker, "Thoracic aorta: motion artifact reduction with retrospective and prospective electrocardiography-assisted multi-detector row ct," *Radiology*, volume 222, numero 1, pagine 271–277, 2002.

[381] P. Carrascosa, C. Capuñay, A. Deviggiano, G. A. Rodríguez-Granillo, M. I. Sagarduy, P. Cortines, J. Carrascosa, e J. C. Parodi, "Thoracic aorta cardiac-cycle related dynamic changes assessed with a 256-slice ct scanner," *Cardiovasc. Diagn. Ther.*, volume 3, numero 3, pagina 125, 2013.

[382] D. Chemla, S. Millasseau, O. Hamzaoui, J.-L. Teboul, X. Monnet, F. Michard, e M. Jozwiak, "New method to estimate central systolic blood pressure from peripheral pressure: A proof of concept and validation study," *Frontiers in Cardiovascular Medicine*, volume 8, 2021.

[383] J. C. Greenfield Jr e D. J. Patel, "Relation between pressure and diameter in the ascending aorta of man," *Circ. Res.*, volume 10, numero 5, pagine 778–781, 1962.

[384] N. V. Navkar, E. Yeniaras, D. J. Shah, N. V. Tsekos, e Z. Deng, "Extracting geometric features of aortic valve annulus motion from dynamic mri for guiding interventions," in *2011 IEEE International Symposium on Biomedical Imaging: From Nano to Macro*. IEEE, 2011, pagine 1302–1305.

[385] T. Plonek, M. Berezowski, J. Kurcz, P. Podgorski, M. Sasiadek, B. Rylski, A. Mysiak, e M. Jasinski, "The evaluation of the aortic annulus displacement during cardiac cycle using magnetic resonance imaging," *BMC Cardiovasc. Disord.*, volume 18, numero 1, pagine 1–6, 2018.

[386] S. Kozerke, M. B. Scheidegger, E. M. Pedersen, e P. Boesiger, "Heart motion adapted cine phase-contrast flow measurements through the aortic valve," *Magn. Reson. Med.: An Official Journal of the International Society for Magnetic Resonance in Medicine*, volume 42, numero 5, pagine 970–978, 1999.

[387] C. J. Beller, M. Labrosse, M. Thubrikar, e F. Robicsek, "Finite element modeling of the thoracic aorta: including aortic root motion to evaluate the risk of aortic dissection," *J. Med. Eng. Technol.*, volume 32, numero 2, pagine 167–170, 2008.

[388] S. Lin, X. Han, Y. Bi, S. Ju, e L. Gu, "Fluid-structure interaction in abdominal aortic aneurysm: Effect of modeling techniques," *BioMed research international*, volume 2017, 2017.

[389] D. Farotto, P. Segers, B. Meuris, J. Vander Sloten, e N. Famaey, "The role of biomechanics in aortic aneurysm management: requirements, open problems and future prospects," *J. Mech. Behav. Biomed. Mater.*, volume 77, pagine 295–307, 2018.

[390] F. Cosentino, V. Agnese, G. M. Raffa, G. Gentile, D. Bellavia, M. Zingales, M. Pilato, e S. Pasta, "On the role of material properties in ascending thoracic aortic aneurysms," *Comput. Biol. Med.*, volume 109, pagine 70–78, 2019.

[391] C. M. Scotti e E. A. Finol, "Compliant biomechanics of abdominal aortic aneurysms: a fluid–structure interaction study," *Comput. Struct.*, volume 85, numero 11-14, pagine 1097–1113, 2007.

[392] M. Sermesant, H. Delingette, e N. Ayache, "An electromechanical model of the heart for image analysis and simulation," *IEEE Trans. Med. Imaging*, volume 25, numero 5, pagine 612–625, 2006.

[393] H. Ladjal, B. Shariat, J. Azencot, e M. Beuve, "Appropriate biomechanics and kinematics modeling of the respiratory system: Human diaphragm and thorax," in *2013 IEEE/RSJ International Conference on Intelligent Robots and Systems*. IEEE, 2013, pagine 2004–2009.

[394] N. J. Pelc, R. J. Herfkens, A. Shimakawa, D. R. Enzmann, *et al.*, "Phase contrast cine magnetic resonance imaging," *Magn. Reson. Q.*, volume 7, numero 4, pagine 229–254, 1991.

[395] T. C. Shidhore, H. L. Cebull, M. C. Madden, I. C. Christov, V. L. Rayz, e C. J. Goergen, "Estimating external tissue support parameters with fluid–structure interaction models from 4d ultrasound of murine thoracic aortae," *Engineering with Computers*, volume 38, numero 5, pagine 4005–4022, 2022.

[396] J. T. Hansen, *Netter's Clinical Anatomy-E-Book*. Elsevier Health Sciences, 2021.

[397] E. U. Azeloglu, M. B. Albro, V. A. Thimmappa, G. A. Ateshian, e K. D. Costa, "Heterogeneous transmural proteoglycan distribution provides a mechanism for regulating residual stresses in the aorta," *American Journal of Physiology-Heart and Circulatory Physiology*, volume 294, numero 3, pagine H1197–H1205, 2008.

[398] G. A. Holzapfel e R. W. Ogden, "Modelling the layer-specific three-dimensional residual stresses in arteries, with an application to the human aorta," *Journal of the Royal Society Interface*, volume 7, numero 46, pagine 787–799, 2010.

[399] A. Souche e K. Valen-Sendstad, "High-fidelity fluid structure interaction simulations of turbulent-like aneurysm flows reveals high-frequency narrowband wall vibrations: A stimulus of mechanobiological relevance?" *Journal of Biomechanics*, volume 145, pagina 111369, 2022.

[400] M. Hoeijmakers, I. Waechter-Stehle, J. Weese, e F. Van de Vosse, "Combining statistical shape modeling, cfd, and meta-modeling to approximate the patient-specific pressure-drop across the aortic valve in real-time," *International Journal for Numerical Methods in Biomedical Engineering*, volume 36, numero 10, pagina e3387, 2020.

[401] C. Spadaccio, F. Nappi, N. Al-Attar, F. W. Sutherland, C. Acar, A. Nenna, M. Trombetta, M. Chello, e A. Rainer, "Old myths, new concerns: the long-term effects of ascending aorta replacement with dacron grafts. not all that glitters is gold," *J. Cardiovasc. Transl. Res.*, volume 9, numero 4, pagine 334–342, 2016.

[402] S. Morganti, N. Brambilla, A. Petronio, A. Reali, F. Bedogni, e F. Auricchio, "Prediction of patient-specific post-operative outcomes of tavi procedure:

The impact of the positioning strategy on valve performance," *J. Biomech.*, volume 49, numero 12, pagine 2513–2519, 2016.

[403] C. W. Ong, I. Wee, N. Syn, S. Ng, H. L. Leo, A. M. Richards, e A. M. Choong, "Computational fluid dynamics modeling of hemodynamic parameters in the human diseased aorta: A systematic review," *Annals of Vascular Surgery*, volume 63, pagine 336–381, 2020.

[404] R. Gharleghi, G. Samarasinghe, A. Sowmya, e S. Beier, "Deep learning for time averaged wall shear stress prediction in left main coronary bifurcations," in *2020 IEEE 17th International Symposium on Biomedical Imaging (ISBI)*. IEEE, 2020, pagine 1–4.

[405] E. Pajaziti, J. Montalt-Tordera, C. Capelli, R. Sivera, E. Sauvage, M. Quail, S. Schievano, e V. Muthurangu, "Shape-driven deep neural networks for fast acquisition of aortic 3d pressure and velocity flow fields," *PLOS Computational Biology*, volume 19, numero 4, pagina e1011055, 2023.

[406] I. Goodfellow, Y. Bengio, e A. Courville, *Deep learning*. MIT press, 2016.

[407] W. Wolański, B. Gzik-Zroska, K. Joszko, M. Gzik, e D. Sołtan, "Numerical analysis of blood flow through artery with elastic wall of a vessel," in *Innovations in Biomedical Engineering*. Springer, 2017, pagine 193–200.

[408] M. Calka, P. Perrier, J. Ohayon, C. Grivot-Boichon, M. Rochette, e Y. Payan, "Machine-learning based model order reduction of a biomechanical model of the human tongue," *Computer Methods and Programs in Biomedicine*, volume 198, pagina 105786, 2021.

[409] W. Seed e N. Wood, "Velocity patterns in the aorta," *Cardiovascular research*, volume 5, numero 3, pagine 319–330, 1971.

[410] F. Catapano, G. Pambianchi, G. Cundari, J. Rebelo, F. Cilia, I. Carbone, C. Catalano, M. Francone, e N. Galea, "4d flow imaging of the thoracic aorta: is there an added clinical value?" *Cardiovascular Diagnosis and Therapy*, volume 10, numero 4, pagina 1068, 2020.

[411] K. Shameer, K. W. Johnson, B. S. Glicksberg, J. T. Dudley, e P. P. Sengupta, "Machine learning in cardiovascular medicine: are we there yet?" *Heart*, volume 104, numero 14, pagine 1156–1164, 2018.

[412] E. Politou, E. Alepis, e C. Patsakis, "Forgetting personal data and revoking consent under the gdpr: Challenges and proposed solutions," *Journal of cybersecurity*, volume 4, numero 1, pagina tyy001, 2018.

[413] Y. Liu, S. Ong, e A. Nee, "State-of-the-art survey on digital twin implementations," *Advances in Manufacturing*, volume 10, numero 1, pagine 1–23, 2022.

[414] J. I. Jimenez, H. Jahankhani, e S. Kendzierskyj, "Health care in the cyberspace: Medical cyber-physical system and digital twin challenges," *Digital twin technologies and smart cities*, pagine 79–92, 2020.

[415] G. Jalalahmadi, C. Linte, e M. Helguera, "A numerical framework for studying the biomechanical behavior of abdominal aortic aneurysm," in *Medical Imaging 2017: Biomedical Applications in Molecular, Structural, and Functional Imaging*, volume 10137. SPIE, 2017, pagine 589–604.

[416] L. R. Sprouse II, G. H. Meier III, C. J. LeSar, R. J. DeMasi, J. Sood, F. N. Parent, M. J. Marcinzyck, e R. G. Gayle, "Comparison of abdominal aortic aneurysm diameter measurements obtained with ultrasound and computed tomography: is there a difference?" *Journal of vascular surgery*, volume 38, numero 3, pagine 466–471, 2003.

[417] F. A. Lederle, S. E. Wilson, G. R. Johnson, D. B. Reinke, F. N. Littooy, C. W. Acher, L. M. Messina, D. J. Ballard, H. J. Ansel, C. S. P. C. Center, *et al.*, "Variability in measurement of abdominal aortic aneurysms," *Journal of vascular surgery*, volume 21, numero 6, pagine 945–952, 1995.

[418] A. Valentin, J. D. Humphrey, e G. A. Holzapfel, "A multi-layered computational model of coupled elastin degradation, vasoactive dysfunction, and collagenous stiffening in aortic aging," *Annals of biomedical engineering*, volume 39, pagine 2027–2045, 2011.

[419] C. S. Pilkerton, S. S. Singh, T. K. Bias, e S. J. Frisbee, "Changes in cardiovascular health in the united states, 2003–2011," *Journal of the American Heart Association*, volume 4, numero 9, pagina e001650, 2015.

[420] M. C. Lancaster, A. M. Salem Omar, S. Narula, H. Kulkarni, J. Narula, e P. P. Sengupta, "Phenotypic clustering of left ventricular diastolic function parameters: patterns and prognostic relevance," *JACC: Cardiovascular Imaging*, volume 12, numero 7 Part 1, pagine 1149–1161, 2019.

[421] A. Maier, M. Gee, C. Reeps, J. Pongratz, H.-H. Eckstein, e W. Wall, "A comparison of diameter, wall stress, and rupture potential index for abdominal aortic aneurysm rupture risk prediction," *Annals of biomedical engineering*, volume 38, pagine 3124–3134, 2010.

[422] B.-K. Lee, "Computational fluid dynamics in cardiovascular disease," *Korean circulation journal*, volume 41, numero 8, pagine 423–430, 2011.

[423] B. Chung e J. R. Cebral, "Cfd for evaluation and treatment planning of aneurysms: review of proposed clinical uses and their challenges," *Annals of biomedical engineering*, volume 43, pagine 122–138, 2015.

[424] Z. Zainib, F. Ballarin, S. Fremes, P. Triverio, L. Jiménez-Juan, e G. Rozza, "Reduced order methods for parametric optimal flow control in coronary bypass grafts, toward patient-specific data assimilation," *International Journal for Numerical Methods in Biomedical Engineering*, volume 37, numero 12, pagina e3367, 2021.

[425] X. Li, X. Liu, X. Deng, e Y. Fan, "Interplay between artificial intelligence and biomechanics modeling in the cardiovascular disease prediction," *Biomedicines*, volume 10, numero 9, pagina 2157, 2022.

[426] L. Antiga, M. Piccinelli, L. Botti, B. Ene-Iordache, A. Remuzzi, e D. A. Steinman, "An image-based modeling framework for patient-specific computational hemodynamics," *Medical & biological engineering & computing*, volume 46, pagine 1097–1112, 2008.

List of publications and scientific awards

I.1 Publications

During the MeDiTATe PhD program, the following scientific works have been realized and published:

- *"High fidelity fluid-structure interaction by radial basis functions mesh adaption of moving walls: A workflow applied to an aortic valve"*, **Geronzi L.** et al., Journal of Computational Science, 51, 101327 (2021) [365].
- *"Assessment of shape-based features ability to predict the ascending aortic aneurysm growth"*, **Geronzi L.** et al., Frontiers in Physiology 14: 378, (2023) [172].
- *"Computer-aided shape features extraction and regression models for predicting the ascending aortic aneurysm growth rate"*, **Geronzi L.** et al., Computers in Biology and Medicine, 162, 107052, (2023) [173].
- *"Calibration of the mechanical boundary conditions for a patient-specific thoracic aorta model including the heart motion effect"*, **Geronzi, L.** et al., IEEE Transactions on Biomedical Engineering, (2023) [254].

The following publication related to the automatic segmentation of magnetic resonance images was carried out in collaboration with the Hospital of Dijon, France:

- *"Segmentation of the aorta in systolic phase from 4D flow MRI: multi-atlas vs. deep learning"*, Marin-Castrillon D. M., **Geronzi L.**, Magnetic Resonance Materials in Physics, Biology and Medicine, 1-14, (2023) [254].

The methods proposed in the previous publication were accurately described in the doctoral thesis defended by Diana Marcela Marin-Castrillon at the University of Bourgogne, France.

I.2 Awards

With the work carried out during the 3 years of MeDiTATe, the following academic awards have been won:

- ***PhD level award SB3C Conference 2023.*** First Runner-Up: "Tuning of the mechanical boundary conditions parameters for a patient-specific thoracic aorta model.", June 2023, Vail, Colorado, USA.
- ***Daniel Guilmet award MASH Congress 2023.*** Second place: "A semi-automatic method to obtain metrics of interest for evaluating the ascending aortic aneurysm growth.", May 2023, Bastia, Corse.

I.3 Technology transfer

A publication related to the research contained in Chapters 5 and 8 has been prepared. However, the methods proposed in those parts integrated with the 3D Slicer prototype described in the Appendix are fundamental parts of a business plan evaluated in the regional (Regione Lazio) Start-Cup competition, where the business idea prepared from April 2023 to September 2023 and presented has reached the finals scheduled for the end of October 2023. For these reasons, the publication has not been submitted, the code related to the 3D Slicer extension described in the Appendix A has not yet been published in any open-access online repository and the material is treated with the utmost confidentiality.